KINEMATICS MEASUREMENTS OF REGULAR, IRREGULAR, AND ROGUE WAVES BY PIV/LDV

A Dissertation

by

HAE-JIN CHOI

Submitted to the Office of Graduate Studies of
Texas A&M University
in partial fulfillment of the requirements for the degree of

DOCTOR OF PHILOSOPHY

December 2005

Major Subject: Ocean Engineering

KINEMATICS MEASUREMENTS OF REGULAR, IRREGULAR, AND ROGUE WAVES BY PIV/LDV

A Dissertation

by

HAE-JIN CHOI

Submitted to the Office of Graduate Studies of
Texas A&M University
in partial fulfillment of the requirements for the degree of

DOCTOR OF PHILOSOPHY

Approved by:

Chair of Committee,	Moo-Hyun Kim
Committee Members,	Alan B. Palazzolo
	Cheung H. Kim
	Jun Zhang
Head of Department,	David V. Rosowsky

December 2005

Major Subject: Ocean Engineering

ABSTRACT

Kinematics Measurements of Regular, Irregular, and Rogue Waves by PIV/LDV.

(December 2005)

Hae-jin Choi, B.S., Pusan National University; M.S., Texas A&M University

Chair of Advisory Committee: Dr. Moo-Hyun Kim

A comprehensive experimental study was conducted to produce benchmark wave kinematics data for five different regular waves and the maxima of four different irregular wave trains. Two of the irregular waves generated are in the category of rogue waves. A series of experiments were conducted in a 2-D wave tank at Texas A&M University to measure wave velocities and accelerations using LDV and PIV systems. The wave crests of regular and rogue waves are the focus of this study. With the measured wave velocity field, the wave accelerations were computed using a centered finite difference scheme. Both local and convective components of the total accelerations are obtained from experimental data. Also, the nonlinear wave forces on a truncated slender cylinder are computed by applying the obtained wave kinematics to the Morison equation. The force results based on measured wave kinematics are compared with those based on the kinematics of linear extrapolation, Wheeler stretching, and modified stretching. The Wheeler stretching method generally underestimates the actual wave kinematics. The linear extrapolation method is very sensitive to the cutoff frequency of the wave spectrum. The modified stretching method tends to predict the maximum value of wave kinematics above the still water level (SWL) well except for the convective acceleration. The

magnitude of convective acceleration in the regular waves was negligibly small, whereas the magnitudes of horizontal and vertical convective accelerations in the rogue wave were increased rapidly above the SWL.

This dissertation is dedicated,

with love and respect,

to my parents.

ACKNOWLEDGMENTS

This dissertation would not have been possible without the support, encouragement, and help of many people. Professor Moo-Hyun Joseph Kim, my advisor, continuously supported my studies in many ways. He suggested and guided my dissertation topic. His generous discussions and advice always have given critical moment to my dissertation work. His thorough understanding of water wave mechanics helped me correctly set up the problem. His constant encouragement made me never give up. I am also deeply appreciative for the partial financial support during most of my years of studies.

Professor Cheung Hun Kim has greatly contributed to my dissertation through candid discussion and consistent encouragement. He helped me to develop ideas for my dissertation topic, and his suggestions and encouragement gave me confidence in my work. Professor Jun Zhang has given many critical suggestions during my study. His recommendations were always valuable to prepare my dissertation. Professor Alan Palazzolo has served as a member of my graduate committee with good grace and constant encouragement.

Mr. SeungJae Lee, Mr. Yong-Uk Ryu and Dr. Kwang-Hyo Jung, my friends, have given me help, friendship, valuable discussions, and encouragement during my research. Professor Hyo Jae Jo and Professor Sun Hong Kwon have helped and encouraged me in finding a way out of difficulties in my study.

I owe a deep debt to my wife, JooYoun Lee, for her help during the course of this study. Without her love, sacrifice, patient support, encouragement, and prayer, I could not have come this far.

TABLE OF CONTENTS

LIST OF FIGURES

Page

LIST OF TABLES

CHAPTER I

INTRODUCTION

1.1 General

After the middle of the 1990s, oil and gas fields moved into deep water, 900 m – 3000 m. As the search for oil and gas progresses, various concepts should be considered for deep water offshore structures. In calculating dynamics and loads on offshore structures, a precise understanding of ocean wave kinematics is required. Since George Biddell Airy's long and influential article "Tides and Waves", was published in 1845, much research has been done looking for representation of a realistic ocean wave. The understanding of water waves and the associated kinematics has advanced substantially during the last four to five decades.

There have also been a number of experimental studies in which wave characteristics have been measured within a laboratory wave flume. Laboratory conditions provide substantial advantage in water wave research, such as the control of experimental parameters, the repeatability of experiments and the relatively low cost for carrying out experiments. It is also possible to generate two-dimensional conditions in the laboratory which correspond to theoretical formulations.

This dissertation follows the style and format of Ocean Engineering.

There are a number of experimental observations for regular wave kinematics. In many cases, the agreement between theoretically predicted wave kinematics and experimental observations is reasonably good. To produce a good agreement between theoretical prediction and experimental observation, theoretical equations for periodic waves were developed in the consideration of the effects of viscosity, higher order terms in formulation, and wave-wave interactions. Advanced technologies, such as LDV and PIV, have also improved observations in the laboratory.

However, even though the kinematics of a regular wave has a good agreement with the theory, a realistic ocean wave can not be represented completely in a laboratory wave tank or by theoretical formulations. The realistic ocean wave is multi-chromatic and multi-directional. Precise knowledge of flow kinematics induced by an ocean wave is crucial to a variety of offshore engineering applications, such as the prediction of wave loads on a slender cylinder using the Morison equation and the determination of the dynamic response of compliant structures due to these forces in deep water regions. Therefore, ocean field data is necessary for understanding the kinematics of realistic ocean waves.

The first comprehensive "wave force projects" conducted in nature during the period of 1954-1963 (Thrasher and Aagaard, 1969) inferred water wave kinematics from wave measurements at one or more locations due to the unavailability of suitable instrumentation for measuring kinematics. Indeed, the first field measurements of water particle kinematics under storm conditions were conducted in 1973 (Forristall, et al., 1978). Much of the development in understanding water wave kinematics was spurred predominantly by the interest to ensure that offshore platforms would withstand extreme wave forces. An emphasis on surf zone dynamics that commenced at a similar time and only received

emphasis in the last two decades has also stimulated investigations in water wave research. The nonlinearity and the directionality of water waves are both crucial elements to an adequate understanding of water force, especially for the highest waves generated by complex wind fields such as tropical storms. However, the phenomena of ocean waves are not explained with theoretical predictions based on a regular wave, a uni-directional irregular wave, or a multi-directional short crest wave.

Observations suggest the existence of certain giant waves. Giant waves are significantly higher and steeper than what is expected by current knowledge of wave statistics under the given weather conditions. The height of giant waves is twice the 'significant wave height' of surrounding waves. Giant waves often come unexpectedly from directions other than the prevailing wind and waves. Freak waves or rogue waves are known for their extraordinary height and abnormal shape. Although it is impossible to anticipate rogue waves completely, it has been found that there is a solution to Schrödinger nonlinear hydrodynamics equations for exceptionally high freak waves. However, a solution of Schrödinger nonlinear hydrodynamics equations can not simulate fully the random nature of the sea surface with hydrodynamics. It is important for understanding rogue waves to develop fully nonlinear wave equations. To develop fully nonlinear wave equations, more data on rogue waves are needed because there is no theory for the real ocean waves.

Within the past 20 years, at least 200 supertankers have been lost, each more than 200 m long. The causes of many cases are believed to 'rogue waves', waves of exceptional height and abnormal shape. There are several reports about sudden disasters in extreme waves. For example, two large Norwegian bulk ships *M/S "Norse Variant"* and *M/S "Anita"* disappeared at the same time at the same location. According to the conclusion of the Court of Inquiry, a very large wave suddenly broke several hatch covers on deck, and the ships were filled with water and sank before any emergency call was given. The wave that caused loss of both ships was probably a freak or rogue wave (Kjeldsen, 2001). Cruise ship damage is rare, but recently some cruise liners have been hit hard by rogue waves. The *Queen Elizabeth II*, for example, was struck by a 29 m rogue wave in 1995 in the North Atlantic (Met Office, 1996). The *Caledonian Star*, sailing in the South Atlantic in 2001, was hit by a rogue wave estimated at 30 m. The *Explorer*, on a "semester-at-sea" sailing in the North Pacific, was damaged in January 2005 when the ship, carrying nearly 1000 people including almost 700 college students, was struck by a wave estimated to be 17 m in height. The wall of water smashed into the bridge of the 180 m long ship. These well-built cruise ships suffered little damage and had few injuries from the attack of rogue waves (Mastroianni, 2005). Most recently, the *Norwegian Dawn*, a 3-year-old 294 m long cruise ship carrying more than 2200 passengers and heading back to New York from the Bahamas, was pounded by a rogue wave during a storm in April 2005 off the South Carolina coast. The wave reached the 10th deck of the towering ship and shattered two windows. As a result, 62 cabins were flooded and some public areas were damaged, but only four people were injured, according to the cruise line (Lemire, 2005).

The rogue wave was estimated at 21 m, far higher than surrounding waves. Offshore platforms have also been struck. On January 1, 1995, the Draupner oil rig in the North Sea was hit by a wave whose height was measured by an onboard laser wave measured to be 26 m, with the surrounding waves reaching 12 m (Clauss, 2002). Fig. 1.1 is a photo of a rogue wave during a storm. This photo was taken by Philippe Lijour aboard the supertanker *Esso Languedoc* in South Africa in 1980. The rogue wave approached the ship from behind before breaking over the deck. The height of the wave was in the range of 5-10 m.

Fig. 1.1 Photo of a rogue wave.

Many marine scientists have clung to statistical models that explain rogue waves as a monstrous deviation which could occur only once in a thousand years. Had the ships encountered the 1000-year storm? So how many 1000-year storms have there been and how common are they? MaxWave, a German scientific group, examined 30,000 worldwide satellite photos taken by the European Space Agency (ESA). According to MaxWave, 10

rogue waves, each more than 25 m in height, were identified around the globe within the short three-week research period in 2001 (Rosenthal and Lehner, 2004). These rogue waves, far bigger than any surrounding waves, can occur during storms or calmer seas, and almost anywhere, but it appears they occur more frequently where there are strong currents, such as the Gulf Stream off the eastern coast of North America.

There are three categories for rogue wave research. First, research is being used in trials to program marine radar systems to identify rogue waves. Land-based radar or satellites might eventually be able to track rogue waves (MaxWave, 2005; Rosenthal and Lehner, 2004). Second, radar on ships can be programmed with calculations used in the models to identify an approaching wave and warn the ship, similar to laser systems used in aircraft to detect wind shear (Clauss, 2002). Finally, naval architects and engineers are looking at the design of ships, platforms, ports and other structures to gauge their susceptibility to damage caused by very large waves (Gorf et al., 2001). Inquiries into the sinking of a number of container and cargo ships have recommended stronger hatches be installed to prevent flooding of the main hold. The relative frequency of rogue waves has major safety and economic implications since current ships and offshore platforms are built to withstand maximum wave heights of only 15 m. New design criteria considering the impact of rogue waves on ships and offshore structures are needed. Drilling rigs also may need to be made higher and stronger. Fig. 1.2 shows the bow damage on the Norwegian tanker *Wilstar* in 1974. The combination of pitch motion and a steep incoming wave can cause excessive local structural damage.

Fig. 1.2 Damage to the Norwegian tanker *Wilstar*, which was hit by a rogue wave in 1974.

If we can predict the waves that ships and offshore structures are likely to encounter, then we can design the ships and offshore structures better, reduce losses, and save lives. Recent research related to the rogue wave explains how often to expect rough sea using satellite technologies and mathematical theories. However, they can't predict yet rogue waves. To predict the forces on ships and offshore structures struck by a rogue wave, it is an understanding of the kinematics of rogue waves is needed. However, there is no such technology to measure the kinematics of rogue waves from the ocean yet. It is difficult and expensive to obtain the field data of kinematics of a rogue wave in rough seas.

Most wave buoys analyze the data on board and do not transmit raw data, making it impossible to see freak waves. Similarly, rogue waves cannot be observed directly from data obtained by the radar altimeters of satellites. Researchers who analyzed satellite SAR data have claimed a larger number of high waves than that would have been expected from classical theories. However, these results are controversial because they rely on uncertain assumptions about the radar imaging mechanism.

We know that there is a solution to hydrodynamic equations for nonlinear waves but as of yet we have no theory that fully combines the random nature of the sea surface with hydrodynamics. Without such a theory, we need more data. But to look at rare events we need vast quantities of data and it could take a long time to produce enough to give unequivocal results. This study focuses on measuring the kinematics of rogue waves in a two-dimensional wave tank. Laboratory investigations offer many advantages in this rogue wave research, especially in terms of the control of experimental parameters, repeatability of experiments, relatively low cost, and possibility of comparisons with the corresponding theoretical formulations.

Rogue waves, different from tsunamis that result from earthquakes, are formed in three ways. They grow from strong winds beating against an opposing ocean current, from intersecting waves driven together by storms or from swells having their energy focused by the topography of the sea floor. Whether they are wind-driven waves, currents, ocean bottom topography or inclement weather, these factors can all play a role in rogue wave development. Many researchers (Bonmarin, 2001; Kjeldsen, 2001; Olagnon and Iseghem, 2001) defined rogue waves as waves whose height is twice the 'significant wave height' of surrounding waves. In the first part of this study, a rogue wave is generated in a two-dimensional wave tank using their definition. This study shows how the rogue wave can be generated in the two-dimensional wave tank.

In the second part of this study, the particle velocities of a rogue wave are measured by the PIV technique. The PIV system obtains the whole velocity fields of rogue waves with dense spatial resolution. Therefore, the fastest part of rogue waves can be shown through the measurements. The fastest particle velocity of regular waves is usually in the crest. However, the particle velocity of rogue waves in the crest is not the fastest due to their nonlinearity.

In the third part of this study, particle accelerations are calculated from the particle velocities obtained by the PIV. One period wave consists of twelve fields of view. This means that local accelerations, time derivatives of particle velocities, can be calculated with a time step of $\Delta t = 75$ ms. Also, convective accelerations, which are space derivatives of particle velocities, can be obtained from the PIV fields of view. The contribution of convective accelerations has been known to be very small and is ignored when accelerations are considered in regular waves with relatively small wave steepness. It is noticed that convective accelerations are of significance in estimating total particle accelerations of rogue waves.

In the last part of this study, the kinematics of rogue waves obtained by the laboratory experiment was applied to the Morison equation for calculating the horizontal wave forces on a truncated cylinder. Although the particle velocities were extrapolated under the PIV field of view, the results were reasonable and comparable. The forces of this study were predicted by the wave particle velocities and showed good agreement with the direct force measurements of a two-dimensional laboratory Draupner rogue wave by Kim and Kim (2003a). It shows one of the applications of the particle velocity measurements so that the wave loading forces on offshore structures can be obtained without using pressure gages or

accelerometers. In summary, rogue waves occur more frequently in some places in the world, often come unexpectedly from directions other than prevailing winds and waves, and are expected to give tremendous loads. The aim of this research is to recommend changes in ship design to make ships less vulnerable in the future.

1.2   Literature review

There have been many investigations of water wave kinematics. The first realistic description was presented by Stokes in 1847. He extended Airy's linear wave theory (1845) to the second order. The second-order Stokes wave theory was then extended to the fifth-order for better accuracy in computing the characteristics of regular waves by De (1955) and Fenton (1985). Chappelear (1961) and Dean (1965) extended this theory to much higher orders with the help of computers. Dean (1970) examined the root-mean-square errors in kinematic and dynamic free surface boundary conditions associated with a number of analytic wave theories and numerical theories and concluded that the calculations of the higher-order Stokes wave theories approach the measured data of wave motion in deep water. A more accurate numerical scheme for computing the characteristics of regular waves including heights ranging up to near breaking was developed by Schwartz (1974) and later extended by Cokelet (1977).

Although the higher order terms for the higher-order Stokes wave equations have been obtained in order to reduce discrepancies between calculated and measured periodic wave kinematics, the predictions of the higher-order Stokes wave theory did not match well with the measurements. The regular wave theories were modified to predict wave kinematics with the following three steps: First, Lo and Dean (1986) modified the linear wave theory by adjusting the depth decaying function $\sinh^{-1}(kd)$ to $\sinh^{-1}(k(d+\eta))$. Second, nonlinear terms are added to wave theories, with viscosity being one. The theoretical descriptions noted above have one important point, which is that they all assume wave motion is irrotational, and therefore no vorticity exists throughout the depth of flow fields. However, it is clear from the conduction solution proposed by Longuet-Higgins (1953) that a vorticity profile can exist within the interior of the flow field. There are also a number of experimental observations which appear to support this view. Anastasious et al. (1982) concluded with their observations that the large positive velocities near the surface region were overestimated by the irrotational solution. Swan (1990) considered the effects of a fully diffused vorticity and applied a viscous modification to a third order of wave steepness. He concluded that an irrotational solution overestimates the amplitude of the oscillatory motion in the upper half of the flow field, and underestimates the amplitude in the lower half. However, his viscous modification was only for regular waves of moderate height in water of intermediate depth. Choi et al. (2001) investigated nonlinearity of regular and irregular wave kinematics with LDV measurements of two different wave slopes in deep water. Finally, the third step is to impose no mass transfer in the fluid. Gudmestad and Connor (1986) developed the wave theory on the basis of this third step and showed good agreement with experimental results.

Sobey (1990) has also reviewed the apparent inconsistency of the regular wave theories to predict the wave kinematics. He referred to Fenton (1985) who pointed out that it was necessary to know the wave speed in order to calculate the wave kinematics.

There have been a number of significant efforts to predict the kinematics of irregular surface waves. Wheeler (1970), Rodenbusch and Forristall (1986), and Gudmestad (1990) proposed the fast Fourier transform (FFT) spectral method and its modifications, which were called the Wheeler stretching, the delta stretching, and the Gudmestad stretching, respectively, for engineering purposes. The FFT spectral method is that wave elevations may be decomposed into component waves and then superposes their kinematics equations. The modifications made to the FFT spectral method were mainly aimed at easing the overprediction of horizontal velocities near the crest of irregular waves. Bosma and Vugts (1981) predicted irregular wave kinematics with an equivalent regular wave substitution. The equivalent regular wave substitution is a method that a single relatively steep wave is selected out of irregular waves and approximately equivalent to a regular wave with similar frequency and height. The interaction among component waves that constitute an irregular wave field and travel at different phase velocities is neglected in the FFT spectral method and an equivalent regular wave substitution. The FFT spectral method and other modified methods yield varying results depending on the selection of the cut-off frequency. Wheeler stretching and linear extrapolation underestimate and overestimate the measured velocity values, respectively.

Therefore, an acceptable method with proven accuracy has been needed for predicting the kinematics of irregular wave instead of the FFT spectral method and other modified methods. The kinematics of dual-component waves was investigated both numerically and experimentally by Zhang et al. (1992). They analyzed the effects of the interaction between short and long waves on the kinematics of dual-component waves. Finally, Zhang et al. (1996) developed the Hybrid Wave Model method (HWM). The kinematics of irregular wave could be predicted up to the second order with HWM. The wave elevations, particle velocity time series, largest wave horizontal profiles and largest wave acceleration fields from four unidirectional irregular wave trains measured in the laboratory are compared with the prediction of HWM by Longridge et al. (1996). The hybrid wave model satisfies the Laplace equation, boundary conditions and considers modulation effects induced by wave component interactions. The changes in the velocity profiles of the hybrid wave model are nearly constant with the change in cut-off frequency. The shape and steepness of waves can also be considered as the nonlinearity of realistic ocean waves. It is obvious that nonlinearity is significant for predicting the real world wave kinematics.

The hybrid wave model does not consider wave asymmetries; thus, the computations for the kinematics of asymmetry and steep waves were less accurate in the works of Kim et al. (1992) and Randall et al. (1993). Longridge et al. (1996) measured particle velocities of waves using a laser Doppler anemometer (LDA). The measurement-based acceleration computations showed relatively larger discrepancies compared with estimations of the hybrid wave model in magnitude and direction due to the limitations in wave repeatability and the LDA signal noise. The measurement-based acceleration computations could be improved by applying a filtering scheme to the velocity time series measurements before

the acceleration computation. However, wave repeatability in the LDA experiment may not be improved. Measurements using the LDA system give the particle velocity time series at one point in the field of view. Therefore, it is important to generate identical waves repeatedly to give better accuracy of convective accelerations which are derivatives in space in the LDA measurements. The particle image velocimetry (PIV) technique allows measurements of entire velocity fields during a single trial.

Since laser Doppler velocimetry equipment was introduced in the study of wave kinematics by Skjelbreia et al. (1991), the measurements of wave particle velocities have become more accurate. Regarding the water wave kinematics, the main emphasis has been on water wave velocities as the drag term in the Morison equation, which is proportional to square of the particle velocity. However, it has been much more difficult to obtain accurate values of wave particle accelerations. There have been no direct measurements of wave particle accelerations using currently employed equipments. The values of particle accelerations can be obtained numerically by using measured velocities. For large volume structures, which are dominated by the inertia loading term proportional to the fluid acceleration under waves, the most accurate values of the acceleration should be used. There have been few studies on the measurement of acceleration fields in the literature. The measurement of accelerations is difficult because it involves the subtraction of two velocity fields with small time difference, both of which are subject to random noise. Due to the small time difference between velocity fields, the relative error is then dramatically increased.

Kim et al. (1992) measured particle velocities of transient water waves just prior to breaking using laser Doppler anemometry in a two-dimensional wave tank. Using finite difference techniques and measured velocity data, local accelerations and convective accelerations, which are the time derivatives and the space derivatives of particle velocities, respectively, were numerically evaluated. Zelt et al. (1995) developed numerical techniques to filter and differentiate particle velocity data collected using the LDV equipment in a laboratory in order to estimate local fluid accelerations. The LDV velocity data-based acceleration computations were compared with the results of the Wheeler stretching based theories.

Longridge et al. (1996) also calculated local accelerations and convective accelerations from particle velocity data using the LDA. Their measurement-based acceleration computations had comparisons to the Wheeler stretching, the linear extrapolation and the hybrid wave model wave kinematics prediction techniques. Then, they recommended the use of PIV equipment, which measures the entire velocity field during a single trial to reduce errors due to wave repeatability. Swan et al. (2002) measured the time history of the water particle velocities at a large number of spatial locations, and then the individual data records were curve fitted and numerically differentiated to define the time history of local water particle accelerations and to calculate convective accelerations. They mentioned that the nonlinear wave-wave interactions should be considered in the description of the spatial gradient of the velocity field. Finally, they proposed a fully nonlinear unsteady wave solution based upon a time-stepping procedure and compared with results of their measurement-based acceleration computations.

Particle image velocimetry (PIV) measures instantaneous velocities across an extended area of flow by recording the motion of tracers moving with the fluid. The wave particle velocities in a whole field of view can be measured at a single trial using the PIV system. The spatial derivatives of particle velocities can be calculated with much lower error rate due to unreliable wave repeatability.

Chang and Liu (1998) measured velocities and accelerations in breaking waves. They commented that their PIV system gave rather good accuracy for the cases investigated, but no documentation was given in their brief paper. Jakobsen et al. (1997) measured the velocities and accelerations of standing waves with PIV and found good results for velocities and uncertainties for the acceleration field. To obtain better local acceleration field using the PIV system, Jensen et al. (2001) used a two-camera PIV system to measure local accelerations in the Stokes waves. They measured the velocity fields with two separate time instants using two cameras viewing the same region of view. Then, they calculated measurement-based acceleration in Stokes periodic waves in the two-dimensional wave tank. Their measurements in short crested waves showed relative standard deviations 0.6 % for the velocity measurements and 2 % for the accelerations.

During the last decade, extreme waves have drawn considerable attention from both media and the scientific and ocean engineering communities. There have been episodes of severe damage to offshore structures and ships with few observations of surprisingly large individual waves. Notably, Draper (1965) suggested using the term "freak waves" and developed a theory for application to a real ocean wave spectrum. Although a large number of studies related to freak waves were carried out, no authoritative definition of "freak waves", which represents the observed abnormal waves such as the New Year Draupner

wave, yet existed at this stage. Even the terms for such waves varied as extreme waves, giant waves, mountain waves, exceptional high waves, rogue waves, etc. Recently many researchers have used "rogue waves" as academic terms for freak waves. The use of the term "rogue waves" will also be applied in this study. Many researchers (Dean, 1990; Faukner, 2001; Kjeldsen, 2001; Olagnon and Iseghem, 2001; Haver, 2001) have commonly used the criteria to define rogue waves: waves exceeding a height of $2H_S$, where H_S is the significant wave height of sea state.

The causes of rogue waves in the actual ocean have long been investigated and many hypothetical mechanisms have been proposed from different points of view and corresponding techniques. Over the last 5 years, great progress has been made in the understanding of physical mechanisms of rogue wave phenomenon. With the assumption of the linear wave theory, rogue waves can be considered as the sum of a very large number of independent monochromatic waves with different frequencies and directions. A rogue wave may appear in the process of geometrical focusing, dispersion enhancement (Kharif et al., 2001; Smith and Swan, 2002) and wave-current interactions (Peregrine, 1976; Smith, 1976; Lavrenov, 1998). A combination of the geometrical focusing and dispersion enhancement mechanism to form an extreme wave has also been examined by Wu and Nepf (2002).

Nonlinear theory also suggested the mechanisms of rogue wave formation. All three processes mentioned above are investigated analytically and numerically in the framework of weakly nonlinear models like the nonlinear Schrödinger equation (Trulsen and Dysthe, 1997; Henderson et al., 1999; Dysthe and Trulsen, 1999; Osborne et al., 2000; Onorato et al., 2002), as well as in the laboratory (Tulin and Waseda, 1999). Nonlinear wave-wave

interaction has been addressed in association with rogue wave formation (Mori and Yasuda, 2002; Jansen, 2003).

The phenomenon of rogue waves has been studied using a higher-order nonlinear and dispersive model such as the fully nonlinear potential equations. Grue (2002), Clamond and Grue (2002) performed a fully nonlinear numerical simulation of the long time evolution of a two-dimensional localized long wave packet. However, Haver (2004) mentioned that the events of majestic individual waves produced by a physical process were neither fully understood nor properly captured by present models of surface waves.

Only a few studies have been conducted for rogue waves in two main areas: generating rogue wave in laboratory conditions and defining the criteria of rogue waves. Wu and Yao (2004) investigated rogue wave kinematics by generating a rogue wave in the two-dimensional wave tank using a combined mechanism of dispersion enhancement and wave-current interaction. Kim and Kim (2003b) simulated a Draupner rogue wave in the two-dimensional wave tank and measured the horizontal particle velocity using LDV and horizontal force on a vertical truncated cylinder fixed in the wave. Zou and Kim (2000) generated a strongly asymmetric wave in the two-dimensional wave tank. They adopted two steps which were time distortion and crest distortion to the highest wave in irregular wave train. The definition of rogue wave, $H_{max}/H_S > 2.0$, is challenged due to its shortcomings in representing the full spectrum of the surrounding sea states. Olagnon and Iseghem (2001) mentioned one more criteria, $H_c/H_S > 1.25$, a ratio between maximum wave crest and significant wave height. Bonmarin and Kjeldsen (2001) investigated the effects of geometric and kinematic properties of plunging waves. They concluded that the asymmetry of waves was an important parameter; it made the wave highly nonlinear. A

similar phenomenon was found in an extreme wave, a transient wave, and the wave just prior to breaking. The kinematics of highly nonlinear waves satisfying the criteria of rogue waves should be necessary for a variety of offshore and coastal engineering applications, such as the prediction of wave loads on a slender cylinder using the Morison equation.

1.3   Objectives and scope

The main objective of the study is to provide references for the selection of wave kinematics models for the engineering design of offshore structures and the theoretical models which will be intermediate tools in a process of computing loads from actual environmental conditions. Consequently, the precise knowledge of rogue wave kinematics will be developed.

Although there has been a significant amount of research on the kinematics of nonlinear waves numerically and experimentally, spatial derivative terms of acceleration fields played in rogue waves were rarely included and examined. The main objectives of this study are to generate the rogue wave in a two-dimensional wave tank and investigate the rogue wave kinematics, especially particle convective accelerations.

As mentioned in section 1.1, the first part of this study discusses the generation of rogue waves in a two-dimensional wave tank. A method of generating rogue waves in an irregular wave train is presented.

In the second part of this study, particle velocity fields of water waves are investigated. The fastest water particle of a rogue wave can be observed in the velocity field of the whole length of a rogue wave. It is shown that the velocity field of rogue waves does not follow the linear theory because of nonlinearities in the literature. The particle velocities of regular and irregular waves are also investigated to verify the methodology of this study.

In the third part of this study, particle accelerations are computed with particle velocities measured using the PIV system. Although there have been a few studies of water particle accelerations using the LDV system in the last decades (Kim et al., 1992; Longridge et al., 1996), this study shows that PIV measurements can reduce computational errors caused by wave repeatability. Using the centered finite difference scheme, total particle accelerations of rogue waves are computed through measured velocities. Also, convective accelerations of water waves are illustrated according to wave steepness. In the last part of this study, the horizontal wave forces on a truncated cylinder are calculated with measured velocities and obtained accelerations by applying to the Morison equation.

1.4   Organization

In Chapter II, the instruments and technique used in the experiments are explained. The two-dimensional wave tank is introduced in the first part, and the principles of the LDV system and PIV system are mentioned in the second and third section of Chapter II, separately. Experimental set-up and conditions are presented in last two sections of Chapter II.

In Chapter III, the experimental procedure and methods of data analysis obtained from experiments are presented. Generations of regular, irregular, and rogue waves in the two-dimensional wave tank are explained in the first part of Chapter III. The LDV and PIV techniques are explained in the second part of Chapter III. The reduction of LDV raw data is explained. The LDV measuring particle velocity of wave crest which is above the still water is discussed. In addition, the convergence of the PIV measurement results is tested by changing the FOV size. In the second part of Chapter III, a procedure to obtain mean velocities is also discussed. In the third and fourth part of Chapter, accelerations and forces which are obtained by applying the measured velocities to the Morison equation are presented.

In Chapter IV, three prediction methods of wave kinematics used in this study are presented. The fundamental kinematics equations for regular waves are also presented. In Chapter V, the kinematics of regular waves are discussed. The elevations, particle velocities, particle accelerations, and forces for seven regular waves which consist of five different wave heights for the PIV measurements and two different wave heights for the LDV measurements are discussed. In Chapter VI, the kinematics of rogue waves are discussed. The two rogue waves generated in the two-dimensional wave tank are presented. The particle velocity fields, particle accelerations, maximum forces of rogue waves are presented. Summaries, conclusions, and recommendations for future work are presented in Chapter VII.

CHAPTER II

EXPERIMENTAL EQUIPMENT, TECHNIQUE, SET-UP AND CONDITIONS

2.1   Laboratory facilities

To measure the particle velocities of regular, irregular and rogue waves, we conducted a series of experiments using the narrow wave tank at Texas A&M University. The wave tank was a 35 m long, 0.91 m wide, and 1.22 m deep glass-walled flume as shown in Fig. 2.1 and equipped with a permeable wave absorbing 1:5.5 sloping beach down-stream. A layer of horsehair was placed on the beach to absorb the wave energy and reduce reflection. Before conducting experiments in this wave tank, we found that the reflection coefficient which is the ratio of reflected wave height to incident wave height was 5 % as shown in Fig 2.2. Wave generation was provided by a dry-back, hinged flap wavemaker capable of producing waves with a time period ranging from 0.25 to 4 sec and a maximum height of 25.4 cm. The flap is driven by a synchronous servo-motor controlled by a computer and hydrostatically balanced using an automatic near constant force and a pneumatic control system.
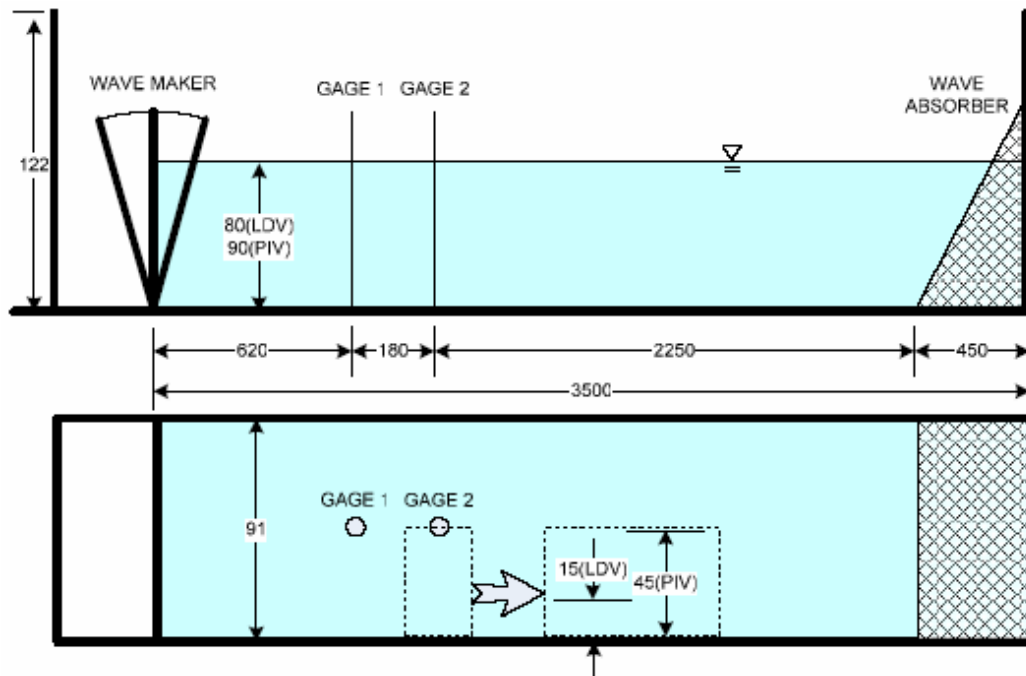
Fig. 2.1 Sketch of the wave tank (unit: cm).

incident wave height = 6.81 cm

reflected wave height = 0.341 cm
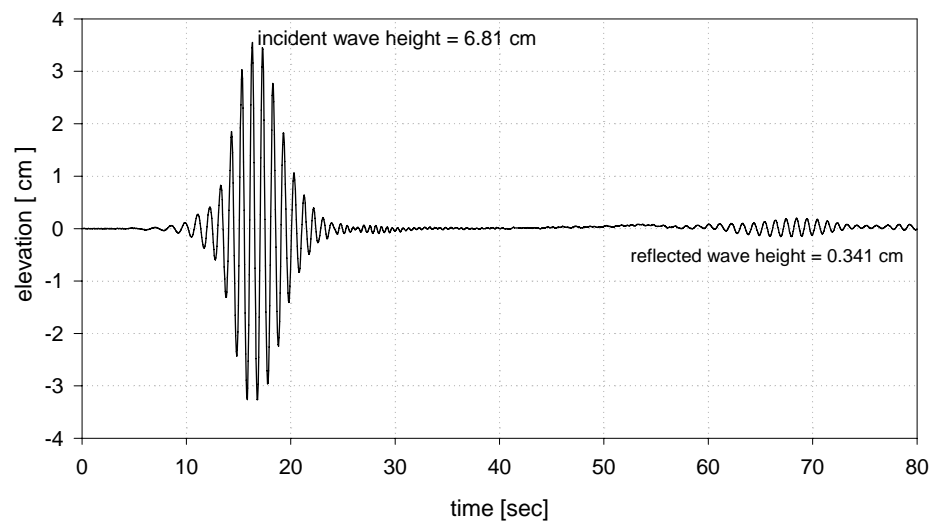
Fig. 2.2 Time series of incident wave and reflected wave for the reflection coefficient of

the wave tank.

The double-wired resistant-type wave gages were used to measure the free surface elevation. The signal from the wave gage was converted to voltage and sent to a data acquisition board housed in a computer. The gage was located at the measurement position of velocities to measure the wave elevation. All data from the wave gages was measured at a sampling rate of 100 Hz. The LDV system was used to obtain the time series of the particle velocities of regular and irregular waves with two different steepnesses. The PIV system was used to measure the particle velocities of five regular waves of different steepness and two rogue waves of different height.

The LDV system used in this study is sketched in Fig. 2.3. The LDV system and the wavemaker were synchronized by computer A, which housed a data acquisition board (National Instruments AT-AO-6/10) which generated analog output DC voltage. The control signals of the LDV system and the wavemaker were synchronized with all the data from the wave gage by computer B.

The PIV system was used to map the velocity field in the study. The PIV system used in this study is sketched in Fig. 2.4. The PIV system and the wavemaker were synchronized by computer A housing a data acquisition board (National Instruments AT-AO-6/10) which generated analog output DC voltage. The timing of laser pulses was controlled by the CCD camera by computer B housing the Programmable-Timing-Unit-Board (Fig. 2.4). The control signals of the PIV system and the wavemaker were synchronized with all the data from the wave gages.
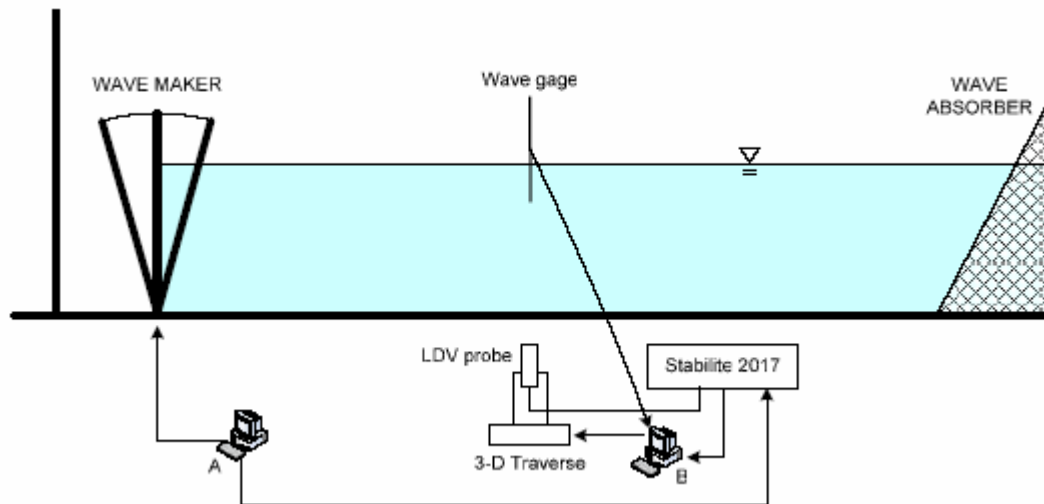
Fig. 2.3 Schematic sketch of the experimental set-up using the LDV system. Computer A: to control the wavemaker and trigger the LDV system. Computer B: to take data from the wave gages.
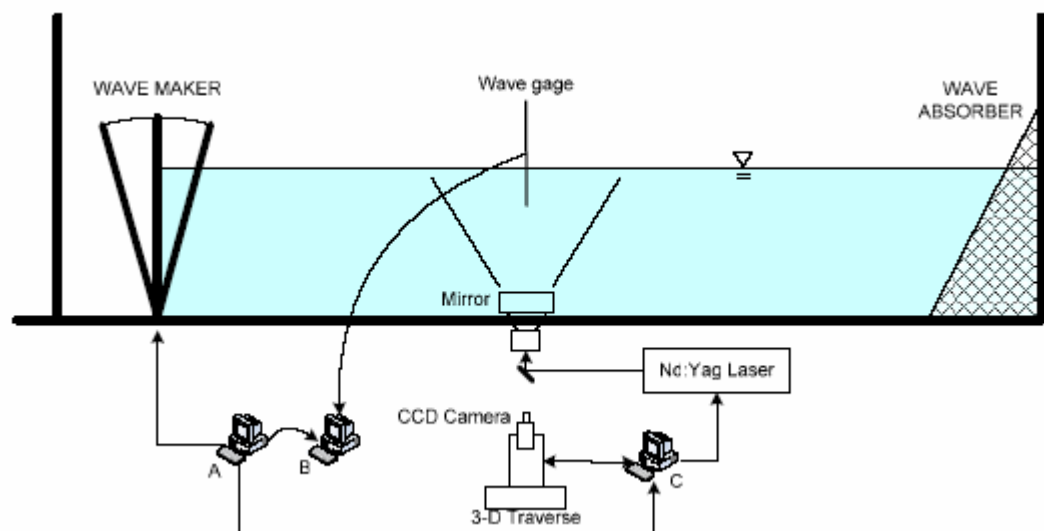
Fig. 2.4 Schematic sketch of the experimental set-up using the PIV system. Computer A: to control the wavemaker and trigger the PIV system. Computer B: to take data from wave the gages. Computer C: to control the laser and CCD camera.

2.2 Laser Doppler velocimetry (LDV) technique

Laser Doppler velocimetry (LDV) was used to measure the particle velocity in the experiment. The fluid velocities can be measured by detecting the Doppler frequency shift of laser light that has been scattered by small particles moving with fluid. The LDV technique is non-intrusive, indirect, and a single point measurement method. It can give time series data with high spatial resolution (0.1mm-1mm) due to the small measurement volume. In order to improve Doppler signal quality, tracer particles were required. The silvered hollow particles with the diameter order of 20 μm and density of approximately 1.2 g/cm^3 were used in this LDV system. Horizontal and vertical velocities were measured using the LDV system. The LDV system was a Dantec, three components, dual beam system, using back scattered light and transmitting and receiving by optic fiber, with a laser of 10 W argon-ion source. It also consists of a computerized traverse mechanism which can control the location of the measurement point (the point at which the two-beams intersected inside the wave channel formed a measurement point). When a particle passes through the intersection volume formed by the two coherent laser beams, the scattered light received by a detector has components from both beams. The components interfere on the surface of the detector. Due to the changes in the difference between the optical path lengths of the two components, this interference produces pulsating light intensity, as the particle moves through the measurement volume. This pattern of bright and dark stripes, shown in Fig. 2.5, is called fringe. The distance is determined through the fringe of the measurement point and the time is measured from scattered light from the particle. Therefore, the particle velocity can be calculated. The distance between a measurement

point and the glass wall of the wave channel was kept at 15 cm. The uncertainties of the

laser measurements were estimated according to the method of Mofat et al. (1985) to 2 %.
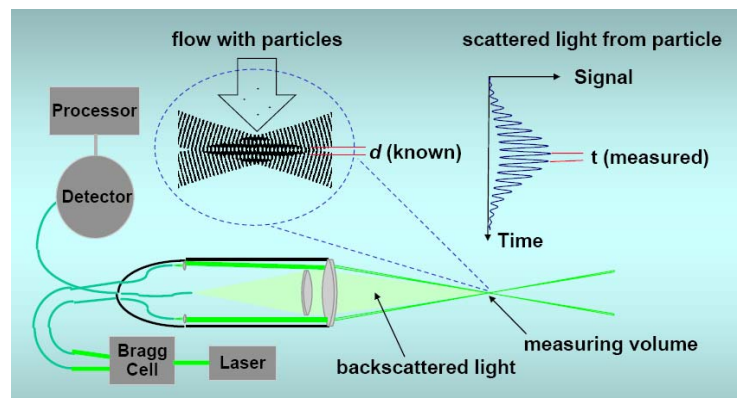
Fig. 2.5 Sketch about the principle of LDV system.

2.3   Particle image velocimetry (PIV) technique

Particle image velocimetry (PIV) was employed to measure the velocity profile in the

experiment. The PIV technique is a non-intrusive, indirect, and whole field method;

therefore, no probe was used to disturb the fluid in the experiment. An artificial seeding

particle is added for velocity measurement, and thousands of velocity vectors can be

obtained simultaneously.

A dual-head Spectra-Physics Nd:YAG laser was used as the PIV illumination source in

the experiment. The laser contains a crystal harmonic generator to double the 532 nm

green light from the original 1064 nm invisible light. The laser has a maximum energy

output of 400 mJ/pulse in the 532nm wavelength, a pulse duration of 10 ns, and a

repetition rate of 10 Hz in each head so that 20 pulses are generated per second. The light sheet optic used a combination of two spherical lenses and one cylindrical lens to generate a thin light sheet (about 1mm) from the 3 mm diameter laser beam as sketched in Fig. 2.6.
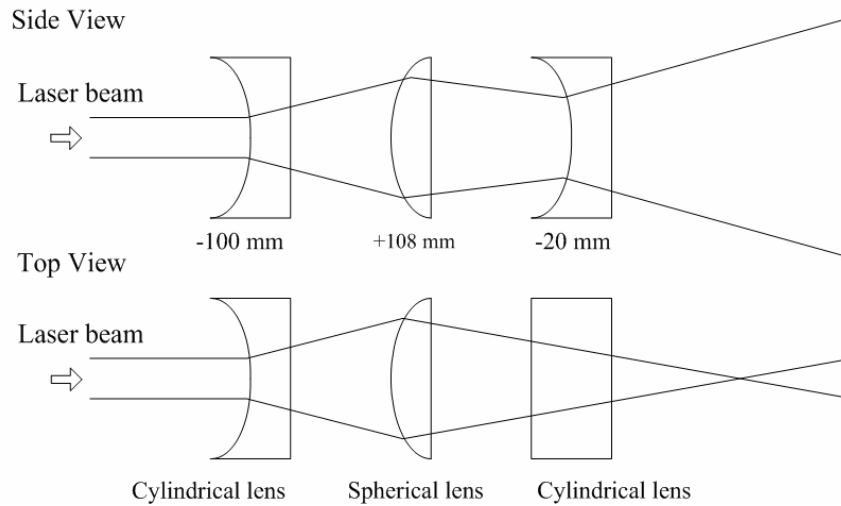
Fig. 2.6 Sketch of the light sheet optics.

Vestosint 2157 natural, which is made of polyamid 12, was used as the seeding particle which has a mean diameter of 57 μm and a specific weight of 1.02. Particle image diameter (d_τ) can be estimated by Adrian (1995).

$$d_\tau = \sqrt{M^2 d_p^2 + d_{diff}^2} \qquad (2.1)$$

where: M is the magnification factor which is the ratio of the width of the CCD sensor to the width of the field of view; dp is the particle diameter; and, ddiff the diffraction limited minimum image diameter is given by

$$d_{diff} = 2.44(1+M)f_{\#}\lambda \qquad (2.2)$$

where f# is the f-number of the lens and λ is the wave length of the light. The measurement uncertainty (RMS random error) in digital cross-correlation PIV evaluation is related to the particle image diameter (Raffel et al. 1998). Because the conditions have been slightly changed in each experiment (3 different sets of experiments in this study), the measurement uncertainty will be discussed in each case.

The camera used to capture images is a digital CCD (Charge-Coupled Device) camera mounted with a 105mm f/1.8 micro focal lens set at f/2.8~4.0. It has 1280×1024 pixels, a 6.7μm×6.7 μm pixel size, 12 bit dynamic range, and 8 Hz framing rate. The PIV images were recorded by the double-frame/single-pulsed method shown in Fig. 2.7.
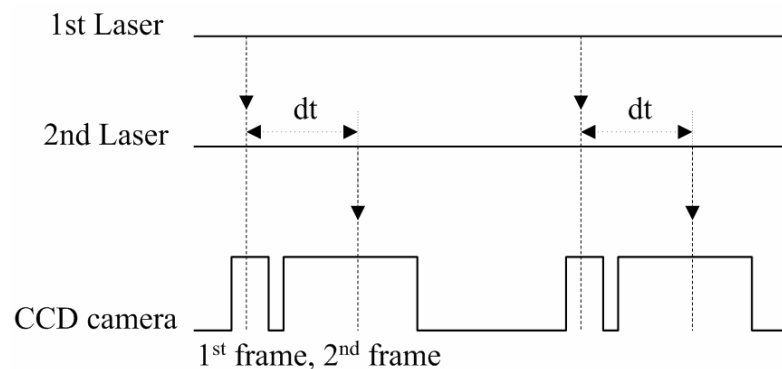
Fig. 2.7 Image recording method: double-frame/single-pulsed method.

The main advantage of this technique is to remove the directional ambiguity. The time difference (dt) between the 1st frame and 2nd frame was adjusted to be about 3~5 ms, which was determined by the maximum displacement to be less than a third of the width of the interrogation window size. A pair of images (1280×1024 pixels, dt= 3 ms) obtained by the double-frame/single-pulsed method is shown in Fig. 2.8.
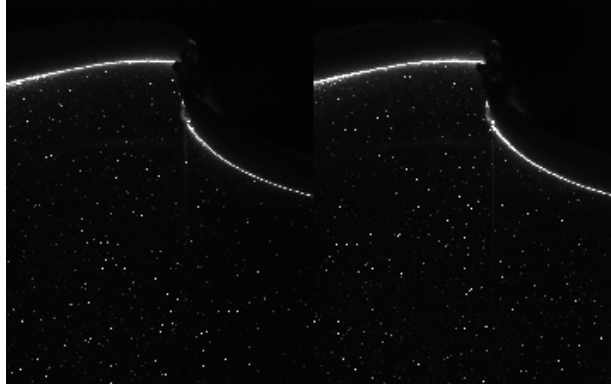
Fig. 2.8 Pair of images taken by the double-frame/single-pulsed method from Case PH3.

A pair of PIV images (in Fig. 2.8) was used to compute the velocity field using the commercial software (DaVis) from LaVision. The background noise was subtracted before the evaluation of velocity vectors. The complex 2-D fast Fourier transform was calculated from the two small areas (called interrogation windows), and the result was multiplied by its complex conjugate. Then, the inverse FFT was applied to yield the cross correlation function. The use of FFT can simplify and significantly speed up the cross-correlation process of two interrogation windows from a pair of images (Willert and Gharib, 1991).

The adaptive multi-pass algorithm was applied to reduce faulty vectors. Firstly, it has calculated a reference velocity vector for each rectangle section which was an initial cell size (four times of an interrogation area). At the next step, this reference velocity vector was used as a cell shift to compute a more accurate vector field. Because this method has shifted an interrogation area to the location where particles moved, the stronger cross-correlation can be taken. Once the velocity vectors have been calculated in the interrogation area (32×32pixels) with a 50% overlap, spurious false vectors were eliminated by the median filter (Westerweel, 1993). The left-over empty spaces were

filled-up with interpolated vectors and smoothed by a simple 3×3 smoothing filter to reduce noise.

2.4 Experimental set-up and condition for using the LDV system

A series of experiments using the LDV system was conducted to measure the particle velocities of regular and irregular waves. The set-up is shown schematically in Fig. 2.3, where x is the horizontal coordinate positive in the direction of wave propagation with $x=0$ at the wavemaker and z is positive upward. We measured the free surface elevation at 700 cm, 800 cm and 900 cm from wavemaker with two different steepness regular waves and irregular waves. The water depth in the wave tank was constant with h=80 cm.

Table 2.1 and Table 2.2 show the experimental conditions for each regular wave and irregular wave test, respectively. Cases LR1 and LR2 are representative of linear and nonlinear test cases for regular waves, respectively, where the wave steepness is H/L =0.023 (Case LR1) and H/L =0.073 (Case LR2). Cases LI1 and LI2 are representative of linear and nonlinear test cases for irregular waves where the wave steepness based on the significant wave height and wavelength computed using the peak period is H_s/L_s =0.031 (CaseLI1) and H_s/L_s =0.075 (Case LI2). Therefore, Case LR1 and Case LI1 can be compared to see the difference between regular and irregular waves with essentially the same characteristics. Similarly, Case LR2 and Case LI2 can be compared for the nonlinear conditions. Table 2.1 and Table 2.2 also list the number of waves N_W used in each record. The wave height, period and wave length of highest crest

height wave in irregular wave train are H, T and L in Table 2.2, respectively. The factor of asymmetric wave which is the ratio of falling part (rear part) of crest to rising part (front part) of crest is indicated as F/R.

Table 2.1 The experimental conditions using the LDV system for regular waves

CASE	TYPE	N_W	H (cm)	H_c (cm)	H_t (cm)	T (sec)	H/L	ka
Case LR1	Regular	10	4.04	2.12	-1.92	0.932	0.023	0.094
Case LR2	Regular	8	8.92	4.87	-4.05	0.885	0.073	0.229

* Water depth h=80 cm

Table 2.2 The experimental conditions using the LDV system for irregular waves

CASE	TYPE	N_W	H_S (cm)	T_S (sec)	H (cm)	H_c (cm)	H_t (cm)	T (sec)	H_S/L_S	H/H_S	H_c/H_S	F/R
Case LI1	Irregular	252	4.04	0.84	6.79	4.04	-2.75	0.75	0.037	1.68	1.00	0.92
Case LI2	Irregular	234	9.15	0.86	11.36	7.50	-3.86	0.94	0.079	1.24	0.82	1.09

* Water depth h=80 cm

The free-surface elevation was recorded using a resistant-type surface-piercing wave gage. The wave kinematics were measured using the LDV system at 8 m from wavemaker for seven vertical positions below SWL and two vertical positions above. The wave crest horizontal velocity of regular waves was measured with a duration of 70 s each. The time series of the steady state portion (10 waves for Case LR1 and 8 waves for Case LR2) was

selected to analyze wave elevation and wave crest/trough, horizontal/vertical particle velocities. For irregular waves, Case LI1 and LI2, a JONSWAP spectrum with $\gamma = 1$ (=Pierson-Moskowitz spectrum) was used. For the irregular wave data analysis, we collected time series at 8 m for 250 s, and each time series was truncated at the beginning to eliminate transient effects. About 250 waves were used for the subsequent statistical analyses.

2.5 Experimental set-up and condition for using the PIV system

A series of experiments using the PIV system was conducted to measure the particle velocities of regular and rogue waves. The set-up is shown schematically in Fig. 2.4, where x is the horizontal coordinate positive in the direction of wave propagation with $x = 0$ at the wavemaker and z is positive upward. As shown in Fig. 2.1, we measured the free surface elevations of rogue waves and regular waves at 620 cm and 800 cm from wavemaker, respectively. Five regular wave trains with the same period T = 0.9 s were generated with five different wave heights. The velocity fields of regular waves were obtained at 800 cm from wavemaker using the PIV system. Four irregular wave trains with PM spectrum were generated with four different significant wave heights. The velocity fields of the maximum height in four irregular wave trains were taken at 620 cm from wavemaker. The water depth in the wave tank was maintained at 90 cm.

Table 2.3 and Table 2.4 show the experimental conditions for each regular wave and irregular and rogue wave test, respectively. Cases PR1, PR2, PR3, PR4 and PR5 will show the nonlinearity of regular wave according to increasing wave height with the same wave

period. The same PM spectrum was used for generation of the waves of Cases PH1, PH2,

PH3 and PH4.

In order to produce different maximum height waves, we changed the maximum crest

part of the original input signal artificially according to the method of Zou and Kim (2000).

The maximum height of the wave train is the highest of the entire wave record. If the

maximum height is much greater than two times the significant wave height of the record,

and the ratio of crest height H_c to significant wave height H_S is greater than 1.25, it

can be called rogue wave (freak wave) (Olagnon and Iseghem, 2001). The maximum

height waves of Case PH3 and PH4 was satisfied with these criteria of rogue waves. The

number of waves N_W is listed in Table 2.3 and Table 2.4. H, T and L of Table 2.4 are the

wave height, period and wave length of highest crest height wave in irregular wave train,

respectively. The factor of asymmetric wave which is the ratio of the falling part (rear part)

of crest to the rising part (front part) of crest is indicated as F/R.

Table 2.3 The experimental conditions using the PIV system for regular waves

CASE	TYPE	N_W	H (cm)	H_c (cm)	H_t (cm)	T (sec)	H / L	ka
Case PR1	Regular	12	4.17	2.05	-2.12	0.90	0.033	0.104
Case PR2	Regular	12	8.13	4.52	-3.61	0.90	0.064	0.202
Case PR3	Regular	12	10.12	5.51	-4.61	0.90	0.080	0.252
Case PR4	Regular	12	12.29	7.27	-5.02	0.90	0.097	0.305
Case PR5	Regular	11	15.29	8.76	-6.53	0.90	0.121	0.380

∗ Water depth h=90 cm

Table 2.4 The experimental conditions using the PIV system for irregular waves

CASE	TYPE	N_W	H_S (cm)	T_S (sec)	H (cm)	H_c (cm)	H_t (cm)	T (sec)	H/L	H/H_S	H_c/H_S	F/R
Case PH1	Irregular	144	6.63	1.25	14.11	7.98	-6.13	0.94	0.102	2.13	1.20	0.93
Case PH2	Irregular	136	6.995	1.27	15.11	8.53	-6.58	0.92	0.114	2.16	1.22	1.24
Case PH3	Rogue	155	7.43	1.19	16.09	9.29	-6.80	0.90	0.127	2.17	1.25	1.61
Case PH4	Rogue	150	7.78	1.18	16.36	10.00	-6.36	0.90	0.130	2.11	1.29	1.87

∗ Water depth h=90 cm

CHAPTER III

EXPERIMENTAL PROCEDURE AND DATA PROCESSING

3.1 Generation of experimental waves

In the first phase experiment, experimental waves were designed and generated in the 2-D wave tank. Regular, irregular and rogue waves were considered in this research. Through the series of investigations of regular and irregular waves, the kinematics of a rogue wave which is a very highly nonlinear wave was an eventual focus in this study. The rogue wave may only be obtained in the wave tank or in the field because there is no available theory for the highly nonlinear waves. We generated the 2-D rogue wave and examined the rogue wave kinematics in the 2-D laboratory wave tank.

3.1.1 Generation of regular waves

There are two objectives of the regular wave experiment in this study. The first of objective was to produce benchmark wave kinematics data sets for both moderate and steep regular waves. As we reviewed the work of previous researchers, many papers showed wave kinematics comparisons between laboratory and theoretical predictions based on linear and high-order wave theory. However, no one has yet shown the comparison against fully nonlinear NWT simulations, especially, extreme velocities above the SWL, which are important for estimating wave impact forces on lender members near

free surface (Bea et al., 1999). A comprehensive experimental study was conducted using the LDV system for two different steepness regular waves which are Case LR1 and Case LR2 and using the PIV system for five different steepness regular waves which are Case PR1, Case PR2, Case PR3, Case PR4 and Case PR5.

The second objective was a preliminary experiment for rogue wave investigations. Though laboratory waves are nonlinear and vary from weak to highly nonlinear, the theory of Stokes 5th order wave was developed (Skjelbreia and Hendrickson, 1962), reproduced and confirmed in a wave flume (Alex and Kim, 2000). There have been also many measurement studies of Stokes wave particle velocity using the LDV system. Before conducting a rogue wave experiment, our LDV system and PIV system accuracy was verified by comparing them to Stokes wave theory. It was found that the results of the LDV system and the PIV system for Case LR1 and Case PR1 which have the same wave condition agreed well, like the results of Cenedese et al. (1994). The generation time of regular waves was controlled by the group velocity of the propagating wave based on the design wave period, the water depth, and the distance from the flap wavemaker to the target wave gage. To get clean wave signal sets, the overlap of an incident wave and a reflected wave at the target wave gage should be avoided. Using these considerations, a 50 sec regular wave generation time was selected. Approximately 55 waves were obtained in the 50 sec wave generation time. Of the waves, several steady state incident waves (ten for LDV system and twelve for PIV system) were selected to measure the wave particle velocities. The root-mean-square wave heights (RMS wave height, H_{rms}) for each case were checked and are shown in Table 3.1.

The RMS wave height was obtained by the equation (3.1), i.e.

$$H_{rms} = \sqrt{\sum_{i=1}^{N} [(H_i - H_{mean})^2 / N]} \tag{3.1}$$

where H_i represents measured wave height for each wave, H_{mean} the average wave height of selected regular waves, and N the number of selected regular waves.

The error rate of selected regular waves was calculated by the equation (3.2).

$$ER_{wave} (\%) = (H_{rms} / H_{mean}) \times 100 \tag{3.2}$$

Table 3.1 The RMS wave heights of selected experimental regular waves

CASE	Case LR1	Case LR2	Case PR1	Case PR2	Case PR3	Case PR4	Case PR5
H_{rms} (cm)	0.02	0.02	0.01	0.02	0.07	0.11	0.20
ER_{wave} (%)	0.38	0.20	0.21	0.23	0.65	0.93	1.33

The time series of regular wave for Case LR1, Case LR2, Case PR1, Case PR2, Case PR3, Case PR4, and Case PR5 are shown in Fig. 3.1, Fig. 3.2, Fig. 3.3, Fig. 3.4, Fig. 3.5, Fig. 3.6, and Fig. 3.7, respectively.
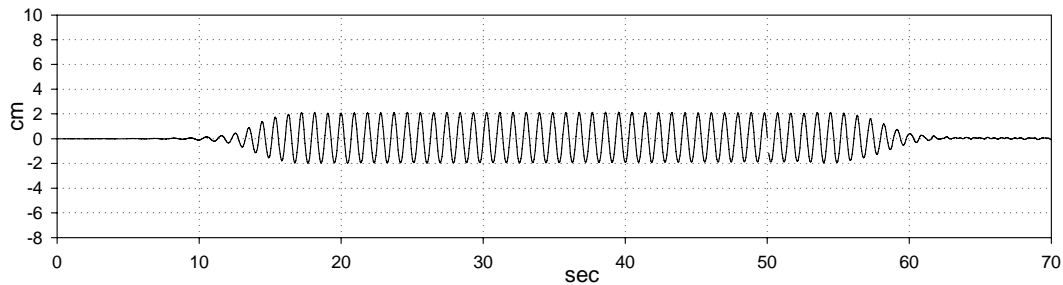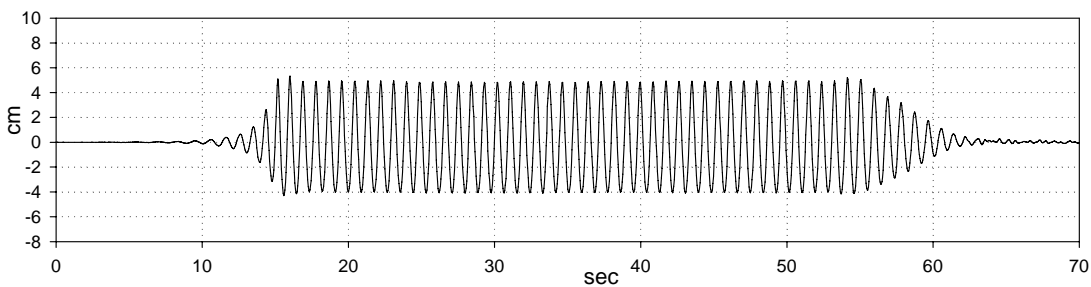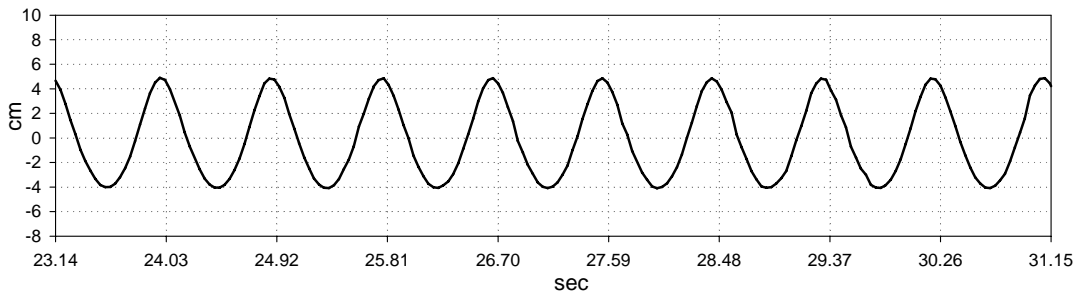
(a) Whole time series (Case LR1).
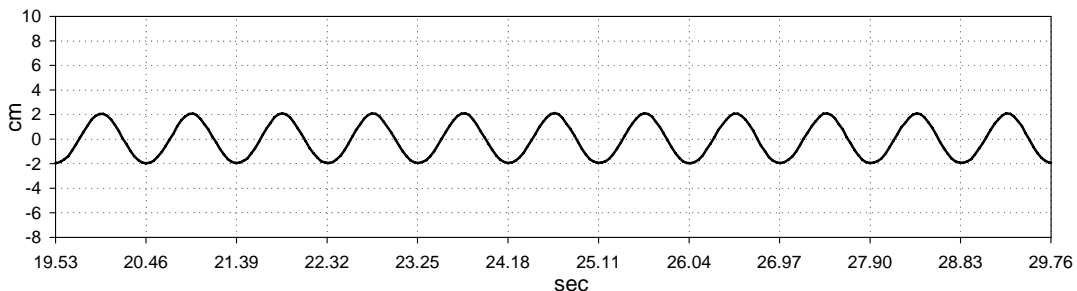
(b) Selected time series for measuring the particle velocities (Case LR1).

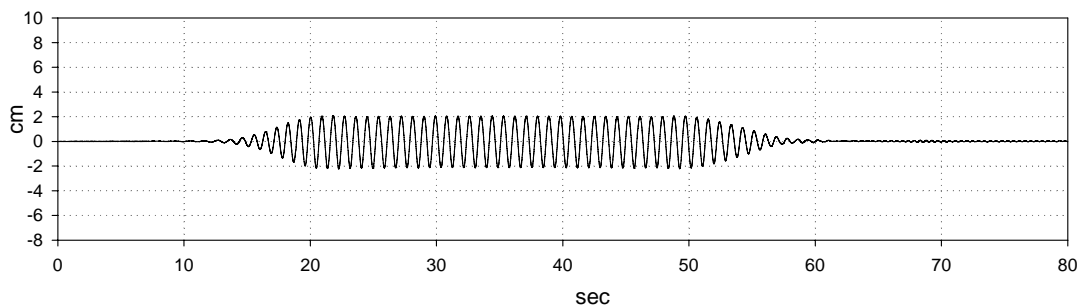Fig. 3.1 Time series of regular waves for Case LR1, T= 0.932 s, H= 4.04 cm.
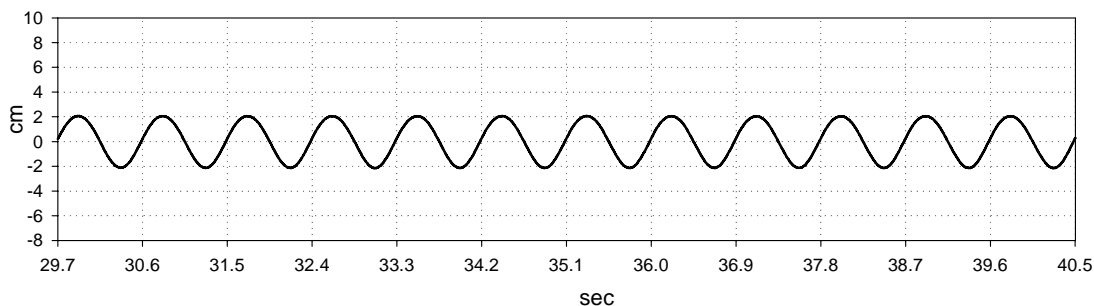

(a) Whole time series (Case LR2).

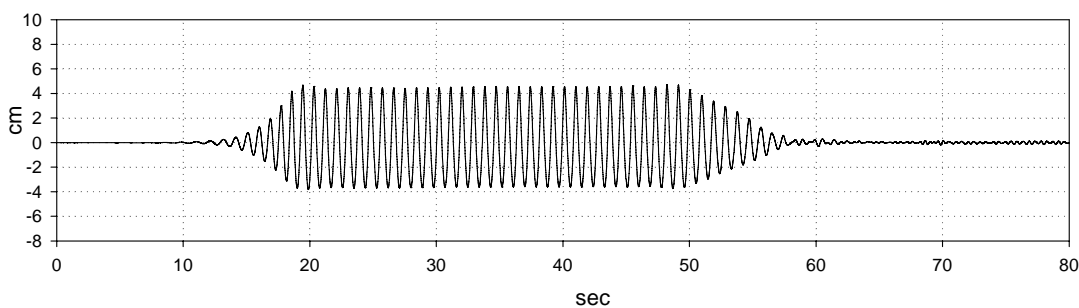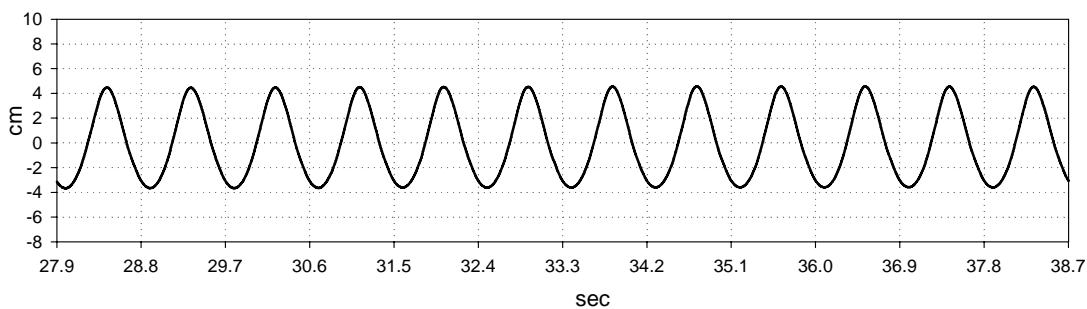(b) Selected time series for measuring the particle velocities (Case LR2).

Fig. 3.2 Time series of regular waves for Case LR2, T= 0.885 s, H= 8.92 cm.

(a) Whole time series (Case PR1).

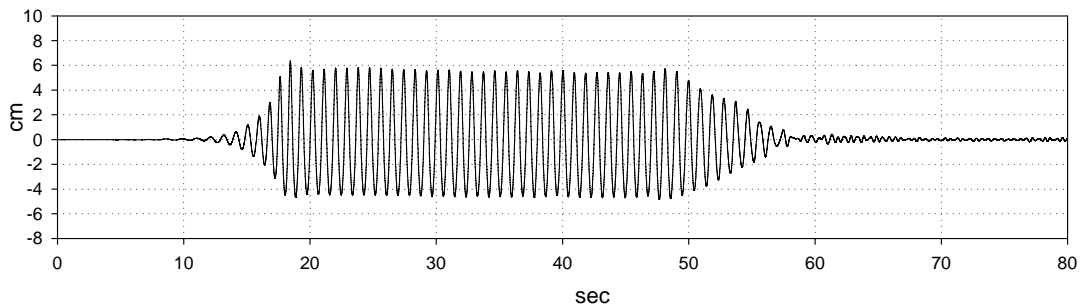(b) Selected time series for measuring the particle velocities (Case PR1).

Fig. 3.3 Time series of regular waves for Case PR1, T= 0.9 s, H= 4.17 cm.
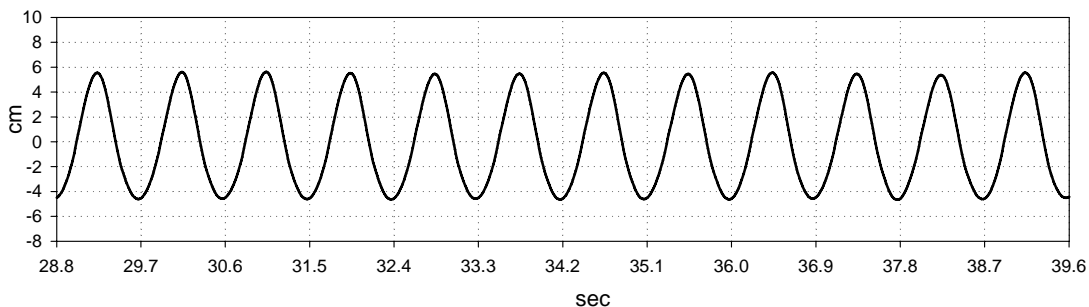

(a) Whole time series (Case PR2).

(b) Selected time series for measuring the particle velocities (Case PR2).

Fig. 3.4 Time series of regular waves for Case PR2, T= 0.9 s, H= 8.13 cm.

(a) Whole time series (Case PR3).

(b) Selected time series for measuring the particle velocities (Case PR3).

Fig. 3.5 Time series of regular waves for Case PR3, T= 0.9 s, H= 10.12 cm.
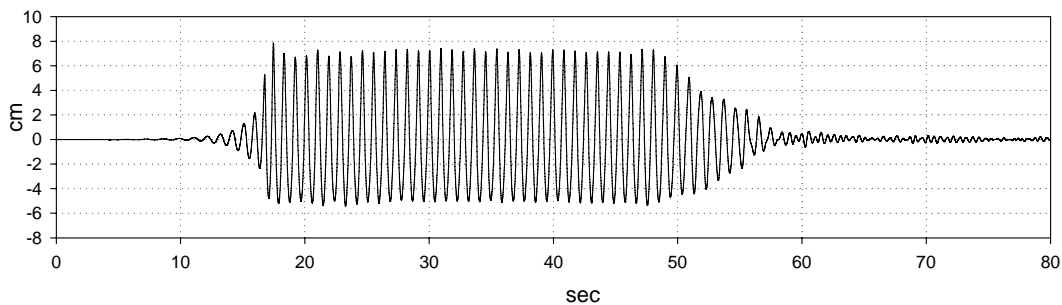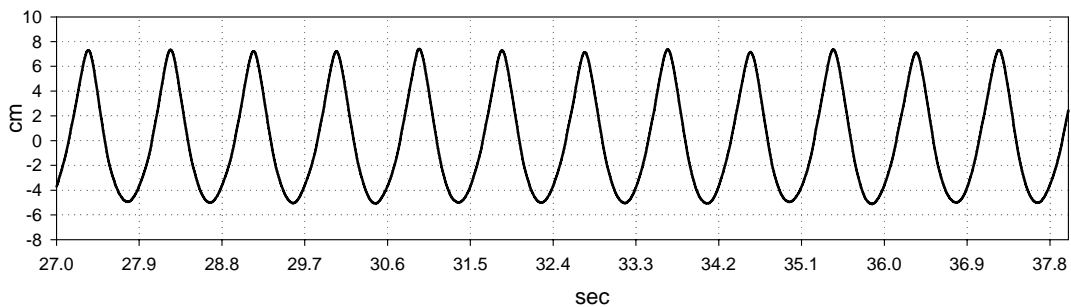

(a) Whole time series (Case PR4).

(b) Selected time series for measuring the particle velocities (Case PR4).

Fig. 3.6 Time series of regular waves for Case PR4, T= 0.9 s, H= 12.29 cm.
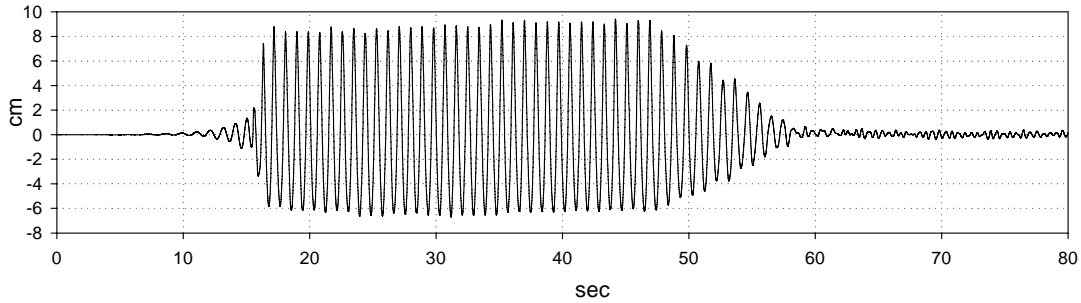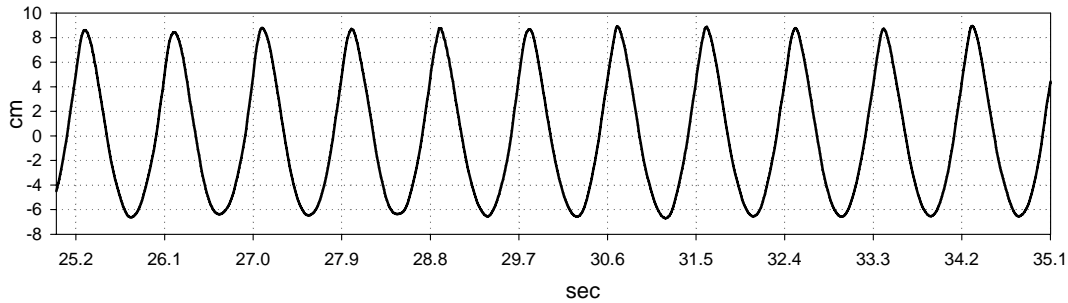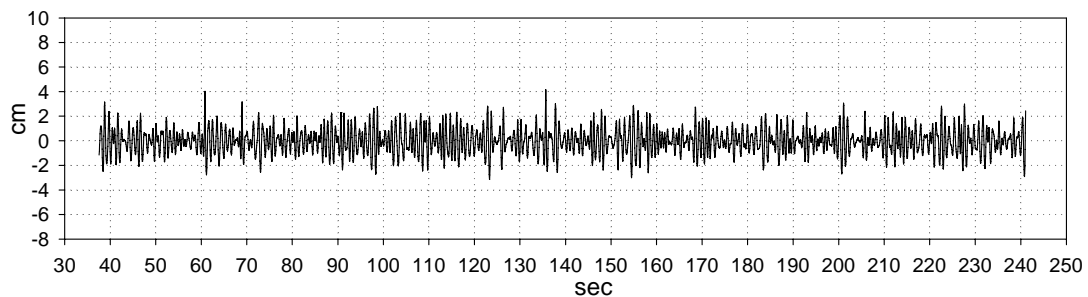
(a) Whole time series (Case PR5).

(b) Selected time series for measuring the particle velocities (Case PR5).

Fig. 3.7 Time series of regular waves for Case PR5, T= 0.9 s, H= 15.29 cm.

### 3.1.2 Generation of irregular waves for the kinematics measurement using the LDV system

A series of unidirectional irregular waves were generated in the 2-D wave tank to measure the particle velocities using the LDV equipment. The kinematics of rogue waves, highly nonlinear waves, in the real field cannot be described with the fifth-order Stokes wave theory due to the various uncertain nonlinearities. A realistic sea state where rogue waves occur also is called the irregular sea state which is composed of many interacting waves with different heights and frequencies. The measurements of the irregular wave kinematics are different from those of a high-order Stokes monochromatic wave with similar wave height and frequency. It is a different phenomena when an irregular wave

induces larger particle velocities near the surface and smaller velocities at greater depths than those for a regular wave. Though the rogue wave kinematics have more uncertain nonlinear effects than the irregular wave kinematics, the realistic sea state can be represented closer by the irregular waves than the regular waves. Therefore, these irregular wave experiments were conducted as the second phase study for the investigations of the rouge wave kinematics. By testing two different steepness irregular waves (mild/steep), the amount of nonlinearity could be shown between differences of the wave steepness. The joint wave observation program for the North Sea (JONSWAP) spectrum with $\gamma=1$ (= Pierson Moskowitz spectrum) was used for the generation of irregular waves (Case LI1 and Case LI2). For the irregular wave data analysis, we collected a time series at 8 m from the wavemaker for 250 s. Each time series was truncated at the beginning to eliminate transient effects. About 250 waves were used for the subsequent statistical analysis. The time series of irregular waves for Case LI1 and Case LI2 are shown in Fig. 3.8 and Fig. 3.9, respectively.
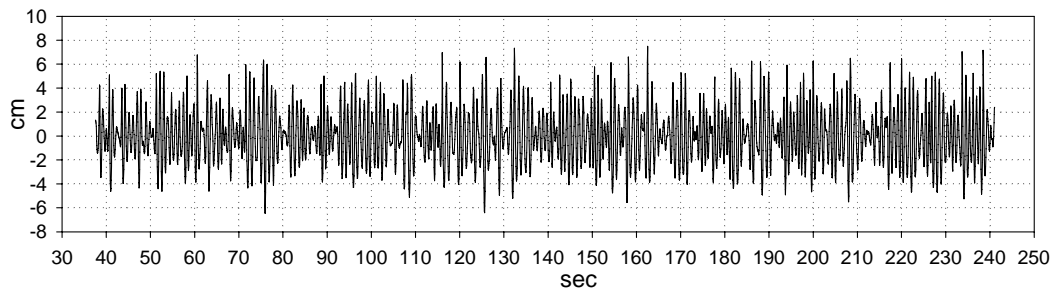

(a) Whole time series for Case LI1, total 252 number of waves.

Fig. 3.8 Time series of irregular waves for Case LI1, T_S=0.84 s, H_S=4.04 cm, the highest elevation wave height, H=6.79cm, T=0.75 s, H/H_s=1.68, H_c/H_s=1.00.
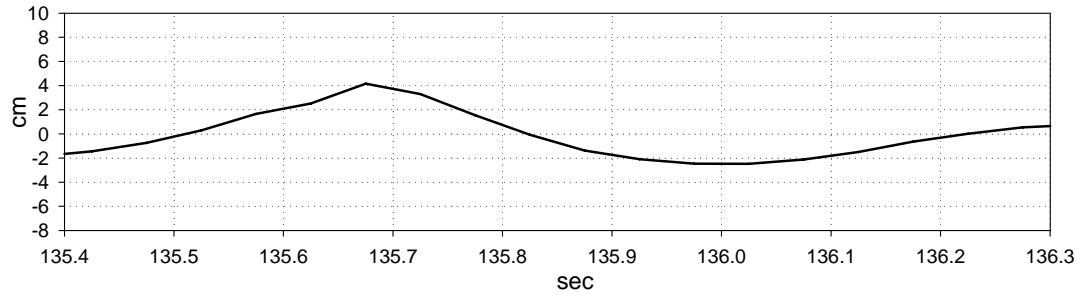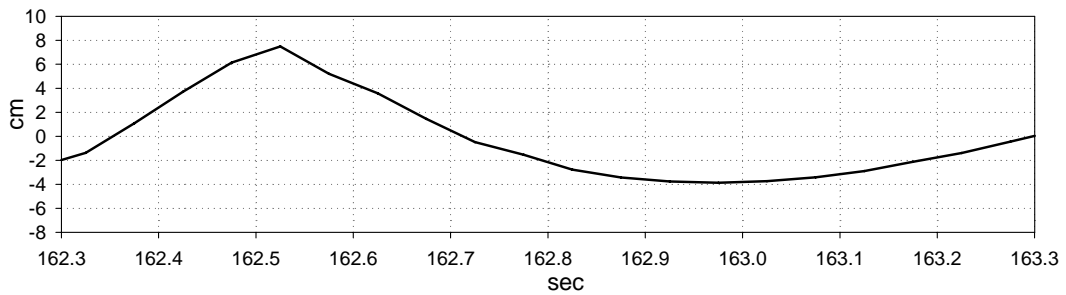
(b) Time series of the highest elevation wave for Case LI1.

Fig. 3.8 continued.

(a) Whole time series for Case LI2, total 234 number of waves.

(b) Time series of the highest elevation wave for Case LI2.

Fig. 3.9 Time series of irregular waves for Case LI2, T_S = 0.86 s, H_S = 9.15 cm, the highest elevation wave height, H= 11.36cm, T= 0.94 s, H/H_s =1.24, H_c/H_s =0.82.

The amplitude spectrums from the experimental data and spectrum equation are compared in Fig. 3.10 for Case LI1 and Case LI2. The JONSWAP spectrum can be written in approximate form in terms of the parameters of wave height and period as follows:

$$S(f) = \beta_J H_{1/3}^2 T_p^{-4} f^{-5} \exp[-1.25(T_p f)^{-4}] \gamma^{\exp[-(T_p f-1)^2/2\sigma^2]}, \qquad (3.3)$$

in which

$$\beta_J = \frac{0.0624}{0.23 + 0.0336\gamma - 0.185(1.9+\gamma)^{-1}}[1.094 - 0.01915\ln\gamma], \qquad (3.4)$$

$$T_p \simeq T_{1/3}/[1 - 0.132(\gamma+0.2)^{-0.559}], \qquad (3.5)$$

$$\sigma = \begin{cases} \sigma_a : f \le f_p, \\ \sigma_b : f \ge f_p, \end{cases} \qquad (3.6)$$

$\gamma = 1 \sim 7$ (mean of 3.3, 1 is chosen in this study), $\sigma_a \simeq 0.07$, $\sigma_b \simeq 0.09$.

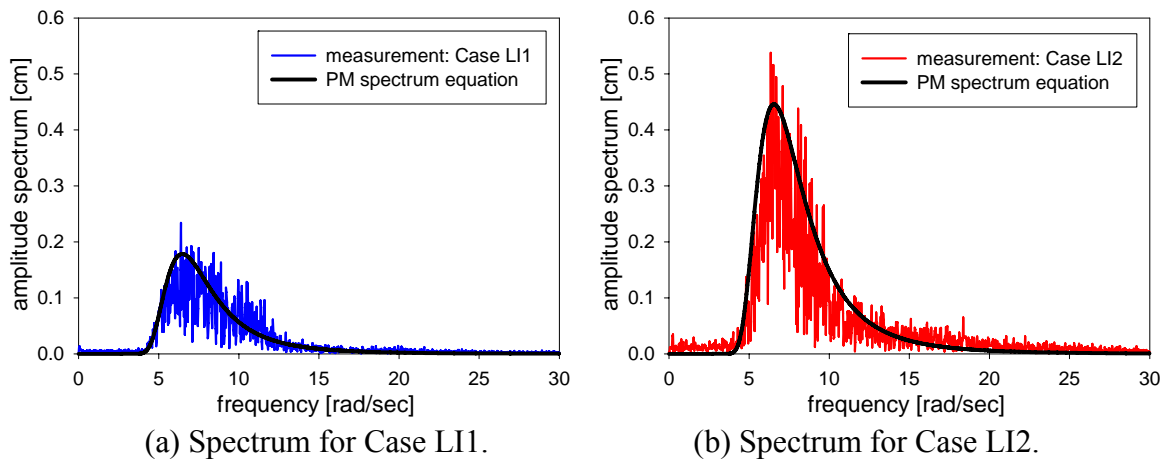(a) Spectrum for Case LI1.   (b) Spectrum for Case LI2.

Fig. 3.10 Comparison of measurement and theory of irregular wave amplitude spectra for the wave kinematics measurements using LDV system.

3.1.3 Generation of irregular and rogue waves for the kinematics measurement using the PIV system

A series of irregular wave trains have been obtained to generate the rogue wave in the 2-D wave tank and to measure the particle velocities using the PIV equipment. The rogue wave may occur in the process of geometrical focusing, dispersion enhancement (Kharif et al., 2001) and wave-current interactions (Peregrine, 1976; Smith, 1976; Lavrenov, 1998) in the real field. A combination of the geometrical focusing and dispersion enhancement mechanism can also be considered as the process of forming an extreme wave (Wu and Nepf, 2002). Many researchers have suggested and developed the nonlinear theory for rogue waves over the last decade. However, the rogue wave which is an event of majestic individual waves and highly nonlinear phenomena is not fully understood with the present modeling of surface waves (Haver, 2004).

For the control of the experiment parameters, the repeatability of experiments, and the relatively low cost for carrying out experiments, the rogue wave generation can be done in a 2-D laboratory wave tank, and may not be different from the rogue wave which occurs in the real ocean.

Two important characteristics of the rogue wave are considered for generating the rogue wave in the 2-D wave tank instead of in the real ocean. The first characteristic was the definition of a rogue wave. If the maximum height is more than twice as large as the significant wave height of the record, and the ratio of crest height H_c to significant wave height H_S is greater than 1.25, it can be called a rogue wave (Olagnon and Iseghem, 2001). The maximum height of a wave train is the highest one in the entire wave record. Therefore, the 2-D rogue waves analyzed in this study have been selected by two criteria, named C_H and C_c.

$$C_H \equiv H / H_S > 2.0 \quad \text{and} \quad C_c \equiv H_c / H_S > 1.25 \tag{3.7}$$

The second important characteristic of the rogue wave is that the highly nonlinear wave is a strongly asymmetric wave. In the ocean, strong asymmetric waves may be generated by the wind whose pressure is higher on the back than on the front of the crest. The highly nonlinear wave was simulated numerically by imposing such pressure on the surface of a wave of a particular period (Cokelet, 1977). Myrhaug and Kjeldsen (1986) analyzed the field data of the extreme seas where many ships were lost and described the extreme wave, as "a shallow and relatively long trough followed by a high and relatively short crest", which is similar to a strongly asymmetric wave. Bonmarin and Kjeldsen (2001) investigated the effects of the geometric and kinematic properties of plunging waves. They concluded that the asymmetry of a wave is an important parameter which contributes to the danger of breaking waves.

We processed three steps to generate the rogue wave in the 2-D wave tank. As the first step to generate the rogue wave, the irregular wave train is designed with JOSWAP spectrum. As the second step to generate the rogue wave, the distortion method was applied to the maximum wave of an irregular wave train. There are three steps to the distortion, amplitude distortion, time distortion, and crest distortion techniques, to generate the asymmetries in the irregular wave in a 2-D wave tank (Funke and Mansard, 1982). Amplitude distortion is intended to increase the crest height and reduce the trough height but keep the input and output amplitude spectra identical and change the phase spectra only. The time distortion is utilized to make the duration of the trough longer and that of the crest shorter but the total period remains the same. Crest distortion is employed to move the location of the highest wave crest forward, and therefore, the front steepness will increase.

Zou and Kim (2000) generated a strong asymmetric wave by using the methods of time distortion and crest distortion to the highest wave. As the third step to generate rogue wave, the input signal for the asymmetric wave was scaled up for the specific period of time (e.g. 40 seconds in this study), in which contains the signal for the highest wave, to increase the wave height of the targeted wave. Namely, the input signal for the highest wave is located at the center of the truncated period of 40 seconds. All the other segments of the time series were not increased, but these segments were connected to each other to make the reasonable long resultant wave elevation time series.

Fig. 3.11 (a) shows the reconstructed wave elevations before, being distorted and after being distorted. Their amplitude spectrums are represented in Fig. 3.11 (b). Both the spectra, before and after distortion, are different in the high frequency region. But their magnitudes are negligibly small. The number of occurrences for phase spectra of before and after distortion is different as shown in Fig. 3.11 (c) and (d).
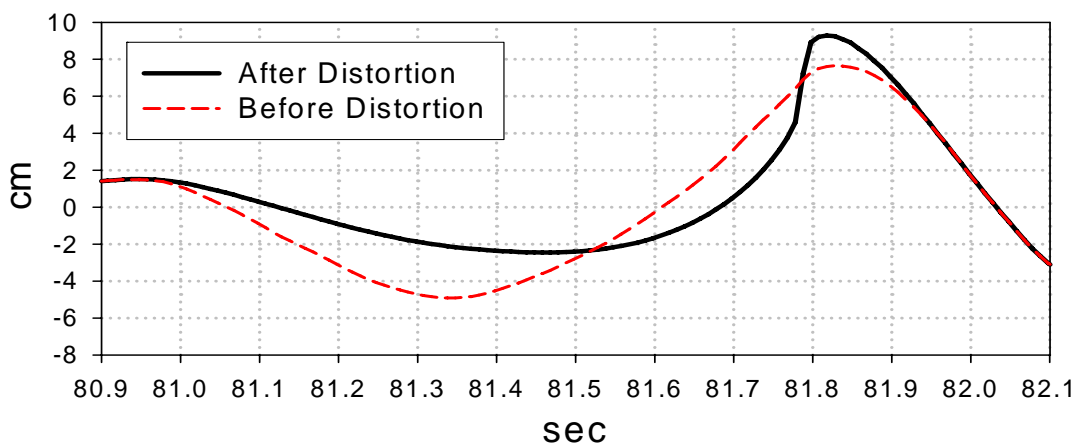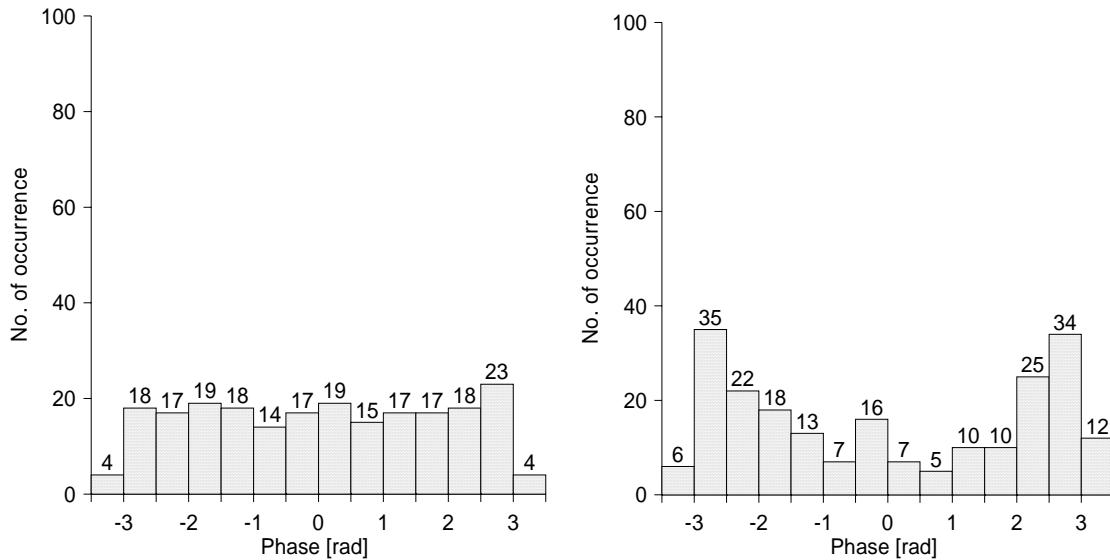
(a) Wave elevations.
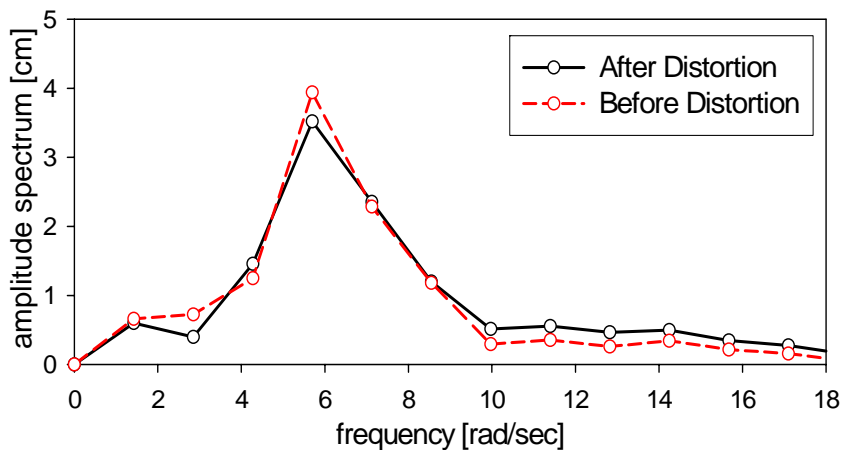
(b) Comparison of spectrum.

Fig. 3.11 Distortion of the highest elevation wave in irregular wave train.

(c) Histogram of phase (before distortion).   (d) Histogram of phase (after distortion).

Fig.3.11 Continued.

For the irregular wave data analysis, we collected time series of wave elevations at 620 cm from the wavemaker for 190 s. The time series of the irregular wave for Case PH1, Case PH2, Case PH3, and Case PH4 are shown in Fig. 3.12, Fig. 3.13, Fig. 3.14, and Fig. 3.15, respectively. Fig. 3.12 shows the largest wave for Case PH1 which was generated with the JONSWAP spectrum and the adopted distortion method. To satisfy the criteria of the rogue wave, we gradually increased the scale factor for step 3 of rogue wave generation. The largest wave of Case PH3 and Case PH4 meet the criteria for a rogue wave as shown in Fig. 3.14 and Fig. 3.15, respectively. Fig. 3.13 shows that the highest wave of Case PH2 is strongly asymmetric, but did not reach the criteria of a rogue wave.
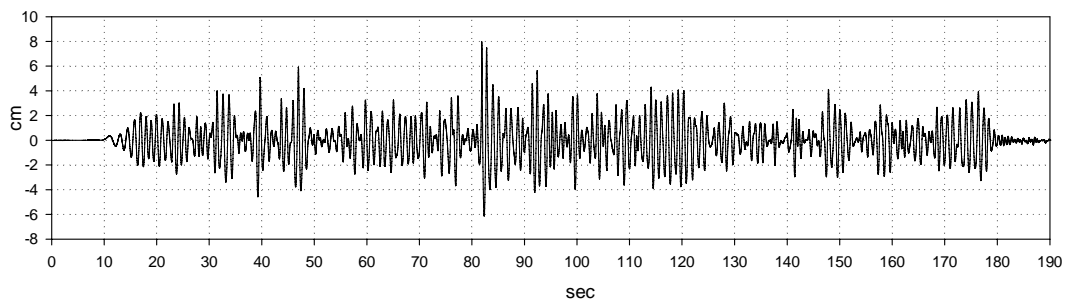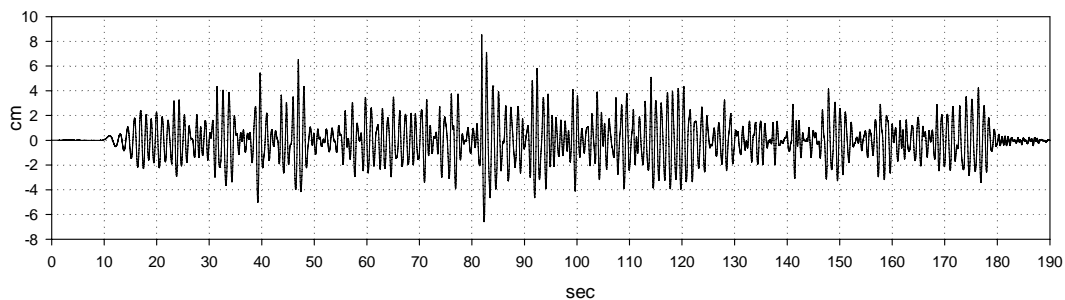
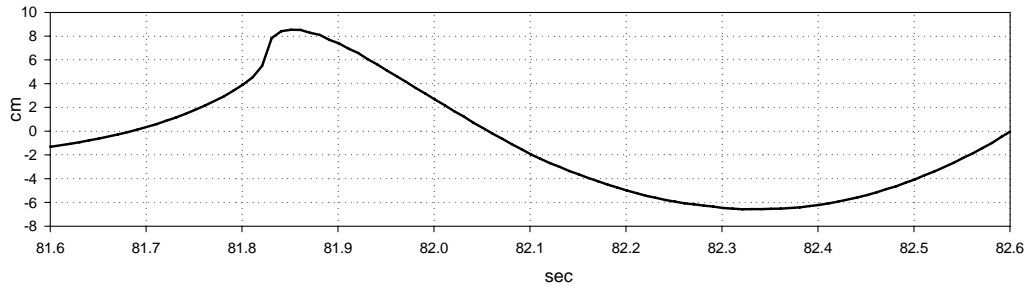(a) Whole time series for Case PH1, total 144 number of waves.
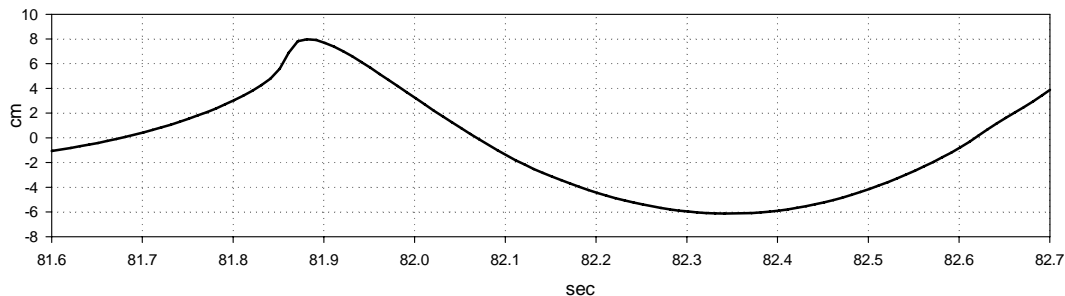
(b) Time series of the highest elevation wave for Case PH1.

Fig. 3.12 Time series of irregular waves for Case PH1, $T_S = 1.25$ s, $H_S = 6.63$ cm, the highest elevation wave height, H= 14.11 cm, T= 0.94 s, H/H_s =2.13, H_c/H_s =1.20.
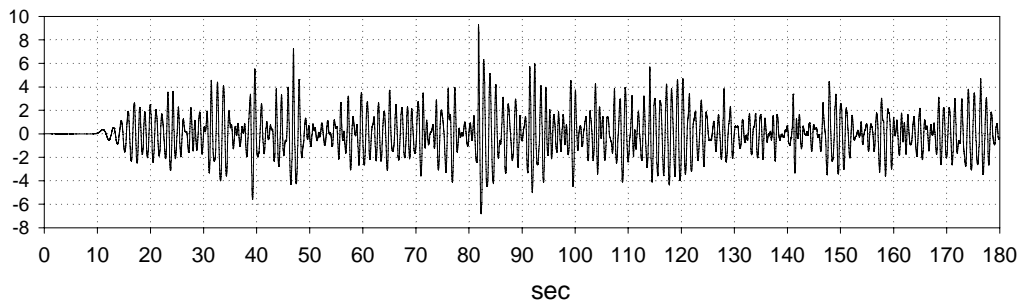

(a) Whole time series for Case PH2, total 136 number of waves.

Fig. 3.13 Time series of irregular waves for Case PH2, $T_S = 1.27$ s, $H_S = 6.995$ cm, the highest elevation wave height, H= 15.11 cm, T= 0.92 s, H/H_s =2.16, H_c/H_s =1.22.
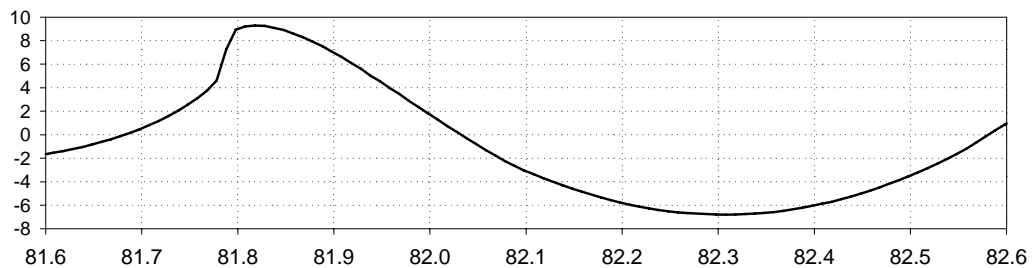
(b) Time series of the highest elevation wave for Case PH2.

Fig. 3.13 Continued.

(a) Whole time series for Case PH3, total 155 number of waves.

(b) Time series of the highest elevation wave for Case PH3.

Fig. 3.14 Time series of irregular waves for Case PH3, T_S = 1.19 s, H_S = 7.43 cm, the

highest elevation wave height, H= 16.09 cm, T= 0.9 s, H/H_s =2.17, H_c/H_s =1.25.
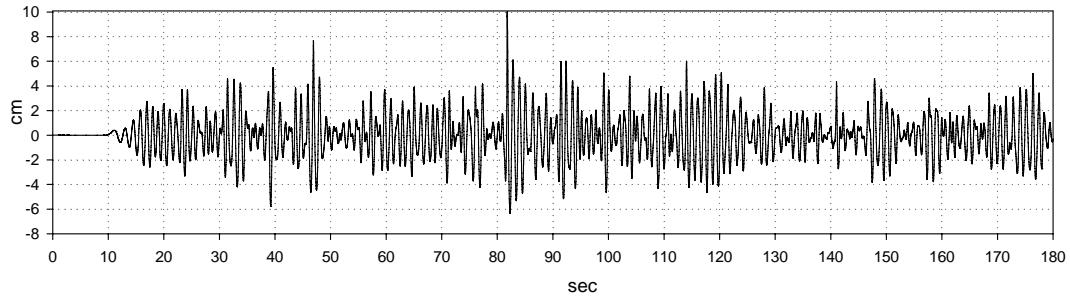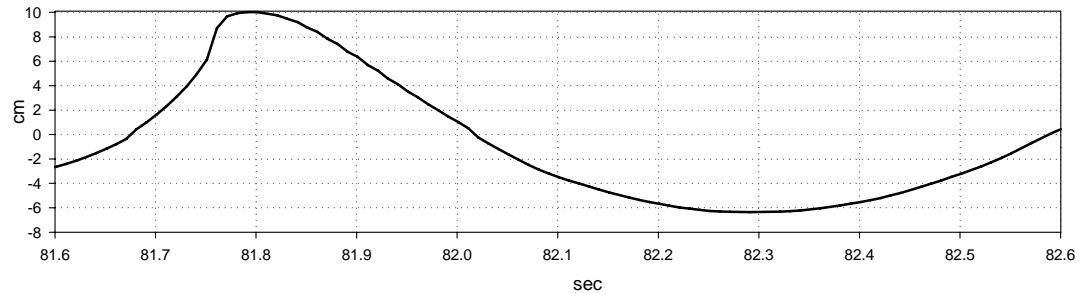
(a) Whole time series for Case PH4, total 150 number of waves.

(b) Time series of the highest elevation wave for Case PH4.

Fig. 3.15 Time series of irregular waves for Case PH4, $T_S = 1.18$ s, $H_S = 7.78$ cm, the highest elevation wave height, H= 16.36 cm, T= 0.9 s, $H/H_s = 2.11$, $H_c/H_s = 1.29$.

3.2 Data acquisition of particle velocity measurements

3.2.1 LDV raw data reduction

The sample rate of 3000 Hz of the LDV system in this study is very high. However, the validation of a sample rate depends on experimental conditions which are characteristic of flow, distribution of seeding material in the flow, intensity of laser light, etc. Therefore, it is possible that the LDV system is unable to obtain data at every time step. The raw data of the LDV system is needed to average the Δt into a smaller data rate; this is called reduction processing of the LDV raw data. The reduction process can provide the data with

a constant Δt and reduce the noise from raw data. An example of the reduction process is shown in Fig. 3.16.
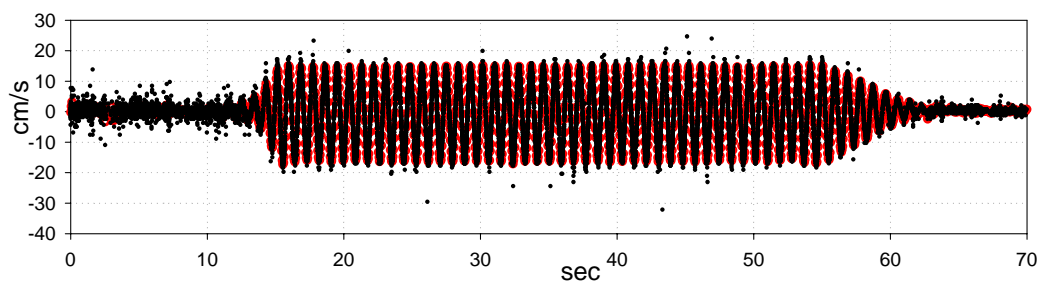
(a) Whole time series of particle velocity at z =-13.5 cm for Case LR2.
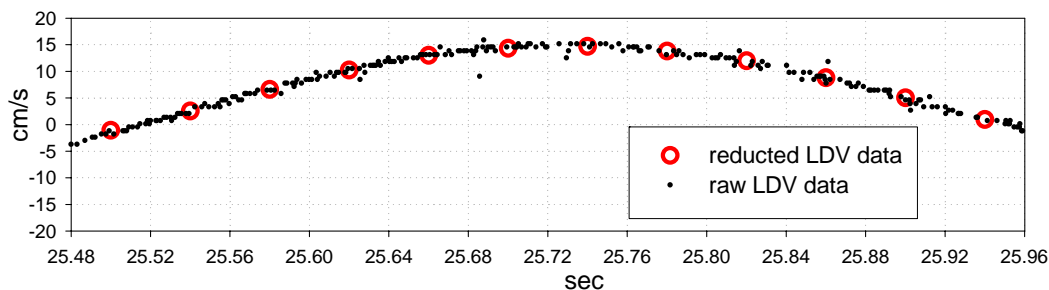
(b) Selected time series of particle velocity at z =-13.5 cm for Case LR2.

Fig. 3.16 LDV raw data (black dot) and reduction processed data (red circle) of the particle velocity at z =-13.5 cm for Case LR2.

3.2.2   Measuring particle velocities above the still water using the LDV system

The probe of the LDV system needs a proper distribution of seeding materials in the flow.   Fig 3.17 is the photo shot during the LDV experiment. Fig 3.18 shows the time series of particle velocities measured at the water depth of -13.5 cm from the free surface for Case LR2. It is found in Fig. 3.18 that adequate particle velocities are obtained for the entire measuring time. However, the particle velocities are seen only at the crest part in Fig.

3.19. The measuring point for Fig. 3.19 is 0.9 cm from the free surface. The data could not be obtained under the 0.9 cm because of no water. The seeding materials used in this study were silvered hollow particles with a diameter of 20 μm and a density of approximately 1.2 g/cm^3. The LDV laser light was scattered properly, but seeding materials dropped to the bottom as time increased during propagating wave. Therefore, we should gently add seeding materials on the running wave in order to not disturb the waves. In spite of these considerations, we had to allow the effects of human errors related to the injection of seeding material through the experiment using the LDV system.
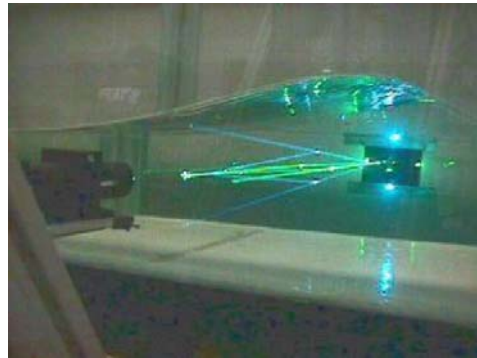

Fig. 3.17 Photo of laser beams of LDV system during measuring the particle velocity of propagating waves in the 2-D wave tank of Texas A&M University.
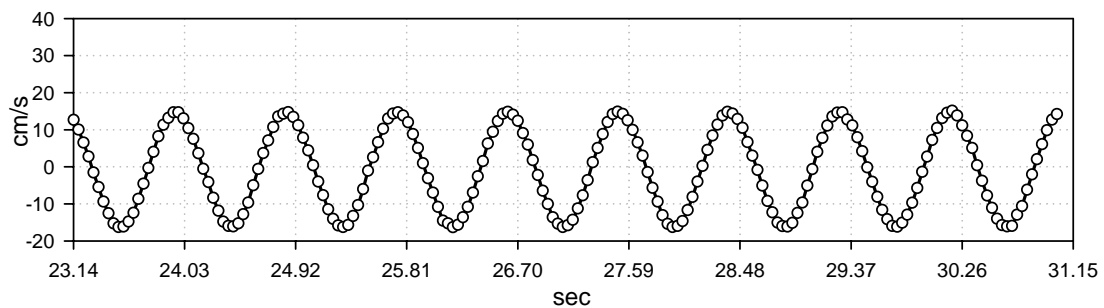

Fig. 3.18 Selected time series of the particle velocity under the trough using the LDV system at z =-13.5 cm for Case LR2.
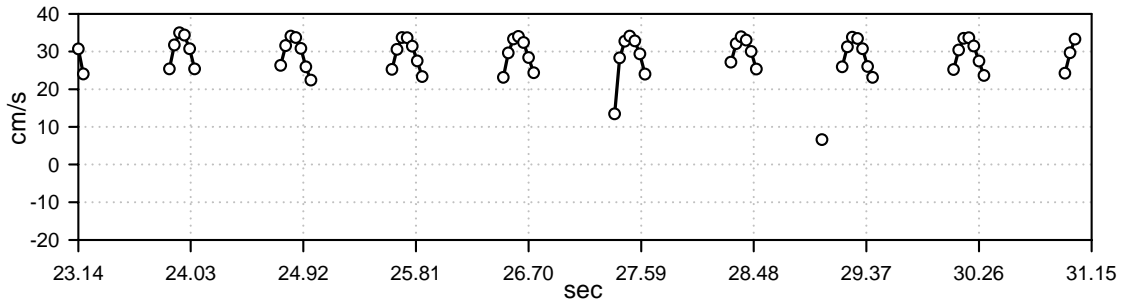
Fig. 3.19 Selected time series of the particle velocity above the still water using the LDV system at z =0.9 cm for Case LR2.

The measurements using the LDV and PIV systems were compared as shown in Fig. 3.20. Though the good agreement of the results of the LDV system and the PIV system has been concluded by Cenedese, Doglia and Romano (1994), a couple of comparisons with the results of the LDV and PIV systems are represented in this study. Fig 3.20 shows that most measurements follow the trend of analytical solutions of kinematics. However, it is found that the value of the LDV measurement data is less than that of the theory near the free surface. These discrepancies are resulted from disturbed waves by injecting tracer seeding materials to measure the velocity data of the wave above the still water level. A reasonable injection system should be considered to correct these discrepancies. It is also concluded that the measurements using the PIV system have a better agreement with the solutions of the third-order Stokes wave theory through all vertical positions in this study.
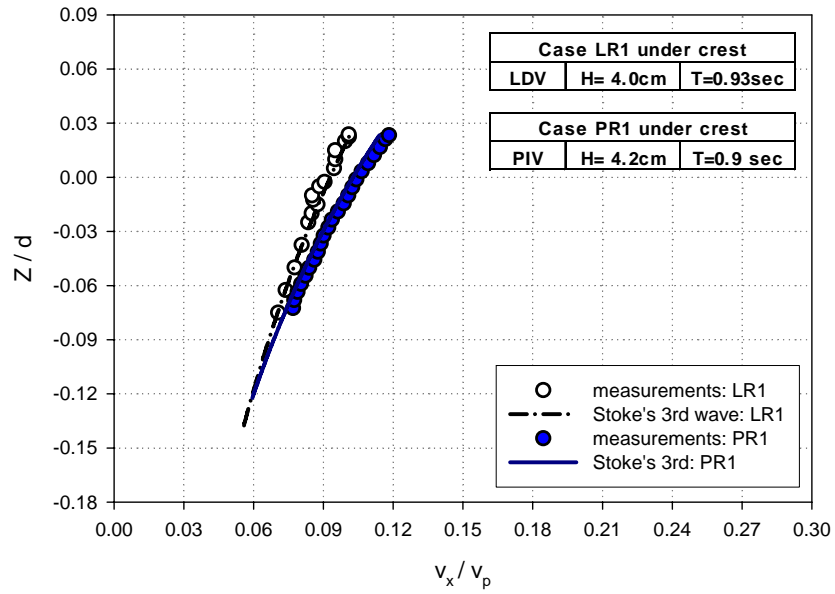
(a) Case LR1 and Case PR1.
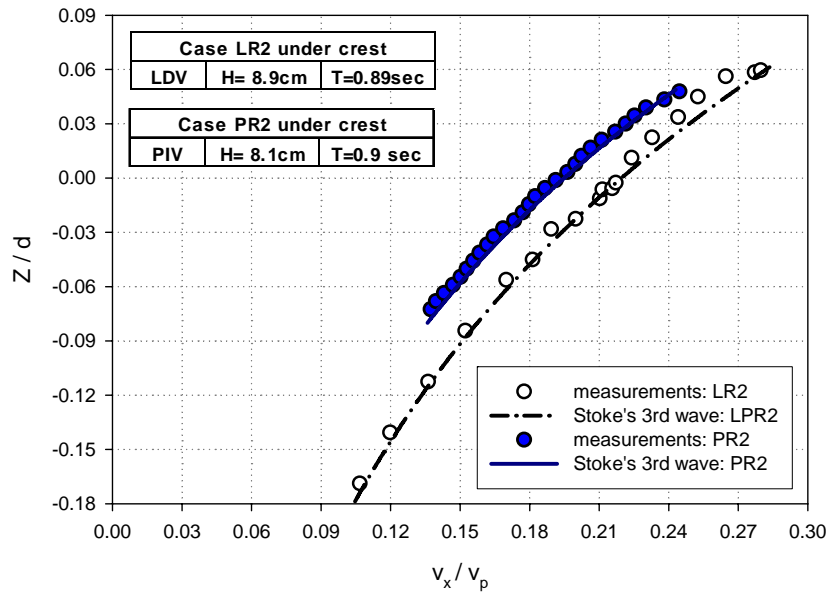
(b) Case LR2 and Case PR2.

Fig. 3.20 Comparison of horizontal particle velocity measurements under the crest point using the LDV system and the PIV system.

3.2.3   Size of field of view (FOV) and uncertainties of velocity in using the PIV system

The measurements were taken from twelve waves which are reached a steady state and did not include the reflected waves coming back. Using the phase-average method, the mean velocity is obtained. Twelve pairs of images were taken at each phase for twelve different phases for the PIV velocity measurements. Two fields of view (FOV) were arranged to obtain the velocity field at the wave gage as shown in Fig. 3. 21. The sizes of the fields of view are 127×159 mm^2 for FOV 1, and 172×215 mm^2 for FOV 2. The velocity fields of regular and irregular waves were taken with FOV 1. The larger FOV, FOV 2, was used to cover the relatively large areas of rogue waves. The smaller FOV, FOV 1, has a better spatial resolution and accuracy because the flow characteristics need to be examined for their variation of a spatial resolution. The coordinate system is also shown in Fig. 3.21 with $z = 0$ being the stationary free surface elevation and $x = 0$ the location of wave gage. The 32×32 pixels interrogation windows corresponded to a spatial resolution of 2.07×2.07 mm^2 for FOV 1, and 2.72×2.72 mm^2 for FOV 2. The time separation (*dt*) between the first and second laser pulses was 3.0 ms for FOV 1 and FOV 2. When choosing proper FOV for the accuracy and the best spatial resolution, the velocities measured by the PIV system have uncertainties due to a various aspects such as interrogation window size, particle image density, displacement gradients, etc (Raffel, 1998). Handling uncertainty of the velocity to decrease noises will be discussed in section 3.3.2.
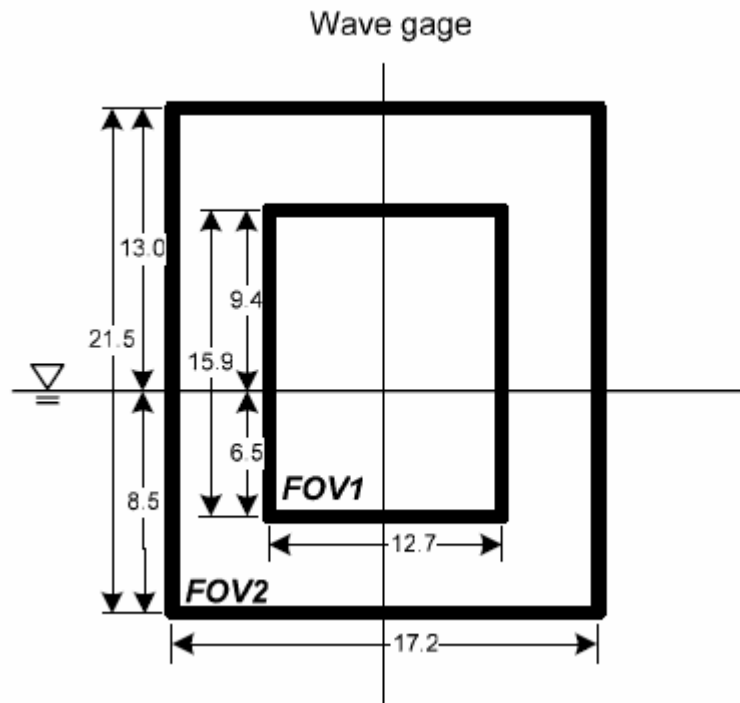
Fig. 3.21 PIV fields of view (unit: cm).

3.2.4 Mean flow in using the PIV system

The mean velocity is used to analyze regular wave kinematics in this study. The mean velocity was obtained by phase-averaging the measured instantaneous velocities at each phase, i.e.,

$$U_k = \frac{1}{N} \sum_{l=1}^{N} u_k^{(l)} \tag{3.8}$$

where, U_k is the phase-averaged mean velocity, $u_k^{(l)}$ is the k-component velocity obtained from the lth instantaneous velocity measurement, and N the total number of instantaneous velocities at that phase. The RMS horizontal particle velocity was obtained by the equation (3.9), i.e.

$$U_{rms} = \sqrt{\sum_{i=1}^{N} [(U_i - U_k)^2 / N]} \qquad (3.9)$$

where U_i represents the measured wave height for each wave, U_k the phase-averaged mean velocity of selected regular waves, and N the number of selected regular waves.

The error rate of horizontal velocities of selected regular waves was calculated by the equation (3.10).

$$\text{ER}_{\text{U}} \ (\%) = \ (U_{rms}/U_k) \times 100 \qquad (3.10)$$

The RMS values of particle velocities are checked for all cases. The RMS values for Case PH5 which has the largest wave height are represented in Fig. 3.22. The error rate of the mean velocity for Case PH5 was within 5%. With this error rate, the instantaneous particle velocities were utilized to analyze the rogue wave kinematics.
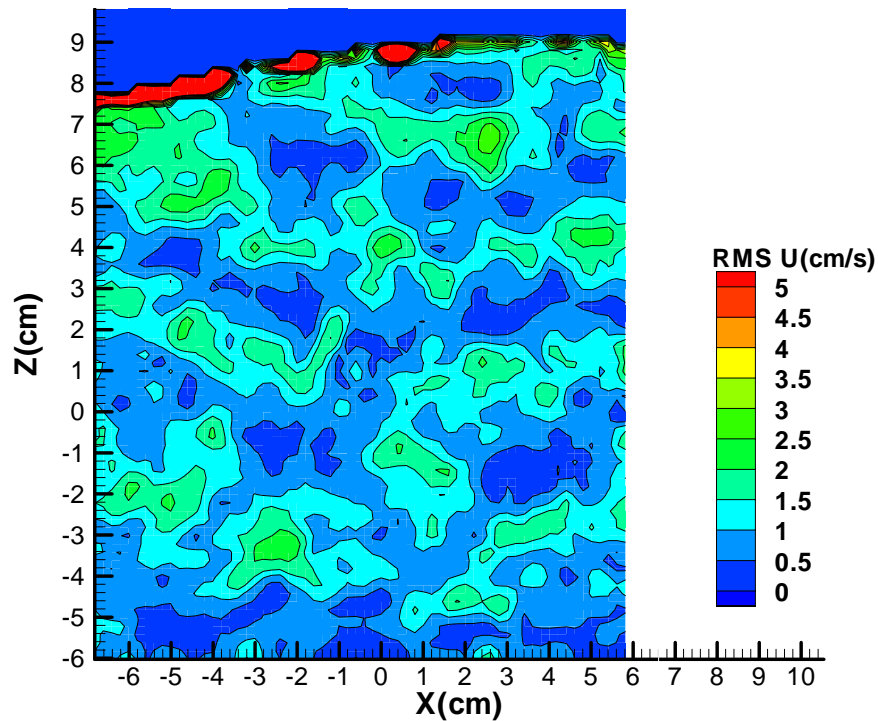

Fig. 3.22 The RMS horizontal particle velocity field under the wave crest for Case PH5.

3.3 Calculation of particle accelerations based on the measured velocities

The total acceleration derivative is composed of two types of terms: the local acceleration which is the change of velocities observed at a point in time, and the convective acceleration terms which are the changes of velocities that result due to the motion of the particle. We used the following equations of the total acceleration in this 2-D study, i.e.,

$$\frac{du}{dt} = \underbrace{\frac{\partial u}{\partial t}}_{local} + \underbrace{u\frac{\partial u}{\partial x} + w\frac{\partial u}{\partial z}}_{convective} \tag{3.11}$$

$$\frac{dw}{dt} = \underbrace{\frac{\partial w}{\partial t}}_{local} + \underbrace{u\frac{\partial w}{\partial x} + w\frac{\partial w}{\partial z}}_{convective} \tag{3.12}$$

where $\dfrac{du}{dt}$ represents horizontal particle total acceleration, $\dfrac{dw}{dt}$ vertical particle total acceleration.

3.3.1 Local acceleration of water wave particle

The local acceleration fields were computed by applying a centered finite difference scheme to measured velocity fields. The equation of a center difference method for a local acceleration is represented as follows:

$$a_t = \frac{(u_{t+1} - u_{t-1})}{2 \cdot \Delta t} \tag{3.13}$$

The LDV equipment is a single point measurement tool, but the PIV system can obtain the velocity field with a single test. Each regular wave of the PIV measurements consists of twelve phases or twelve field views per wave length. We took field views continuously

with a constant time step for the PIV measurements of irregular waves. The time step Δt in the equation (3.13) used 0.04 s and 0.075 s for the LDV and PIV systems, respectively in this study. The Fig. 3.23 shows images which were used in the local acceleration of the PIV measurement based computation with a centered finite difference method. The twelve phases correspond to the timing of PIV measurements. Since the wave period was 0.9 s, the time interval between each PIV phase was 0.075 s. The horizontal local acceleration at phase 8 was computed using equation (3.13) as follows:

$$local\ a_x(phase8)\ =\ \frac{V_x(phase9) - V_x(phase7)}{2 \times \Delta t} \tag{3.14}$$

As seen in Fig. 3.23, the local acceleration near the free surface of phase 8 could not be obtained because of no data near the free surface corresponding to the location of phase 7 and phase 9. This missing local acceleration can be reduced with smaller time steps between phases.

The local accelerations which were computed based on measurements using the LDV and PIV systems were compared as shown in Fig. 3.24. The local acceleration of LDV measurements has good agreement generally with that of the third-order Stokes wave theory through the measurement of the vertical position. The results of LDV measurement near the free surface show an inconsistent trend with the third-order Stokes wave theory. The local acceleration of PIV measurements has followed the trend of that of the third-order Stokes wave theory, but has smaller values. Various aspects which can be considered as the cause of discrepancies are shown in Fig. 3.24. Two reasons for the cause of discrepancies could be the time step which can produce inherent error in the finite difference local acceleration computation and the injection of seeding materials in the LDV system.

(a) Phase 9 (velocity)   (b) Phase 8 (local acceleration)   (c) Phase 7 (velocity)
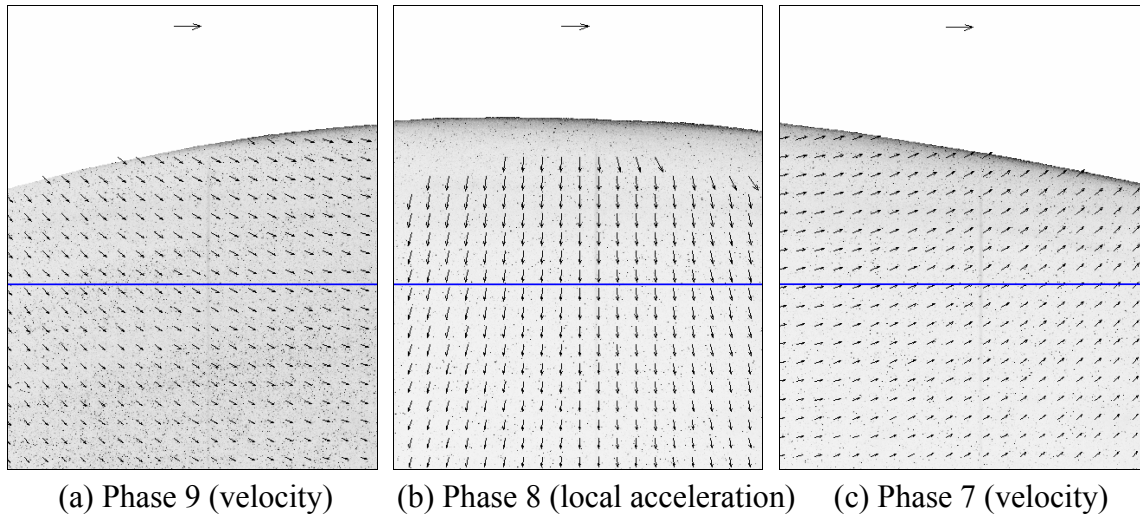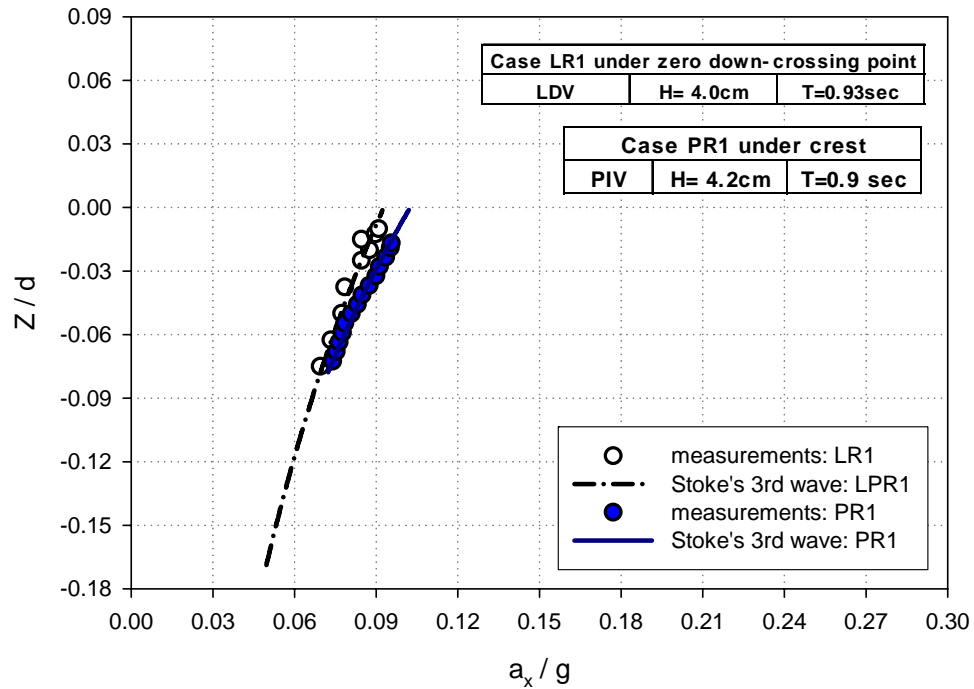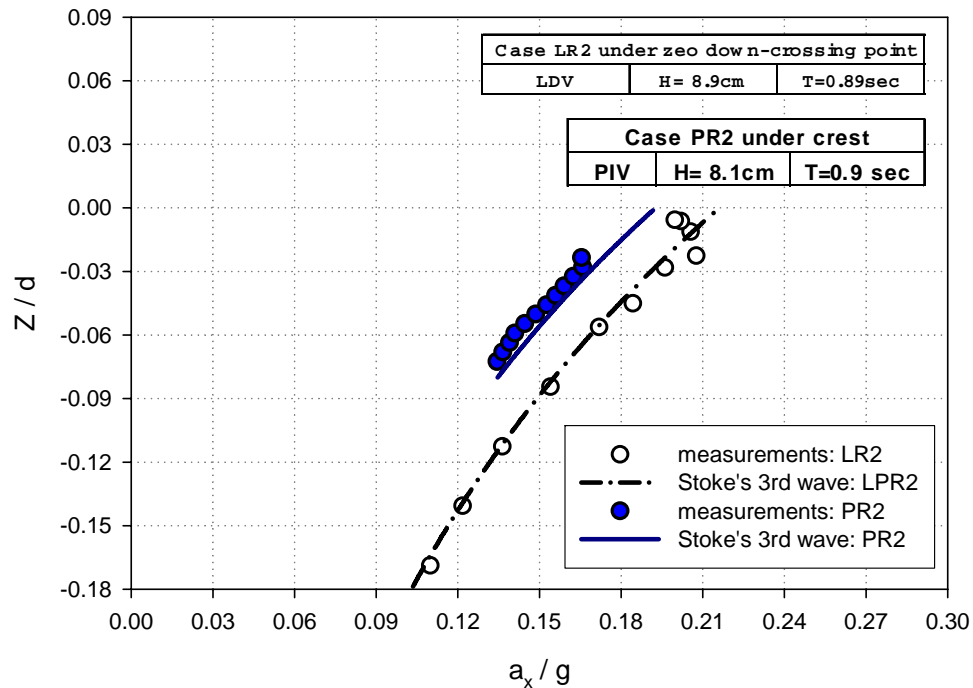
Fig. 3.23 Images and corresponding kinematics vector fields for local accelerations of the PIV measurement based computations for Case PR3.

(a) Case LR1 and Case PR1.

Fig. 3.24 Comparison of horizontal local acceleration measurements under the down crossing point using the LDV system and the PIV system.

(b) Case LR2 and Case PR2.

Fig. 3.24 Continued.

3.3.2   *Convective acceleration of water wave particle*

The convective acceleration fields were computed by applying a centered finite difference scheme to measured velocity fields using the PIV system. The convective accelerations from the PIV measurement-based computation are scattered as shown in Fig. 3.25 (a). Each estimate of velocity using the PIV system is associated with a measurement uncertainty (the value of error) whose magnitude depends on a wide variety of aspects such as an interrogation window size, a particle image density, displacement gradients, etc. Since differential estimates from the velocity data require the computation of differences on neighboring data the noise increases inversely proportional to the difference, $V_{i+1} - V_{i-1}$,

as the spacing between the data $\Delta X = |X_{i+1} - X_{i-1}|$ is required. That is, the estimation of uncertainties in the differential is scaled with *uncertainty*$/\Delta X$. The noise shown in Fig.3.25 (b) with Δx and $\Delta z = 6$ mm is three times smaller than that in Fig.3.25 (a) with Δx and $\Delta z = 2$ mm. The space steps, Δx and Δz, for acceleration computations done by applying a centered finite differential scheme were 6 mm in this study.

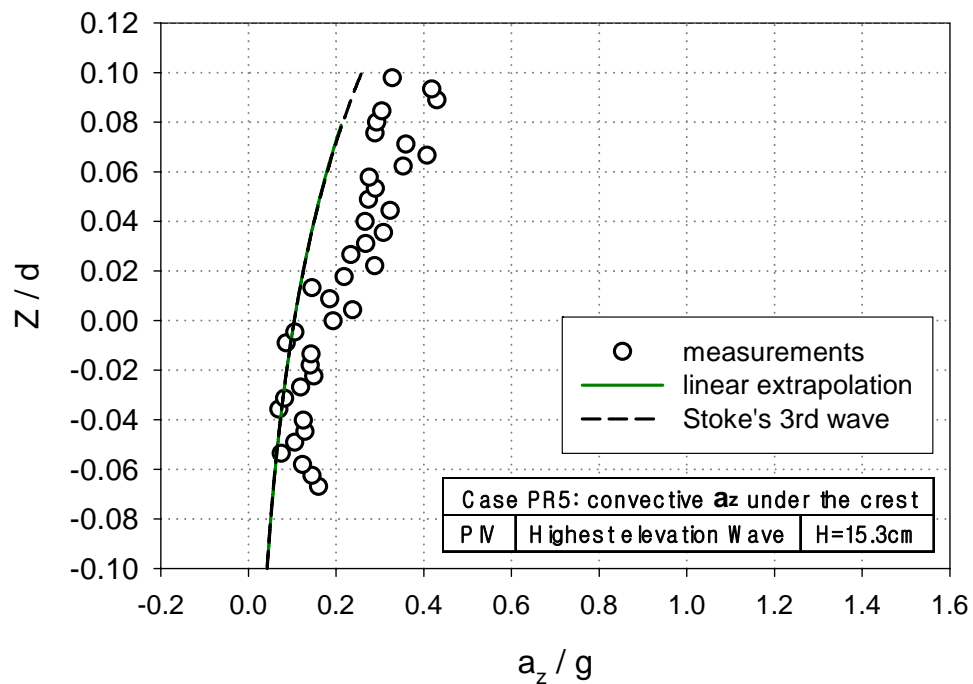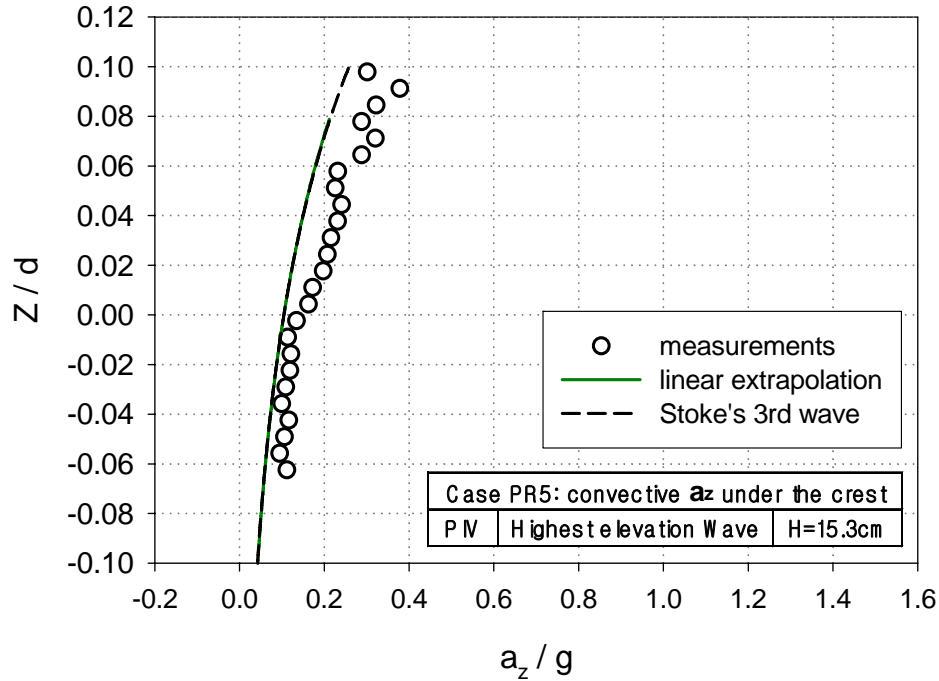(a) Δx and $\Delta z = 2$mm.

Fig. 3.25 Vertical convective accelerations of the PIV measurement based computations under the crest part for Case PR5.

(b) Δx and $\Delta z = 6$mm.

Fig. 3.25 Continued.

3.4 Wave force: application of obtained wave kinematics to the Morison equation

The measured kinematics of waves were applied to the Morison equation to predict the load force of a wave on the slender body. The Morison equation is stated as follows,

$$F = C_m \rho \pi r^2 \int_{-d}^{\eta} \dot{u} dz + C_D \rho r \int_{-d}^{\eta} |u| \cdot u dz \qquad (3.15)$$

Fig. 3.26 is a diagram of the computations of wave forces for a vertical truncated cylinder. The measurements of forces for a vertical truncated cylinder have not been conducted in this study. However, the wave forces for a vertical truncated cylinder could be computed by using measurements and measurement-based computation. The draft of a

truncated cylinder was 30 cm to compare with the results of Kim and Kim (2003b). However, the local accelerations of waves could not be obtained near the wave crest and under the -6cm due to the time step of 75 ms and limitation of field of view, respectively as shown in Fig. 3.27. We also computed wave forces only with basis of the PIV measurements for rogue waves.
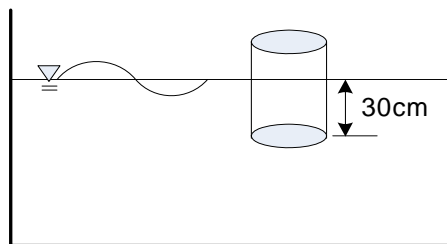

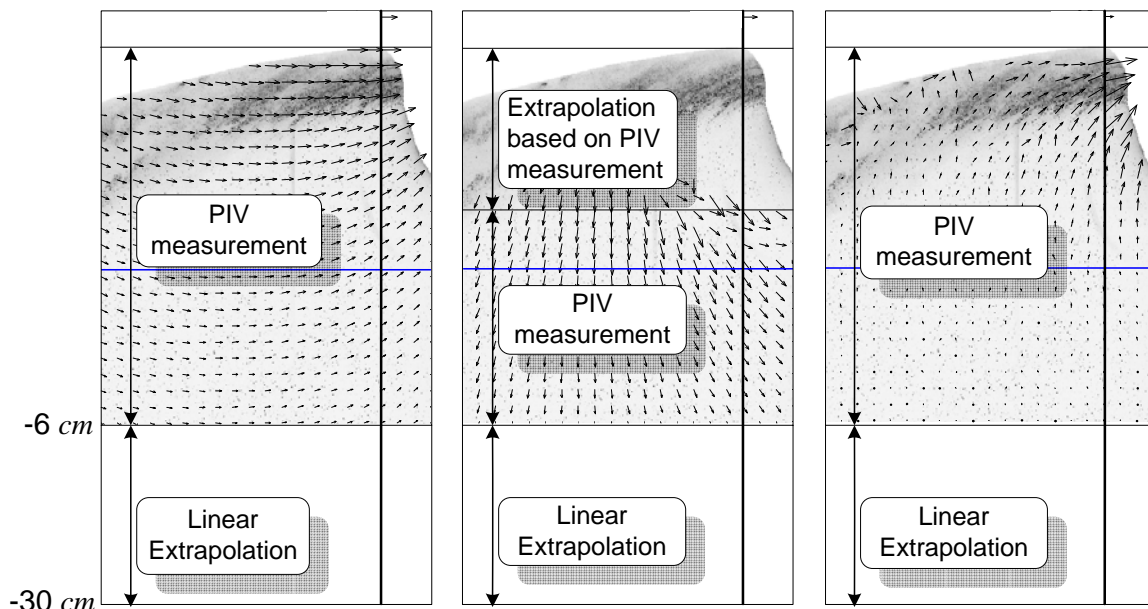Fig. 3.26 Diagram for the application of measured wave kinematics.

Fig. 3.27 Schematic sketch of the wave forces of the PIV measurement based computations.

CHAPTER IV

WAVE KINEMATICS FORMULA AND PREDICTION METHODS OF IRREGULAR WAVE KINEMATICS IN DEEP WATER

4.1   General

In this chapter, we will present the fundamentals of progressive regular wave kinematics and various methods to predict irregular wave kinematics in deep water. The regular wave theories have very accurately predicted wave kinematics under regular waves (Skjelbreia and Hendrickson, 1962; Cokelet, 1977; Gudmestad, 1990; Zhang et al., 1992). The basic equations will be described to provide fundamental knowledge of wave kinematics. It is important to state these basic formulas because there are difficulties in the attempts to obtain exact solutions even for a two-dimensional regular wave. Nonlinear terms in the free surface boundary can be linearized by the linear wave theory. Also, the linear solution relevant to the linear wave theory is attributed to the Stokes wave theory by using a perturbation method.

Many methods have been developed to predict the unidirectional irregular wave kinematics. These prediction methods include the traditional spectrum method (using FFT), the linear extrapolation, the Wheeler stretching method (Wheeler, 1970), yhe delta stretching (Rodenbusch and Forristall, 1986), the Gudmestad stretching (Gudmestad and Connor, 1986), the Heideman stretching (Skjelbreia et al., 1991), and the hybrid wave model (Zhang, 1996). The modified stretching method was developed to predict the strong

asymmetric wave kinematics (Kim et al., 1997).

Measurements using the PIV system and three different prediction methods for irregular waves will be compared for irregular and rogue waves of this study. Therefore, the three selected methods, which are the linear extrapolation, the Wheeler stretching, and the Kim's modified stretching method, will be discussed in this chapter.

4.2   Basic formulas of progressive regular water particle kinematics

The velocity potential $\phi(x, z, t)$ of the a two-dimensional fluid must satisfy the Laplace equation

$$\frac{\partial^2 \phi}{\partial x^2} + \frac{\partial^2 \phi}{\partial z^2} = 0 \tag{4.1}$$

subjected to the boundary conditions

$$\frac{\partial \phi}{\partial z} = 0 \quad \text{at} \quad z = -h \tag{4.2}$$

$$\frac{\partial \eta}{\partial t} + \frac{\partial \phi}{\partial x} \frac{\partial \eta}{\partial x} - \frac{\partial \phi}{\partial z} = 0 \quad \text{at} \quad z = \eta \tag{4.3}$$

$$\frac{\partial \phi}{\partial t} + \left[\left(\frac{\partial \phi}{\partial x} \right)^2 + \left(\frac{\partial \phi}{\partial z} \right)^2 \right] + g\eta = B \quad \text{at} \quad z = \eta \tag{4.4}$$

where h is the still water depth, $\eta(x, t)$ is the free surface elevation measured above the still water level $z = 0$, and B is the Bernoulli constant. Equation (4.3) is the kinematic boundary condition and equation (4.4) is the dynamic boundary condition.

The linear wave solution can be summarized as:

Water surface displacement

$$\eta(x, z, t) = \frac{H}{2} \cdot \cos(kx - \omega t) \tag{4.5}$$

The velocity potential

$$\phi(x,z,t) = -\frac{H \cdot g}{2 \cdot \omega} \cdot \frac{\cosh k(h+z)}{\cosh kh} \cdot \sin(kx - \omega t) \tag{4.6}$$

The horizontal and vertical velocities

$$u(x,z,t) = -\frac{\partial \phi}{\partial x} = \frac{H \cdot g \cdot k}{2 \cdot \omega} \cdot \frac{\cosh k(h+z)}{\cosh kh} \cdot \cos(kx - \omega t) \tag{4.7}$$

$$w(x,z,t) = -\frac{\partial \phi}{\partial z} = \frac{H \cdot g \cdot k}{2 \cdot \omega} \cdot \frac{\sinh k(h+z)}{\cosh kh} \cdot \sin(kx - \omega t) \tag{4.8}$$

The horizontal and vertical local accelerations

$$\dot{u}(x,z,t) = \frac{\partial u}{\partial t} = \frac{H \cdot g \cdot k}{2} \cdot \frac{\cosh k(h+z)}{\cosh kh} \cdot \sin(kx - \omega t) \tag{4.9}$$

$$\dot{w}(x,z,t) = \frac{\partial w}{\partial t} = -\frac{H \cdot g \cdot k}{2} \cdot \frac{\sinh k(h+z)}{\cosh kh} \cdot \cos(kx - \omega t) \tag{4.10}$$

The horizontal and vertical convective accelerations

$$u \cdot \frac{\partial u}{\partial x} + w \cdot \frac{\partial u}{\partial z} \tag{4.11}$$

$$u \cdot \frac{\partial w}{\partial x} + w \cdot \frac{\partial w}{\partial z} \tag{4.12}$$

$$\text{with } \frac{\partial u}{\partial x} = -\frac{H \cdot g \cdot k^2}{2 \cdot \omega} \cdot \frac{\cosh k(h+z)}{\cosh kh} \cdot \sin(kx - \omega t) \tag{4.13}$$

$$\frac{\partial u}{\partial z} = \frac{H \cdot g \cdot k^2}{2 \cdot \omega} \cdot \frac{\sinh k(h+z)}{\cosh kh} \cdot \cos(kx - \omega t) \tag{4.14}$$

$$\frac{\partial w}{\partial x} = \frac{H \cdot g \cdot k^2}{2 \cdot \omega} \cdot \frac{\sinh k(h+z)}{\cosh kh} \cdot \cos(kx - \omega t) \tag{4.15}$$

$$\frac{\partial u}{\partial x} = \frac{H \cdot g \cdot k^2}{2 \cdot \omega} \cdot \frac{\cosh k(h+z)}{\cosh kh} \cdot \sin(kx - \omega t) \tag{4.16}$$

where H is wave height, $\omega = 2\pi/T$, $k = 2\pi/L$ and T is the wave period.

Stokes (1847), furthermore, used a perturbation method in which successive approximations can be developed. It is assumed that the velocity potential $\phi(x,z,t)$ and the associated variables $(\eta, u, w, ...)$ may be written in the form

$$\phi(x,z,t) = \varepsilon\phi_1 + \varepsilon^2\phi_2 + O(\varepsilon^3) \qquad (4.17)$$

in which ε is the perturbation parameter and O is the order of magnitude. The Stokes' wave expansion method is formally valid for the very small amplitude wave, i.e.,

$$H/h \ll (kh)^2 \quad \text{for} \quad kh < 1 \quad \text{and} \quad H/L \ll 1 \qquad (4.18)$$

4.3 Prediction methods of irregular wave kinematics

The wave kinematics measured from the experiments with the PIV system were compared with the calculated one. The three approximate methods used to calculate the water wave kinematics are introduced in this section. These are the linear extrapolation, the Wheeler stretching method, and the modified stretching method.

Using the Fourier transform, a two-dimensional wave elevation can be decomposed into a series of component waves,

$$\eta(x,t) = \sum_{i=1}^{N} A_i \cos(k_i t - \omega_i t + \phi_i) \qquad (4.19)$$

where A_i, k_i, ω_i, and ϕ_i are the amplitude, wave-number, frequency and initial phase of the component wave with index i. The integer N is related to the cut-off frequency. The wave-number and frequency are related to each other based on the linear dispersion relation,
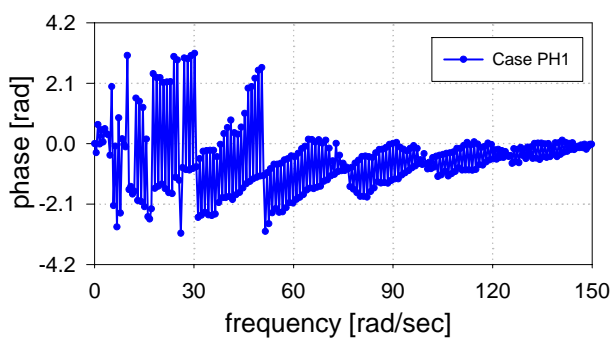
$$\omega_i^2 = g \cdot k_i \cdot \tanh(k_i h) \qquad (4.20)$$
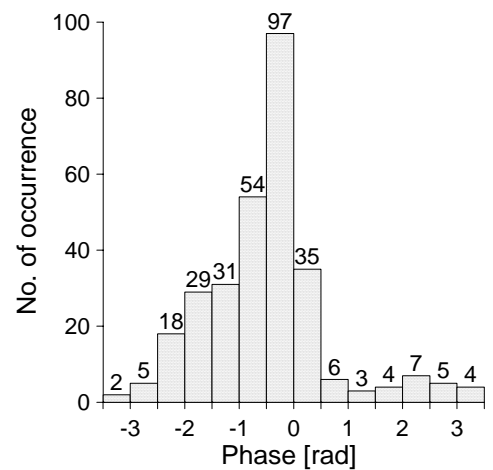
where h is the water depth.

The elevations of the irregular wave was calculated with the equation (4.19) and compared with the measured wave elevation as shown in Fig. 4.1, Fig. 4.2, Fig. 4.3 and Fig. 4.4. for Case PH1, Case PH2, Case PH3 and Case PH4, respectively.
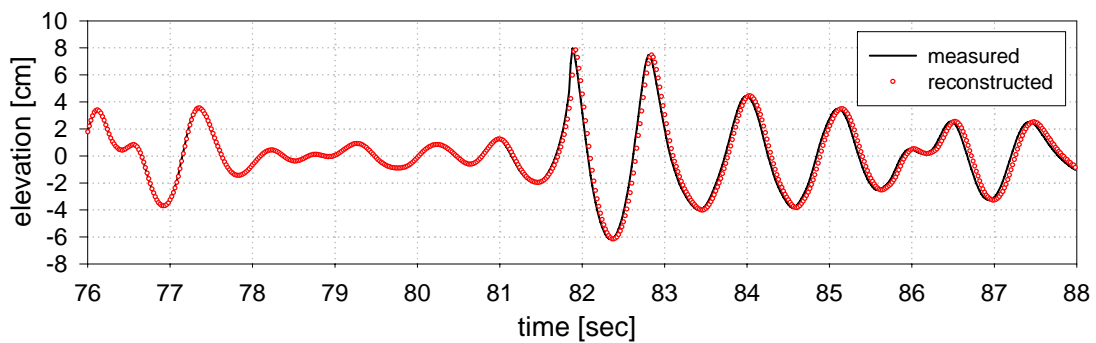
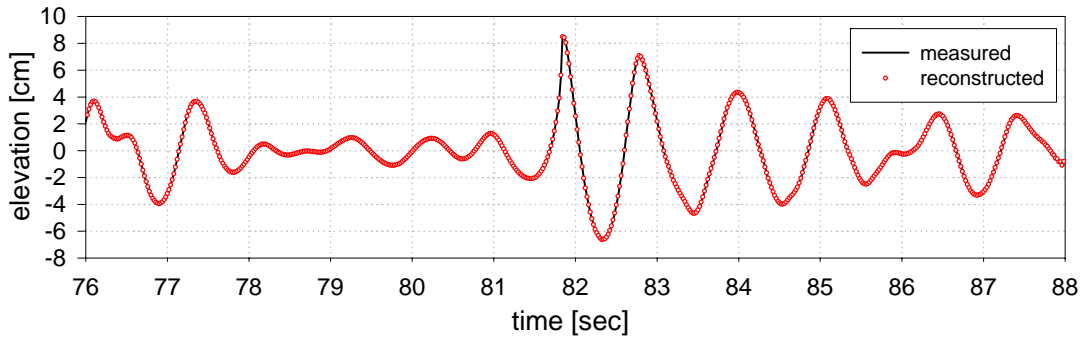(a) Laboratory measured wave (solid line), and simulated wave(red dot) for Case PH1.

(b) Phases.

(c) Histogram of phases.

Fig. 4.1 Wave elevations and wave phases decomposed using the FFT for Case PH1.

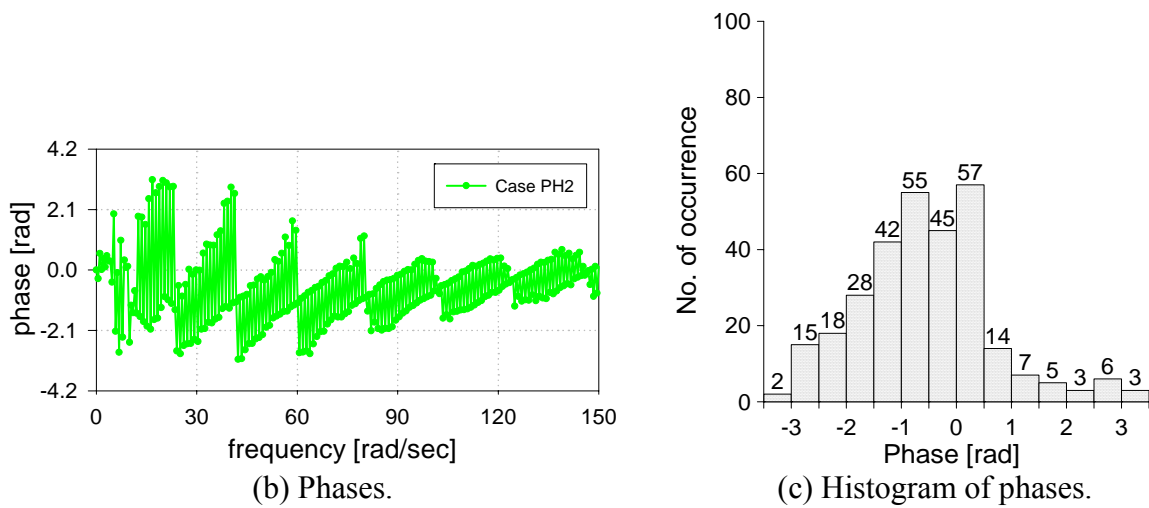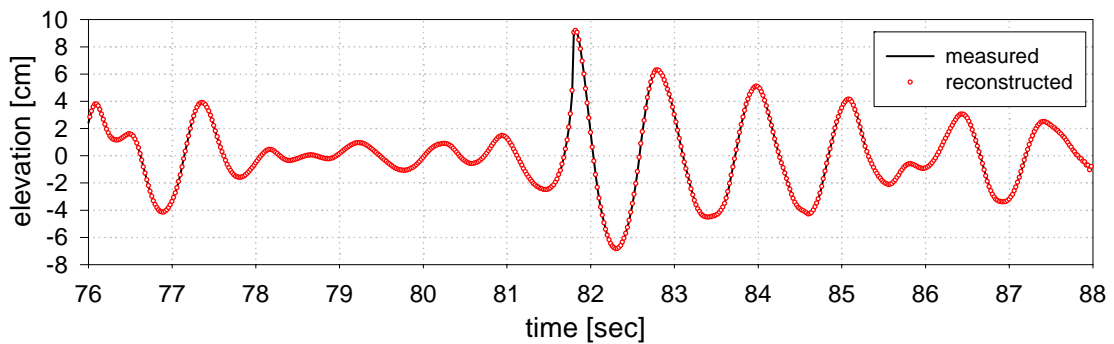(a) Laboratory measured wave (solid line), and simulated wave(red dot) for Case PH2.

(b) Phases.

(c) Histogram of phases.

Fig. 4.2 Wave elevations and wave phases decomposed using the FFT for Case PH2.

(a) Laboratory measured wave (solid line), and simulated wave(red dot) for Case PH3.

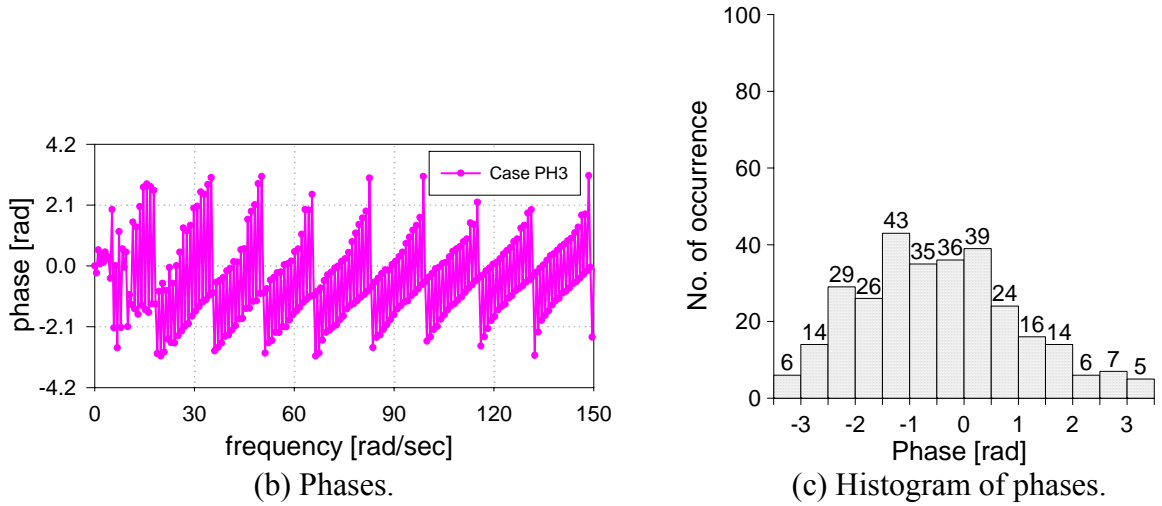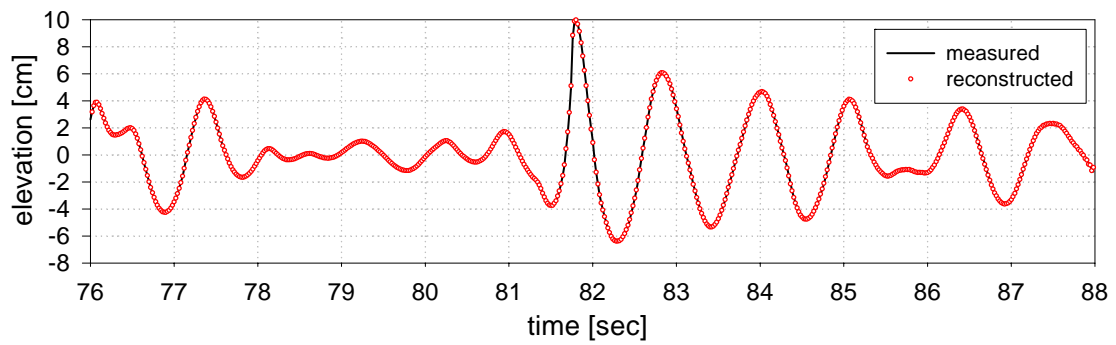Fig. 4.3 Wave elevations and wave phases decomposed using the FFT for Case PH3.

(b) Phases.

(c) Histogram of phases.

Fig. 4.3 Continued.

(a) Laboratory measured wave (solid line), and simulated wave(red dot) for Case PH4.
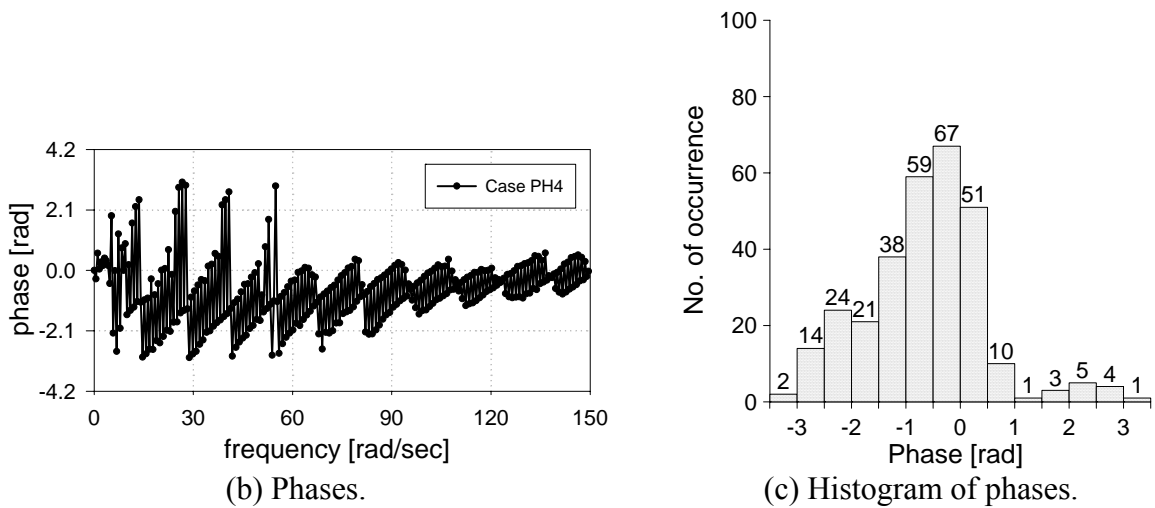

(b) Phases.

(c) Histogram of phases.

Fig. 4.4 Wave elevations and wave phases decomposed using the FFT for Case PH4.

According to the linear wave theory described in section 4.2, the horizontal and vertical velocity can be computed given the wave elevation as follows,

$$u(x,z,t) = \sum_{i=1}^{N} A_i \frac{g \cdot k_i}{\omega_i} \cdot \frac{\cosh[k_i \cdot (h+z)]}{\cosh k_i h} \cdot \cos(k_i x - \omega_i t + \phi_i) \tag{4.21}$$

$$w(x,z,t) = \sum_{i=1}^{N} A_i \frac{g \cdot k_i}{\omega_i} \cdot \frac{\sinh[k_i \cdot (h+z)]}{\cosh k_i h} \cdot \sin(k_i x - \omega_i t + \phi_i) \tag{4.22}$$

Other wave kinematics, the local and convective accelerations, can also be calculated using solutions of the linear wave theory presented in the previous section.

The linear extrapolation method for prediction of irregular wave kinematics is that equation (4.21) and equation (4.22) are modified only in the region under the crests and above the mean water level (MWL) by replacing them with their linear Taylor expansion about the MWL ($z = 0$):

$$u(x,z,t) = u(x,0,t) + z \frac{\partial u}{\partial z}(x,0,t), \text{ for } 0 \le z \le \eta \tag{4.23}$$

Each contribution to the resultant horizontal velocity and to the resultant vertical velocity from the waves at the tail of the spectrum can be very large near the wave crests because of large exponential amplification $\dfrac{\cosh[k_i \cdot (h+z)]}{\cosh k_i h}$, $\dfrac{\sinh[k_i \cdot (h+z)]}{\cosh k_i h}$ for $k_i \eta \gg 1$, respectively. To eliminate this unrealistic exponential amplification, the tail part of the wave spectrum cut can be ignored at a proper frequency. The amplitude spectrums and the ranges of cutoff frequencies used in each prediction method are shown in Fig. 4.5.
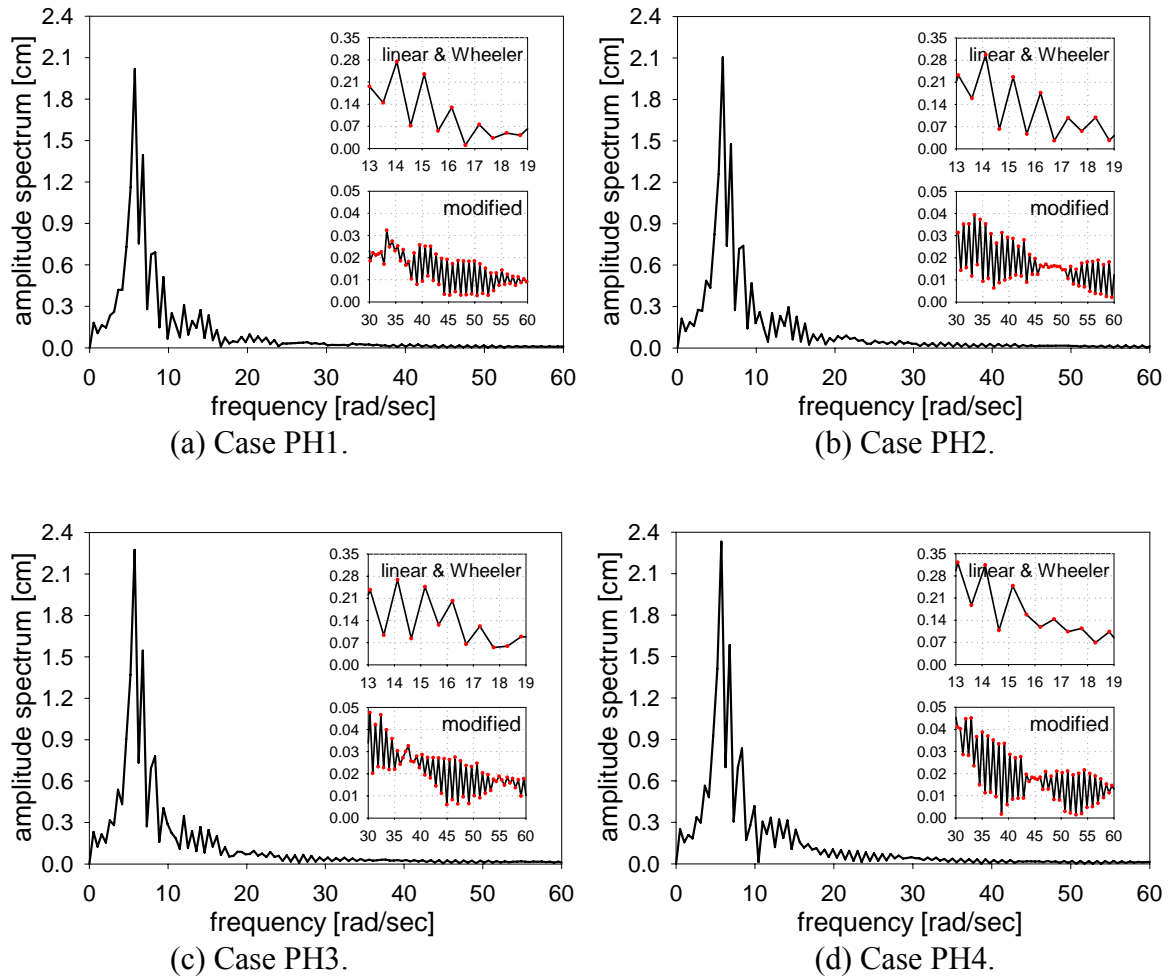
Fig. 4.5 Amplitude spectrums and cutoff frequency regions used in prediction of irregular wave kinematics for four irregular wave trains.

Fig. 4.6 shows the predicted horizontal velocities by the extrapolation method according to choosing cutoff frequency of spectrum. The results of linear extrapolation method are very sensitive depending on this cutoff frequency as shown in Fig. 4.6 (a), (b), (c), and (d). The results of the linear extrapolation method were various above the SWL.
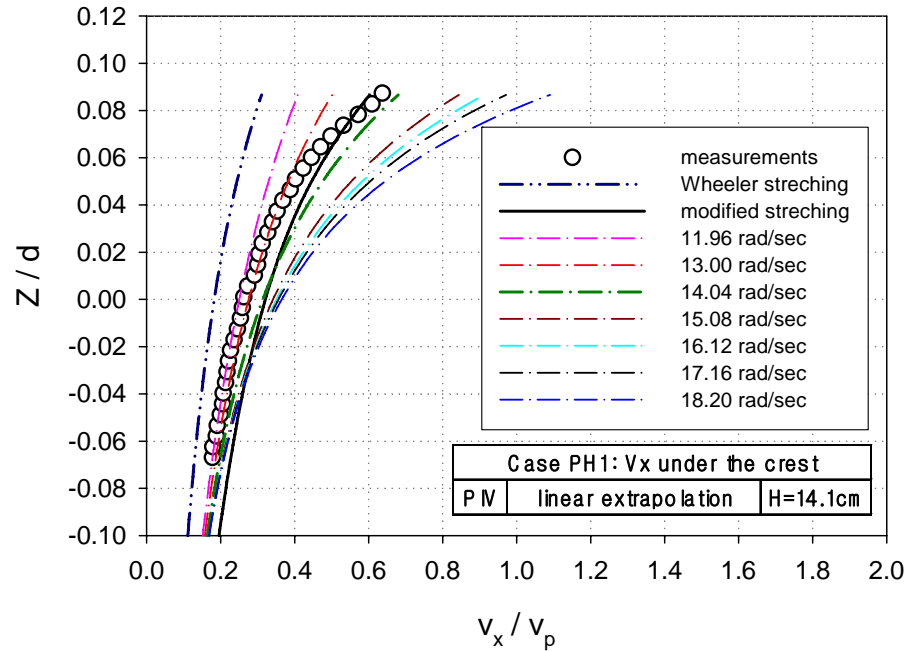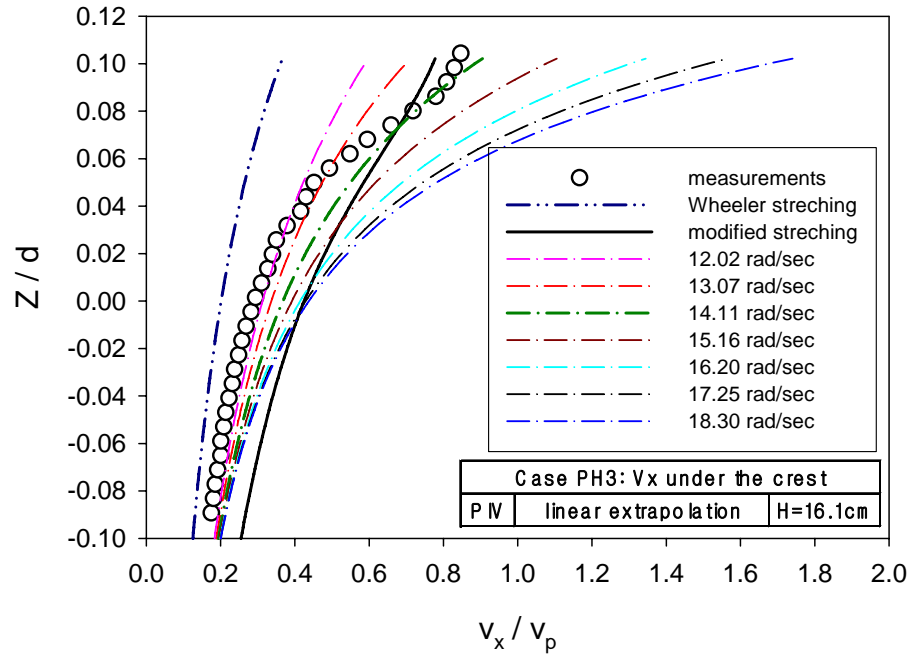
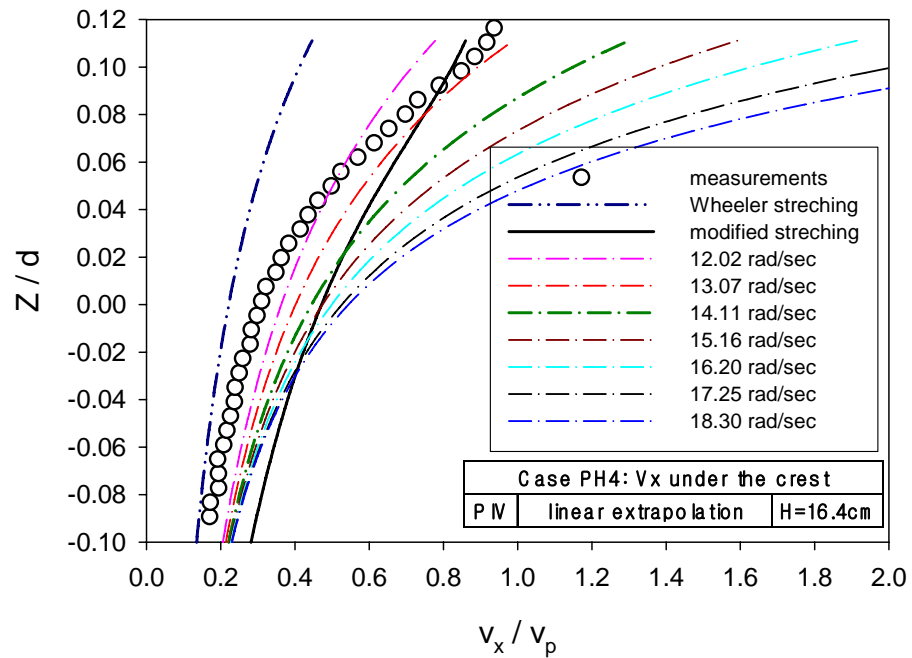(a) Horizontal velocity for Case PH1.
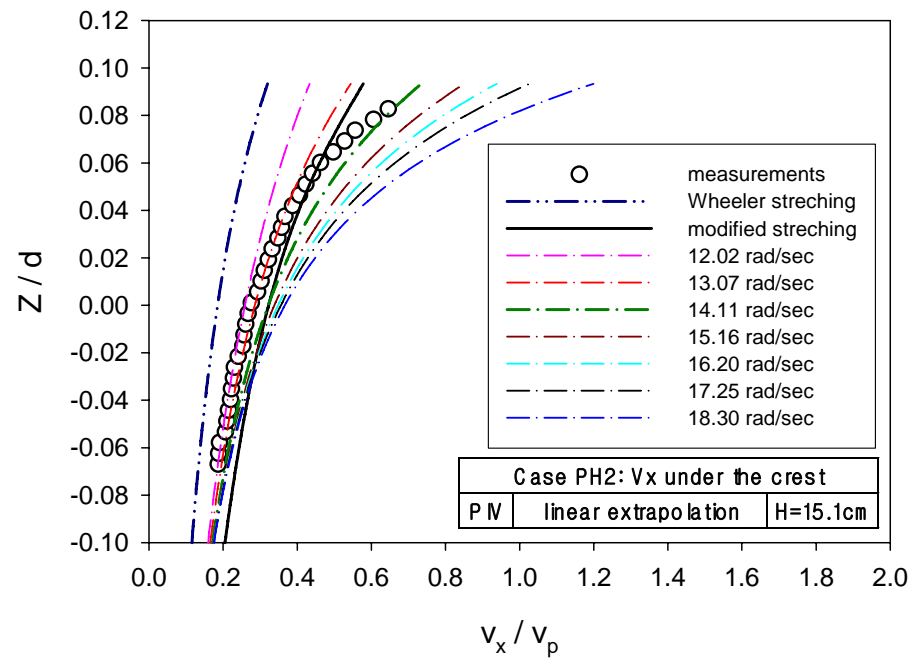
(b) Horizontal velocity for Case PH2.

Fig. 4.6 The changes in predicted horizontal velocities by the linear extrapolation method

due to seven different cutoff frequencies.

(c) Horizontal velocity for Case PH3.

(d) Horizontal velocity for Case PH4.

Fig. 4.6 Continued.

To avoid the divergence of the velocity at the SWL in the linear extrapolation method, Wheeler (1970) modified the equation (4.18) and named it the 'Wheeler stretching' method. The modification is made to map the vertical coordinate z (from the seabed to the instantaneous measured free surface) onto a computational vertical coordinate z_e (the effective vertical coordinate, $-h \le z_e \le 0$),

$$z_e = \frac{h \cdot (z_a - \eta)}{h + \eta} \qquad (4.24)$$

where z_a is the actual vertical coordinate ($-h \le z_z \le H_c$).

The horizontal water velocity, equation (4.25) was developed as follows,

$$u(x, z, t) = \sum_{i=1}^{N} A_i \frac{g \cdot k_i}{\omega_i} \cdot \frac{\cosh[k_i \cdot (\frac{z_a + h}{1 + \eta/h})]}{\cosh k_i h} \cdot \cos(k_i x - \omega_i t + \phi_i) \qquad (4.25)$$

We applied the equation (4.21) to the vertical water velocity as follows,

$$w(x, z, t) = \sum_{i=1}^{N} A_i \frac{g \cdot k_i}{\omega_i} \cdot \frac{\sinh[k_i \cdot (\frac{z_a + h}{1 + \eta/h})]}{\cosh k_i h} \cdot \sin(k_i x - \omega_i t + \phi_i) \qquad (4.26)$$

Prediction by the Wheeler stretching method is stable with the cutoff frequency as shown in Fig. 4.7. Although the Wheeler stretching method shows general improvement to predict the kinematics, there are still differences with measurement. The Wheeler stretching is expected to underpredict the wave kinematics in the wave crest.
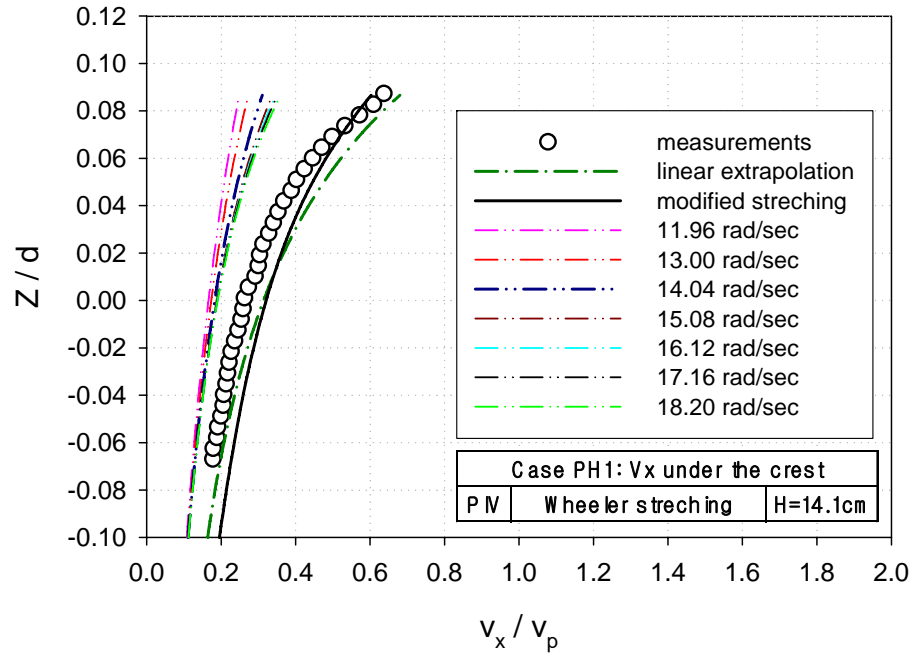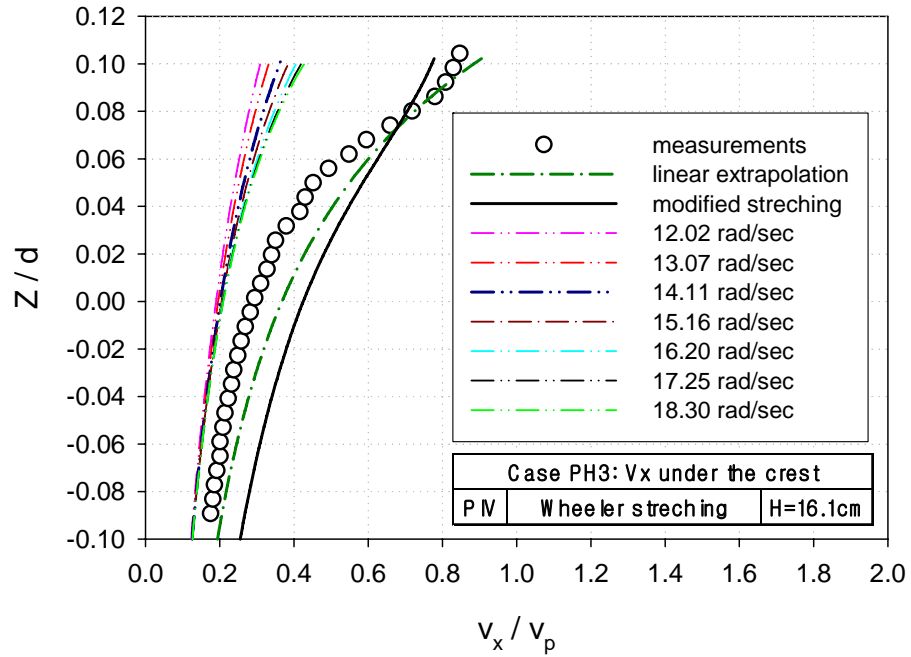
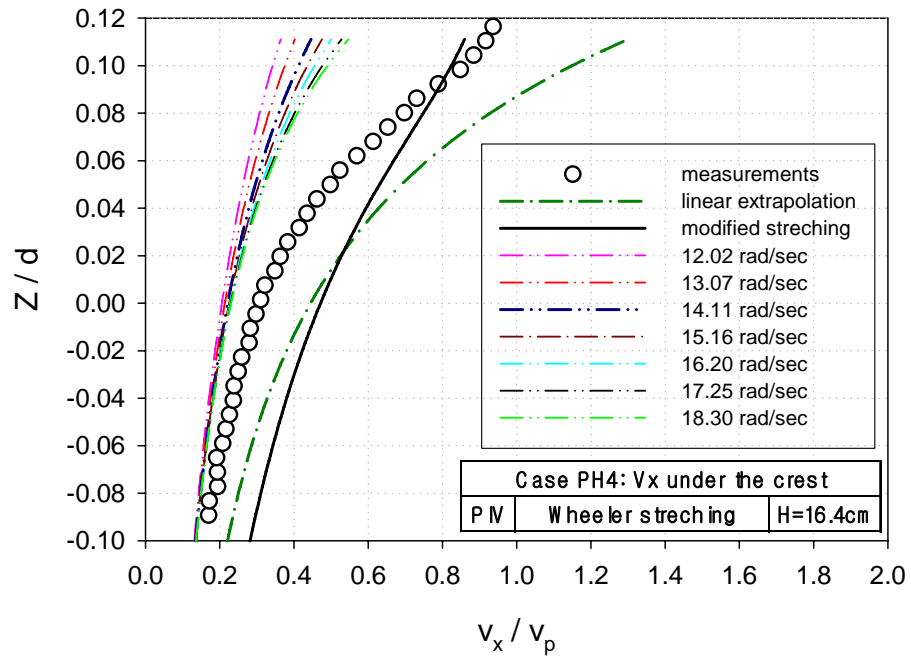(a) Horizontal velocity for Case PH1.
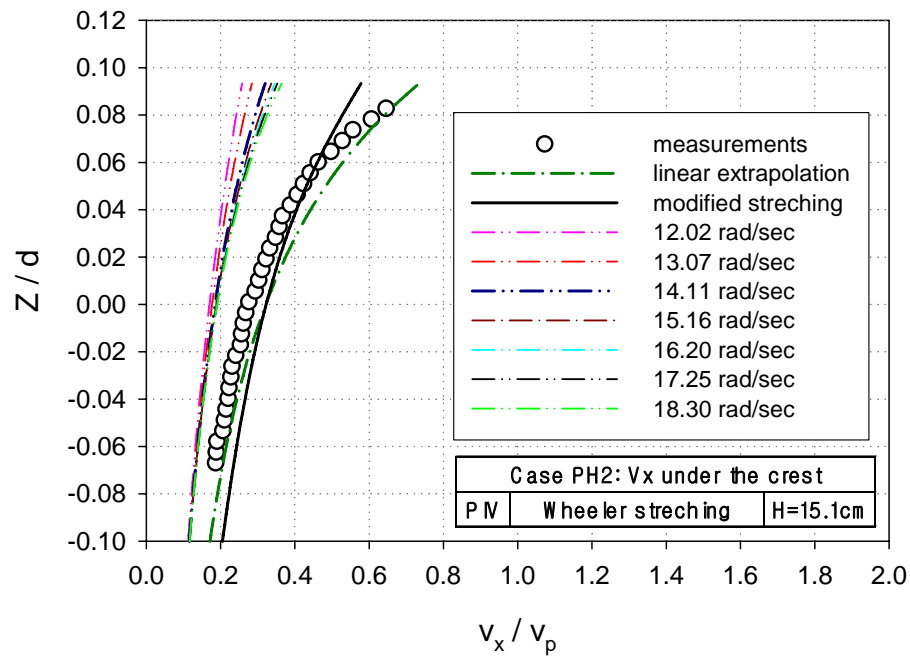
(b) Horizontal velocity for Case PH2.

Fig. 4.7 The changes in predicted horizontal velocities by the Wheeler stretching method

due to seven different cutoff frequencies.

(c) Horizontal velocity for Case PH3.

(d) Horizontal velocity for Case PH4.

Fig. 4.7 Continued.

The linear extrapolation method and Wheeler stretching are based on linear wave theory and are used for a linear wave and a weakly nonlinear wave. Kim et al. (1997) modified the stretching model to take into account the asymmetries of the wave in prediction of the highly nonlinear wave kinematics. The asymmetric factors of the rogue wave are defined as shown in Fig. 4.8.
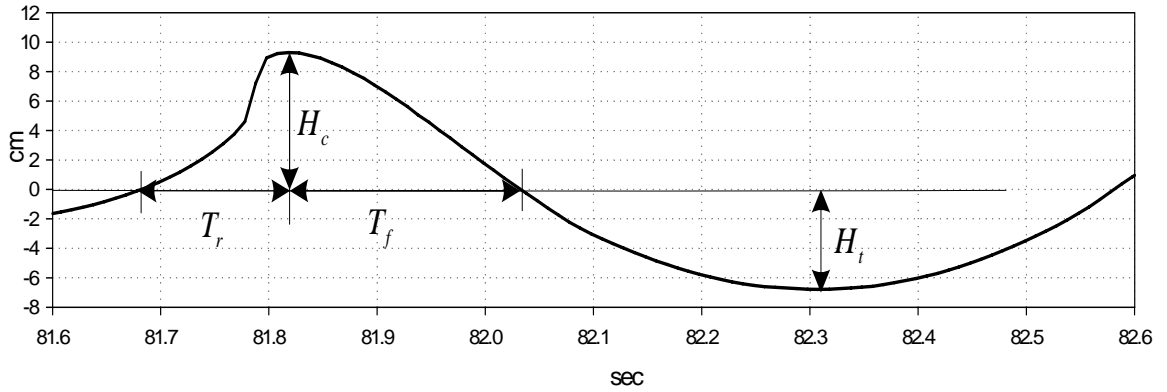
Fig. 4.8 Nomenclature defining laboratory rogue wave for Case PH3.

The modified stretching method is given by

$$z_e = az_a^3 + bz_a^2 + cz_a + d \qquad \text{for} -h \le z_a \le H_c \tag{4.27}$$

with $a = [(-h + H_c) + k(h + H_c)]/(h + H_c)^3$ \qquad (4.28)

$$b = [-2(h^2 - hH_c + H_c^2) - k(h + H_c)(H_c - 2h)]/(h + H_c)^3 \tag{4.29}$$

$$c = [H_c(H_c^2 - H_c h + 4h^2) + kh(h + H_c)(h - 2H_c)]/(h + H_c)^3 \tag{4.30}$$

$$d = -\{h^2 H_c[kh(h + H_c) + 2H_c]\}/(h + H_c)^3 \tag{4.31}$$

$$k = (2.00 - \lambda)H_t / H \tag{4.32}$$

$$\lambda = T_f / T_r \tag{4.33}$$

If $H_c / H_t \leq 1.0$, then $\lambda = 1.0$, and if $\lambda > 1.95$, then $\lambda = 1.95$.

where z_e is the effective vertical coordinate $(-h \leq z_e \leq 0)$, and z_a is the actual vertical coordinate $(-h \leq z_z \leq H_c)$.

The horizontal velocity of the highly nonlinear wave can be obtained through substituting equation (4.27), the effective coordinate, into equation (4.21) for a highly nonlinear wave as follows:

$$u(x, z, t) = \sum_{i=1}^{N} A_i \frac{g \cdot k_i}{\omega_i} \cdot \frac{\cosh[k_i \cdot (h + z_e)]}{\cosh k_i h} \cdot \cos(k_i x - \omega_i t + \phi_i) \tag{4.34}$$

In addition, the vertical velocity of the highly nonlinear wave can be obtained through substituting equation (4.27), the effective coordinate, into equation (4.22) for a highly nonlinear wave as follows:

$$w(x, z, t) = \sum_{i=1}^{N} A_i \frac{g \cdot k_i}{\omega_i} \cdot \frac{\sinh[k_i \cdot (h + z_e)]}{\cosh k_i h} \cdot \sin(k_i x - \omega_i t + \phi_i) \tag{4.35}$$

Other wave kinematics, such as the local and convective accelerations can be computed with the method in the following discussion. Predictions of the wave kinematics by the modified stretching method are very reliable, since the solutions are insensitive to the choice of cutoff frequency when the wave energy in the cutoff tail is small as shown in Fig. 4.9.
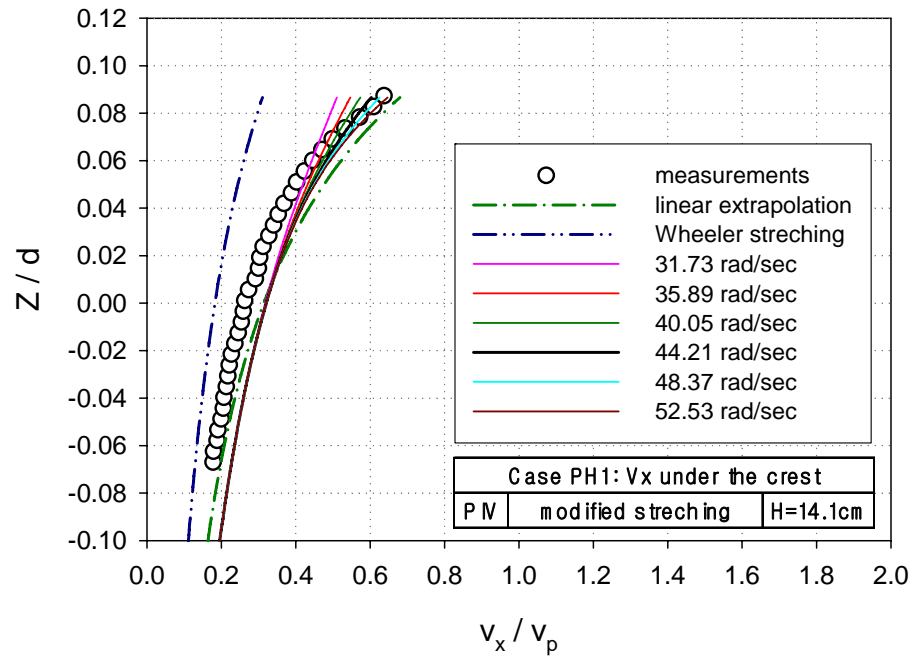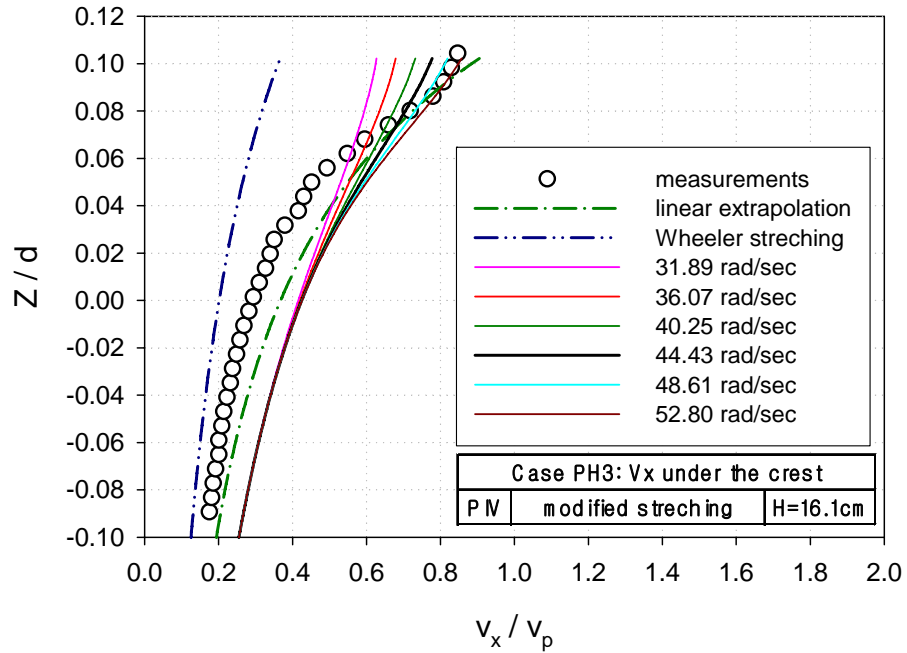
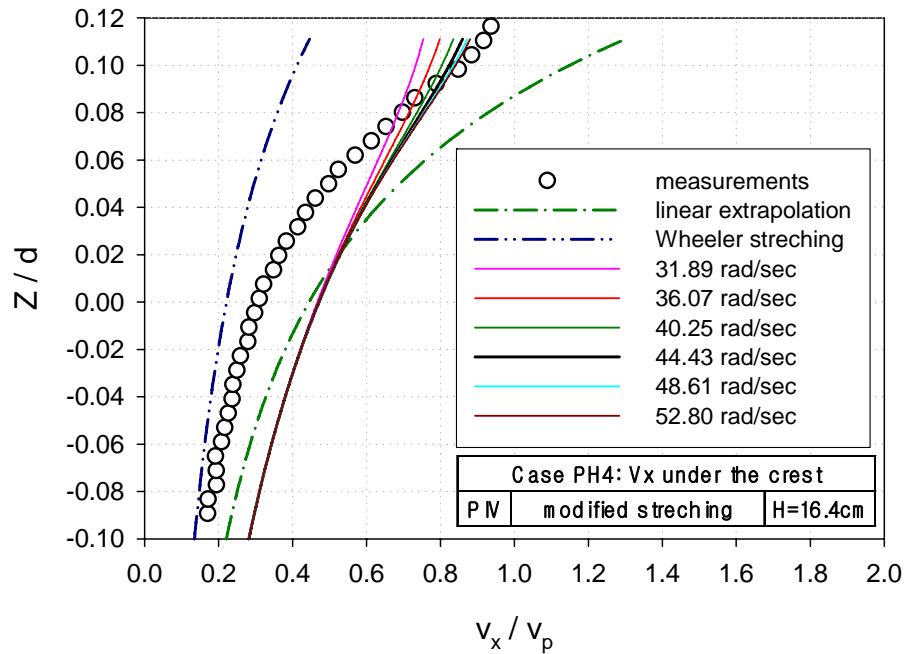(a) Horizontal velocity for Case PH1.
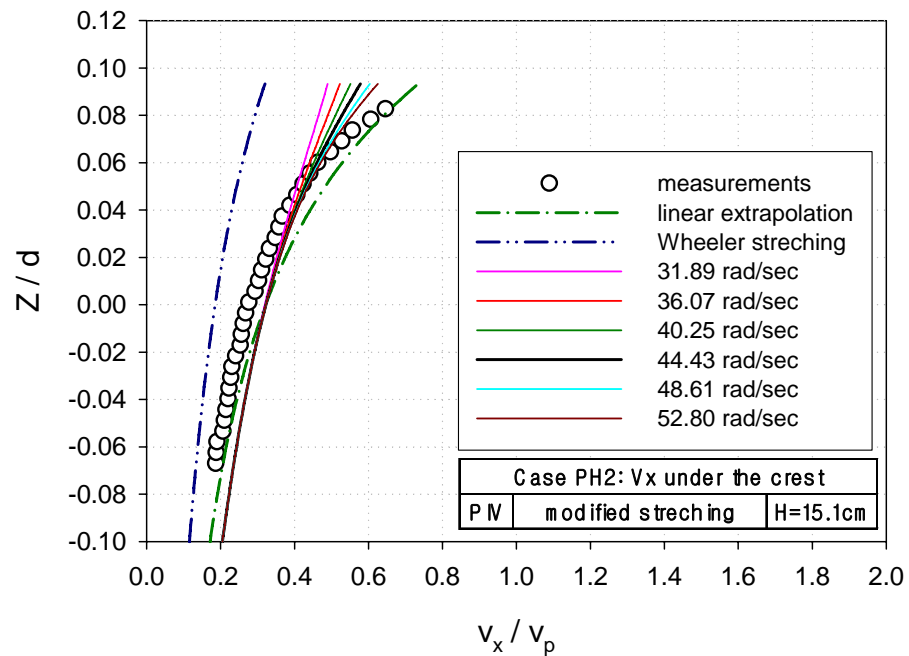
(b) Horizontal velocity for Case PH2.

Fig. 4.9 The changes in predicted horizontal velocities by the modified stretching method

due to seven different cutoff frequencies.

85

(c) Horizontal velocity for Case PH3.

(d) Horizontal velocity for Case PH4.

Fig. 4.9 Continued.

CHAPTER V

EXPERIMENTAL RESULTS FOR REGULAR WAVE KINEMATICS

5.1   Particle velocity of regular waves

In this section, the particle velocities of regular wave kinematics will be discussed. A series of experiments were conducted to obtain the particle velocity fields using the PIV system for the five different wave slope regular waves (see Table 2.3). Since one wavelength regular wave consists of twelve velocity fields, i.e. the twelve phases per wave length, the vertical and horizontal components of particle velocity are measured under the wave crest, the wave trough, the zero-up crossing point and the zero-down crossing point for regular waves. The wave crest and trough are defined as the highest elevation point and the lowest elevation point of the wave, respectively. If the wave elevation goes down according to the direction of progressive wave propagation and passes the still water level (SWL), the point of wave elevation can be called the zero-down crossing point. The zero-up crossing point of a wave is the opposite, i.e. the wave elevation goes up. The definitions of wave crest, wave trough and wave zero crossing points are shown in Fig. 5.1. Measured velocities are presented in normalized value; i.e., the measured vertical position Z is normalized by water depth d and the horizontal velocity u and the vertical velocity w are normalized by wave phase velocity v_p.
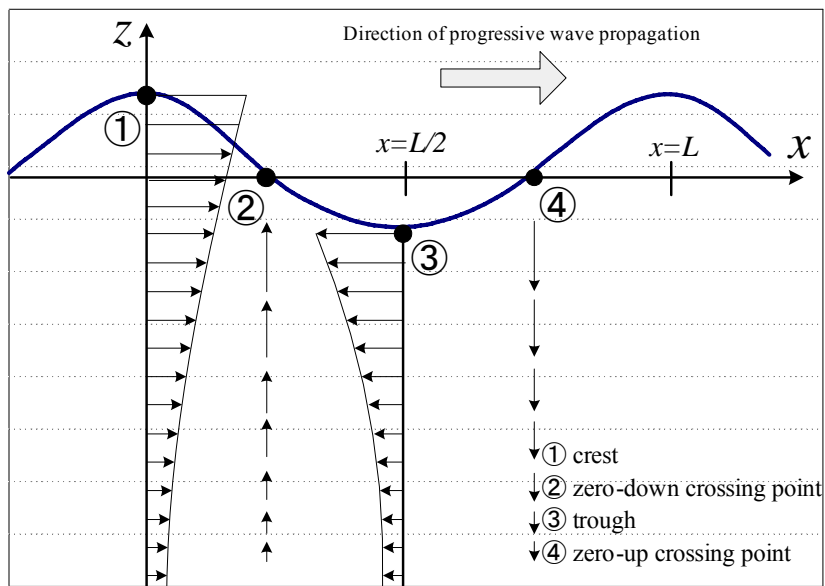
Fig. 5.1 Definition sketch for the crest, trough, zero-up and down crossing point of water wave and distribution of water particle velocities in progressive waves.

Horizontal velocities of Case PR1 ($ka = 1.04$) according to the vertical measuring positions under the wave trough and crest are shown in Fig. 5.2 (a) and (b), respectively. The measured data are presented with the results from the linear theory and the third-order Stokes theory. In general, both analytical results matched very well with experimental data. It is also seen in Fig. 5.2 (b) that the linear theory and the third-order Stokes wave theory are almost identical due to the small amplitude of Case PR1. Compared with Fig. 5.2 (a) and (b), the amount of measured data under the trough is larger, i.e. 3.9 % larger, than those of the third-order Stokes wave theory and those of measured velocity under the crest at the corresponding vertical measuring positions.
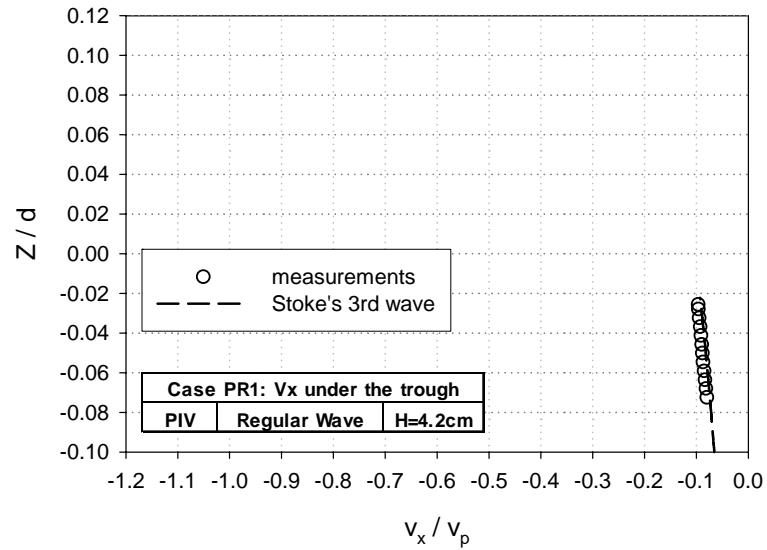
(a) Under the trough.
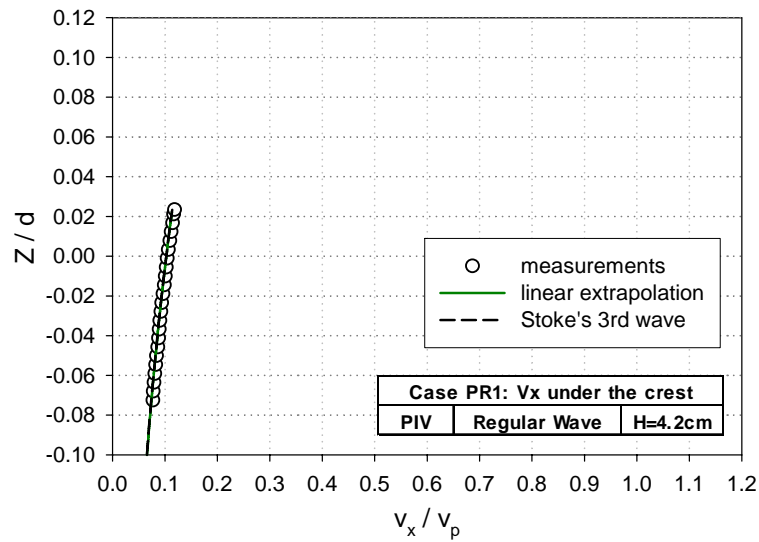
(b) Under the crest.

Fig. 5.2 Comparison with horizontal velocities for Case PR1.

Fig. 5.3 (a) and (b) present the horizontal velocities under the wave trough and crest for

Case PR2 ($ka = 0.202$), respectively. Compared to Case PR1, the experimental results of

Case PR2 agree excellently with analytical solutions although they have twice the wave

slope. Both analytical solutions are equal to each other with 1.0 % difference at the wave

crest as shown in Fig. 5.3 (b). It is more noticeable compared to Case PR1 that the values of Case PR2 measured data under the trough is slightly larger, i.e. 5.0 %, than those of the 3rd-order Stokes wave theory and those of measured velocity under the crest at the corresponding measured vertical positions as shown in Fig. 5.3 (a).
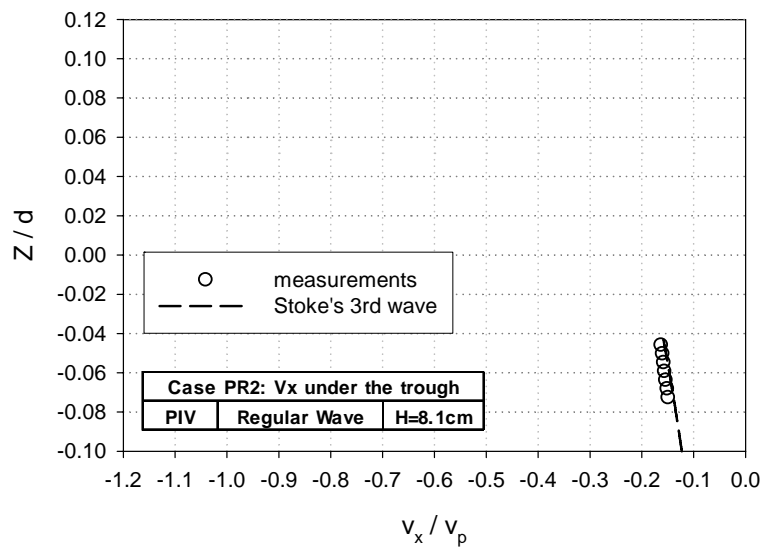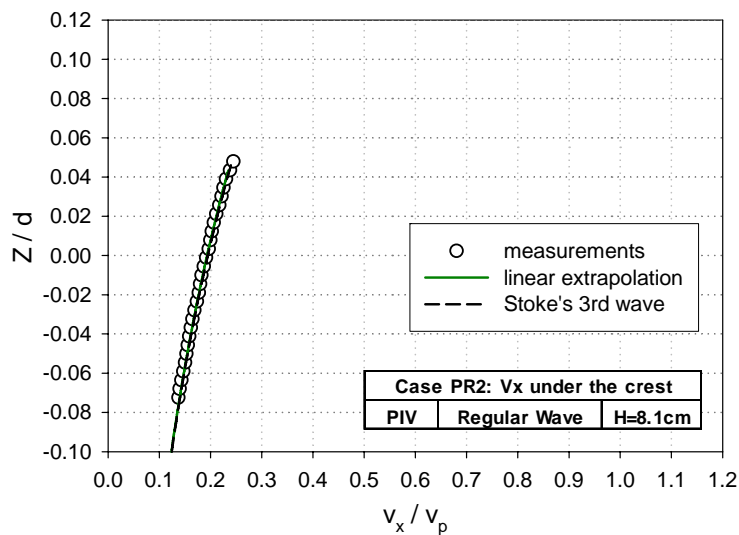

(a) Under the trough.

(b) Under the crest.

Fig. 5.3 Comparison with horizontal velocities for Case PR2.

Fig. 5.4 (a) and (b) show the horizontal velocities under the wave trough and crest for Case PR3 ($ka = 0.252$), respectively. The experimental results of Case PR3 are in good agreement with analytical solutions, although there is a 2.5 times larger wave slope than that of Case PR1. Compared with Case PR1 and Case PR2, however, analytical solutions from both of the linear extrapolation and the third-order Stokes wave theory are very similar with 2.0 % difference at the wave crest as shown in Fig. 5.4 (b). It can be seen by comparing with Case PR1, Case PR2 and Case PH3 the values of Case PR3 measured data under the trough is 9.6 % larger than those from the third-order Stokes wave theory and those of measured velocity under the crest at the corresponding measured vertical positions as shown in Fig. 5.4 (a).
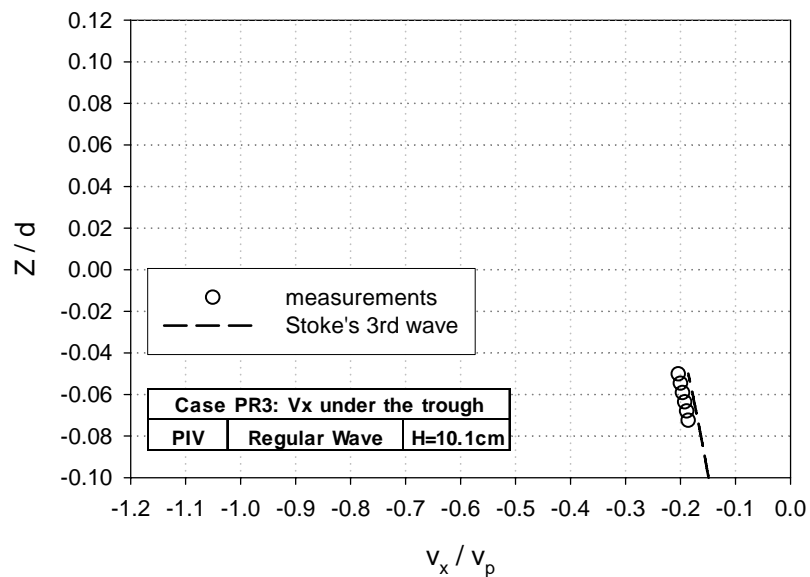

(a) Under the trough.

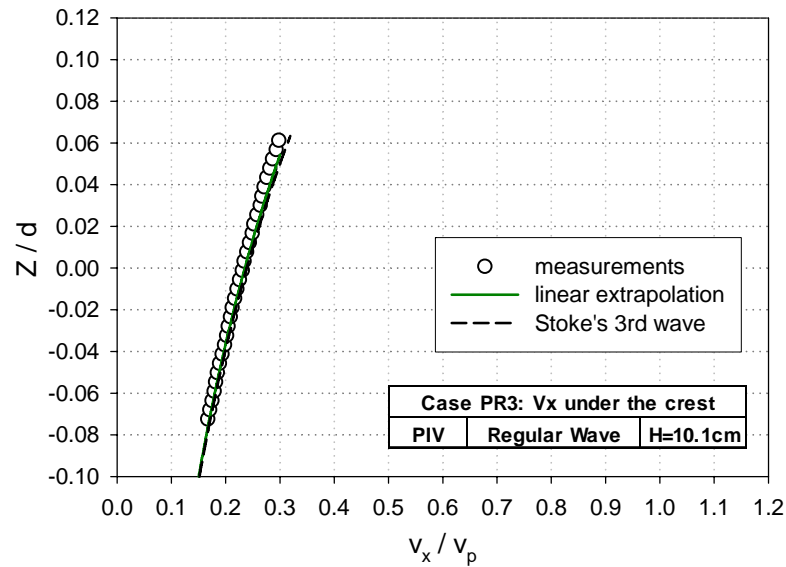Fig. 5.4 Comparison with horizontal velocities for Case PR3.

(b) Under the crest.

Fig. 5.4 Continued.

The horizontal velocities of Case PR4 ($ka = 0.305$) under the wave trough and crest are

presented in Fig. 5.5 (a) and (b), respectively. The measured data of Case PH4 agree well

with both the solutions of linear theory and the third-order Stokes wave theory below the

free surface. The measurements above the free surface values are larger than those of linear

wave theory and the third-order Stokes wave theory as shown in Fig. 5.5 (b). The wave

slope of Case PR4 is 3.7 times larger than that of Case PR1. It is shown in Fig. 5.5 that the

steeper wave of Case PR4 shows the nonlinearity phenomenon which does not follow the

high-order Stokes wave theory. It is also seen in Fig 5.5 (b) that the solutions above the

free surface of the third-order Stokes wave theory are maximum 3.8 % larger than those of

linear theory. The trough horizontal velocities for Case PR4 are presented in four vertical

measuring positions under the wave trough because of the size of FOV. Compared with

Fig. 5.5 (a) and (b), the magnitudes of measured data below the trough are very similar to those of measured velocity below the crest at the corresponding vertical measuring positions, unlike Case PR1, Case PR2 and Case PR3.
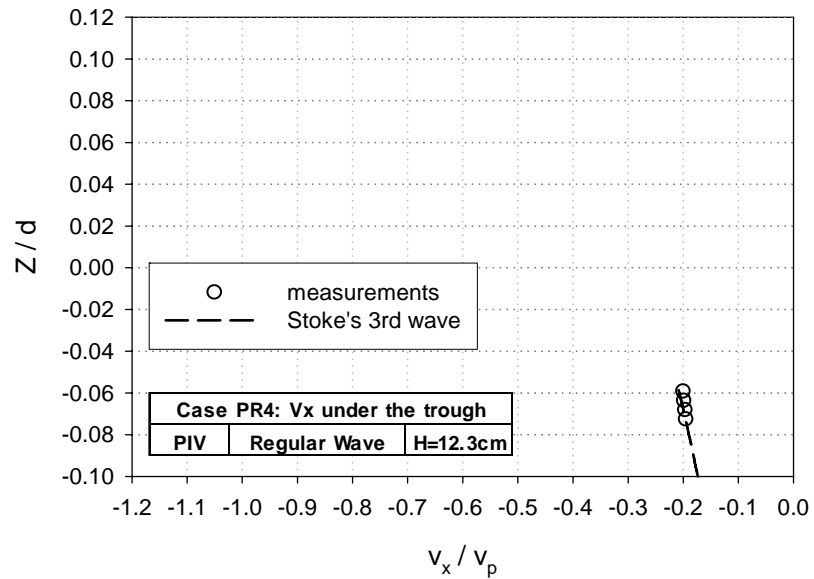
(a) Under the trough.
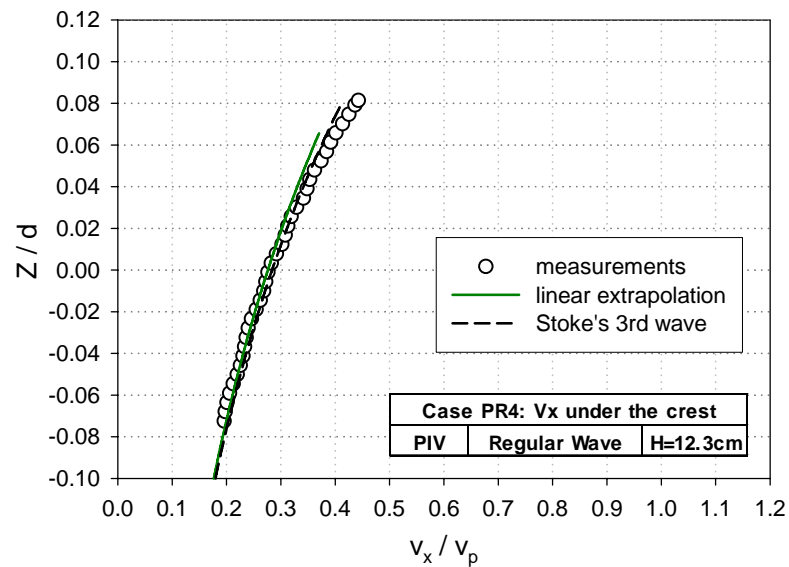
(b) Under the crest.

Fig. 5.5 Comparison with horizontal velocities for Case PR4.

The wave crest height and trough depth are marked in Fig. 5.6. It is found in Fig 5.6 that

the trough depth of the third-order Stokes wave theory is smaller than that of experimental

measurements, and the crest height of the third-order Stokes wave theory is larger than that

of experimental measurements in Case PR1, Case PR2, Case PR3 and Case PR5. However,

the values of wave crest and trough of Case PR4 are marked oppositely as shown in
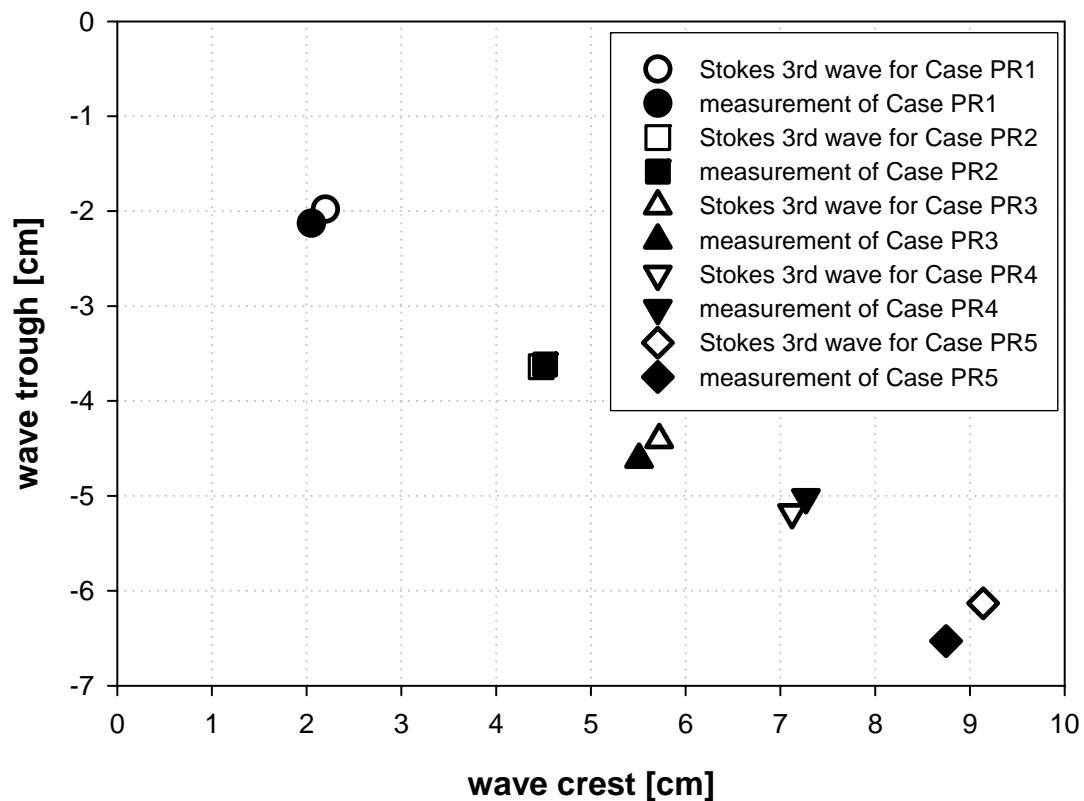
Fig.5.6.

Fig. 5.6 Scatter plot of measured regular wave crest versus measured regular wave trough.

Horizontal velocities under the wave crest of Case PR5 ($ka = 0.38$) are shown in Fig. 5.7. The FOV did not cover the wave trough of Case PR5. The trough horizontal velocities for Case PR5 could not be obtained because the size of FOV should be kept the same as that of other cases to get the same spatial resolutions for comparison with other cases during regular wave experiments. The experimental results of Case PR5 agreed with the Airy linear extrapolation. However, when compared with the third-order Stokes wave theory, appreciable reductions are observed for the measured crest horizontal velocities above the trough level (at $z/d = -0.07$). The phenomenon was also observed in Swan's (1990) experiment, where he attributed the difference in the effects of vorticity to be caused by vertical viscous diffusion. This kind of viscous effect cannot be reproduced by the Airy linear wave theory or the third-order Stokes wave theory.
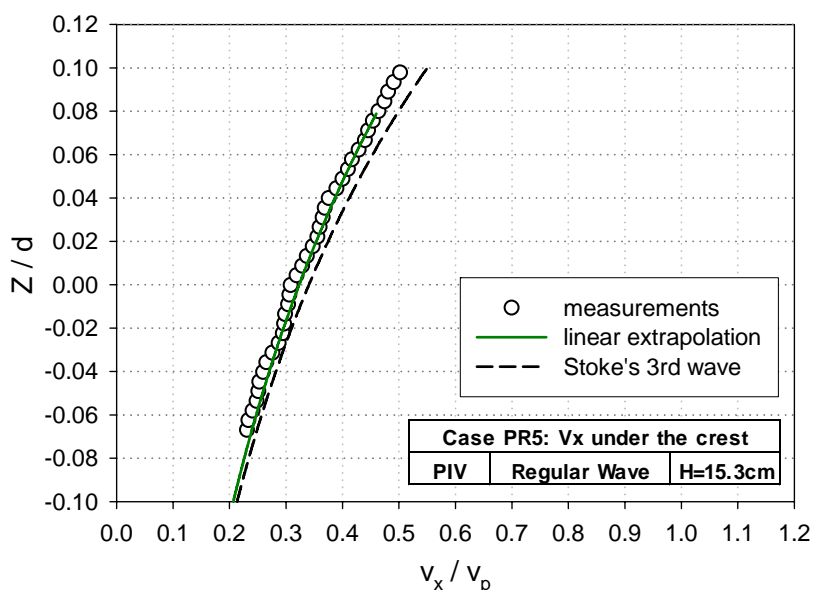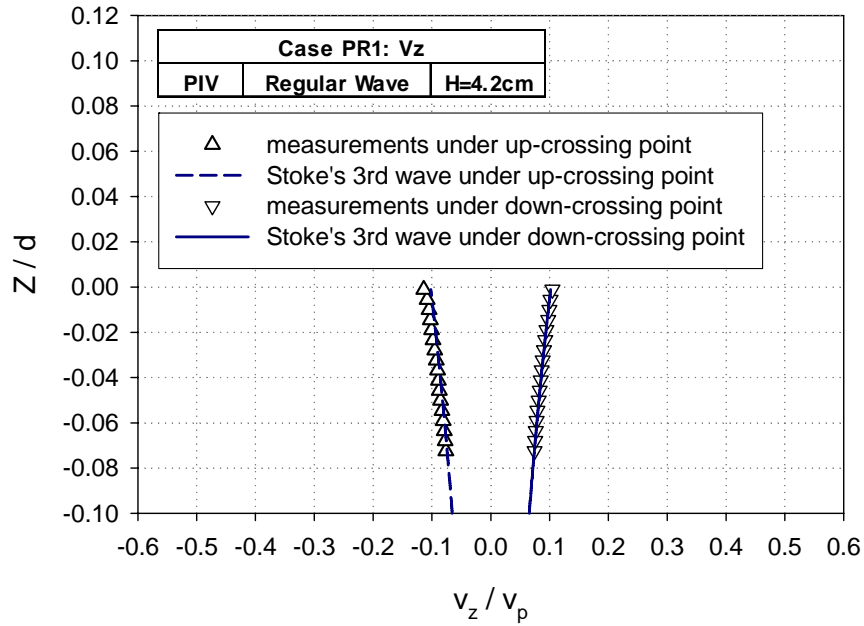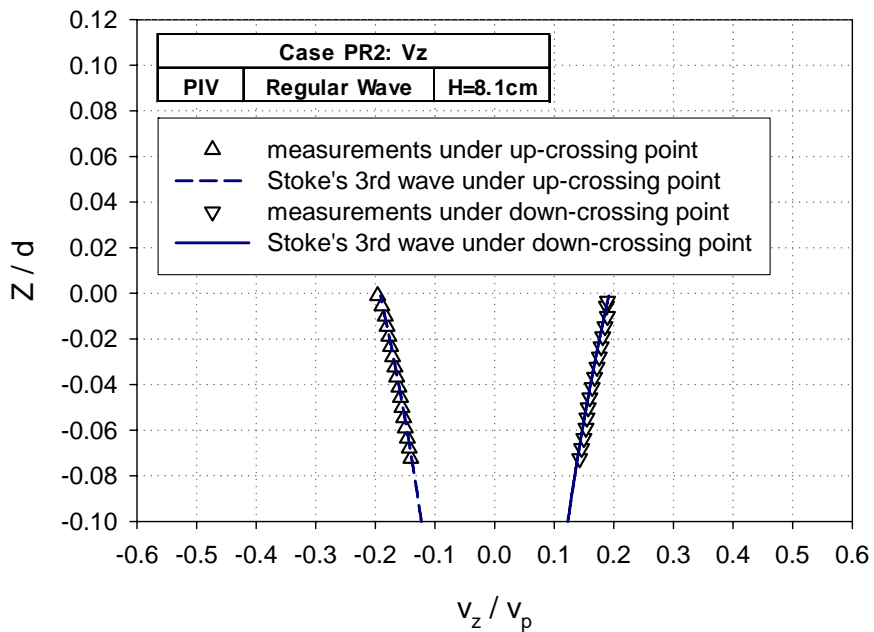

Fig. 5.7 Comparison with horizontal velocities under the wave crest for Case PR5.

Fig. 5.8 (a), (b), (c), (d), and (e) present the vertical velocities under the wave zero-up and down crossing point for Case PR1 ($ka = 0.104$), Case PR2 ($ka = 0.202$),Case PR3 ($ka = 0.252$), Case PR4 ($ka = 0.305$) and Case PR5 ($ka = 0.38$), respectively. Fig. 5.8 (f) shows the comparison of the vertical velocities under zero crossing for Case PR5 and Case PH4. Fig. 5.8 shows the best agreement between measurements and calculations, except the vertical velocities under zero-down crossing point of Fig. 5.8 (e). This means that the higher-order Stokes wave theory can predict the water particle velocities under zero-up and down crossing point of regular wave accurately within a wave slope of $ka = 0.305$. It is also noticed in Fig. 5.8 that the magnitude of vertical velocities under the zero-up crossing point decreases as the wave slope increases. For the vertical velocities under zero-down crossing point, it is shown that they increased as the wave slope is steeper. It is an obviously noticeable phenomenon unlike the results under the wave crest and trough. However, this amount of change is relatively small. The maximum difference of vertical velocity under zero-up and down crossing point for Case PR5 is less than 3 cm/s. This result confirms that the vertical velocity under the zero crossing point can be predicted well with the third-order Stokes wave theory. It is shown in Fig. 5.8 (f) that the velocities under the zero crossing point are compared with Case PR4 and Case PR5. Despite increasing the wave slope, the results are more similar than the velocities under the wave crest. It is also possible for rogue waves to predict the vertical velocities under the zero crossing point with the third-order Stokes wave theory as shown in Fig. 5.8 (f).
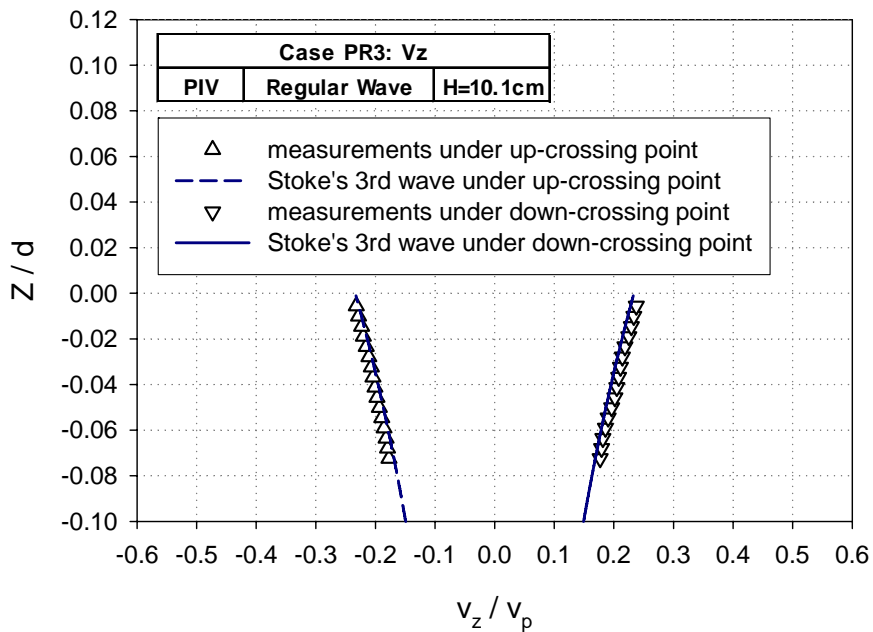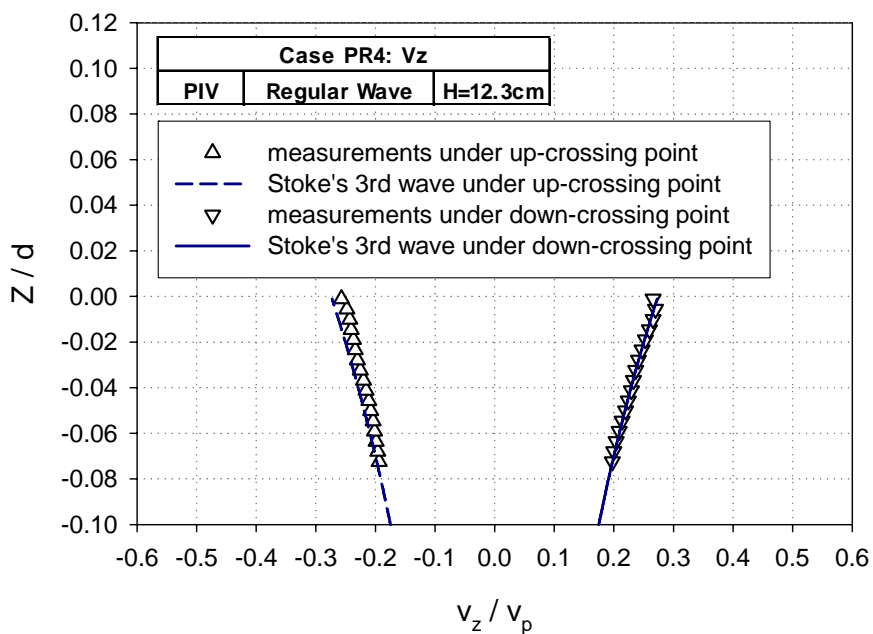
(a) Case PR1.

(b) Case PR2.

Fig. 5.8 Comparison with vertical velocities under wave zero-up and wave zero-down
crossing point for Case PR1, Case PR2, Case PR3, Case PR4, Case PR5, Case PH4.

(c) Case PR3.

(d) Case PR4.

Fig. 5.8 Continued.
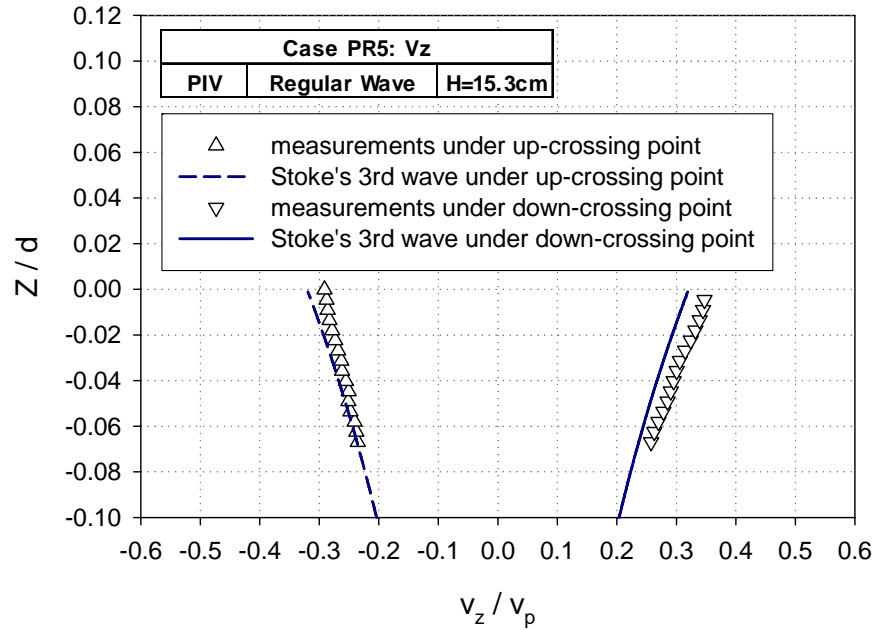
(e) Case PR5.
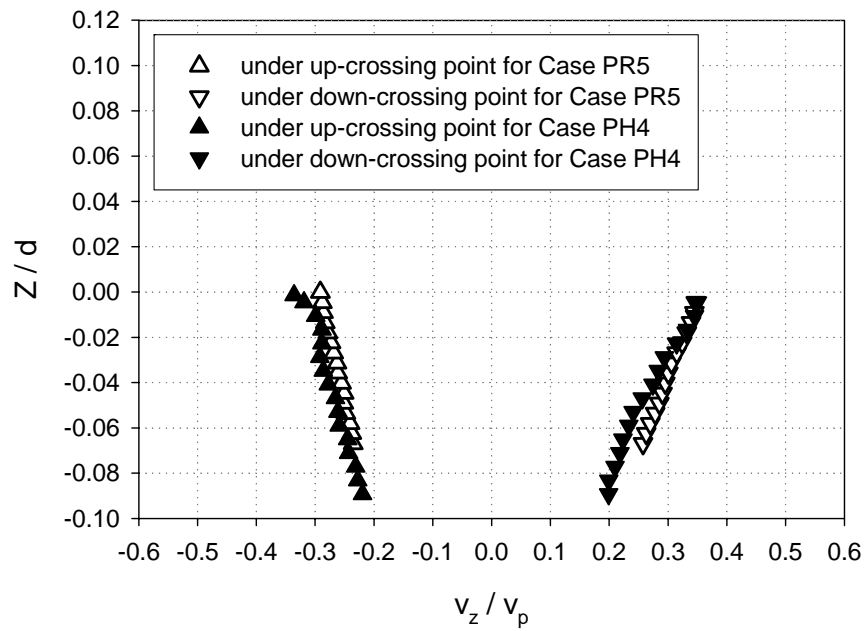
(f) Case PH4 and Case PR5.

Fig. 5.8 Continued.

Fig. 5.9 is a PIV image of the wave zero crossing points and wave crest for Case PH4. It is interesting that the vertical velocities under wave zero crossing points of the asymmetric rogue wave have similar values with the equivalent wave height regular wave.
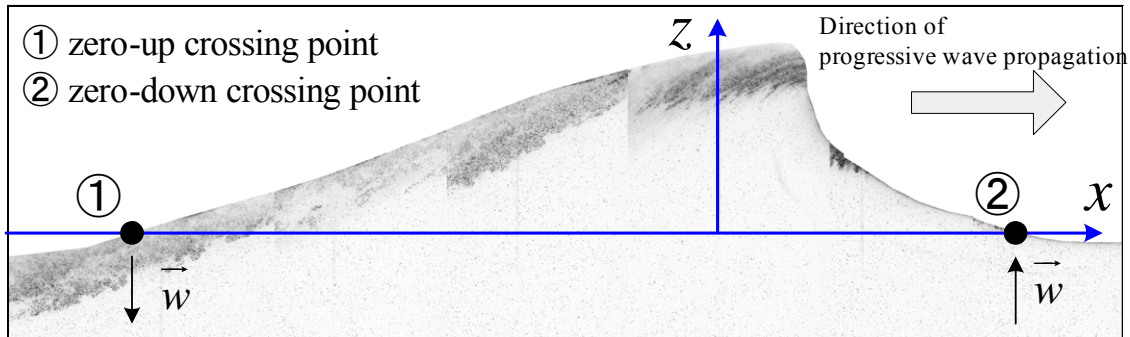
Fig. 5.9 PIV image of the zero-up and down point and the crest for Case PH4.

5.2 Particle local acceleration of regular waves

The local acceleration fields were computed based on PIV measurements of the particle velocities under the regular wave crest. The numerical scheme used for computation was a centered finite difference method with Δt=75 ms. The measured local accelerations are presented with normalized value, i.e. the measured vertical position Z is normalized by water depth d, and the vertical local acceleration is normalized by gravity acceleration g of regular wave. Fig. 5.10 (a), (b), (c), (d) and (e) present the vertical local accelerations under the wave crest for Case PR1 ($ka = 0.104$),Case PR2 ($ka = 0.202$),Case PR3 ($ka = 0.252$), Case PR4 ($ka = 0.305$) and Case PR5 ($ka = 0.38$), respectively.

The experimental results of Case PR1 and Case PR2 show strong agreement with the

analytical solutions as shown in Fig. 5.10 (a) and Fig. 5.10 (b), respectively. It is found in Fig. 5.10 (d) that the value of vertical local accelerations computed based on measurement above the free surface level for under the wave crest of Case PR4 are larger than those of both linear extrapolation and the third-order Stokes wave theory. However, analytical solutions from both the linear extrapolation and the third-order Stokes wave theory predict the vertical local accelerations above the free surface level for under the wave crest for Case PR3 and Case PR5 are larger than the computed values based on measurement as shown in Fig. 5.10 (c) and Fig. 5.10 (e), respectively.

Compared to the measurements using the LDV system, which are for Case LR1 and Case LR2 as shown in Fig. 3.23, the time step Δt used for each system was different, i.e. 40 ms s for LDV system and 75 ms for PIV system. This different time step may account for this discrepancy in the computing of local accelerations, especially steeper wave cases. Jensen et al. (2001) measured the velocities and accelerations in the periodic wave with a wave slope of $ka = 0.16$. They calculated the relative standard deviation of 0.6 % for the velocity measurements and 2 % for the acceleration measurements with a time step Δt 60 ms. However, the relative accuracy of our present experiments and corresponding measurements may be quantified in terms of the RMS due to an ensemble of measurements. The RMS velocity was observed as less 1.2 % in Case PR3 ($ka = 0.202$). It is indicated in section 3.2.3 that such accuracy may be generally achieved by selecting the size of the field of view carefully. The difference between the local accelerations of computations based on measured velocities and solutions of the third-order Stokes wave theory in Case PR5 was 4 % with time step and the size of field of view used for PIV measurement.

(a) Case PR1.

(b) Case PR2.

Fig. 5.10 Comparison of vertical local accelerations under the regular wave crest.
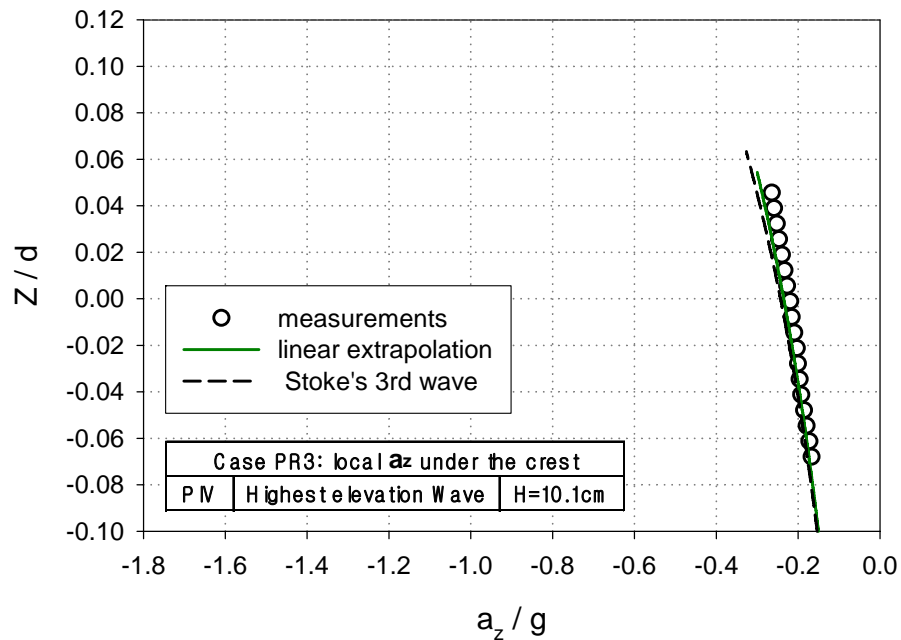
(c) Case PR3.
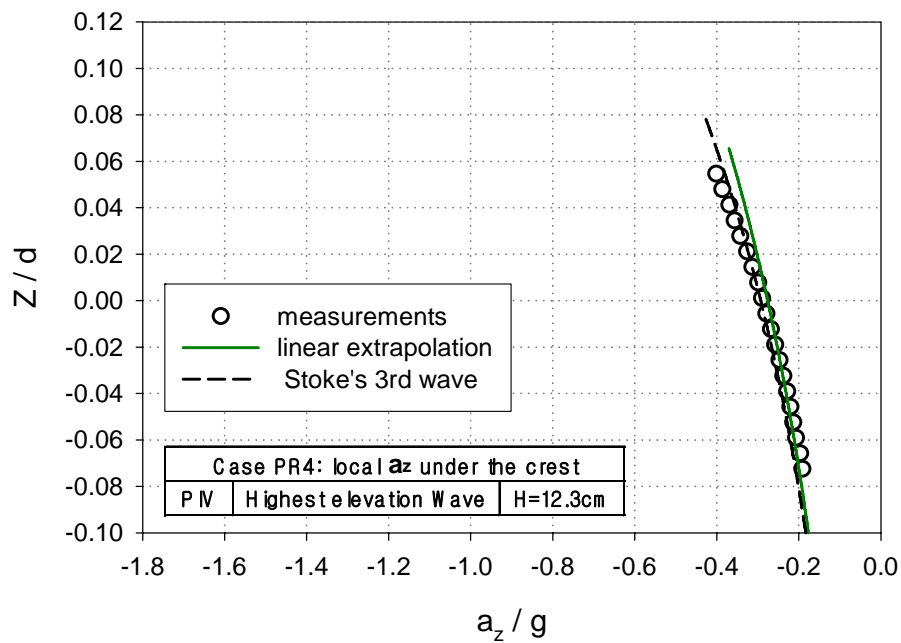
(d) Case PR4.

Fig. 5.10 Continued.
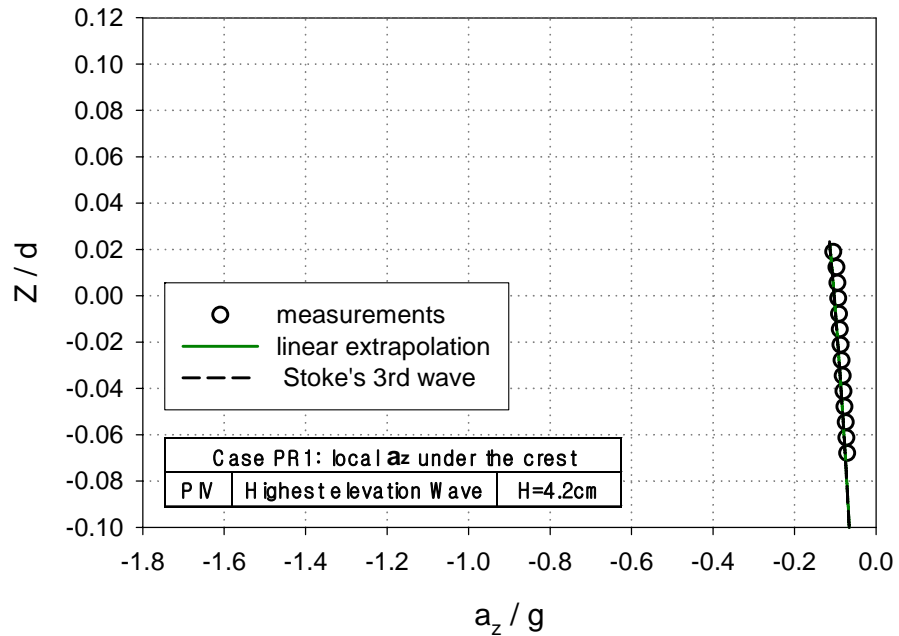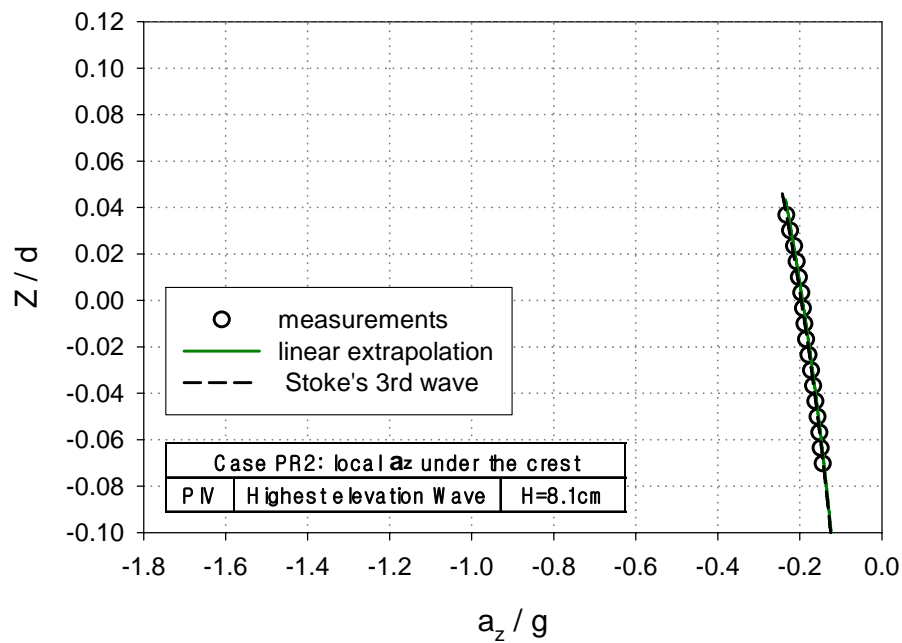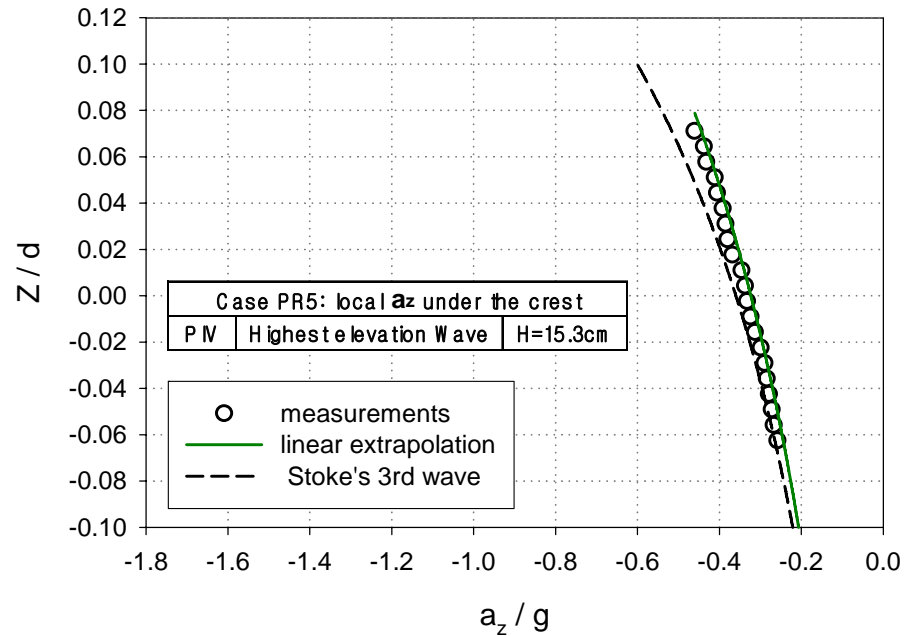
(e) Case PR5.

Fig. 5.10 Continued.

5.3   Particle convective acceleration of regular waves

The convective acceleration fields were computed based on the PIV measurements of the particle velocities under the regular wave crest. The used numerical scheme for the computation was a centered finite difference method with Δx and $\Delta z = 6$ mm. The measured local accelerations are presented with normalized values, i.e. measured vertical position Z is normalized by water depth d and vertical local acceleration is normalized by gravity acceleration, g, of the regular wave. Fig. 5.11 (a), (b), (c), (d) and (e) present the vertical convective accelerations under the wave crest for Case PR1 ($ka = 0.104$), Case PR2 ($ka = 0.202$), Case PR3 ($ka = 0.252$), Case PR4 ($ka = 0.305$) and Case PR5 ($ka = 0.38$), respectively.

The experimental results of Case PR1 and Case PR2 agree well with the solutions of the linear extrapolation and the third-order Stokes wave theory as shown in Fig. 5.11 (a) and Fig. 5.10 (b), respectively. It is found in Fig. 5.11 (c) that the vertical convective accelerations from the measurement-based computation under the wave crest of Case PR3 also agree with those of both the linear extrapolation and the third-order Stokes wave theory, but a small reduction is observed for the measured vertical convective accelerations above the free surface level as shown in Fig. 5.11 (c).

Fig. 5.11 (d) plots the vertical convective accelerations computed from measured velocities, solutions of the linear extrapolation, and the third-order Stokes wave theory under the wave crest of Case PR4. The experimental results below half of the wave crest height ($Z/d = 0.04$) level for Case PR4 correlate well with solutions of analytical wave theories. However, it is observed in Fig. 5.11 (d) that the vertical convective accelerations computed from measured velocities above the half of wave crest height ($Z/d = 0.04$) level for Case PR4 increase abruptly and mark appreciably larger values than those of analytical wave theories. It is possible the effects of nonlinearity are more significant as the wave steepness increases, i.e. the wave slope of $ak = 0.305$ for Case PR4.

Fig. 5.11 (e) presents the computed values based on the measurement of vertical convective accelerations under the wave crest of Case PR5. The results based on measurements are larger than those of the third-order Stokes wave theory. It is also noticeable in Fig. 5.11 (e) that the experimental results above the SWL for Case PR5 are appreciably larger than those of solutions of analytical wave theories.

The experimental results are disturbed by error from several different sources, e.g. background noise, displacement gradient, image quantization, residual error and systematic error. To reduce the disturbance of experimental data, the size of FOV will be used for measurements of the rogue wave. A difference in the solutions of the first and third-order Stokes wave theory for convective accelerations of regular waves are not found as shown in Fig. 5.11.
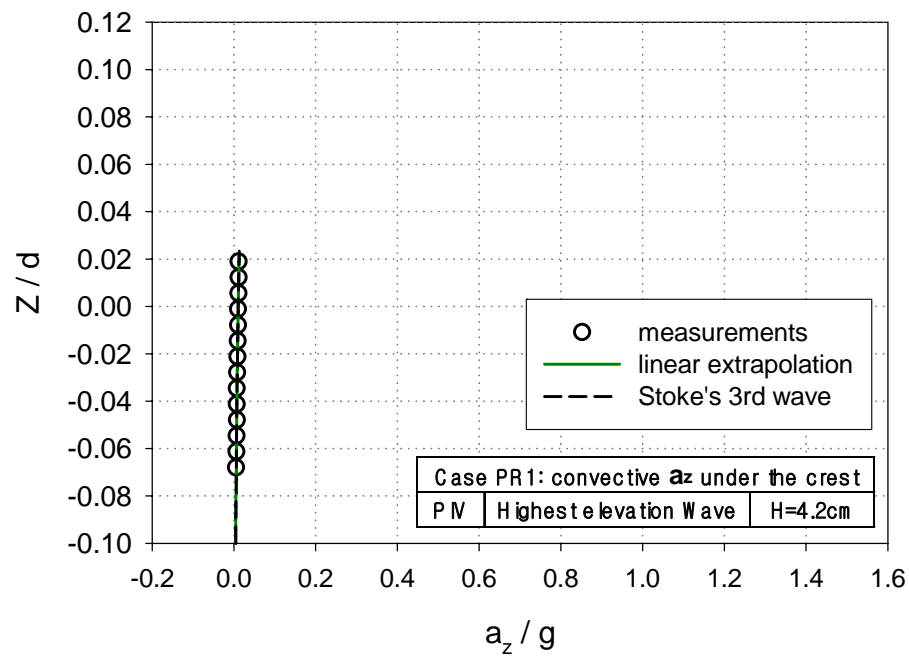
(a) Case PR1.

Fig. 5.11 Comparison of vertical convective accelerations under the regular wave crest.
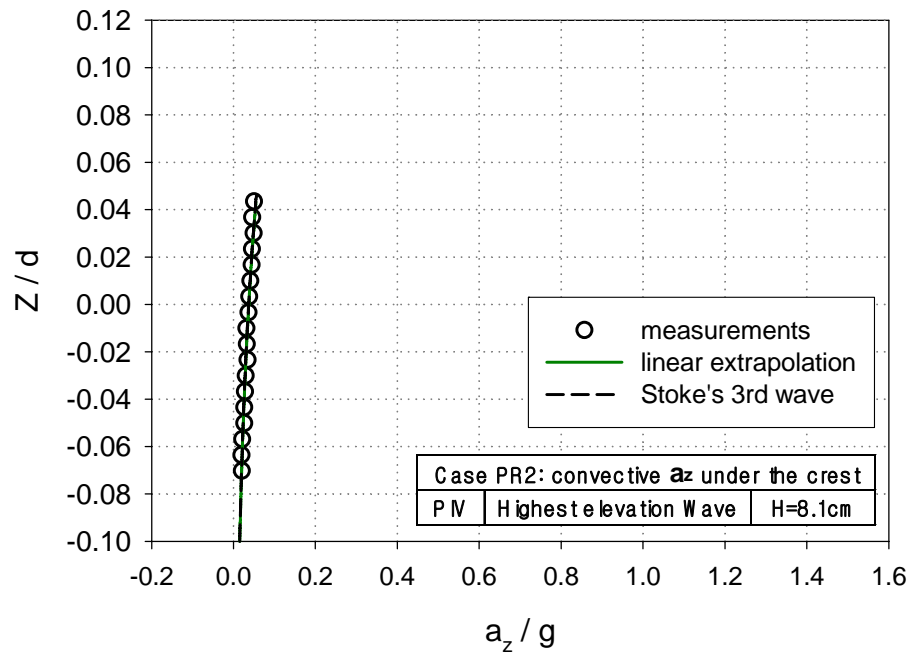
(b) Case PR2.

(c) Case PR3.

Fig. 5.11 Continued.
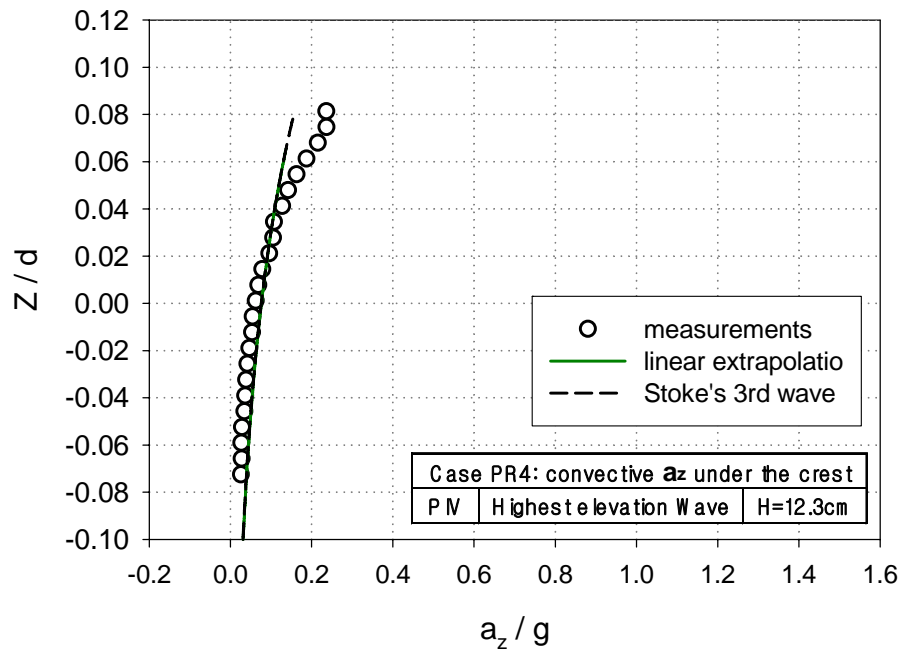
(d) Case PR4.
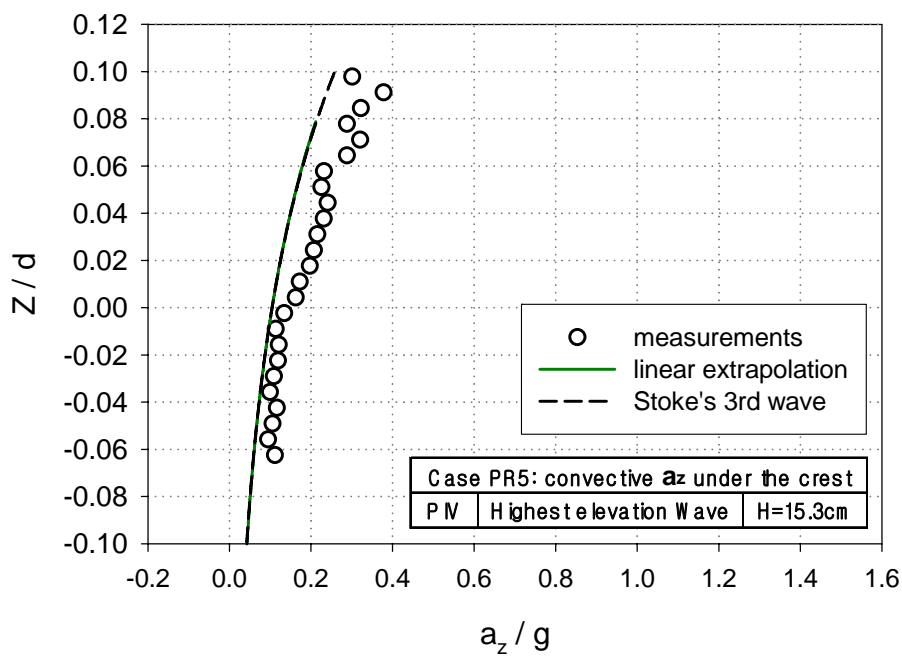
(e) Case PR5.

Fig. 5.11 Continued.

5.4   Kinematics fields for near the wave crest of Case PR5

The kinematics of the regular waves, which are horizontal velocities, vertical velocities, vertical local accelerations and vertical convective accelerations for Case PR5, were to be examined at five horizontal locations near the wave crest. There are two reasons for checking the kinematics for Case PR5. First, the wave for Case PR5 is a high steepness wave with a wave slope of $ka = 0.38$. As compared with the results of regular wave cases, 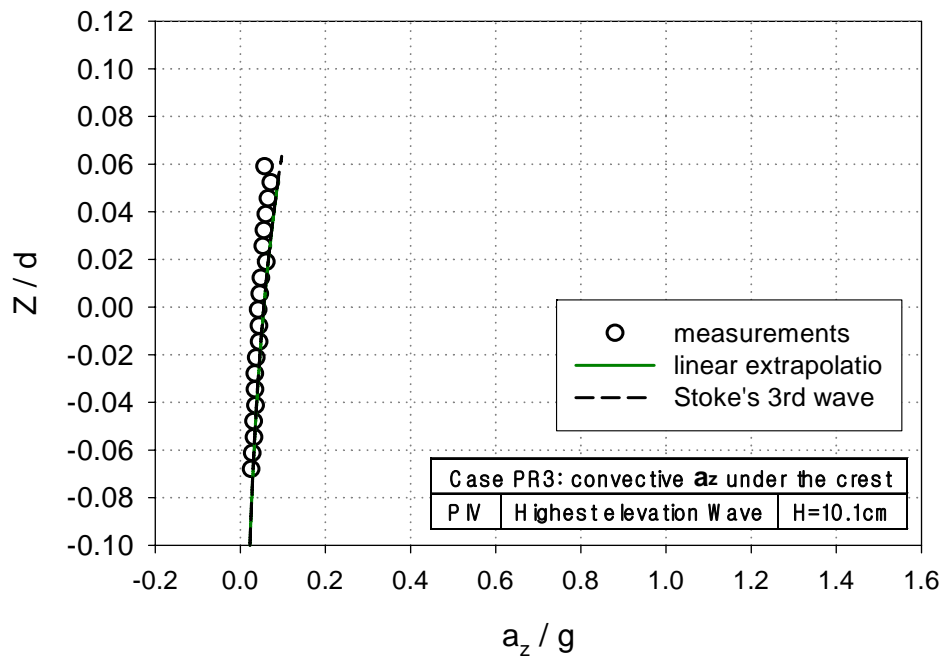several results show that the steep wave kinematics of Case PR5 could be predicted by the third-order Stokes wave theory. To understand the nonlinear results of Case PR5, the kinematics at the five horizontal locations near the crest should be checked. Second, the study of regular wave kinematics is preliminary study for rogue wave kinematics. The rogue wave kinematics obtained from experiments will be also examined to understand nonlinear effects at several horizontal locations.

The velocity vectors near the wave crest in field of view and comparisons with measurements at five different horizontal locations for Case PR5 ($ka = 0.38$) are presented in Fig. 5.12 (a), (b), and (c). Fig 5.12 (a) shows the velocity vectors near the wave crest are presented in field of view for Case PR5.   The still water level (SWL) is marked with the horizontal solid blue line in Fig. 5.12 (a).

Fig. 5.12 (b) shows the measured horizontal velocities of five different horizontal locations near the wave crest for Case PR5. The range of horizontal measuring position in which the wave crest is in the center of this range is 4.8 cm. The horizontal velocities measured at five horizontal locations agree very well. However, it is found above the SWL that all measurements are less than the solution of the third-order Stokes wave theory. It is possibly explained that the calculated wave crest height (9.14 cm) of the third-order Stokes wave is larger than the measured wave crest height (8.76 cm) with the same wave height (15.29 cm). This means that there may be a correlation between the wave crest and the wave velocity.

Fig. 5.12 (c) shows the measured vertical velocities of five different horizontal locations near the wave crest for Case PR5. The range of horizontal measuring position in which the wave crest is in the center of this range is 4.8 cm. The vertical velocities measured at the five horizontal locations have very varied trends. It means that the direction of the acceleration under the wave crest is vertical. The value of vertical velocities under the wave crest of Stoke wave theories even in the higher order is zero, but the measured value of vertical velocities under the wave crest is some positive values. Compared with small amplitude wave cases, it seems that the steep wave vertical velocity trends at the horizontal measuring locations are shifted to the wavemaker side. The zero value of vertical velocity should be measured under the wave crest in the relatively small amplitude waves, i.e. Case PR1 ($ka = 0.104$) or Case PR2 ($ka = 0.202$). However, the zero value vertical velocity for Case PR5 was found at 1.2 cm far away from the wave crest to the wavemaker as shown in Fig. 5.12 (c).
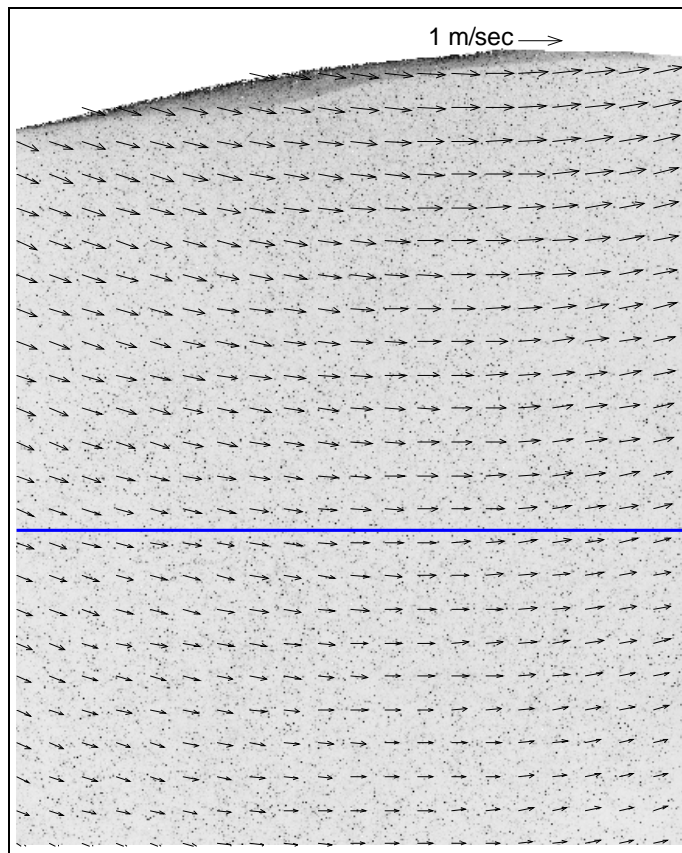
(a) Velocity field.
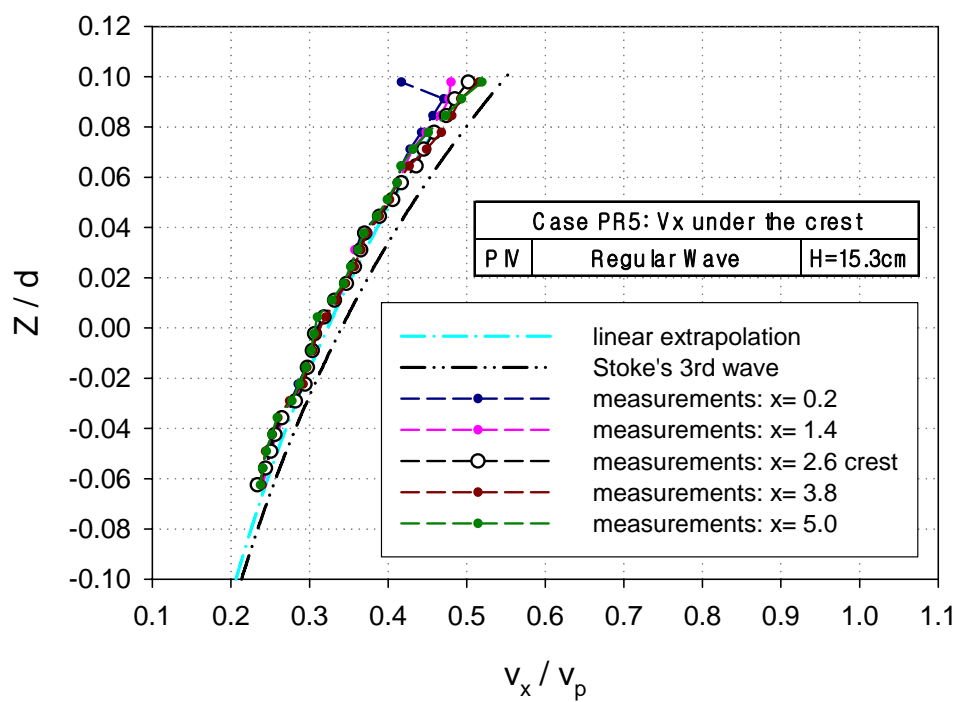
(b) Horizontal velocities.

Fig. 5.12 Velocities near the wave crest for Case PR5.
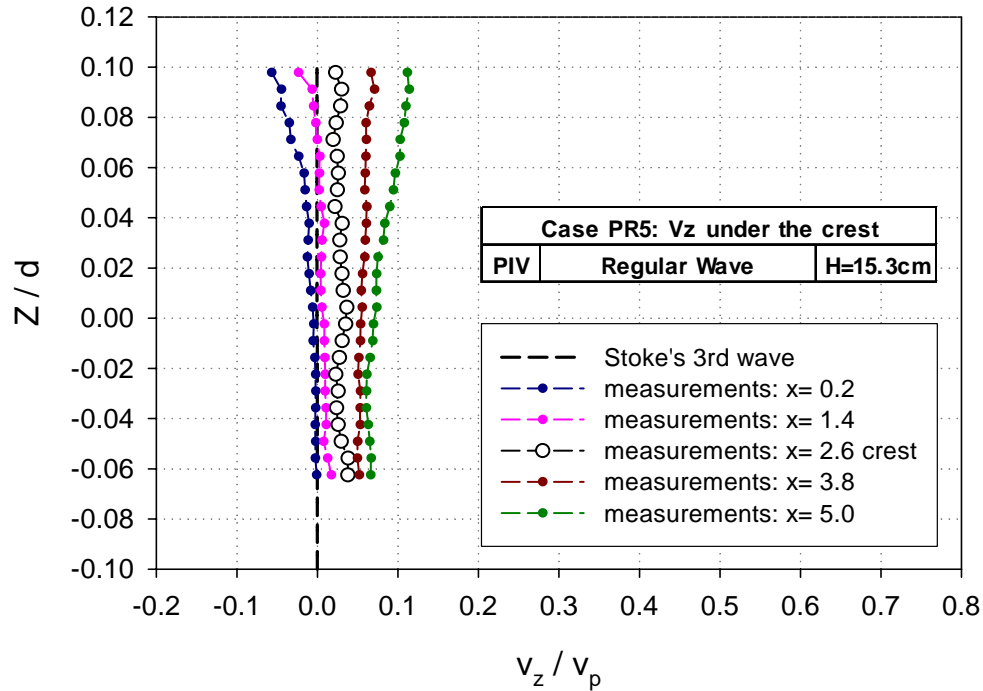
(c) Vertical velocities.

Fig. 5.12 Continued.

The vertical local acceleration vectors near the wave crest in field of view and comparisons with measurements at five different horizontal locations for Case PR5 ($ka = 0.38$) are presented in Fig. 5.13 (a) and (b). Fig 5.13 (a) shows the vertical local acceleration vectors near the wave crest are presented in field of view for Case PR5. The still water level (SWL) is marked with the horizontal solid blue line in Fig. 5.13 (a).

Fig. 5.13 (b) shows the measured vertical local accelerations of five different horizontal locations near the wave crest for Case PR5. The range of horizontal measuring position where the wave crest is in the center of this range is 4.8 cm. In general, the vertical local accelerations measured at five horizontal locations agree with each other. However, it is found above the SWL that all measurements are less than the solution of the third-order Stokes wave theory and similar with the extrapolation based on Airy theory wave. This

trend was also found in the velocity field. A possible explanation is that the calculated wave crest height (9.14 cm) of the third-order Stokes wave is larger than the measured wave crest height (8.76 cm) with the same wave height (15.29 cm). It could be also concluded that the wave local acceleration has correlated with the wave crest. The vertical local accelerations are missing at several locations from the free surface because the time step Δt used in measurements was 75 ms.

(a) Local acceleration field.

Fig. 5.13 Local accelerations near the wave crest for Case PR5.

(b) Vertical local accelerations.
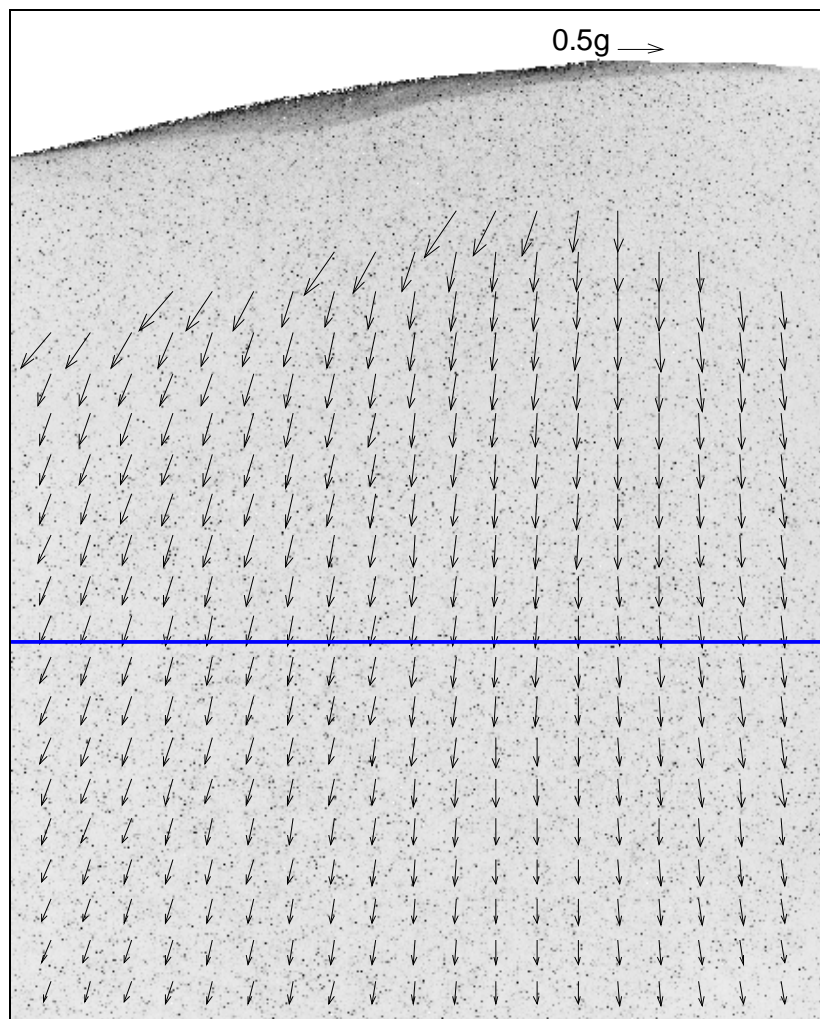
Fig. 5.13 Continued.

The vertical convective acceleration vectors near the wave crest in field of view and comparisons with measurements at five different horizontal locations for Case PR5 ($ka = 0.38$) are presented in Fig. 5.14 (a) and (b). Fig 5.14 (a) shows the vertical convective acceleration vectors near the wave crest are presented in field of view for Case PR5.

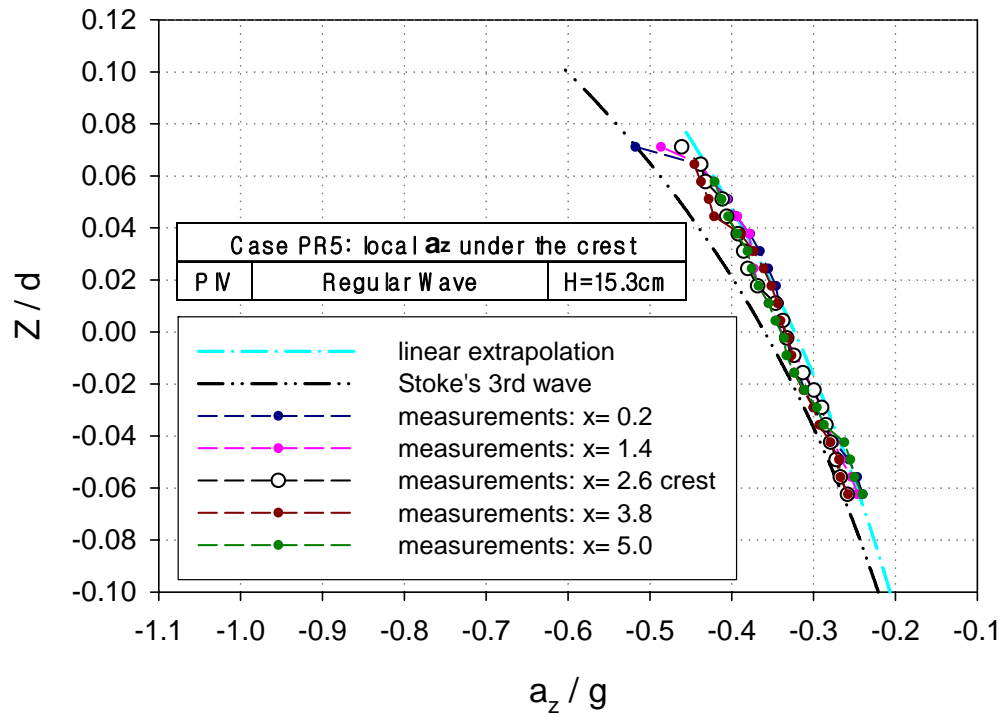The still water level (SWL) is recognized with the horizontal solid blue line in Fig. 5.14 (a). As seen in Fig. 5.14 (a), it is noticed that the vertical convective acceleration is related to the wave shape. It is true because convective accelerations are spatial derivatives of velocities.

Fig. 5.14 (b) shows the measured vertical convective accelerations of five different horizontal locations near the wave crest for Case PR5. It is observed below the SWL that the vertical convective accelerations measured at five horizontal measuring locations agree generally with each other. It is also found above the SWL that all measurements follow a trend of the linear extrapolation and the third-order Stokes wave theory with appreciable discrepancies as shown in Fig. 5.14 (b). It means that the wave shape changes appreciably above the SWL. It is also seen in Fig. 5.14 (b) that there is no difference between both analytical solutions, which are the third-order Stokes wave theory and extrapolation based on Airy theory. In the small amplitude wave, the magnitude of vertical convective accelerations under the wave crest is less than 10 % of the magnitude of vertical local accelerations. However, compared with Fig. 5.13 (b) and Fig. 5.14 (b), it is found that the difference between the magnitude of vertical convective accelerations and vertical local accelerations for Case PR5 ($ka = 0.38$) gets reduced to a maximum of 30 %.
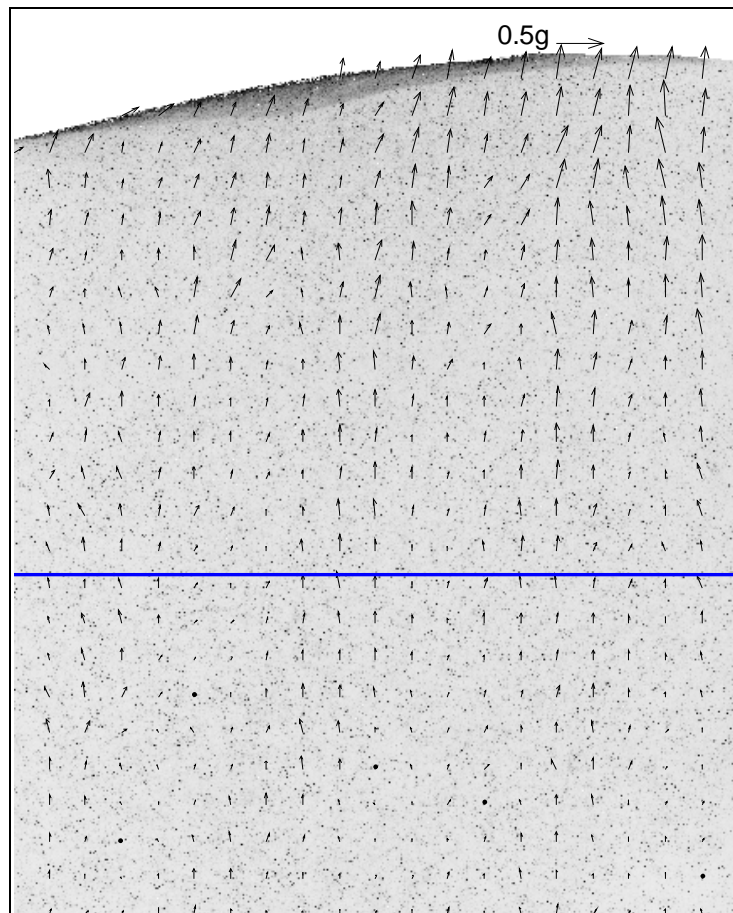
(a) Convective acceleration field.
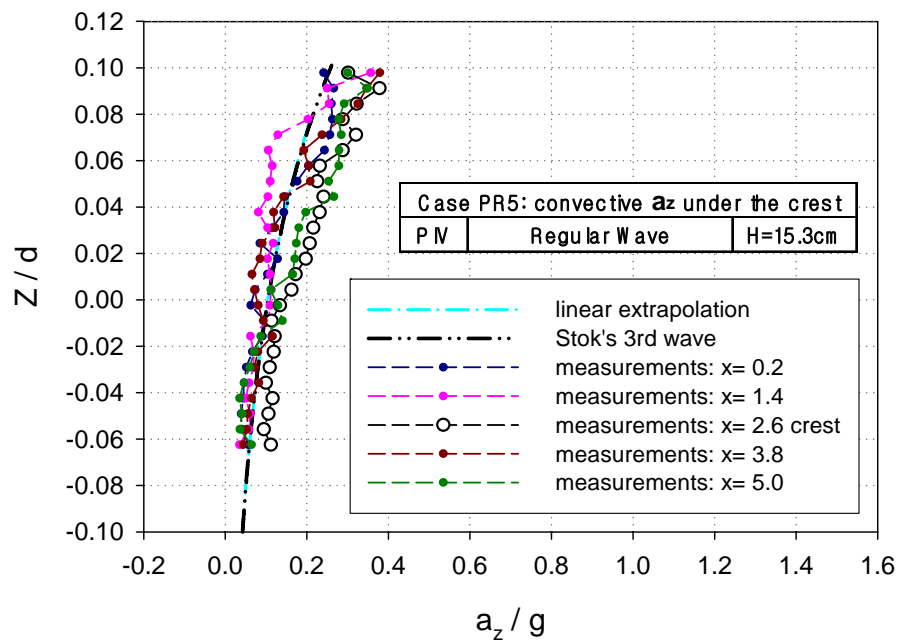
(b) Vertical convective accelerations.

Fig. 5.14 Convective accelerations near the wave crest for Case PR5.

5.5   Horizontal wave forces on slender truncated cylinder in the regular waves

The maximum horizontal forces on a slender truncated cylinder in the regular waves were computed applying measurements of velocities and accelerations to the Morison equation. The kinematics calculated from the third-order Stokes wave theory and extrapolation based on the Airy wave theory were also applied to the Morison equation and compared with measurement based computation of forces. Fig. 5.15 shows the horizontal forces of a regular wave, and the horizontal force F_x is normalized by $\rho g D^3$ and the wave height H is normalized by wave length L. The local acceleration is used for accelerations of the inertia force term in the Morison equation. It is found in Fig. 5.15 that the computations based on measurement agree very well with solutions of the third-order Stokes wave theory and extrapolation based on the Airy wave theory.
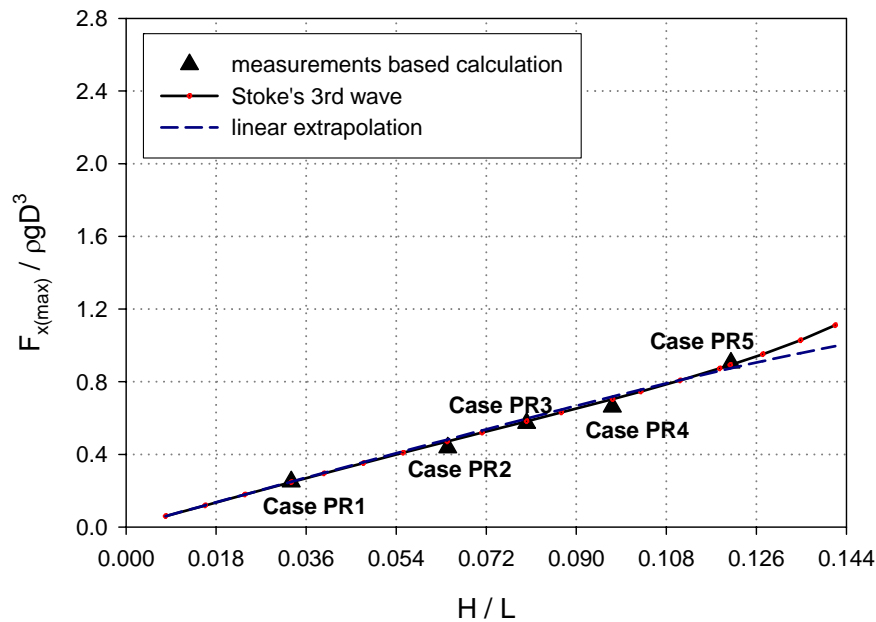

Fig. 5.15 Maximum horizontal force on the truncated cylinder in the regular waves.

5.6   Concluding remarks

Regular wave kinematics, including elevation, velocity, local acceleration, convective acceleration, and wave force, are investigated experimentally using the particle image velocimetry (PIV) system. The regular waves of five different wave slopes are generated in the 2-D wave tank. The velocities under the wave crest, wave trough, wave zero-up crossing point, and wave zero-down crossing point were measured using the PIV system and compared with solutions of the third-order Stokes wave theory and extrapolation based on the Airy wave theory. The local accelerations and convective accelerations of regular waves were computed by applying measurements of velocities to the centered finite difference scheme. The values of the measurement-based computation were compared with analytical solutions. The velocities and accelerations of regular waves were applied to the Morison equation to predict horizontal wave loading forces on a slender truncated cylinder in the regular waves.

Compared with experimental data of regular wave kinematics, the wave elevation is correlated with wave velocities under the wave crest because the velocities under the wave crest are increased in proportion to the wave crest height in the same wave period. However, it is observed in relatively high wave slope cases that the velocities under the wave crest above the SWL increased abruptly, which is not predicted by the higher-order Stokes wave theory.

The local accelerations of regular waves in this study were obtained successfully and compared with analytical solutions. The local accelerations could not be obtained at the very near crest wave due to the limitation in terms of time step of the PIV system used in this study.

We focused on the convective contribution of total accelerations in regular waves. It is found that the convective terms form a small part of the total acceleration in the moderate steepness regular waves ($ka = 0.104$ and 0.203). Although no appreciably amounts of convective accelerations in other wave slopes of regular waves, it is observed that the contribution of convective terms of total acceleration is increased as the wave slope get higher in steep regular waves ($ka = 0.252$, 0.305 and 0.38).

The maximum horizontal wave forces on the slender truncated cylinder in the regular waves were computed with the measured regular wave kinematics using the Morison equation. The computed forces were compared with analytical solutions

CHAPTER VI

EXPERIMENTAL RESULTS FOR ROGUE WAVE KINEMATICS

6.1 Particle velocity of rogue waves

The particle velocities of rogue wave kinematics are presented in this section. The four irregular wave trains are generated from the JONSWAP spectrum with significant wave height H_S of 6.6 cm, 7 cm, 7.4 cm and 7.8 cm, and a mean wave period T_m of 1.2 s and a peak enhancement factor γ of 6.5 in the 2-D wave tank (see the Table 2.4). The velocity fields of irregular wave trains are obtained using the PIV system. The investigated region of particular interest is under the crest of the maximum wave in the irregular wave trains. The maximum wave is defined as the highest wave crest in the wave train. The wave crest heights of the maximum wave in Case PH1, Case PH2, Case PH3 and Case PH4 are 8.0 cm, 8.5 cm, 9.3 cm and 10.0 cm, respectively. The maximum waves of Case PH3 and Case PH4 are rogue waves which satisfy with two criteria of rogue waves. Twenty eight instantaneous flow fields of view were obtained by measuring velocities of neighboring wave crest. The time step, time interval of every two phases, was 75 ms, the same as experiments of regular wave kinematics. The measurements of horizontal and vertical velocities are investigated under the wave crest of maximum waves or rogue waves. It is necessary to examine the vertical velocities under the rogue wave crest due to high nonlinearities of rogue waves. For the same reason, the local and convective terms of total accelerations will be investigated for two components, horizontal and vertical

accelerations. The three different prediction methods, Wheeler stretching, linear extrapolation and modified stretching, for calculating kinematics of maximum wave in the irregular waves are used for comparison with experimental results. The results of linear extrapolation are presented as two predictions considering sensitivity to the cutoff frequency of the spectrum. The selected cutoff frequencies for linear extrapolation1 and linear extrapolation2 are 14.04 rad/s and 18.2 rad/s, respectively. The solution of equivalent height with the third-order Stokes wave is also compared with the results of the PIV system. The measured velocities are presented with the normalized value; i.e., the measured vertical position Z is normalized by water depth d and horizontal velocity, u, and vertical velocity, w, are normalized by the phase velocity v_p of the maximum wave.

Fig. 6.1 (a), (b), (c) and (d) are images of velocity fields at maximum wave crest in irregular wave trains for Case PH1, Case PH2, Case PH3 and Case PH4, respectively. The velocity vectors are presented in the PIV images as shown in Fig. 6.1 (a), (b), (c) and (d). The still water level (SWL) is referred to by the horizontal solid blue line in the images of Fig. 6.1. The reference vector is just above the wave crest and just below the end of the reference vector is the wave crest. The length of the reference vector of the images marks 1m/s.

Fig. 6.1 (a) is the thirteenth phase image of velocity fields for Case PH1 ($H_{max}/L_{max} = 0.102$). The velocity vectors under the maximum wave crest for Case PH1 are presented in Fig. 6.1 (a). The maximum wave crest is defined geometrically as the highest elevation in the irregular wave train. Fig. 6.1 (a) figures out that the PIV system, non-intrusive velocity measurement system, can obtain the velocity vectors up to very near the free surface successfully in Case PH1.

Fig. 6.1 (b) is the thirteenth phase image of velocity fields for Case PH2 ($H_{max}/L_{max} = 0.114$) and presents the velocity vectors under the maximum wave crest. Fig. 6.1 (b) shows that the PIV system, non-intrusive velocity measurement system, can obtain the velocity vectors up to very near the free surface successfully in Case PH2.

Comparing Case PH1 and Case PH2, the difference of the maximum wave height for both cases is 1 cm. And the differences of wave crest and wave trough for both cases are 0.55 cm and 0.45 cm, respectively. The criteria C_H of both cases are over 2 while the criteria C_c of both cases are less than 1.25. Therefore, the maximum waves of Case PH1 and Case PH2 do not satisfy the criteria of a rogue wave.

Fig. 6.1 (c) is the twelfth phase image of velocity fields for Case PH3 ($H_{max}/L_{max} = 0.127$) and shows the velocity vectors under the maximum wave crest. Fig. 6.1 (c) shows that the PIV system, non-intrusive velocity measurement system, can measure the velocities up to very near the free surface in Case PH3.

Fig. 6.1 (d) is the twelfth phase image of velocity fields for Case PH4 ($H_{max}/L_{max} = 0.13$) and shows the velocity vectors under the maximum wave crest. Fig. 6.1 (d) shows that the velocities up to very near the free surface in Case PH4 are obtained by using the PIV system.

(a) Case PH1.
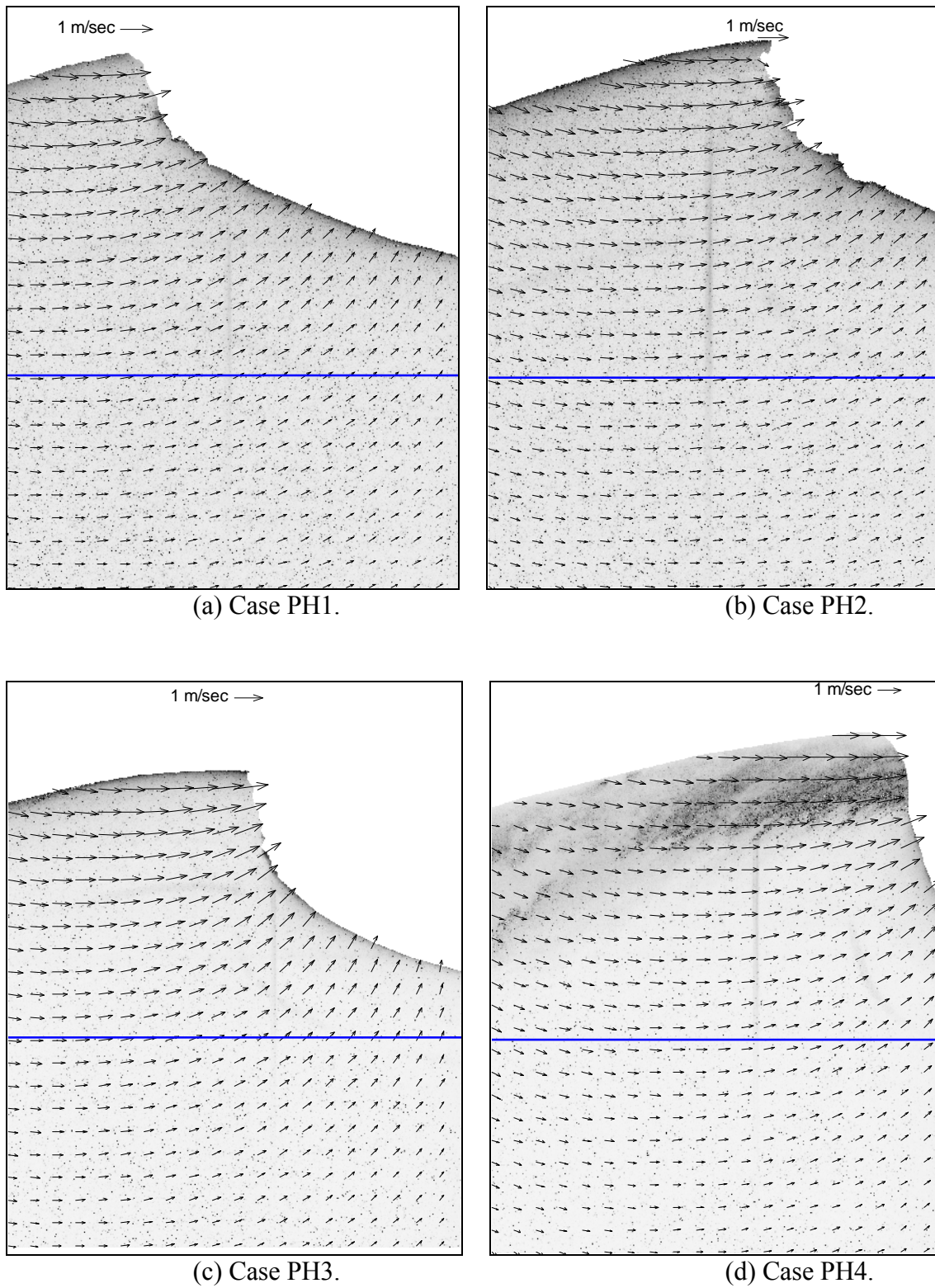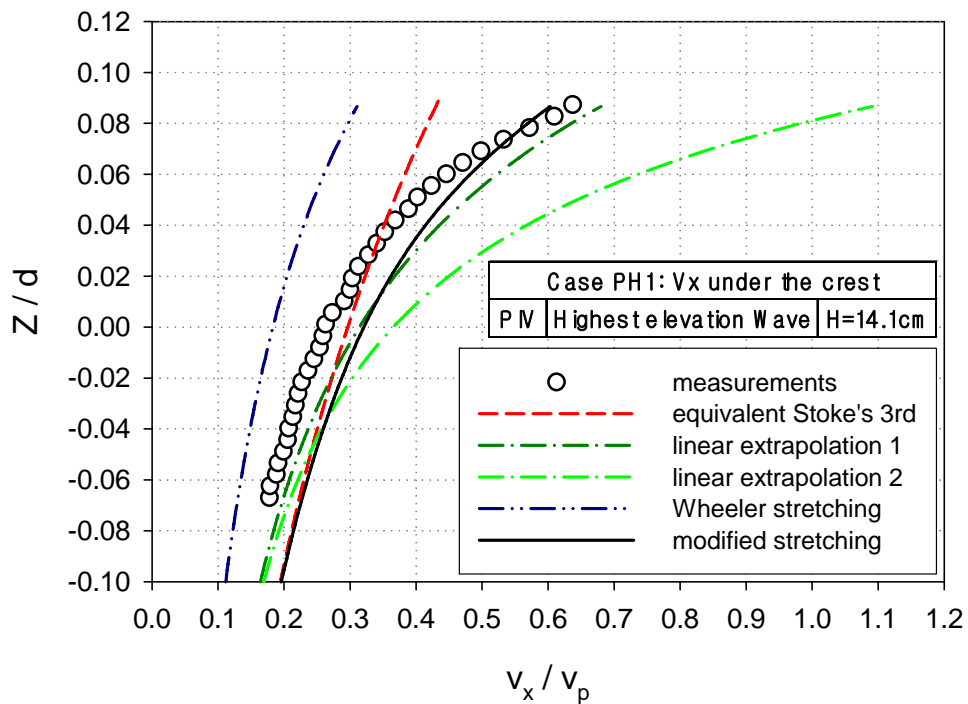
(b) Case PH2.

(c) Case PH3.

(d) Case PH4.

Fig. 6.1 Velocity fields of the maximum wave crest.

Comparing Case PH1 and Case PH3, the difference of the maximum wave height for both cases is 1.8 cm. And the differences of wave crest and wave trough are 1.31 cm and 0.67 cm, respectively. Comparing Case PH1 and Case PH4, the difference of the maximum wave height for both cases is 2.25 cm. The differences of wave crest and wave trough for both cases are 2.02 cm and 0.23 cm, respectively. The criteria C_H of Case PH3 and Case PH4 are over 2, and the criteria C_c of Case PH3 and Case PH4 are also over 1.25. Therefore, the maximum waves of Case PH3 and Case PH4 can be called rogue waves.

Fig. 6.2 (a) shows the comparisons of measured horizontal velocities and four kinds of kinematics predictions under the wave crest of Case PH1. It is noticed in Fig. 6.2 (a) that the Wheeler stretching prediction underestimated the measured horizontal velocity for Case PH1. The prediction of linear extrapolation1 (cutoff frequency= 14.04 rad/s) agrees well with measurements, but the result of linear extrapolation 2 (cutoff frequency=18.2rad/s) is overestimated through the vertical measuring locations. It is seen in Fig. 6.2 (a) that the results of modified stretching predict well the measured horizontal velocities for Case PH1, especially, above the normalized vertical measuring position Z/d= 0.06. The equivalent height wave kinematics, derived from the third-order Stokes wave theory, is also compared with the measured horizontal velocities for Case PH1. The results of equivalent wave method for Case PH1 overestimated the measurements below normalized vertical measuring position Z/d= 0.02 and underestimated experimental data above the normalized vertical measuring position Z/d= 0.02. The overestimated values of equivalent wave method for Case PH1 are larger than those of linear extrapolation1 and linear extrapolation2.

Fig. 6.2 (b) presents the comparisons of measured vertical velocities and three kinds of kinematics predictions under the wave crest of Case PH1. The magnitude of measured vertical velocity is less than 10 % of the phase velocity of equivalent height wave with height maximum wave in Case PH1. It is found that the results of Wheeler stretching and linear extrapolation1 (cutoff frequency= 14.04 rad/s) underestimated the measured vertical velocities for Case PH2 as shown in Fig. 6.2 (b). It is also seen in Fig. 6.2 (b) that linear extrapolation2 (cutoff frequency= 18.2 rad/s) agrees well with the measured vertical velocity below the normalized vertical measuring position $Z/d=0.03$ but overestimated severely than the measured vertical velocity above the normalized vertical measuring position $Z/d=0.03$. The predictions by modified stretching method for Case PH1 are in the middle of the results of two linear extrapolations and underestimated the measured vertical velocity slightly as shown in Fig. 6.2 (b).

The range of linear extrapolation predictions for the maximum wave kinematics in the irregular wave train is very broad due to the effect of high frequencies as presented in Fig. 6.2 (a) and (b). Though the linear extrapolation prediction is sensitive depending on cutoff frequencies, it is known that proper cutoff frequency can make accurate prediction for Case PH1.
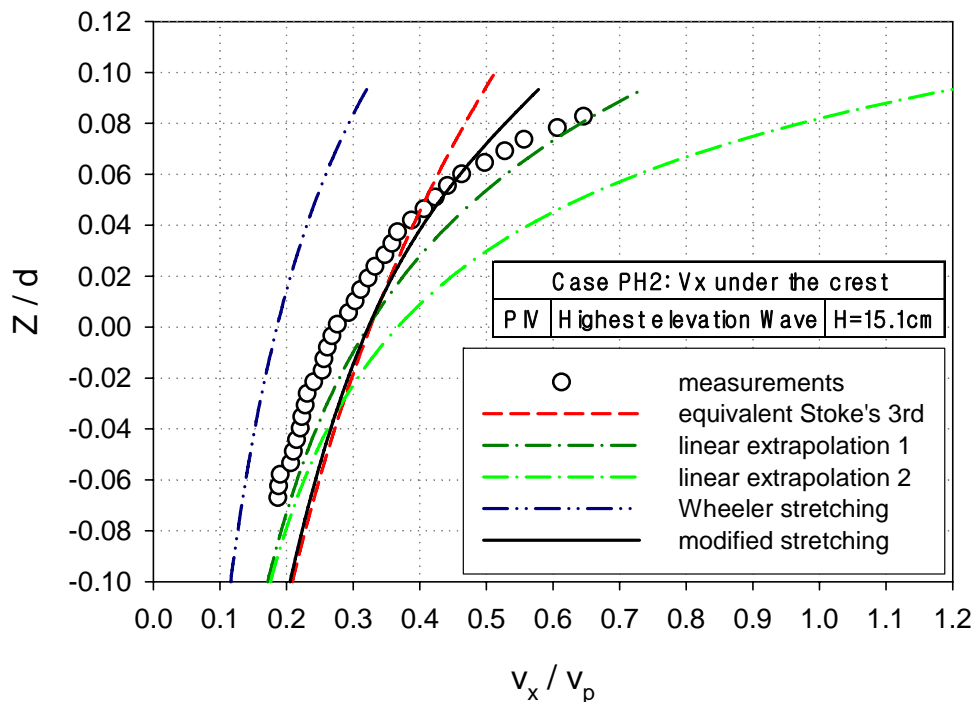
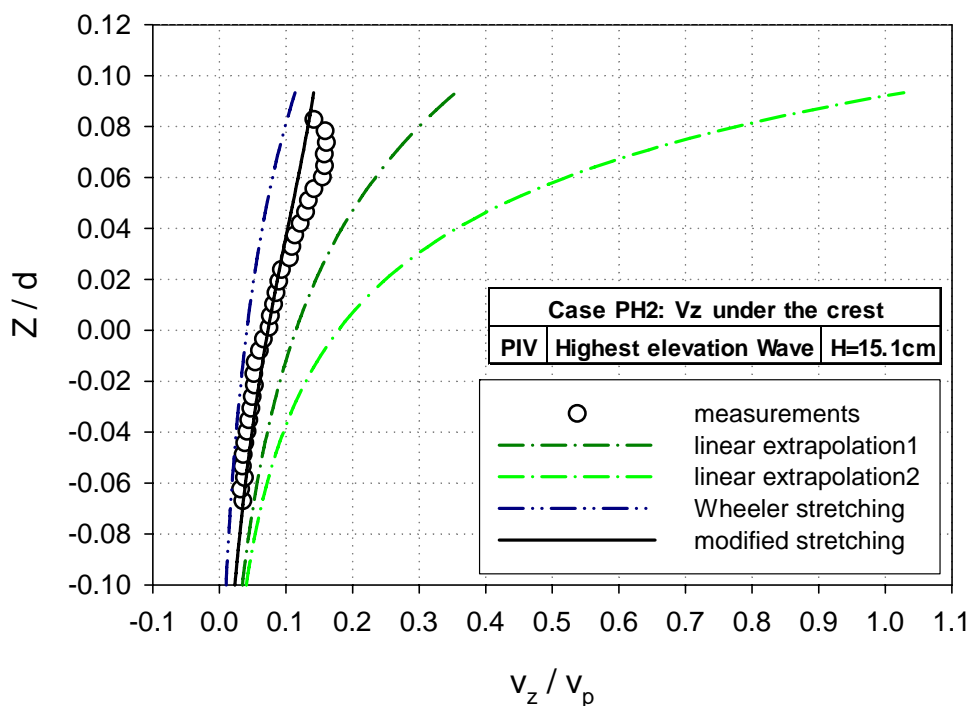(a) Horizontal velocities under the maximum wave crest.
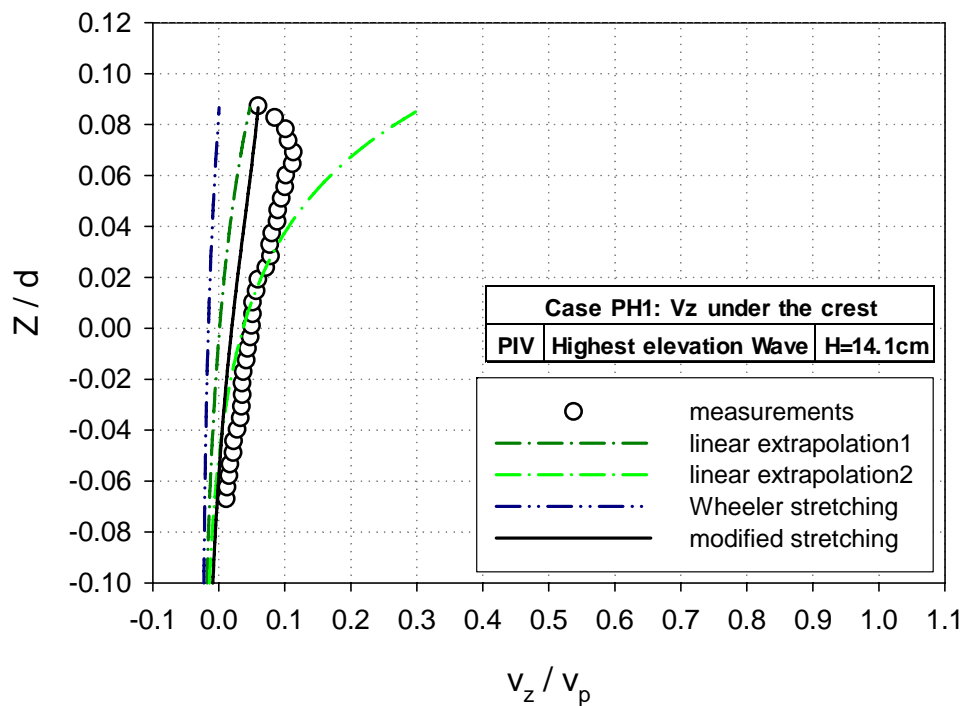
(b) Vertical velocities under the maximum wave crest.

Fig. 6.2 Velocities under the maximum wave crest in Case PH1.

Fig. 6.3 (a) shows the measured horizontal velocities under the maximum wave crest of Case PH2. The experimental results are compared with four kinematics predictions for Case PH2. Compared with these prediction methods, it is presented in Fig. 6.3 (a). The result of Wheeler stretching method for Case PH2 is underestimated for the horizontal velocities. The prediction of linear extrapolation1 (cutoff frequency= 14.11 rad/s) agreed well with measurements, but it is slightly overestimated through out the whole measuring vertical locations. The result of linear extrapolation2 (cutoff frequency= 18.3 rad/s) is overestimated and even increased abruptly. And the modified stretching prediction for the horizontal velocities of Case PH2 is overestimated under the normalized vertical measuring position $Z/d= 0.04$ but agreed well with measurements above the normalized vertical measuring position $Z/d= 0.04$. The results of equivalent wave method for Case PH2 are overestimated the measurements below the normalized vertical measuring position $Z/d= 0.04$ and underestimated experimental data above the normalized vertical measuring position $Z/d= 0.04$. The overestimated values of equivalent wave method for Case PH2 are larger than those of linear extrapolation1 and linear extrapolation2.

(a) Horizontal velocities under the maximum wave crest.

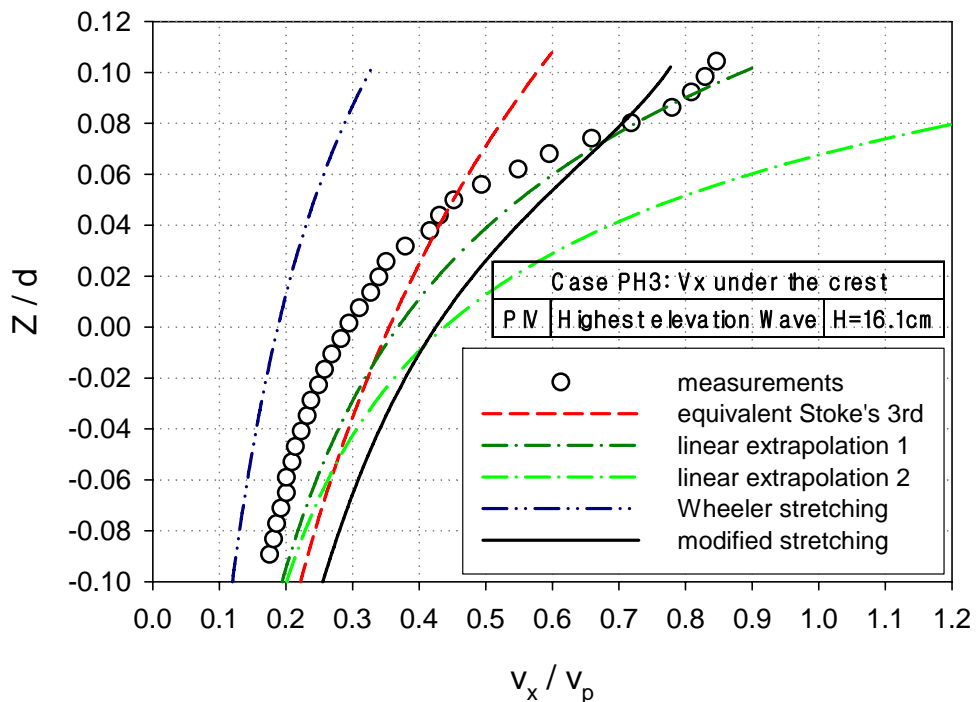(b) Vertical velocities under the maximum wave crest.

Fig. 6.3 Velocities under the maximum wave crest in Case PH2.

Fig. 6.3 (b) presents the measured vertical velocities under the maximum wave crest of Case PH2. The measured results are compared with three kinds of kinematics predictions under the wave crest of Case PH2. The magnitude of measured vertical velocity is less than 15 % of phase velocity of equivalent height wave with height maximum wave in Case PH2 at $Z/d= 0.06$ as presented in Fig. 6.3 (b). The Wheeler stretching prediction for vertical velocities of Case PR2 is underestimated as seen in Fig. 6.3 (b). It is seen in Fig. 6.3 (b) that the predictions for the measured vertical velocities of Case PH2 of linear extrapolation 1 and 2 are overestimated. The results of linear extrapolation 2 (cutoff frequency= 18.3 rad/s) for the vertical velocity of Case PH2 are unrealistically overestimated as seen in Fig. 6.3 (b). It is shown in Fig. 6.3 (a) and (b) that the linear extrapolation predictions for the maximum wave kinematics in irregular wave train vary depending on the cutoff frequency of wave spectrum. It is found, as presented Fig. 6.3 (a), that it is possible to predict the measured horizontal velocities accurately by the linear extrapolation method selecting proper cutoff frequency of wave spectra.
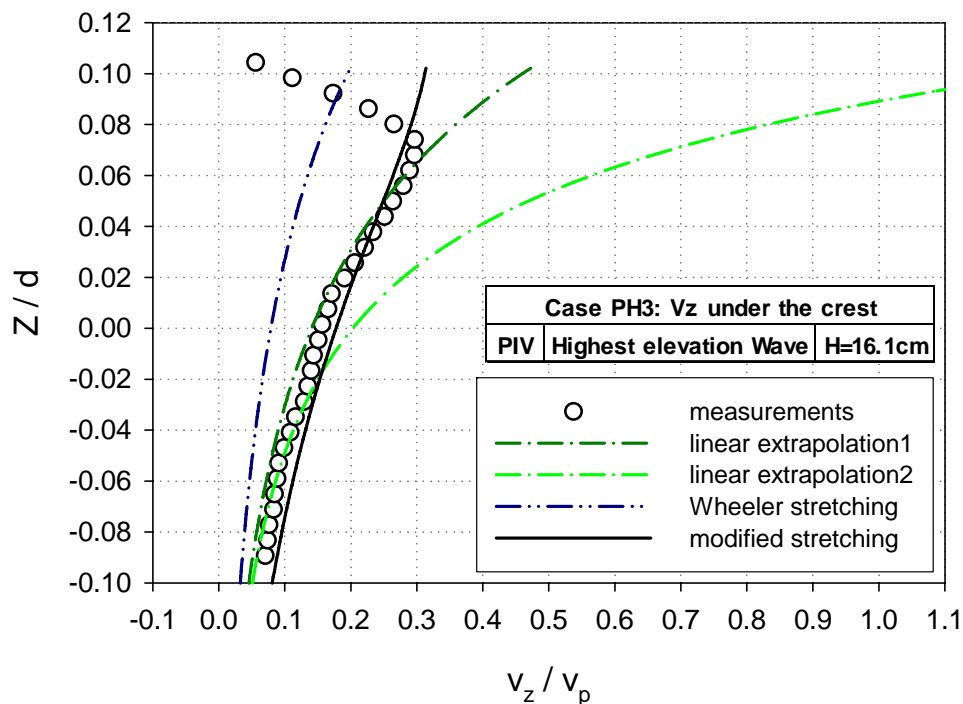
Fig. 6.4 (a) and (b) show the horizontal and vertical velocities under maximum wave crest for Case PH3. The maximum wave of Case PH3 is satisfied with criteria of rogue wave definition. Fig. 6.4 (a) presents comparisons of measured horizontal velocities and four kinds of kinematics predictions under the wave crest of Case PH3. It is noticed in Fig. 6.4 (a) that Wheeler stretching prediction for the measured horizontal velocity in Case PH3 is underestimated. The difference between Wheeler stretching predictions and experimental results above normalized measuring vertical position $Z/d= 0.02$ is unrealistically large as shown in Fig. 6.4 (a). The prediction of linear extrapolation1 (cutoff frequency= 14.04 rad/s) generally agreed well with measurements while the result of linear

extrapolation2 (cutoff frequency= 18.2 rad/s) is overestimated. It is seen in Fig. 6.4 (a) that the modified stretching method overpredicts the measured horizontal velocities below normalized vertical measuring position Z/d= 0.06 for Case PH3. The equivalent height wave kinematics which is derived from the third-order Stokes wave theory is also compared with the measured horizontal velocities for Case PH3. The results of equivalent wave method for Case PH3 are overestimated the measurements below normalized vertical measuring position Z/d= 0.04 and underestimated experimental data above normalized vertical measuring position Z/d= 0.04. The overestimated values of equivalent wave method for Case PH3 are larger than those of linear extrapolation1 and linear extrapolation2 below the SWL.

Fig. 6.4 (b) presents the comparisons of measured vertical velocities and three kinematics predictions under the wave crest of Case PH3. The magnitude of measured vertical velocity is 30 % less than the phase velocity of equivalent height wave with the maximum wave height in Case PH3. It is found, as shown in Fig. 6.4 (b), that the results of the Wheeler stretching is underestimated the measured vertical velocities for Case PH3 as shown in Fig. 6.4 (b). It is also seen in Fig. 6.4 (b) that the vertical velocities of the linear extrapolation1 (cutoff frequency= 14.11 rad/s) and the modified stretching method agree very well up to normalized vertical measuring position Z/d= 0.08. The predictions by linear extrapolation2 (cutoff frequency= 18.3 rad/s) for Case PH3 are agreed with experimental measurements below normalized vertical measuring position Z/d= 0.02 and overestimated measured vertical velocity as shown in Fig. 6.4 (b). It is shown in Fig. 6.4 (a) and (b) that choice of cutoff frequency is important to predict the rogue wave particle velocities accurately by the linear extrapolation method.

(a) Horizontal velocities under the rogue wave crest.
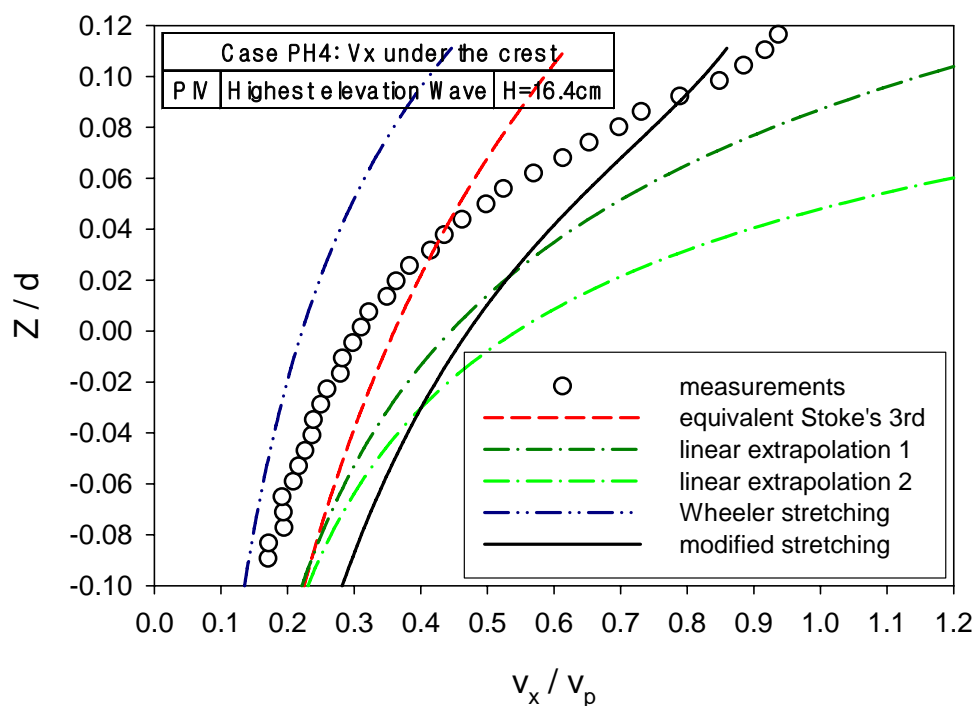

(b) Vertical velocities under the rogue wave crest.

Fig. 6.4 Velocities under the rogue wave crest in Case PH3.

Fig. 6.5 (a) and (b) show the horizontal and vertical velocities under maximum wave crest for Case PH4. The maximum wave of Case PH4 is satisfied with criteria of rogue wave definition. Fig. 6.5 (a) shows the measured horizontal velocities under the rogue wave crest in Case PH4. The experimental results are compared with four kinematics predictions for Case PH4. The comparisons with the prediction methods are presented in Fig. 6.5 (a). The Wheeler stretching method for Case PH2 is underestimated the horizontal velocities through the whole vertical measuring locations. The predictions of linear extrapolation1 (cutoff frequency= 14.11 rad/s) and linear extrapolation2 (cutoff frequency= 18.3 rad/s) are overestimated considerably in the whole measuring vertical locations. The modified stretching method overpredict the horizontal velocities under normalized vertical measuring position $Z/d=0.08$ for Case PH4 but predicts experimental values accurately above normalized vertical measuring position $Z/d=0.08$. The results of equivalent wave method for Case PH4 are overestimated below normalized vertical measuring position $Z/d=0.04$ and underestimated experimental data above normalized vertical measuring position $Z/d=0.04$. The overestimated values of equivalent wave method for Case PH4 are smaller than those of linear extrapolation1 and linear extrapolation2.

Fig. 6.5 (b) presents measured vertical velocities under the rogue wave crest of Case PH4. The measurements are compared with three kinematics predictions under the wave crest of Case PH4. The magnitude of measured vertical velocity is 30 % less than the phase velocity of equivalent height wave with the maximum wave height in Case PH4. at the $Z/d=0.06$ as presented in Fig. 6.5 (b). The Wheeler stretching prediction for vertical velocities of Case PR4 is underestimated as seen in Fig. 6.5 (b). It is also seen in Fig. 6.5

(b) that the vertical velocities of the linear extrapolation 1 (cutoff frequency= 14.11 rad/s) and the linear extrapolation 2 (cutoff frequency= 18.3 rad/s) for Case PH4 agree very well up to normalized vertical measuring position Z/d= 0.06 and 0.04 , respectively. Though the modified stretching prediction follows the trend of measured results, considerable reductions are observed from Z/d= -0.02 to Z/d= 0.09 as shown in Fig. 6.5 (b).

(a) Horizontal velocities under the rogue wave crest.

Fig. 6.5 Velocities under the rogue wave crest in Case PH4.
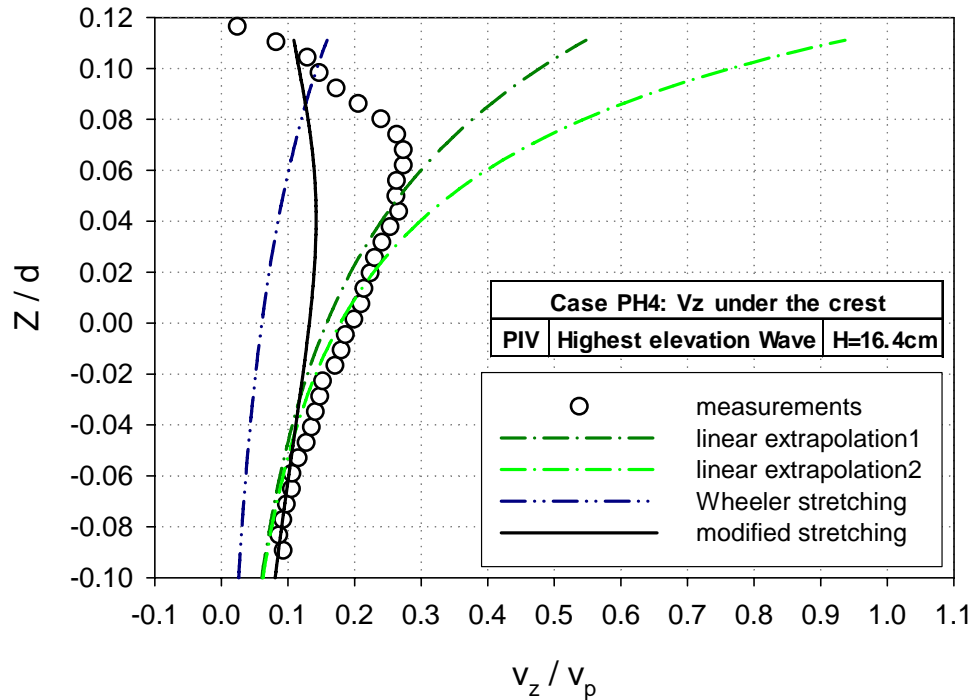
(b) Vertical velocities under the rogue wave crest.

Fig. 6.5 Continued.

6.2   Particle local acceleration of rogue waves

The particle local accelerations of rogue wave kinematics are presented in this section. The local acceleration fields were computed based on PIV measurements of the particle velocities under the maximum wave crest of the four irregular wave trains. The numerical scheme used for computation of local acceleration was a centered finite difference method with $\Delta t = 75$ ms. The time derivative, local term of total accelerations, is investigated in horizontal and vertical components. The three different prediction methods, which are the Wheeler stretching, the linear extrapolation, and the modified stretching, for calculating kinematics of maximum wave in the irregular wave are used in comparing with calculated

results based on measurement. Two linear extrapolation predictions are presented by selection of cutoff frequency of wave spectrum. The local accelerations computed based on measurement are presented in normalized values; i.e., measured vertical position Z is normalized by water depth d and horizontal and vertical local accelerations are normalized by gravity acceleration g $(= 9.806$ m/s$^2)$.

Fig. 6.6 (a), (b), (c) and (d) are images of the local acceleration fields at maximum wave crest in irregular wave trains for Case PH1, Case PH2, Case PH3 and Case PH4, respectively. The local acceleration vectors are presented in the image as shown in Fig. 6.6 (a), (b), (c) and (d). The still water level (SWL) is referenced by the horizontal solid blue line in Fig. 6.6. The reference vector is at just above the wave crest and just below of end of reference vector is the wave crest. The length of reference vector of images marks $0.5g$ $(=4.903)$m/s^2.The local acceleration vectors near the free surface in images are missing because the wave free surface was changed abruptly at the time step $\Delta t =0.75$ ms.

Fig. 6.6 (a) is the thirteenth phase image of local acceleration fields for Case PH1 $(H_{\max}/L_{\max} = 0.102$).The local acceleration vectors under the maximum wave crest for Case PH1 are presented in Fig. 6.6 (a). Fig. 6.6 (b) is the thirteenth phase image of local acceleration fields for Case PH2 $(H_{\max}/L_{\max} = 0.114$) and presents the local acceleration vectors under the maximum wave crest. Fig. 6.6 (c) is the twelfth phase image of local acceleration fields for Case PH3 $(H_{\max}/L_{\max} = 0.127$) and shows the local acceleration vectors under the rogue wave crest. Fig. 6.6 (d) is the twelfth phase image of local acceleration fields for Case PH4 $(H_{\max}/L_{\max} = 0.13$) and shows the local acceleration vectors under the rogue wave crest.

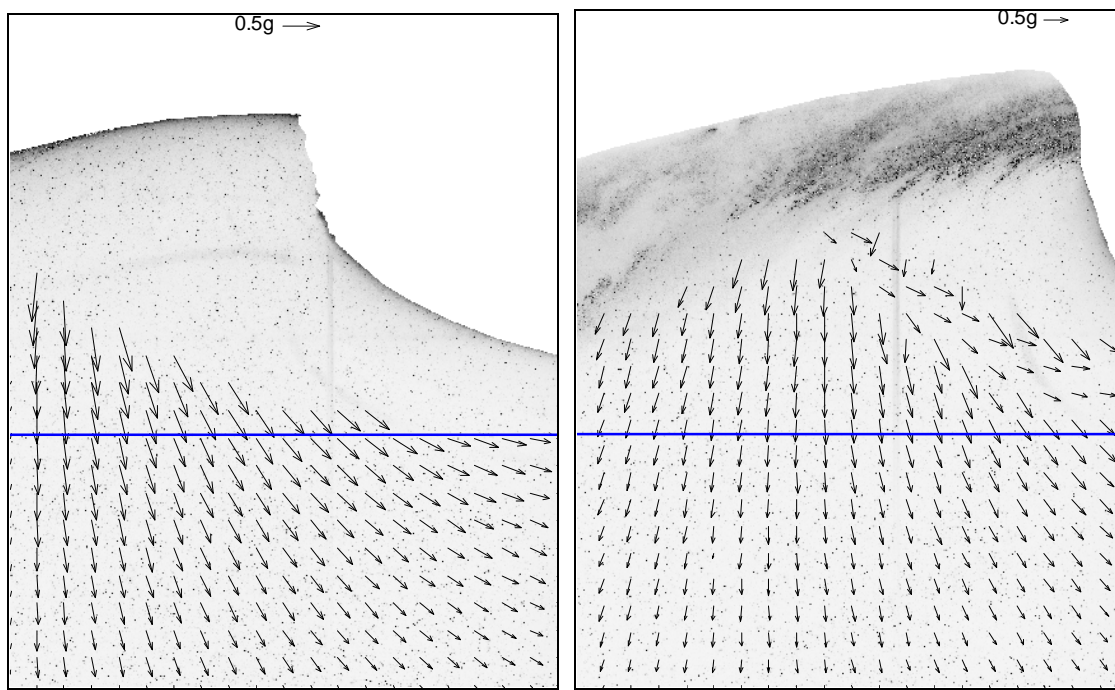(a) Case PH1.   (b) Case PH2.
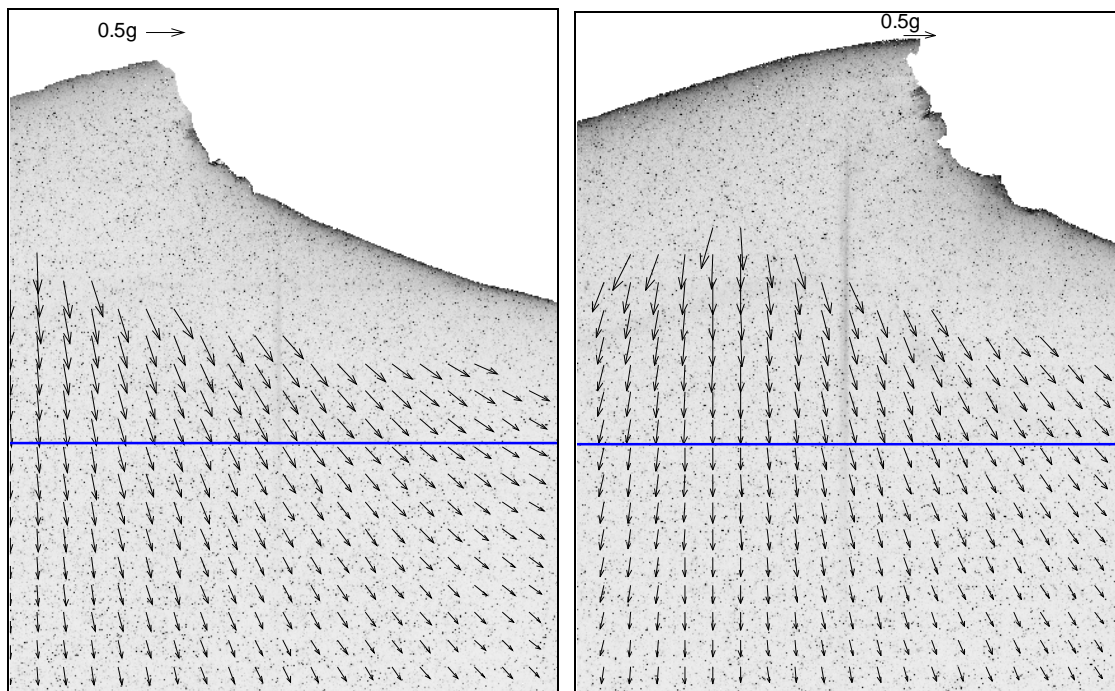
(c) Case PH3.   (d) Case PH4.

Fig. 6.6 Local acceleration fields of the maximum wave crest.

Fig. 6.7 (a) shows the comparisons of horizontal local acceleration from the measurement-based computation and three kinematics predictions under the wave crest of Case PH1. It is noticed in Fig. 6.7 (a) that Wheeler stretching prediction is underestimated. The prediction of linear extrapolation 1 (cutoff frequency= 14.04 rad/s) and modified stretching agreed very well with the values of measurement-based computation for horizontal local acceleration, but the result of linear extrapolation 2 (cutoff frequency= 18.2 rad/s) is overestimated through the whole vertical measuring locations. It is also found in Fig. 6.7 (a) that the magnitude of horizontal local acceleration above the SWL under the wave crest for Case PH1 is considerable. The horizontal local acceleration under the regular wave crest had almost magnitude of zero.

Fig. 6.7 (b) presents the measurement-based computation for vertical local acceleration and four kinematics predictions under the wave crest of Case PH1. It is found that the Wheeler stretching prediction underestimates the vertical local accelerations for Case PH1 as shown in Fig. 6.7 (b). It is also seen in Fig. 6.7 (b) that linear extrapolation 1 and linear extrapolation 2 overestimate vertical local acceleration of Case PH1 except below the normalized vertical measuring position $Z/d=$ -0.02. The modified stretching and equivalent height wave show solid agreement with experimental data of horizontal acceleration for Case PH1. The modified stretching prediction above the SWL shows more agreement with experimental data.
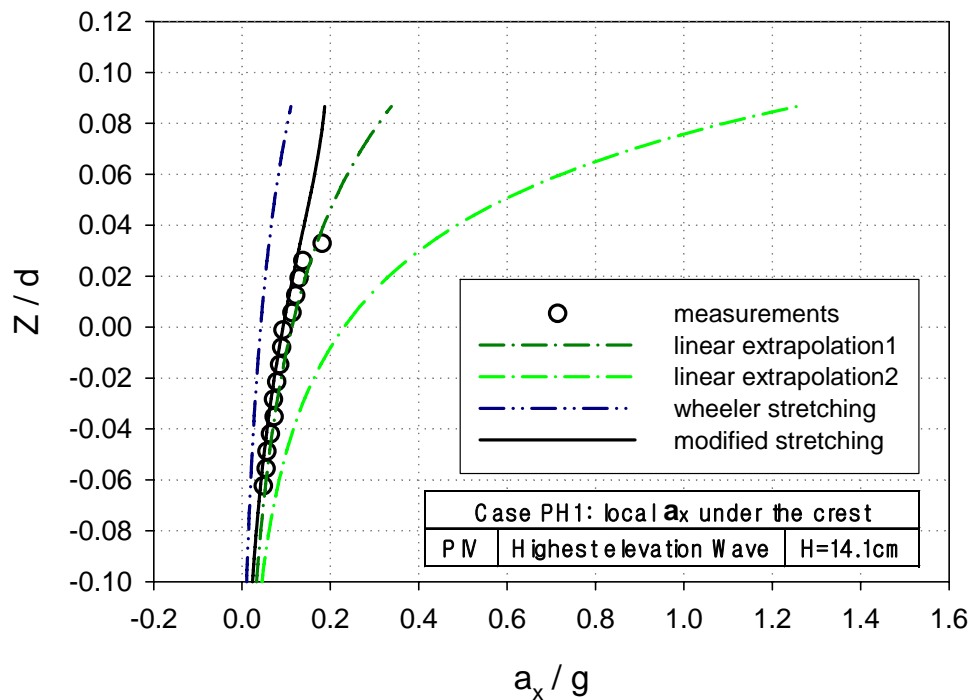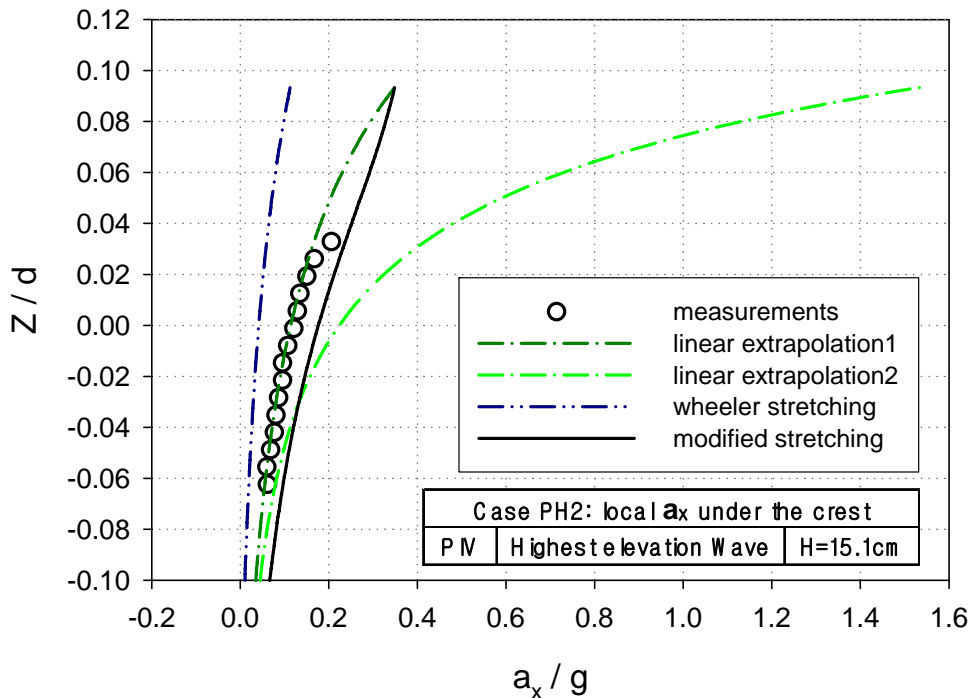
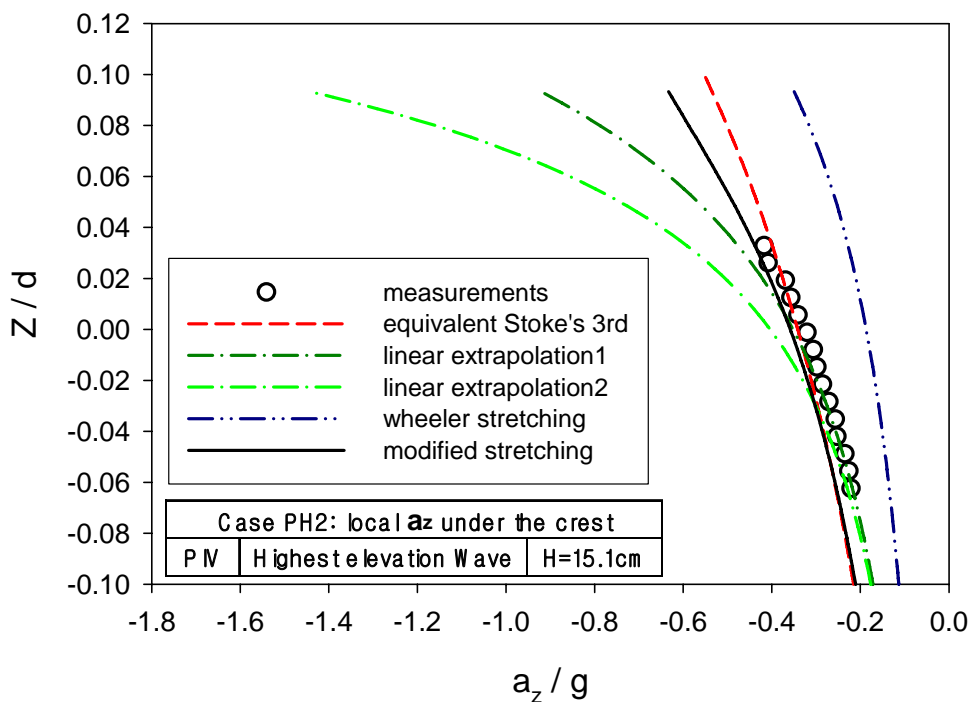(a) Horizontal local accelerations under the maximum wave crest.
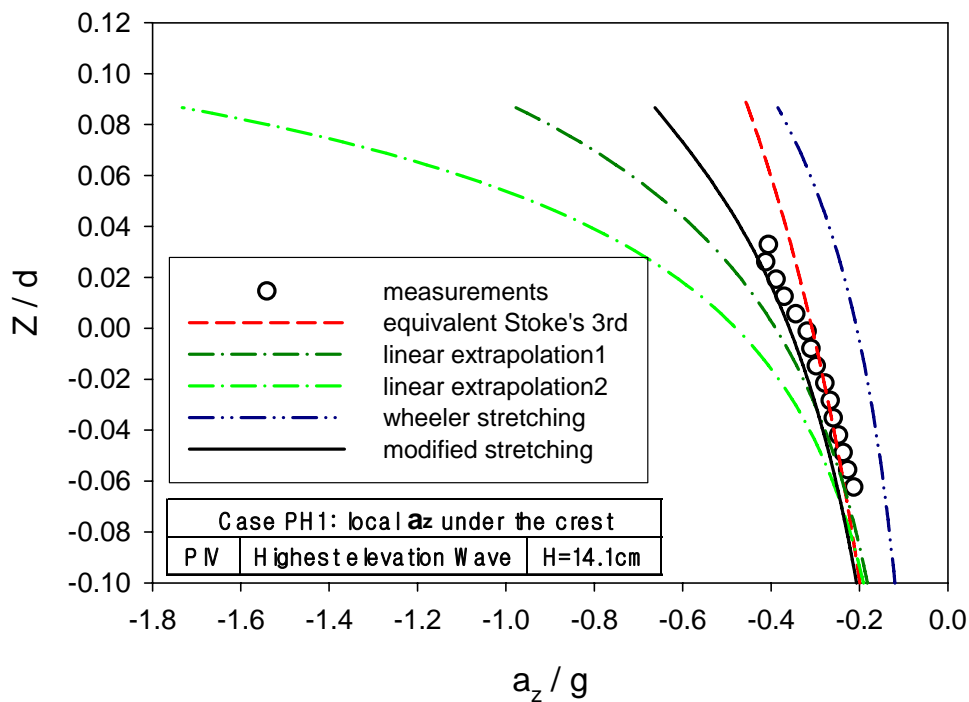
(b) Vertical local accelerations under the maximum wave crest.

Fig. 6.7 Local accelerations under the maximum wave crest for Case PH1.

(a) Horizontal local accelerations under the maximum wave crest.

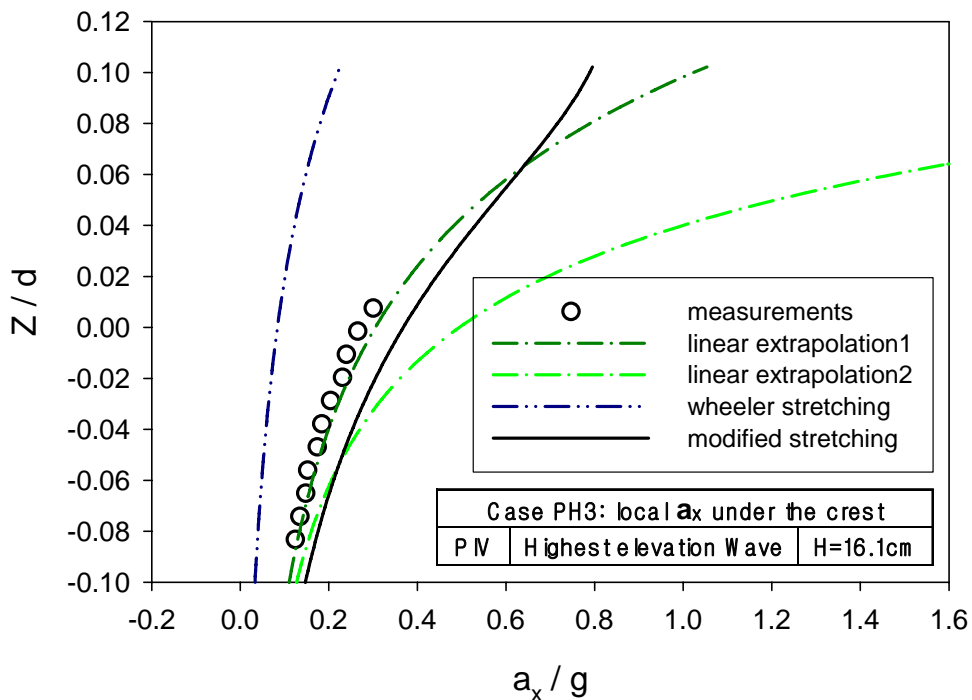(b) Vertical local accelerations under the maximum wave crest.

Fig. 6.8 Local accelerations under the maximum wave crest for Case PH2.

Fig. 6.8 (a) presents the comparisons of horizontal local acceleration of computation based on measurements and three kinematics predictions under the wave crest of Case PH2. It is seen in Fig. 6.8 (a) that the Wheeler stretching prediction is underestimated. Prediction of linear extrapolation1 (cutoff frequency= 14.11 rad/s) and the modified stretching agreed very well with the values of measurement-based computation for horizontal local acceleration, but the linear extrapolation2 (cutoff frequency= 18.3 rad/s) is overestimated for whole vertical region. It is also found, in comparison of Fig. 6.7 (a) and Fig. 6.8 (a), that the magnitude of experimental horizontal local acceleration does not change much.

Fig. 6.8 (b) presents the measurement-based computation for vertical local acceleration and four kinematics predictions under the wave crest of Case PH2. It is found that the Wheeler stretching prediction underestimates the vertical local accelerations for Case PH2 as shown in Fig. 6.7 (b). It is also seen in Fig. 6.7 (b) that linear extrapolation1 and linear extrapolation2 overestimate vertical local acceleration of Case PH2 except below normalized vertical measuring position Z/d= 0.02. The modified stretching and equivalent height wave show good agreement with experimental data of vertical acceleration for Case PH2.

Fig. 6.9 (a) shows horizontal local accelerations from measurement-based computation and three kinematics predictions under the wave crest of Case PH3. The Wheeler stretching prediction is underestimated as shown in Fig. 6.9 (a). Prediction using the linear extrapolation1 (cutoff frequency= 14.11 rad/s) and the modified stretching show good agreement with values of measurement-based computation for horizontal local acceleration. The linear extrapolation 1 shows better agreement. However, the linear extrapolation2 (cutoff frequency= 18.3 rad/s) overestimates it through whole vertical region.

Fig. 6.9 (b) shows vertical local accelerations from measurement-based computation and four kinematics predictions under the wave crest of Case PH3. The Wheeler stretching prediction underestimates vertical local accelerations for Case PH3 as shown in Fig. 6.9 (b). It is seen in Fig. 6.7 (b) that linear extrapolation 1 and linear extrapolation 2 overestimate vertical local acceleration of Case PH3. It is seen in Fig. 6.9 (b) that the modified stretching and equivalent height wave show good agreement with the vertical local accelerations from measurement-based computation for Case PH3. The modified stretching prediction shows better agreement than that of the equivalent height wave method as shown in Fig. 6.9 (b). It is seen in Fig. 6.9 (a) and (b) that the magnitude of horizontal and vertical local accelerations from measurement-based computation under the wave crest for Case PH3 is almost the same.

(a) Horizontal local accelerations under the rogue wave crest.
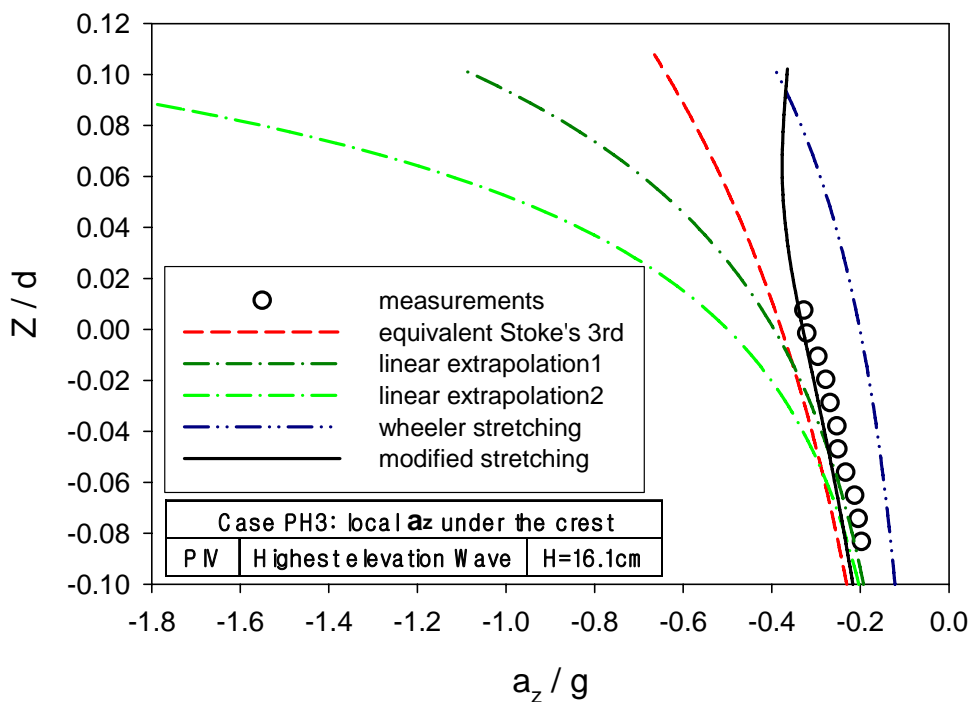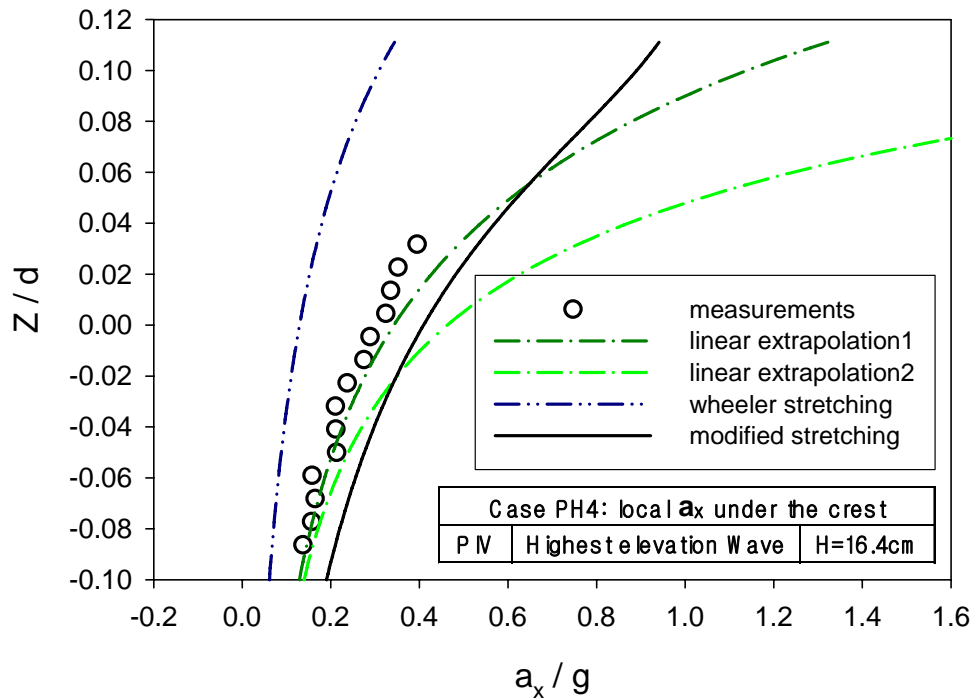

(b) Vertical local accelerations under the rogue wave crest.
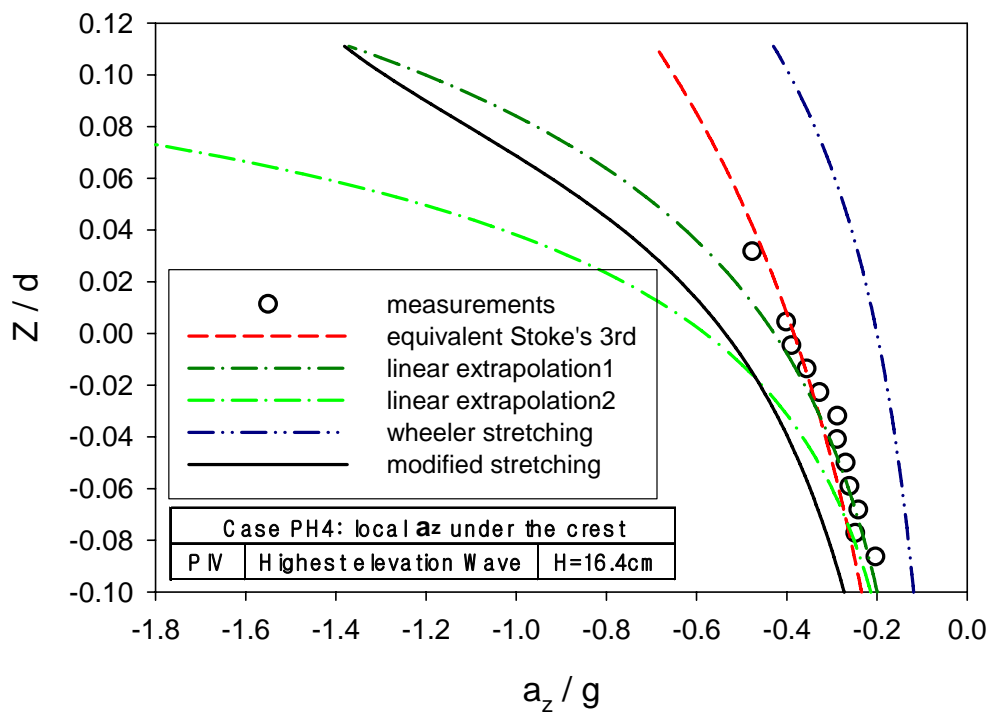
Fig. 6.9 Local accelerations under the rogue wave crest for Case PH3.

Fig. 6.10 (a) presents horizontal local acceleration from measurement-based computation and three kinematics predictions under the wave crest of Case PH4. The Wheeler stretching underestimated horizontal local acceleration as shown in Fig. 6.10 (a). Prediction of linear extrapolation1 is agreed very well with results of measurement-based computation for horizontal local acceleration, but the linear extrapolation2 and the modified stretching overestimate it for whole vertical region.

Fig. 6.10 (b) presents vertical local acceleration from measurement-based computation and four kinematics predictions under the wave crest of Case PH4. The Wheeler stretching prediction underestimates vertical local accelerations for Case PH4 as shown in Fig. 6.10 (b). It is seen in Fig. 6.10 (b) that the modified stretching and linear extrapolation2 overestimate vertical local acceleration of Case PH4. The linear extrapolation1 and equivalent height wave show good agreement with the vertical local acceleration from measurement-based computation for Case PH4. It is found in Fig. 6.10 (a) and (b) that magnitude of horizontal and vertical local acceleration from measurement-based computation under the wave crest for Case PH4 is almost same. The some experimental results are also scattered above the SWL as shown in Fig. 6.10 (b).

(a) Horizontal local accelerations under the rogue wave crest.

(b) Vertical local accelerations under the rogue wave crest.

Fig. 6.10 Local accelerations under the rogue wave crest for Case PH4.

## 6.3   Particle convective acceleration of rogue waves

Particle convective accelerations of rogue wave kinematics are presented in this section. Convective acceleration fields were computed based on PIV measurements of particle velocities under the maximum wave crest of four irregular wave trains. Applied numerical scheme for computation of convective acceleration is a centered finite difference method with Δx and Δz =6 mm for Case PH1 and Case PH2 and Δx and Δz =8 mm for Case PH3 and Case PH4. The spatial derivative, convective term of total accelerations, is investigated in horizontal and vertical components.

The three different prediction methods, Wheeler stretching, linear extrapolation, and modified stretching, for calculating kinematics of maximum wave in irregular waves are used for comparing with computation based on measurement. Two linear extrapolation predictions are presented by selection of cutoff frequency of wave spectrum. Convective accelerations from measurement-based computation are presented with normalized value; i.e., measured vertical position Z is normalized by water depth d and horizontal and vertical local accelerations are normalized by gravity acceleration g (= 9.806 m/s^2).

Fig. 6.11 (a), (b), (c) and (d) are image of convective acceleration fields at the maximum wave crest in irregular wave trains for Case PH1, Case PH2, Case PH3 and Case PH4, respectively. They present convective acceleration vectors in those images. The still water level (SWL) is referred with the horizontal solid blue line in Fig. 6.11. The reference vector is at just above the wave crest and the just below of end of reference vector is the wave crest. The length of reference vector of images marks $0.5g$ ($= 4.903 \text{m/s}^2$).

Fig. 6.11 (a) is the thirteenth phase image of convective acceleration fields for Case PH1 ($H_{max}/L_{max} = 0.102$).Convective acceleration vectors under the maximum wave crest for Case PH1 are presented in Fig. 6.11 (a). Fig. 6.11 (b) is the thirteenth phase image of convective acceleration fields for Case PH2 ($H_{max}/L_{max} = 0.114$) and presents convective acceleration vectors under the maximum wave crest.

Fig. 6.11 (c) is the twelfth phase image of convective acceleration fields for Case PH3 ($H_{max}/L_{max} = 0.127$) and shows convective acceleration vectors under the rogue wave crest. Fig. 6.11 (d) is the twelfth phase image of convective acceleration fields for Case PH4 ($H_{max}/L_{max} = 0.13$) and shows convective acceleration vectors under the rogue wave crest.
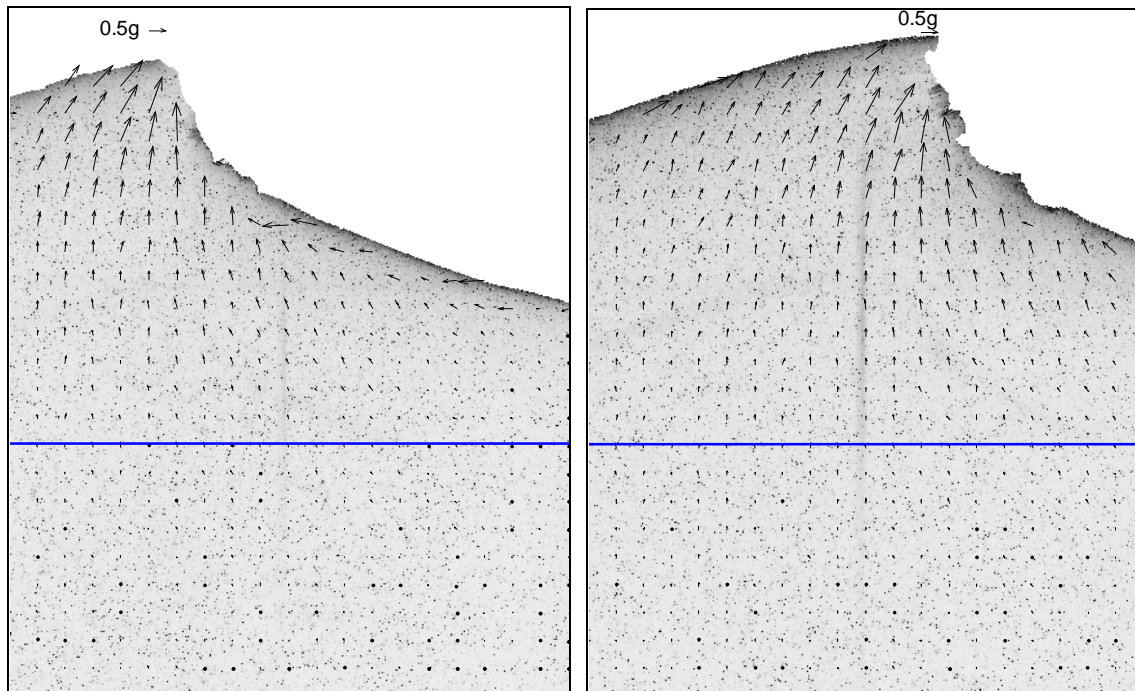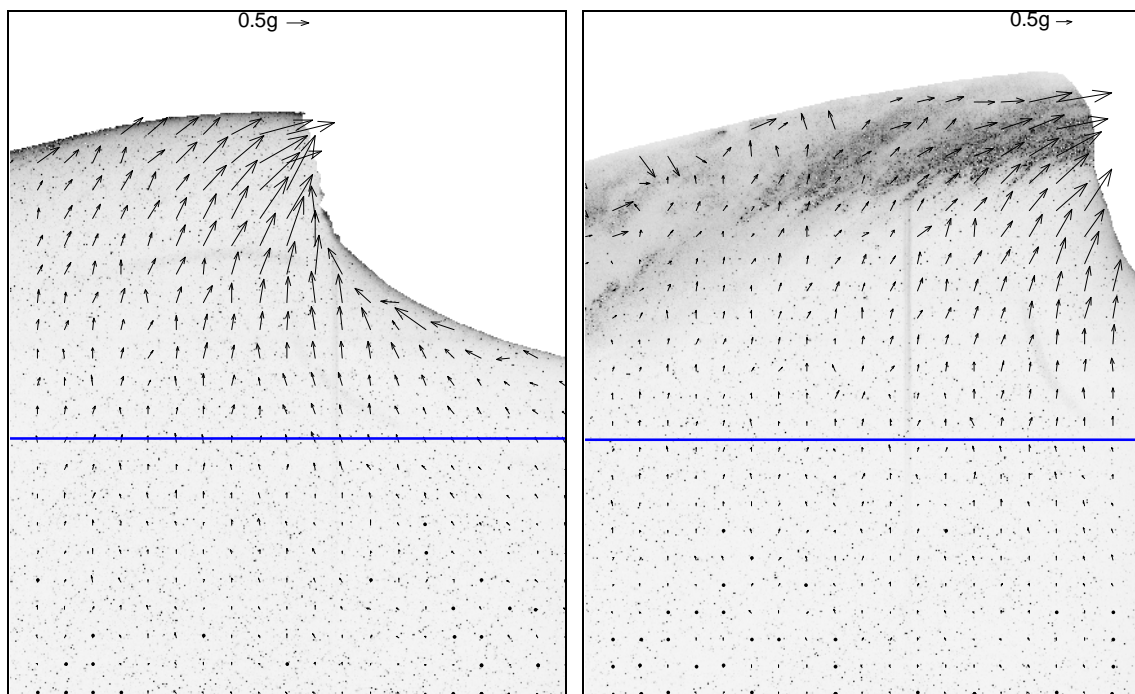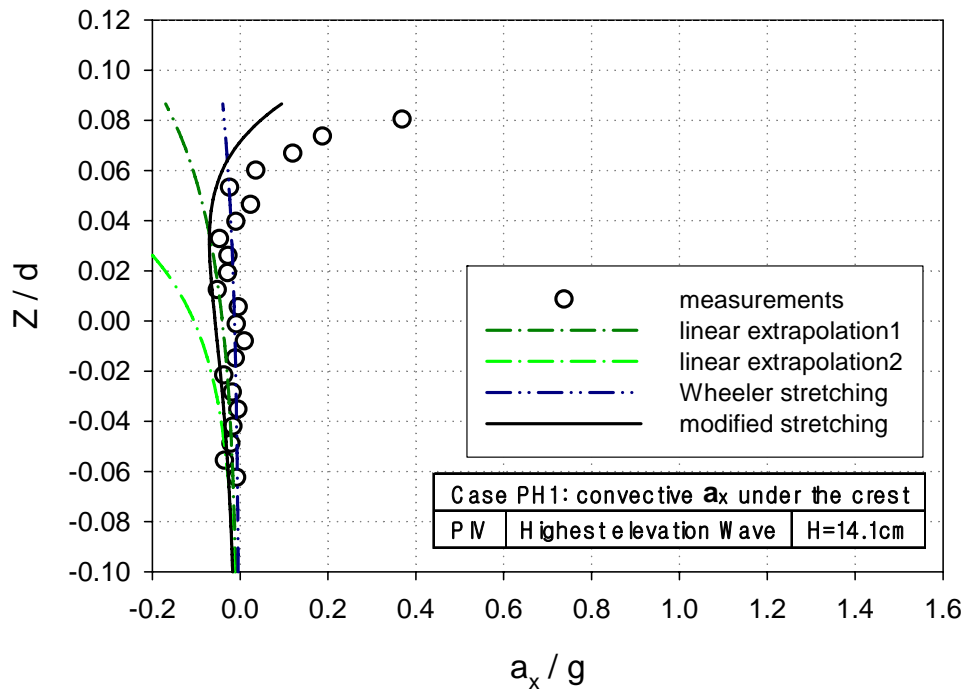
(a) Case PH1.
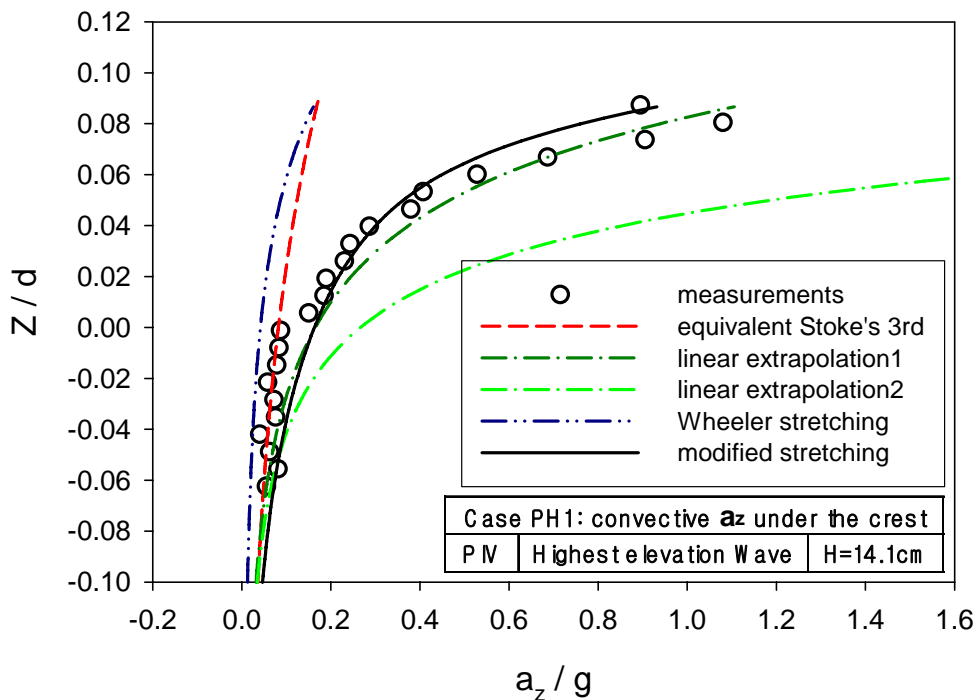
(b) Case PH2.

(c) Case PH3.

(d) Case PH4.

Fig. 6.11 Convective acceleration fields of the maximum wave crest.

Fig. 6.12 (a) shows horizontal convective acceleration from measurement-based computation and three kinematics predictions under the wave crest of Case PH1. All predictions are agreed well with experimental results up to $Z/d= 0.06$. However, the linear extrapolation2 (cutoff frequency= 18.2 rad/s) starts overestimation of the measurements with an opposite sign trend of experimental data at $Z/d= -0.02$. The modified stretching prediction for Case PH1 agrees well with the values of measurement-based computation for horizontal convective, especially above $Z/d= 0.06$ as shown in Fig. 6.12 (a). Magnitude of horizontal convective acceleration for Case PH1 is negligibly small up to $Z/d= 0.06$ but above the $Z/d= 0.06$

Fig. 6.12 (b) shows the vertical convective acceleration from measurement-based computation and four kinematics predictions under the wave crest of Case PH1. All predictions are well agreed with experimental results up to $Z/d= -0.04$. Prediction of the Wheeler stretching and equivalent height wave show similar results and underestimate vertical convective accelerations for Case PH1 above the SWL as shown in Fig. 6.12 (b). It is seen in Fig. 6.12 (b) that linear extrapolation1 (cutoff frequency= 14.04 rad/s) and modified stretching show the very good agreement with experimental results. The linear extrapolation2 overestimates vertical convective accelerations for Case PH1 as seen in Fig. 6.12 (b)

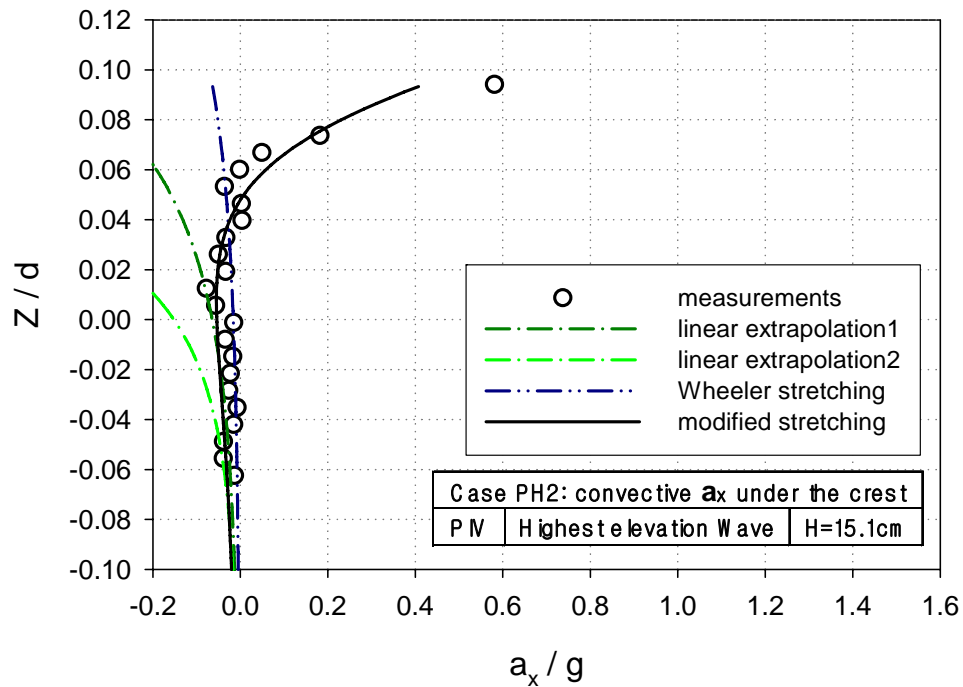(a) Horizontal convective accelerations under the maximum wave crest.

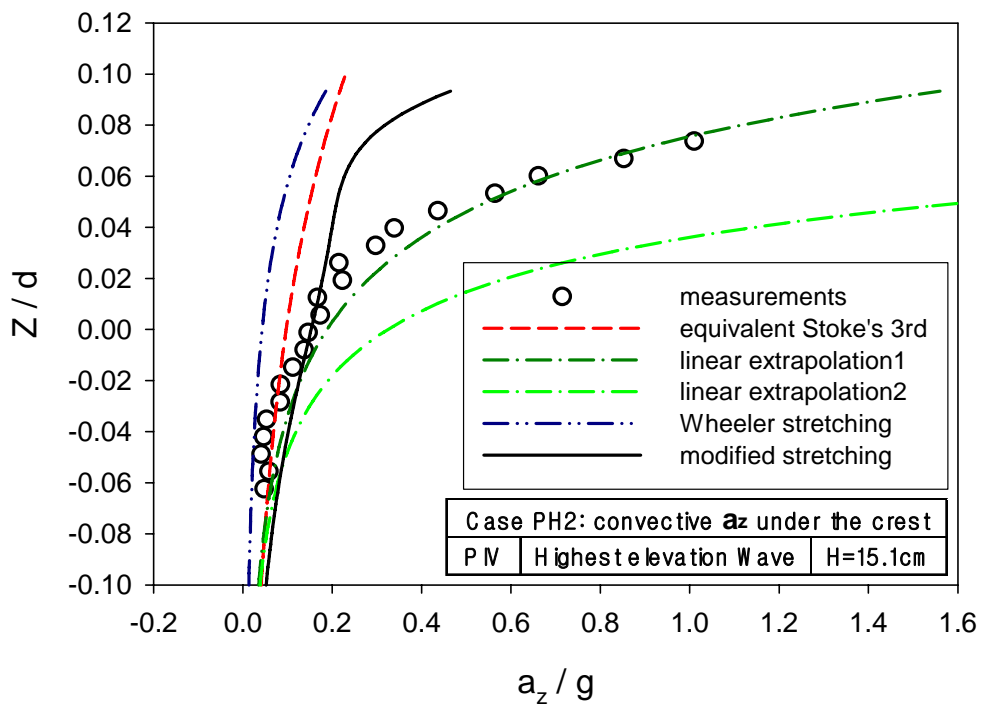(b) Vertical convective accelerations under the maximum wave crest.

Fig. 6.12 Convective accelerations under the maximum wave crest for Case PH1.

Fig. 6.13 (a) presents horizontal convective acceleration from measurement based computation and three kinematics predictions under the wave crest of Case PH2. Predictions of linear extrapolation1, The Wheeler stretching, and the modified stretching are agreed well with experimental results up to $Z/d= 0.02$. However, the linear extrapolation2 overestimates the experimental results. The linear extrapolation and equivalent height wave overpredict oppositely the horizontal convective acceleration from measurement-based computation above $Z/d= 0.02$ and $Z/d= 0.06$, respectively. The modified stretching prediction for Case PH1 shows very good agreement with the values of measurement-based computation for horizontal convective, especially above $Z/d= 0.06$ as shown in Fig. 6.13 (a). Magnitude of horizontal convective acceleration for Case PH2 is negligibly small up to $Z/d= 0.06$ but above $Z/d= 0.06$, like the results of Case PH1.

Fig. 6.13 (b) presents vertical convective acceleration from measurement-based computation and four kinematics predictions under the wave crest of Case PH2. All predictions are well agreed with experimental results up to $Z/d= -0.04$. Prediction of the Wheeler stretching, the equivalent height wave and the modified stretching show the similar results with small discrepancy and underestimate the experimental results for Case PH1 above the SWL as shown in Fig. 6.13 (b). It is seen in Fig. 6.13 (b) that linear extrapolation1 shows good agreement with experimental data. The linear extrapolation2 overestimates them as shown in Fig. 6.13 (b).

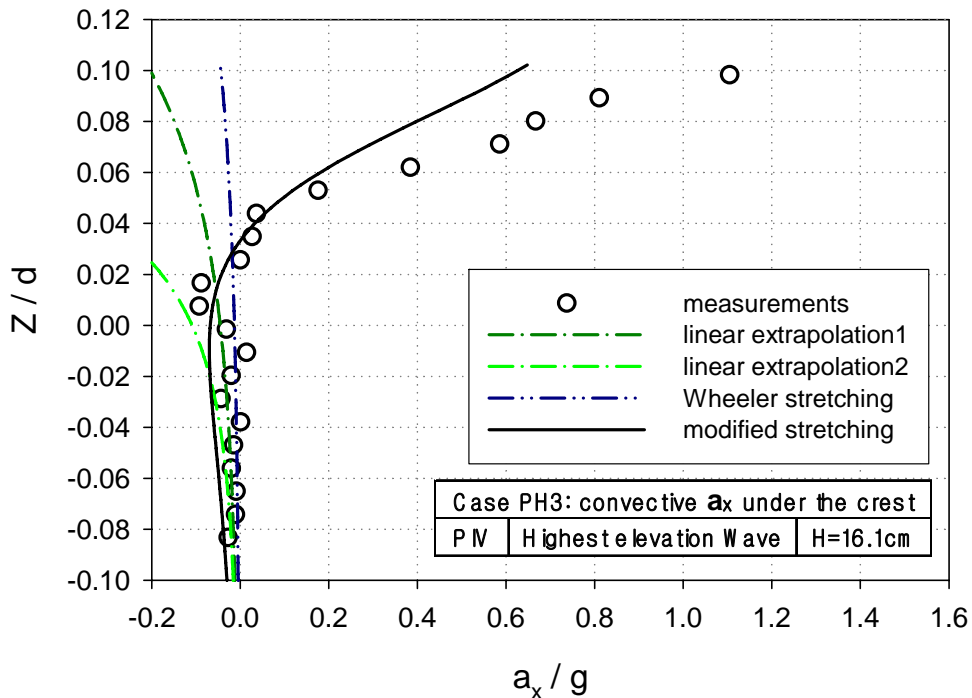(a) Horizontal convective accelerations under the maximum wave crest.

(b) Vertical convective accelerations under the maximum wave crest.
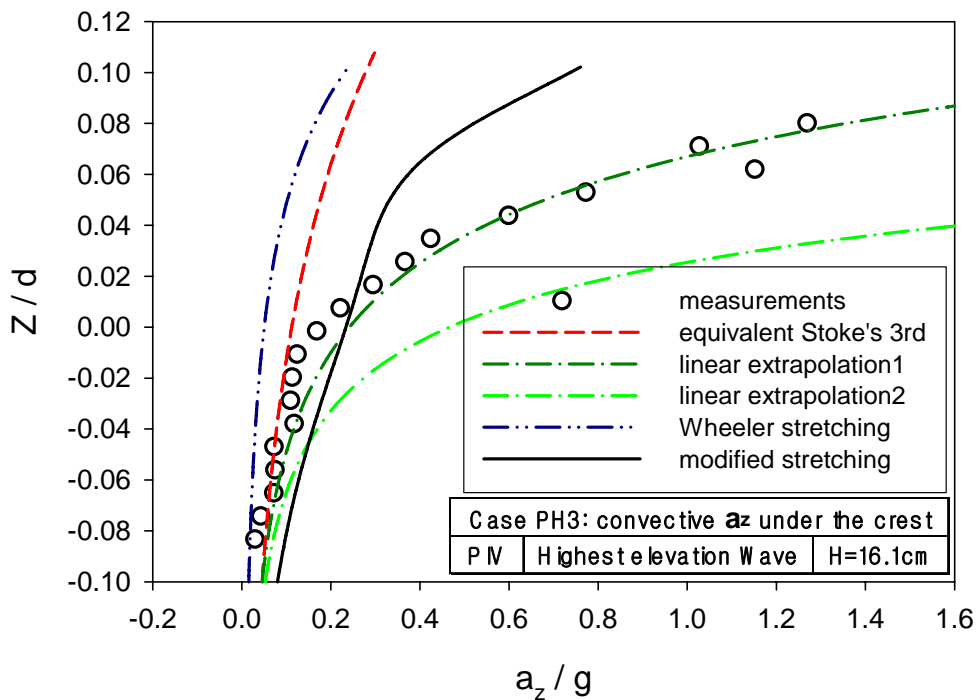
Fig. 6.13 Convective accelerations under the maximum wave crest for Case PH2.

Fig. 6.14 (a) shows horizontal convective acceleration from measurement-based computation and three kinematics predictions under the wave crest of Case PH3. All predictions are agreed well with experimental results up to $Z/d= 0.04$. Predictions of linear extrapolation1, linear extrapolation2, and equivalent height wave overestimate the horizontal convective accelerations from measurement-based computation with opposite sign trend of experimental data at $Z/d= 0.02$. Modified stretching prediction for Case PH1 shows good agreement with the results from measurement-based computation as shown in Fig. 6.14 (a). Magnitude of horizontal convective acceleration for Case PH3 is negligibly small up to $Z/d= 0.04$ but the magnitude is very considerable above $Z/d= 0.04$.

Fig. 6.14 (b) shows vertical convective accelerations from measurement-based computation and four kinematics predictions under the wave crest of Case PH3. Most predictions agreed well with experimental results up to the SWL. Prediction of the Wheeler stretching, equivalent height wave and modified stretching are underestimated for Case PH3 above the SWL as shown in Fig. 6.14 (b). However, trend of the modified stretching prediction is similar to experimental results. It is seen in Fig. 6.14 (b) that linear extrapolation1 shows very good agreement with experimental results. The linear extrapolation2 overestimates vertical convective accelerations for Case PH3 as seen in Fig. 6.14 (b)

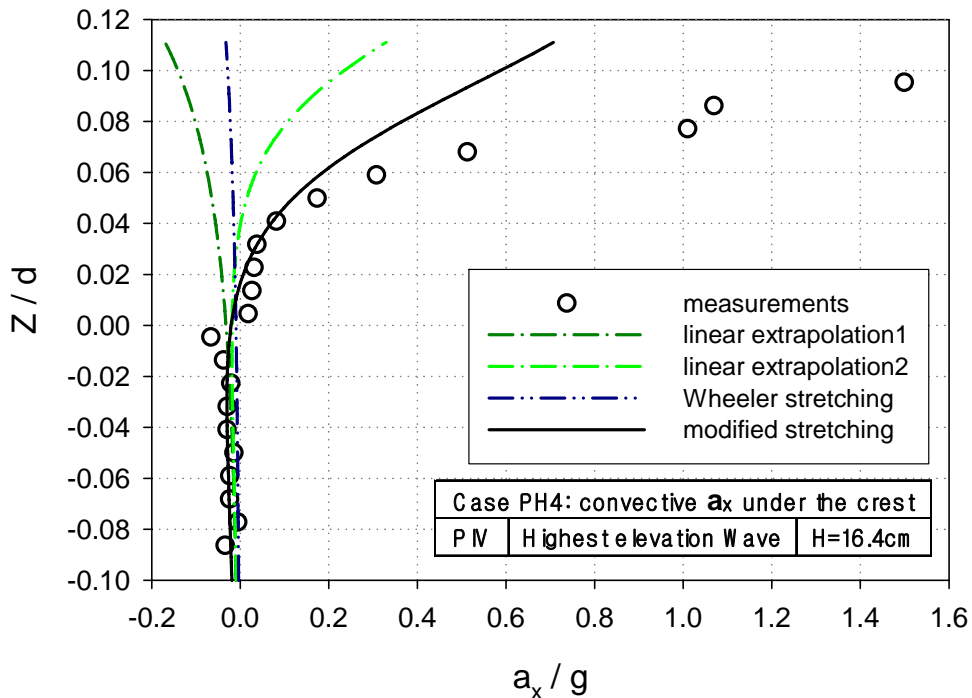(a) Horizontal convective accelerations under the rogue wave crest.

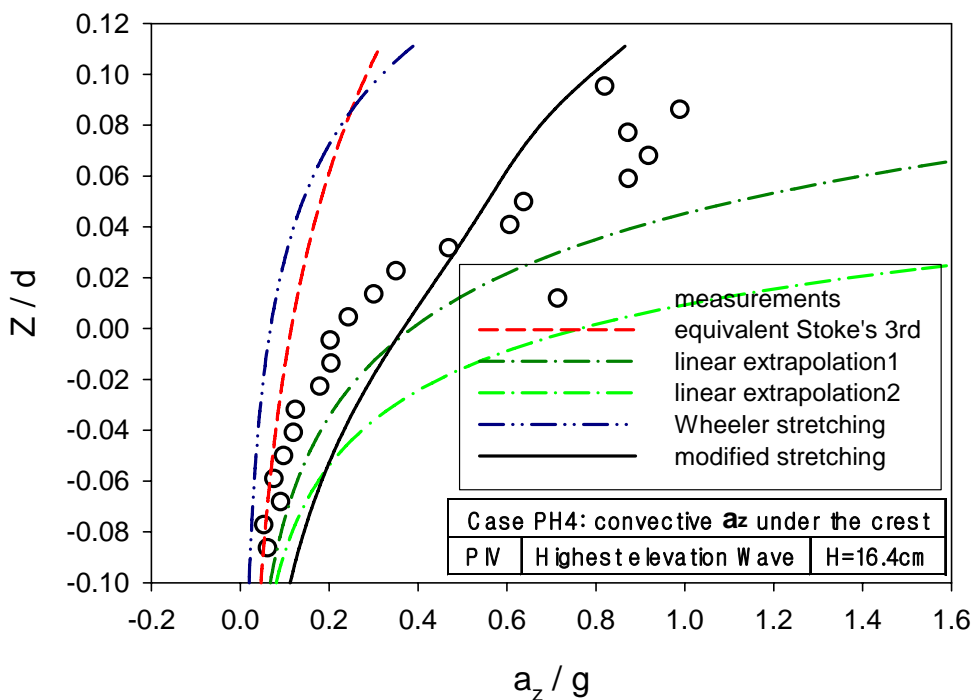(b) Vertical convective accelerations under the rogue wave crest.

Fig. 6.14 Convective accelerations under the rogue wave crest for Case PH3.

Fig. 6.15 (a) presents horizontal convective accelerations from measurement-based computation and three kinematics predictions under the wave crest of Case PH4. All predictions are agreed very well with computation based on measurement up to Z/d= 0.02 as shown in Fig. 15 (a). Predictions of linear extrapolation1, linear extrapolation2, and the Wheeler stretching are underestimated above Z/d= 0.02. It is also seen in Fig. 6.15 (a) that the modified stretching are agreed pretty well with experimental results. Magnitude of horizontal convective acceleration for Case PH2 is negligibly small up to Z/d= 0.03 but the magnitude is very rapidly increased above Z/d= 0.03.

Fig. 6.15 (b) presents vertical convective acceleration from measurement-based computation and four kinematics predictions under the wave crest of Case PH4. Prediction of the Wheeler stretching and equivalent height wave show the similar results and underestimate the experimental results for Case PH4 as shown in Fig. 6.15 (b). It is seen in Fig. 6.15 (b) that linear extrapolation1 and linear extrapolation2 overestimates the experimental results. The modified stretching generally shows the good agreement with experimental data. Magnitude of vertical convective acceleration has similar value of horizontal convective acceleration above Z/d= 0.06 as shown in Fig. 6.15 (b).

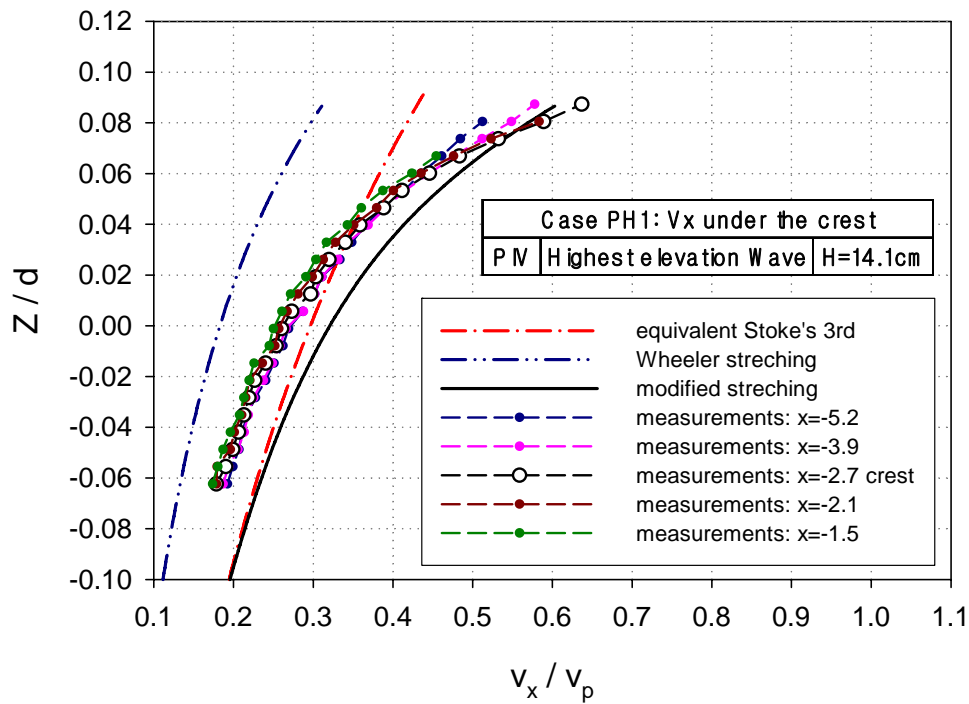(a) Horizontal convective accelerations under the rogue wave crest.

(b) Vertical convective accelerations under the rogue wave crest.

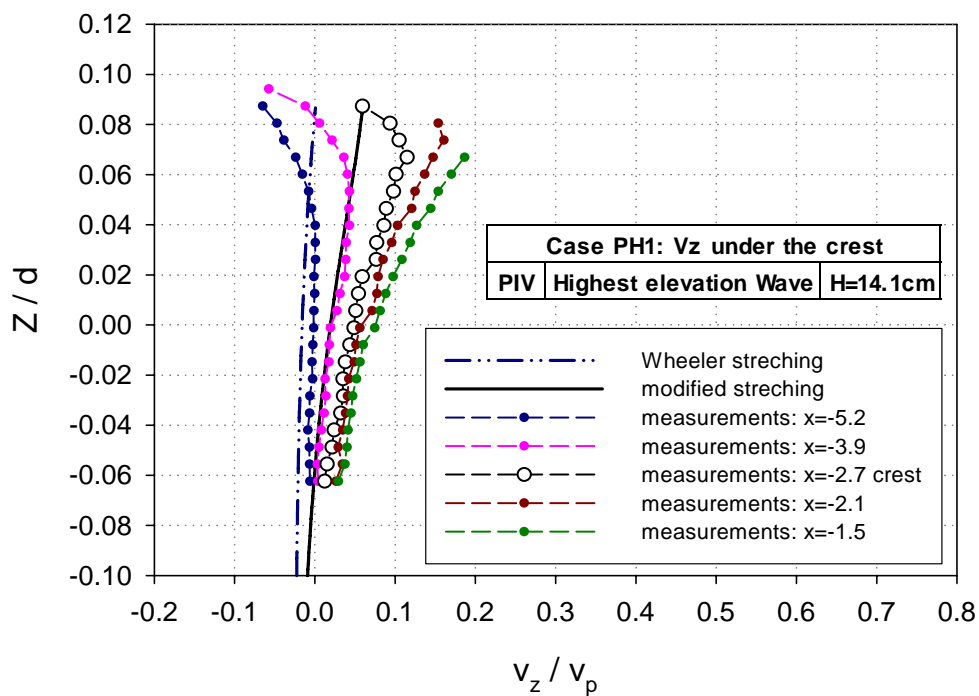Fig. 6.15 Convective accelerations under the rogue wave crest for Case PH4.

6.4 Kinematics fields near the rogue wave crest

Kinematics of rogue wave which includes two components, horizontal and vertical, of velocities, local accelerations and convective accelerations for the maximum wave of Case PH1, Case PH2, Case PH3 and Case PH4. All four cases have been examined at five horizontal locations near the maximum wave crest. The maximum wave crest is defined as the highest elevation of maximum wave in the irregular wave train. After investigating regular wave kinematics, the maximum magnitude of horizontal water particle velocities or vertical water particle accelerations was at the wave crest. However, it is found in the rogue wave kinematics that the maximum magnitude of the horizontal water particle velocities or of vertical water particle accelerations is not in the wave crest of highly nonlinear wave. Through examination of the maximum wave kinematics at a series of horizontal measuring positions, different phenomenon with regular wave kinematics could be found in the rogue wave kinematics. And then, it is possible to have knowledge about mechanism of developing rogue waves.

Fig. 6.16 (a), (b), (c), (d), (e) and (f) show the maximum wave kinematics under five different horizontal locations for Case PH1. It is known as examined in the figures that the crest kinematics are shown as to be shifted to left hand side because the blue dotted line (at x=-2.1 cm) presents the characteristics of regular wave kinematics. The maximum value of horizontal velocities is at the wave crest as shown in Fig. 6.16 (a). It is found through figures of Fig. 6.16 that the maximum horizontal accelerations are not at the wave crest but 1.2 cm (green dotted line) away to right hand side from the wave crest.
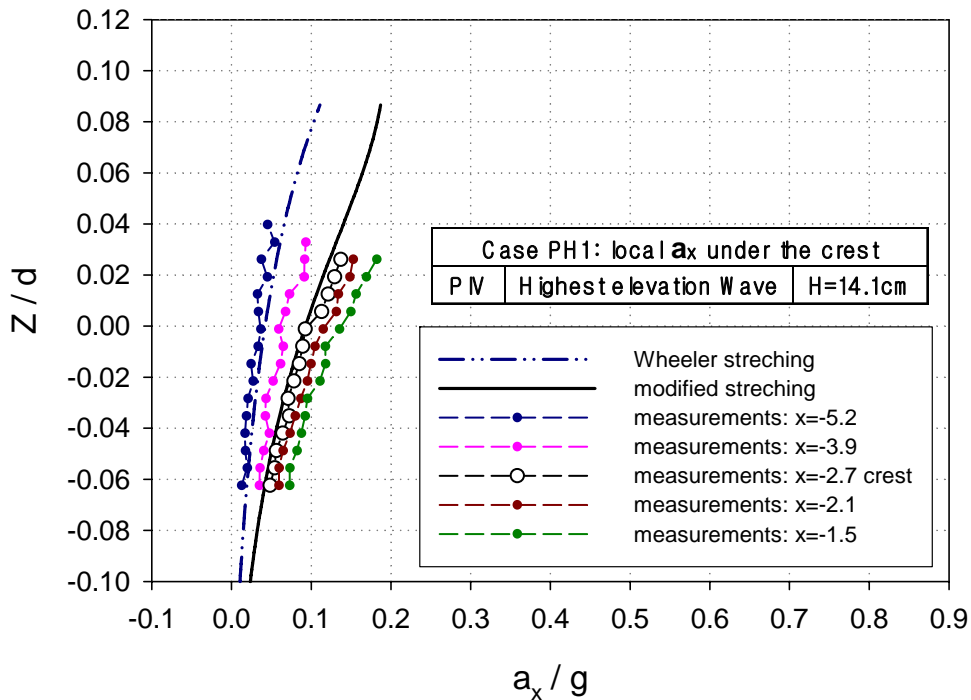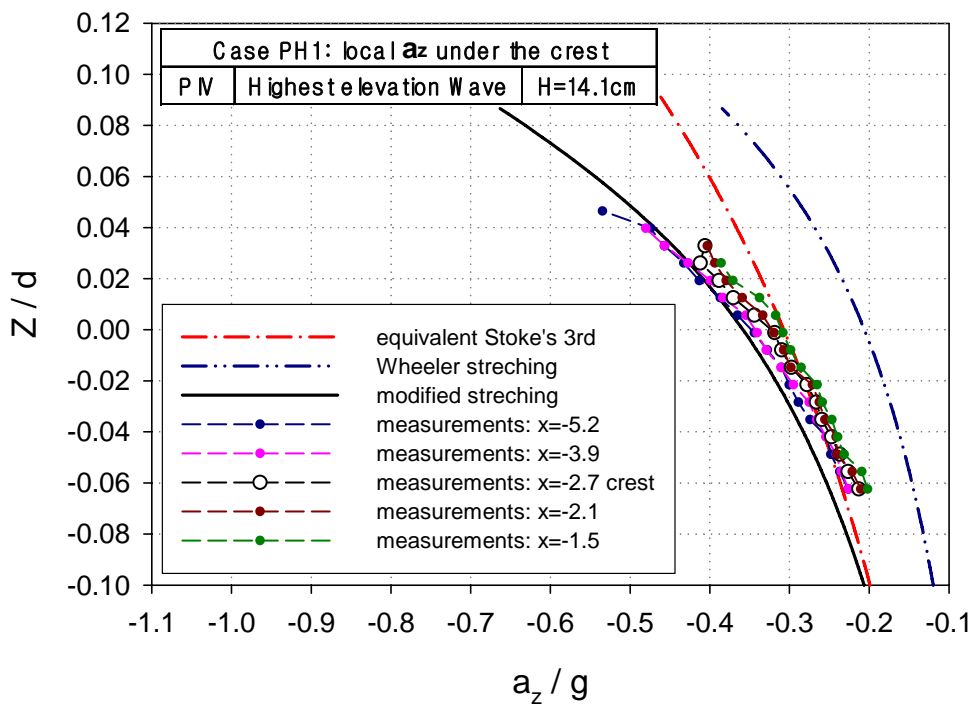
(a) Horizontal velocities.

(b) Vertical velocities.

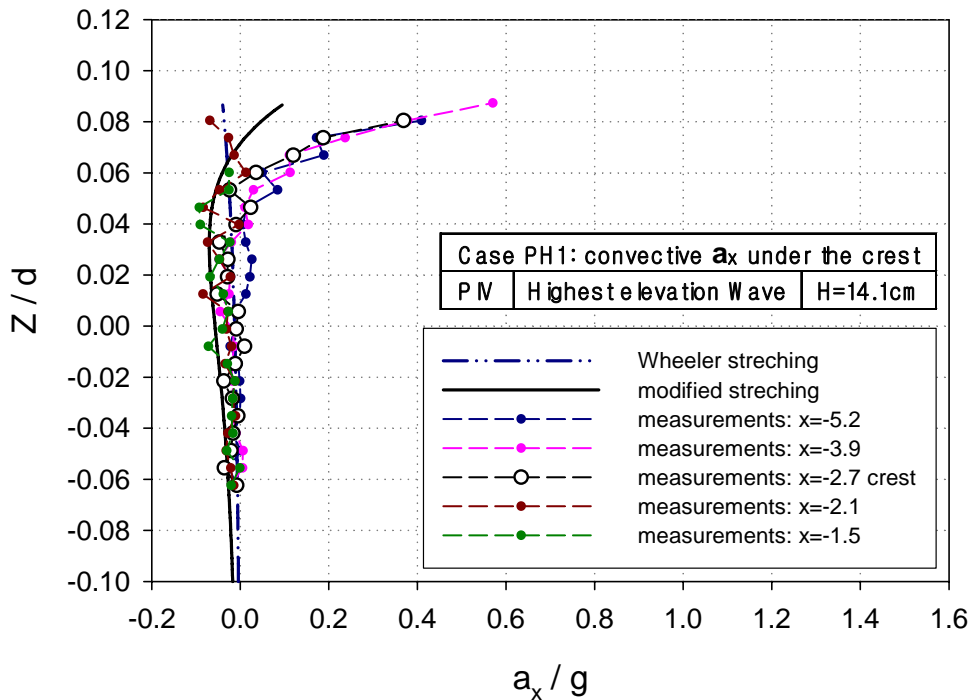Fig. 6.16 Kinematics near the maximum wave crest for Case PH1.

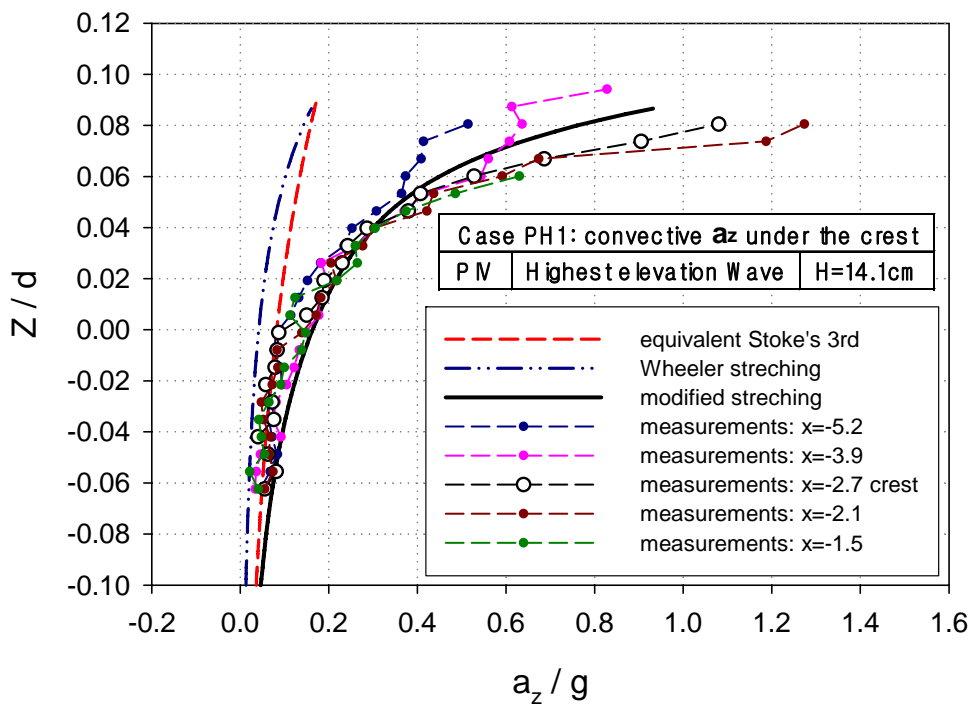(c) Horizontal local accelerations.

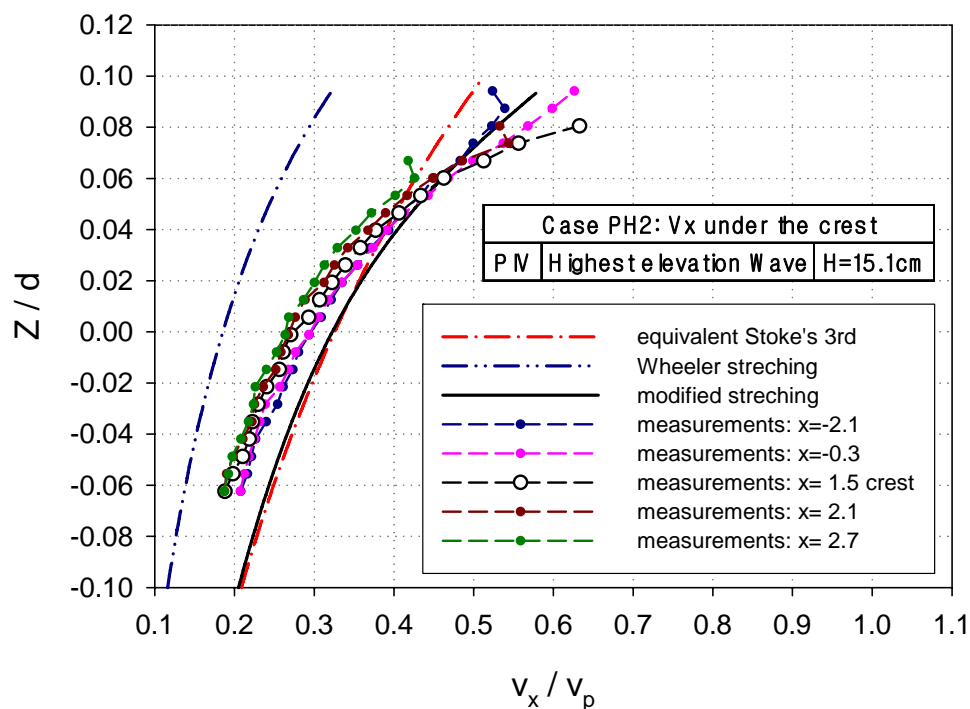(d) Vertical local accelerations.

Fig. 6.16 Continued.

(e) Horizontal convective accelerations.
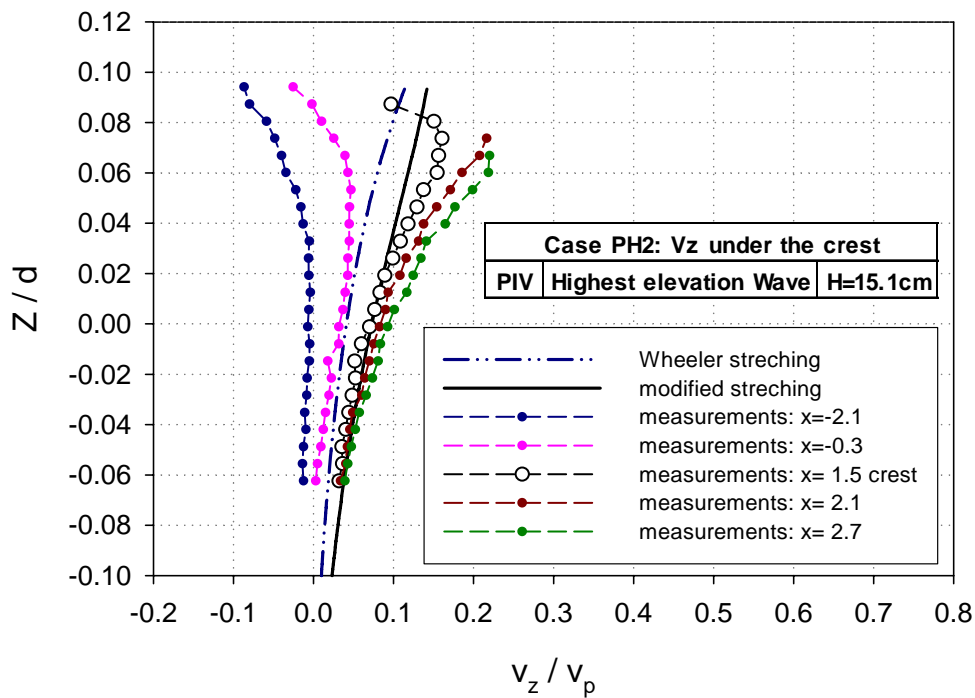

(f) Vertical convective accelerations.

Fig. 6.16 Continued.

Fig. 6.17 (a), (b), (c), (d), (e) and (f) show the maximum wave kinematics in the irregular wave train under five different horizontal locations for Case PH2. It is known as examined in the figures that the crest kinematics are like shifted to left hand side, because blue dotted line (at x=-2.3 cm) presents the characteristics of regular wave kinematics. The maximum value of horizontal velocities is at the wave crest as shown in Fig. 6.17 (a). It is found in Fig. 6.17 that the maximum horizontal accelerations are not at the wave crest but 1.2 cm (green dotted line) away to right hand side from the wave crest. It is also found that the modified stretching method predicts values of measured wave kinematics as shown in Fig. 6.16 and Fig. 6.17.

(a) Horizontal velocities.

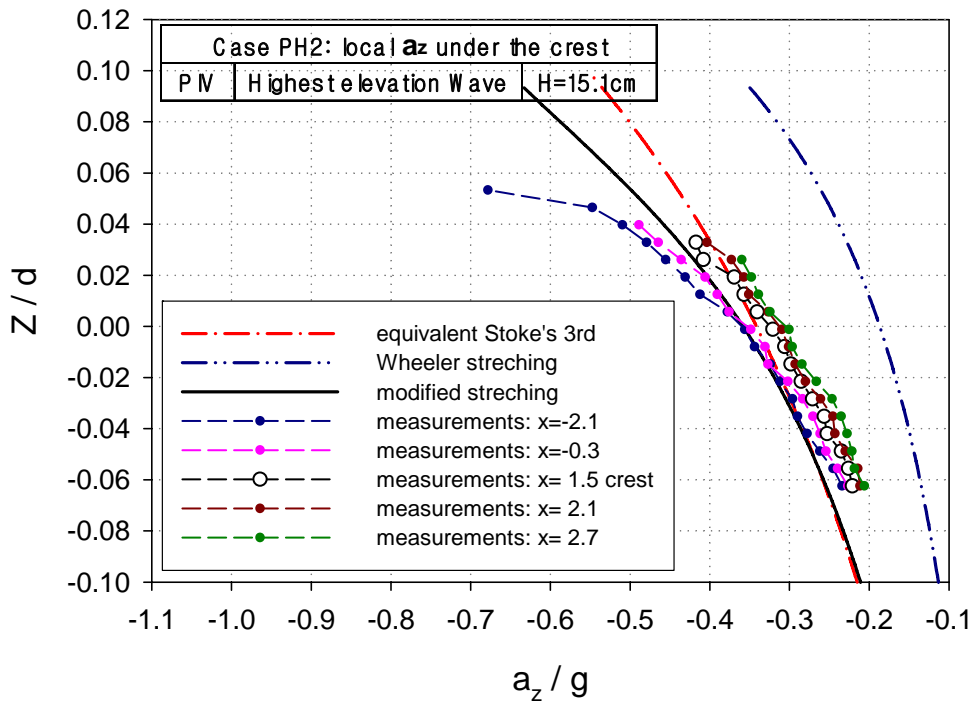Fig. 6.17 Kinematics near the maximum wave crest for Case PH2.
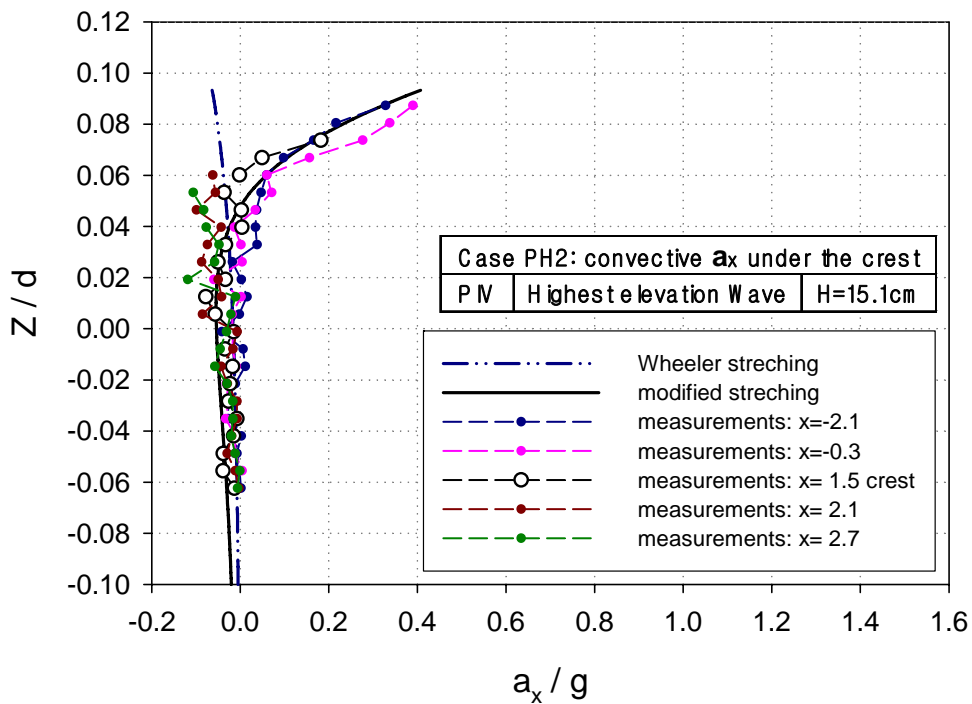
(b) Vertical velocities.
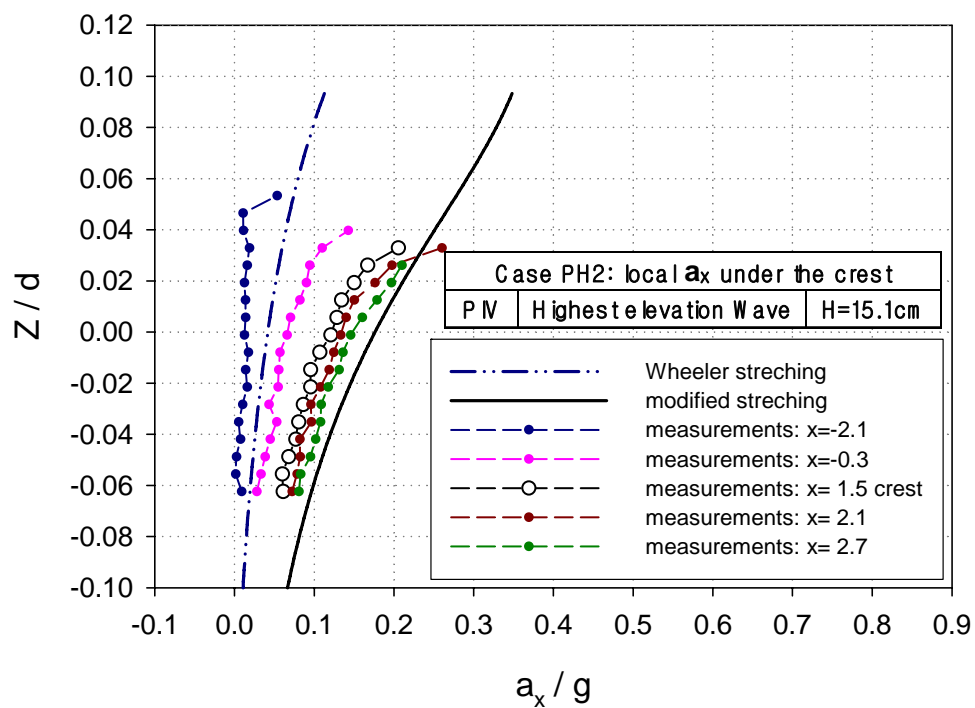
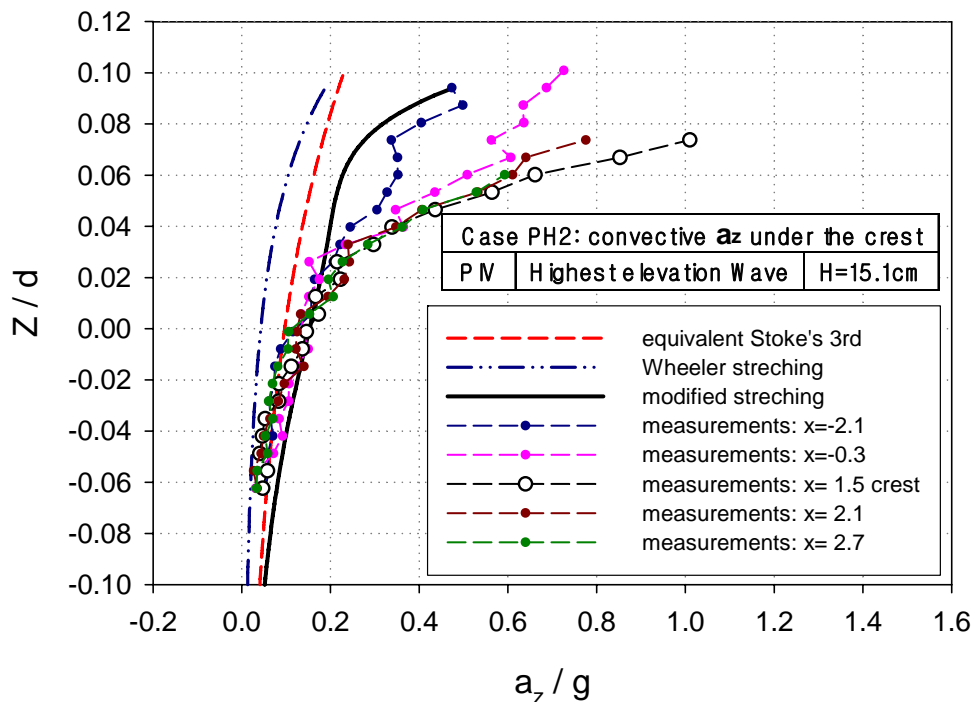(c) Horizontal local accelerations.

Fig. 6.17 Continued.

(d) Vertical local accelerations.

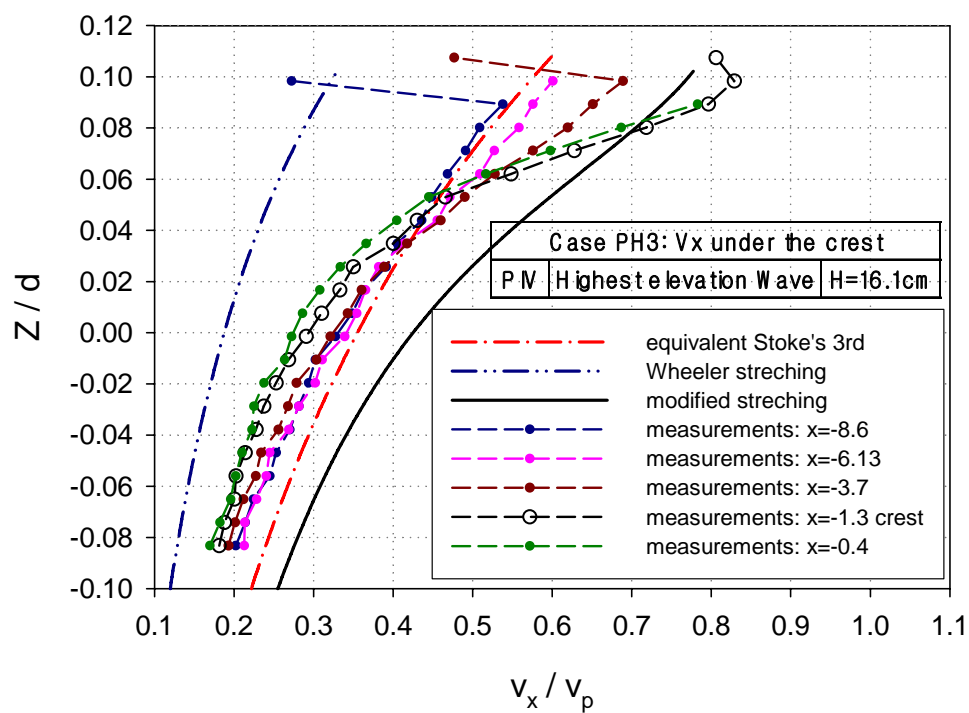(e) Horizontal convective accelerations.

Fig. 6.17 Continued.

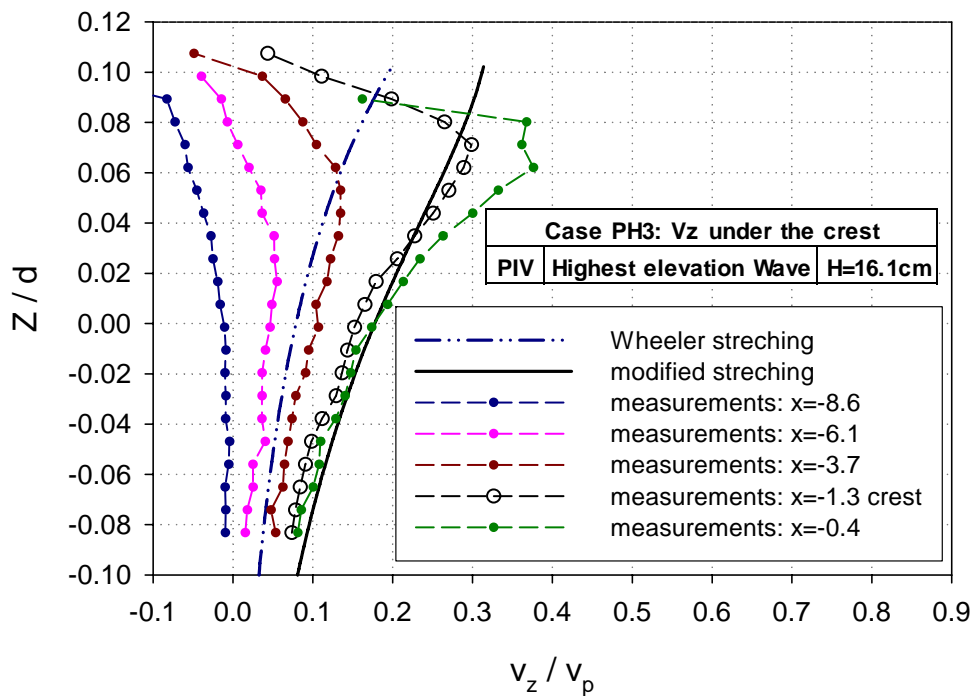(f) Vertical convective accelerations.

Fig. 6.17 Continued.

Fig. 6.18 (a), (b), (c), (d), (e) and (f) show the maximum wave kinematics which includes velocities, local accelerations, and convective accelerations under five different horizontal measuring locations for Case PH3. It is known as examined in the figures that the crest kinematics are shifted to left hand side because blue dotted line (at x= -8.6 cm) presents the characteristics of regular wave kinematics. The maximum value of horizontal velocities is at the wave crest as shown in Fig. 6.18 (a). It is found in Fig. 6.18 that the maximum horizontal accelerations are not at the wave crest but 1.7 cm (green dotted line) away to right hand side from the wave crest. There no local acceleration near the free surface because relatively long time step Δt. The wave elevation at the rogue wave crest

is changed rapidly. Therefore, no data for applying centered finite difference method is available. Magnitude of difference between horizontal and vertical convective accelerations looks same. However, differences between horizontal and vertical for velocities and local accelerations are considerable.
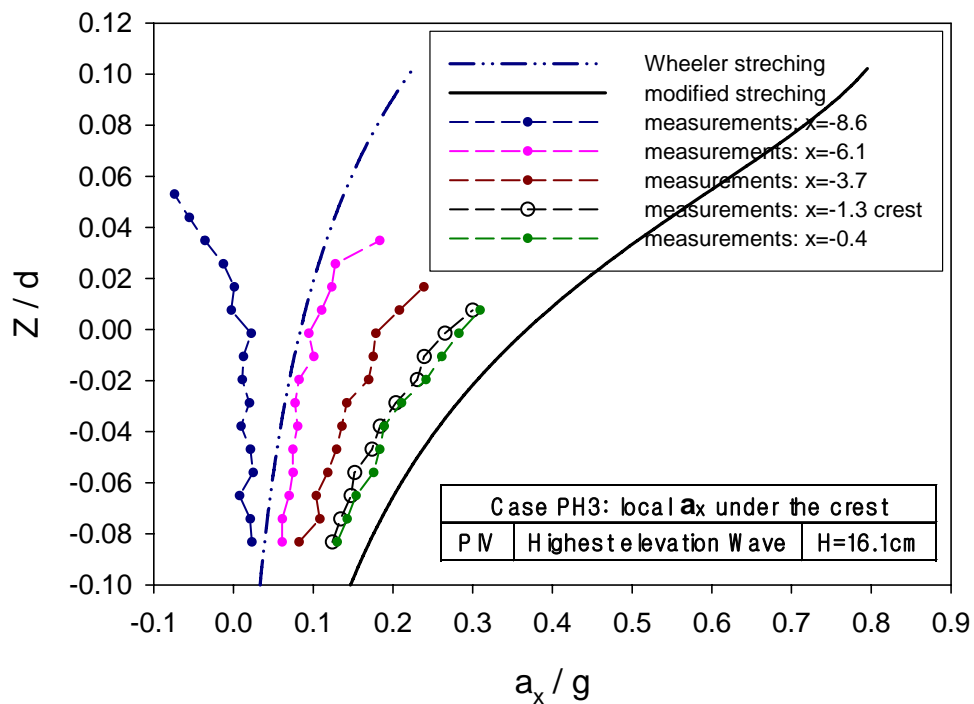

(a) Horizontal velocities.

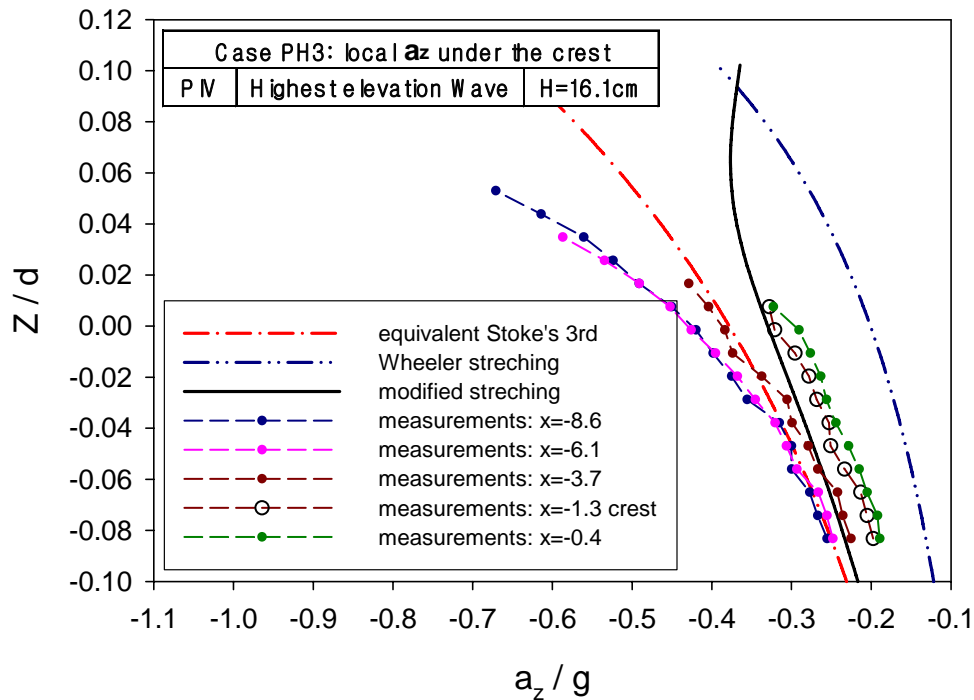Fig. 6.18 Kinematics near the maximum wave crest for Case PH3.
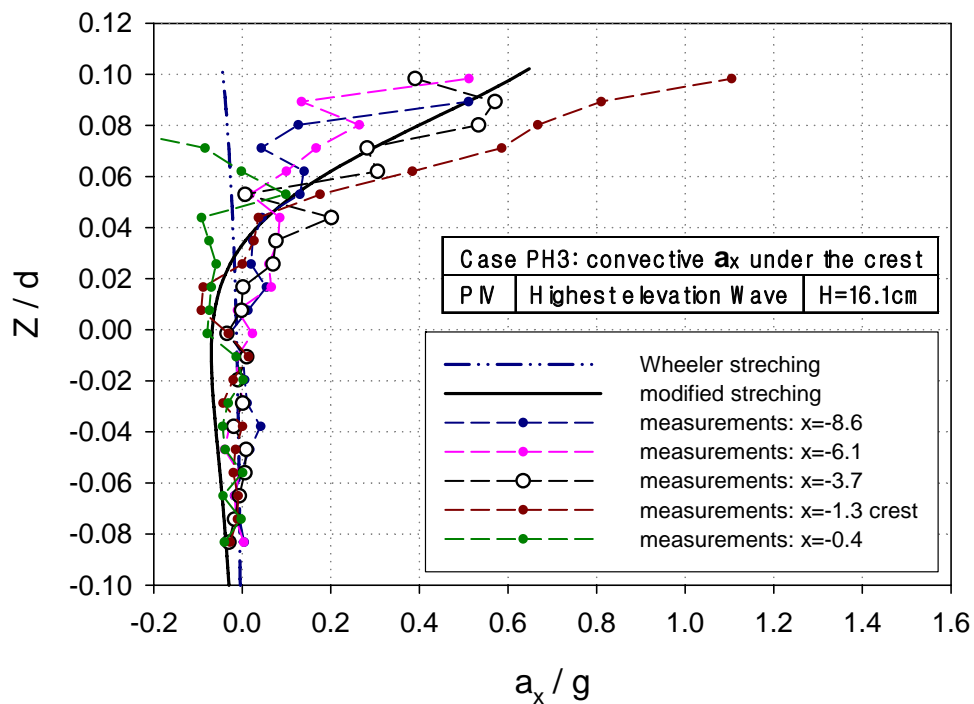
(b) Vertical velocities.

(c) Horizontal local accelerations.
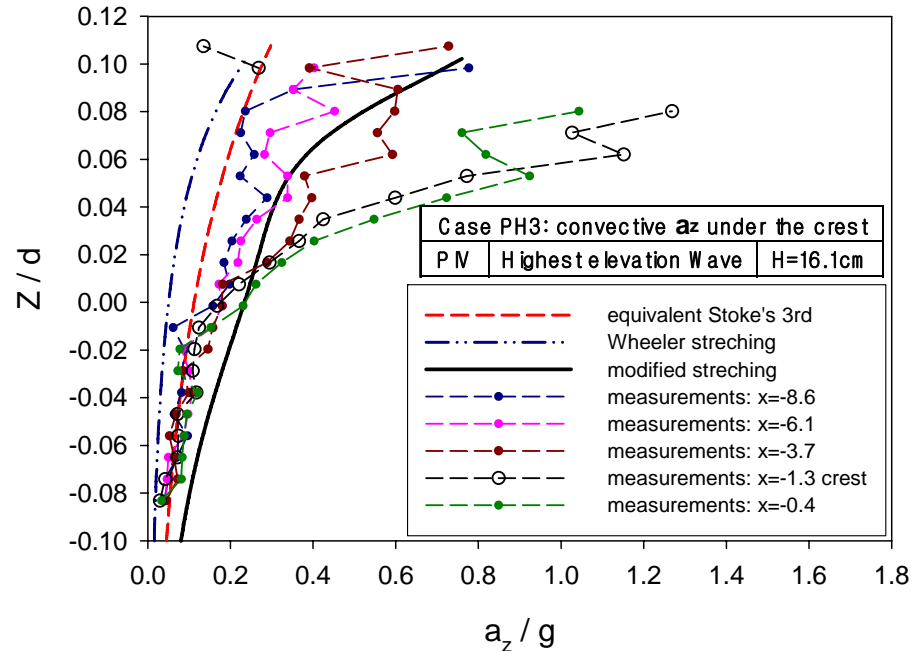
Fig. 6.18 Continued.

(d) Vertical local accelerations.

(e) Horizontal convective accelerations.
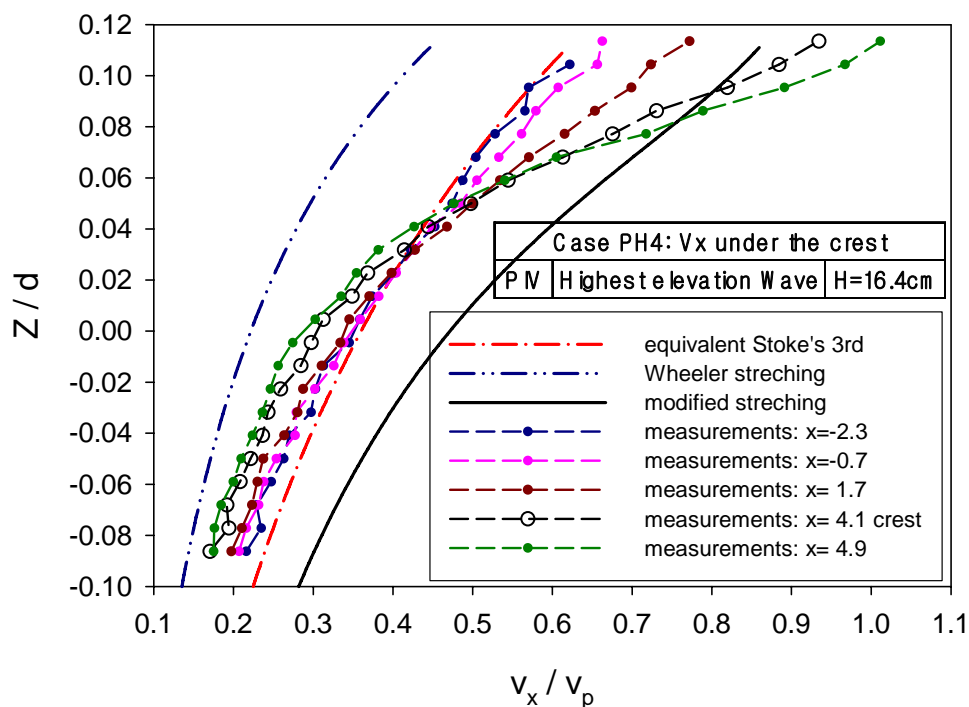
Fig. 6.18 Continued.

(f) Vertical convective accelerations.

Fig. 6.18 Continued.

Fig. 6.19 (a), (b), (c), (d), (e) and (f) show the maximum wave kinematics in the irregular wave train under the five different horizontal locations for Case PH4. It is known as examined in figures that the crest kinematics are shifted to left hand side because blue dotted line (at x=-2.3 cm) presents the characteristics of regular wave kinematics. The maximum value of horizontal velocities occurs at the wave crest as shown in Fig. 6.19 (a). It is found in Fig. 6.19 that the maximum horizontal accelerations are not at the wave crest but 0.8 cm (green dotted line) away to right hand side from the wave crest. It is also found that the modified stretching method predicts the maximum values of measured wave kinematics as shown in Fig. 6.18 and Fig. 6.19. The modified stretching method predicts maximum values of wave kinematics well. The modified stretching method has been

developed to predict maximum values of highly nonlinear wave kinematics near the free surface.

As we examined the rogue wave kinematics, which are Case PH1 and Case PH2 through the series of horizontal measuring locations, the convective term of total acceleration is mainly shown two different phenomena with regular wave kinematics. First, magnitudes of horizontal and vertical convective terms are almost same. Second, values of convective acceleration above the SWL increased rapidly as shown in Fig. 6.18 and Fig. 6.19. For the Case PH1 and Case PH2, rapid increasing values of convective acceleration are found above the $Z/d= 0.04$ as shown in Fig. 6.16 and Fig. 6.17, respectively.
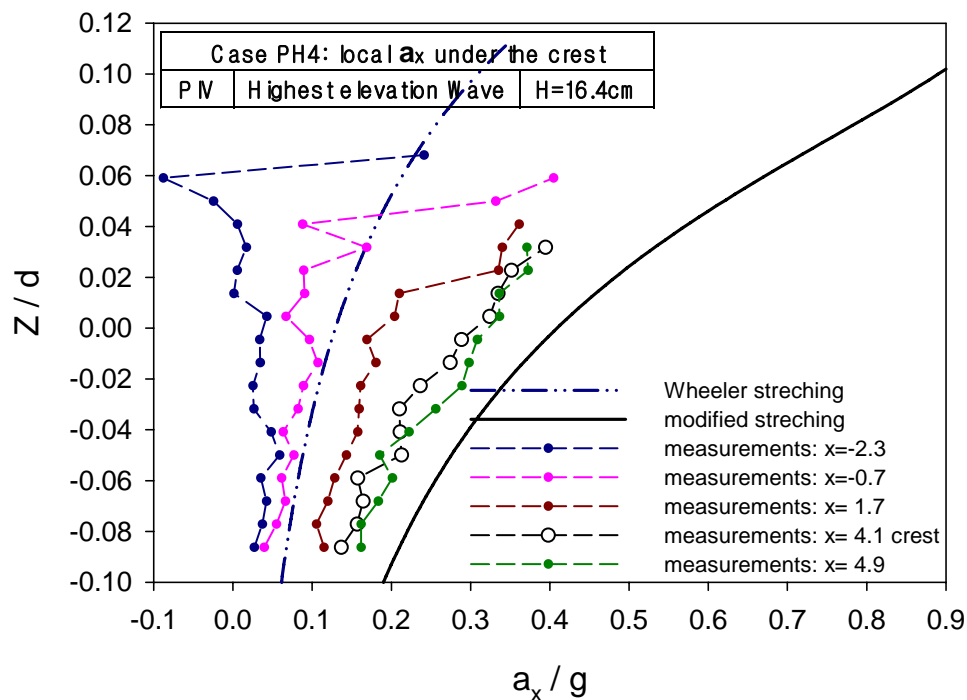

(a) Horizontal velocities.

Fig. 6.19 Kinematics near the maximum wave crest for Case PH4.
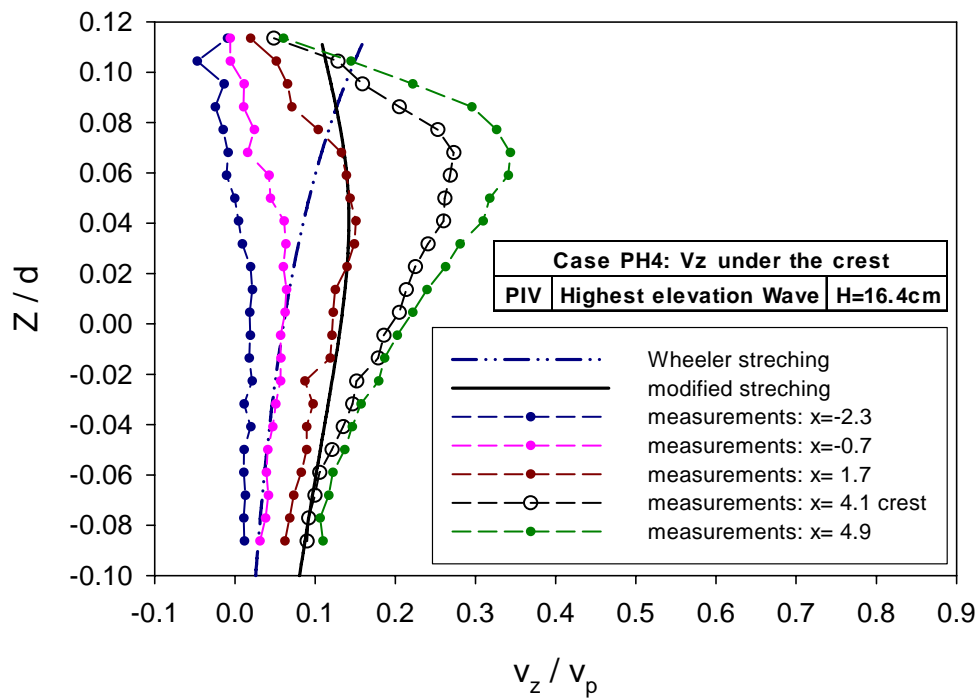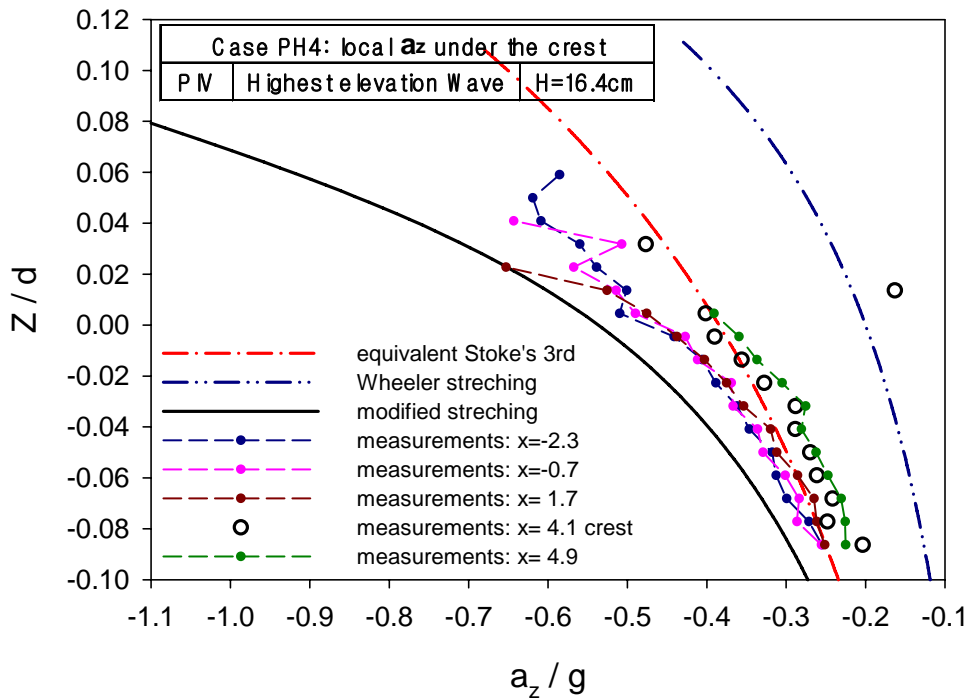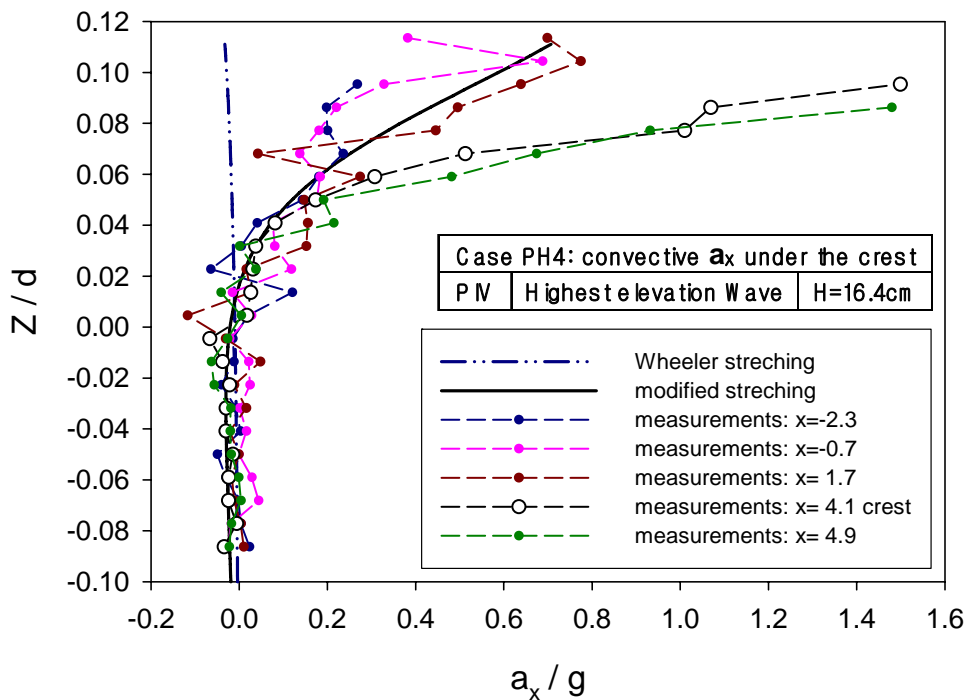
(b) Vertical velocities.

(c) Horizontal local accelerations.
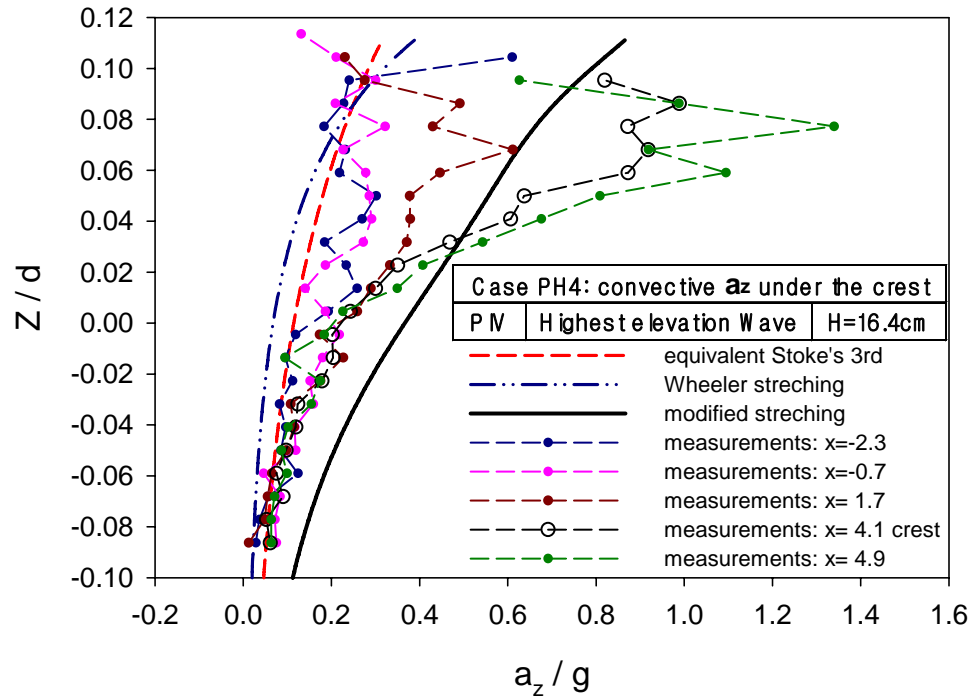
Fig. 6.19 Continued.

(d) Vertical local accelerations.

(e) Horizontal convective accelerations.

Fig. 6.19 Continued.

(f) Vertical convective accelerations.

Fig. 6.19 Continued.

6.5 Horizontal wave forces on slender truncated cylinder in the rogue waves

The maximum horizontal forces on a slender vertical truncated cylinder in irregular waves were computed by applying measurements of velocities and accelerations to the Morison equation. The kinematics calculated from the third-order Stokes wave theory by using the equivalent wave height were also applied to the Morison equation for calculating wave forces on a slender vertical truncated cylinder in irregular waves and compared with wave forces of computations based measurement. Three prediction methods are used for calculating horizontal wave forces on a vertical truncated cylinder and compared with computation based on measurement. These are the linear extrapolation, the Wheeler

stretching, and the modified stretching method. As used in Chapter V, horizontal forces of irregular wave also normalized as followings; i.e., horizontal force F_x is normalized by $\rho g D^3$ and wave height H is normalized by wave length L. Local acceleration and convective acceleration are used for acceleration of inertia force term in the Morison equation.

Two drafts for a truncated cylinder are applied to the Morison equation to compute the horizontal wave force. Kim and Zou (1997) and Kim and Kim (2003a) measured the horizontal wave force on a vertical truncated cylinder with draft of 30 cm. The wave kinematics measured using PIV in this study is for draft of 6 cm and 8 cm. To verify magnitude of wave force, 30 cm draft is applied to the Morison equation. Missing data of local acceleration and under draft of -6 cm is calculated using the linear extrapolation method. The horizontal wave forces were also computed by applying only kinematics from measurement-based computation (= 6 cm draft) to the Morison equation.

Fig. 6.20 (a), (b), (c), and (d) shows wave horizontal forces on a vertical truncated cylinder near the wave crest for Case PH1, Case PH2, Case PH3, and Case PH4, respectively. These horizontal forces were computed with measured velocities of waves and the force components are represented. The summation of all horizontal force components is largest in the wave crest for all cases as shown in Fig. 6.20. The convective term of inertia force of Case PH1 and Case PH2 is negligibly small, but those of Case PH3 and Case PH4 which is rogue wave cases is noticeably observed as seen in Fig. 6.20 (c) and (d). The values of the horizontal wave force are presented without normalization in Fig. 6.20.
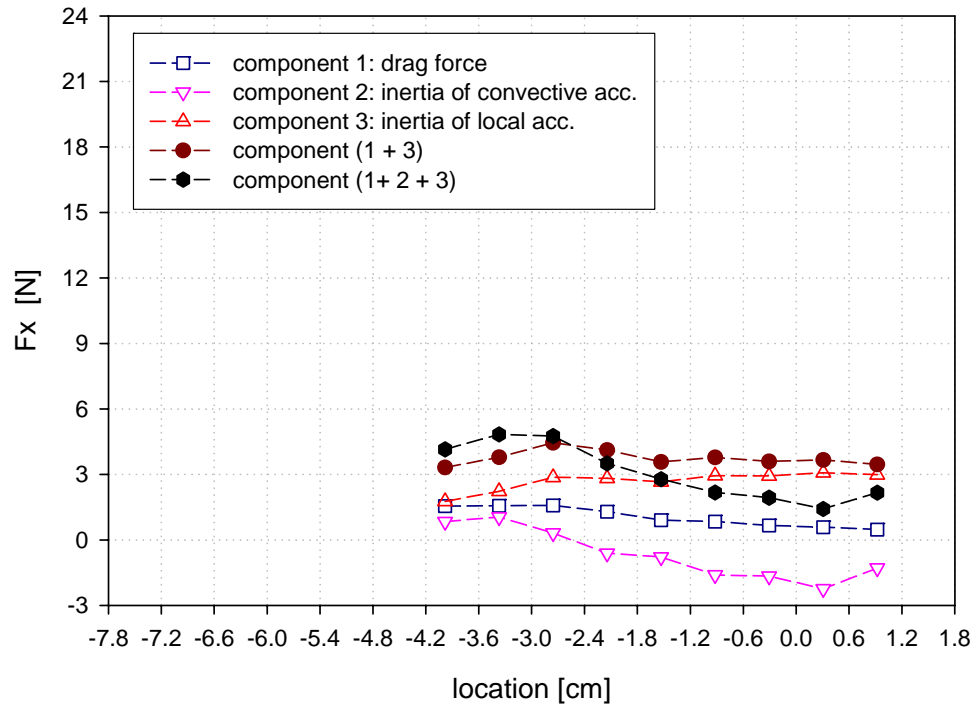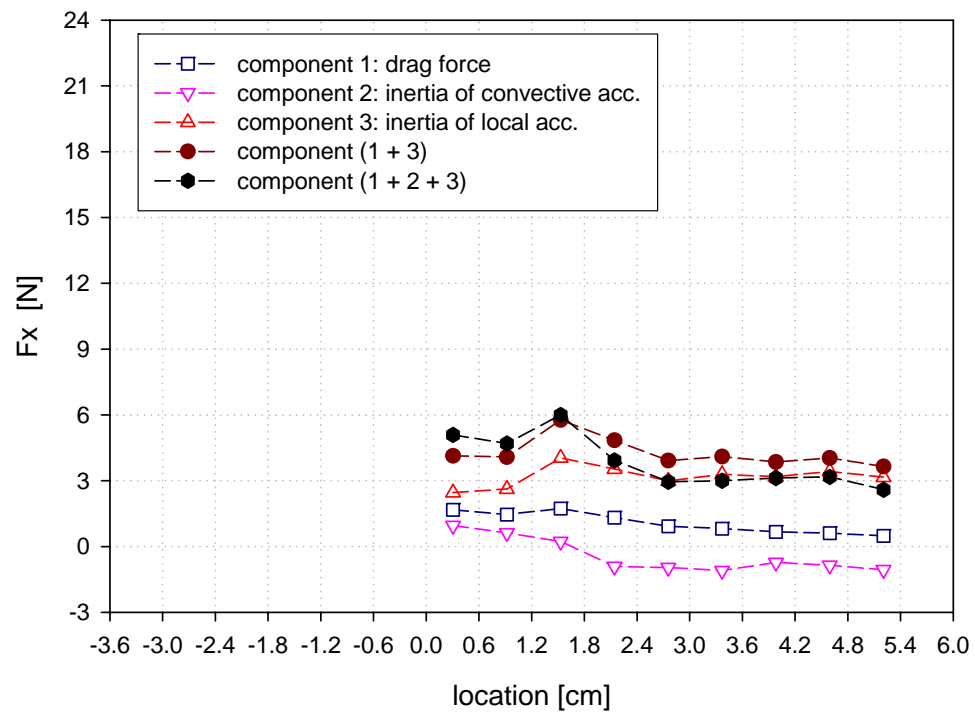
(a) Case PH1 (Crest at x = -2.7cm).

(b) Case PH2 (Crest at x = 1.5cm).

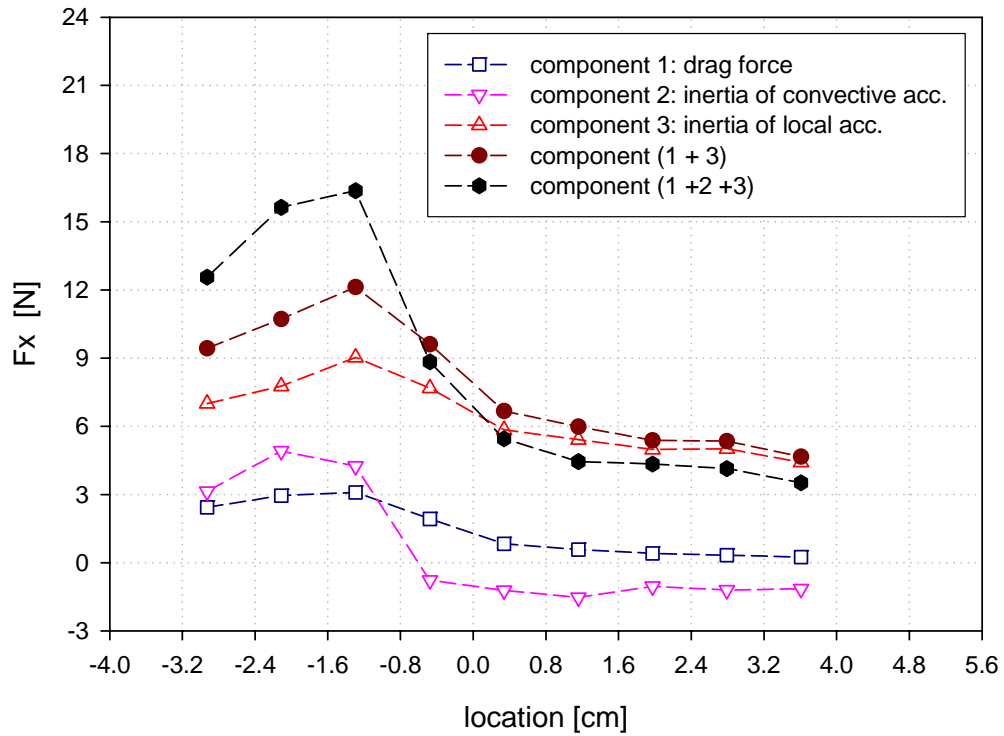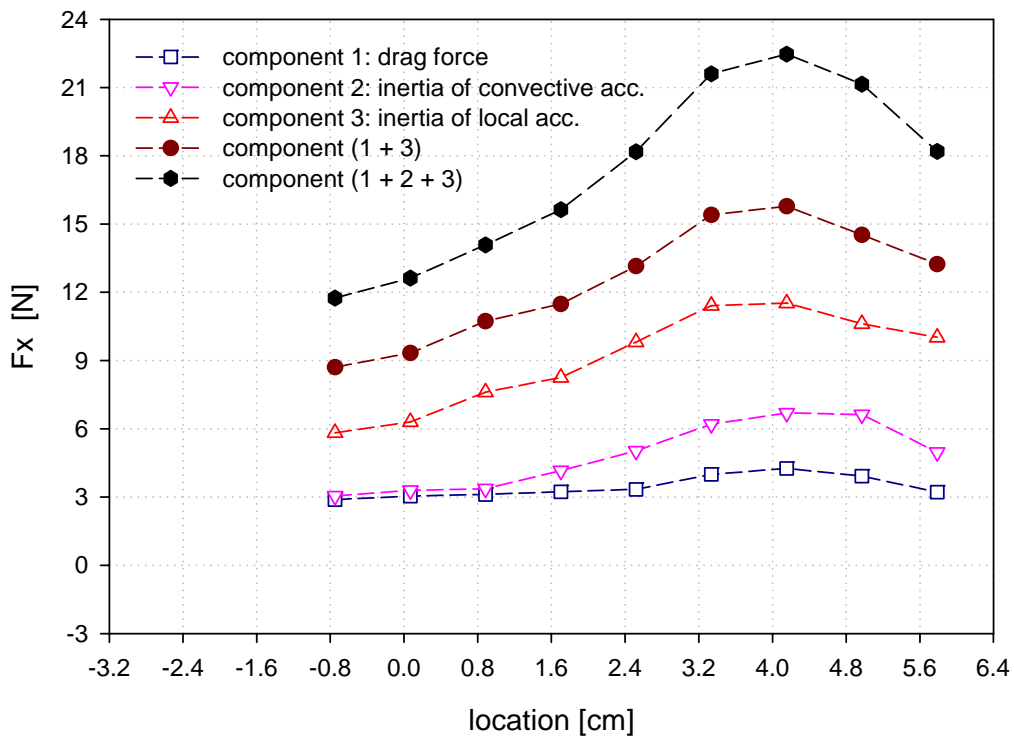Fig. 6.20 Components of horizontal wave force according to the horizontal locations.

(c) Case PH3 (Crest at x= -1.3cm).

(d) Case PH4 (Crest x = -4.1cm).

Fig. 6.20 Continued.

Fig. 6.21 (a), (b), (c), (d), (e) and (f) show the time series of wave horizontal forces on a vertical truncated cylinder at the wave crest for Case PH1 and Case PH2. The draft of a vertical truncated cylinder was -6 cm due to field of view of PIV. Also the highest point of cylinder is 3 cm because of available data of local acceleration. Results of the linear extrapolation and the modified stretching overpredict horizontal wave forces in the Case PH1 and Case PH2 as shown in Fig. 6.21 (a), (c), (d), and (f). Prediction of the Wheeler stretching underpredicts wave forces for both cases as shown in Fig. 6.21 (b) and Fig. 6.21 (e). The horizontal wave forces are not normalized in Fig. 6.21.
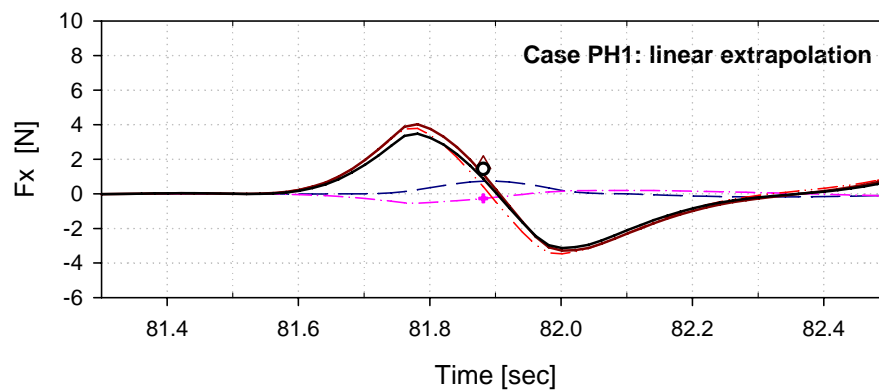
(a) Linear extrapolation method for Case PH1.
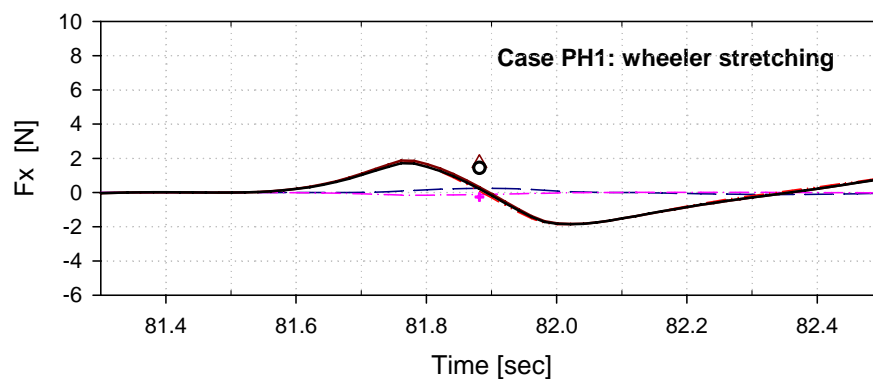
(b) Wheeler stretching method for Case PH1.

Fig. 6.21 Time series of the horizontal wave forces from z = -6cm to z= 3cm according to the prediction methods for the highest elevation waves in the irregular wave train.

(c) Modified stretching method for Case PH1.

(d) Linear extrapolation method for Case PH2.

(e) Wheeler stretching method for Case PH2.
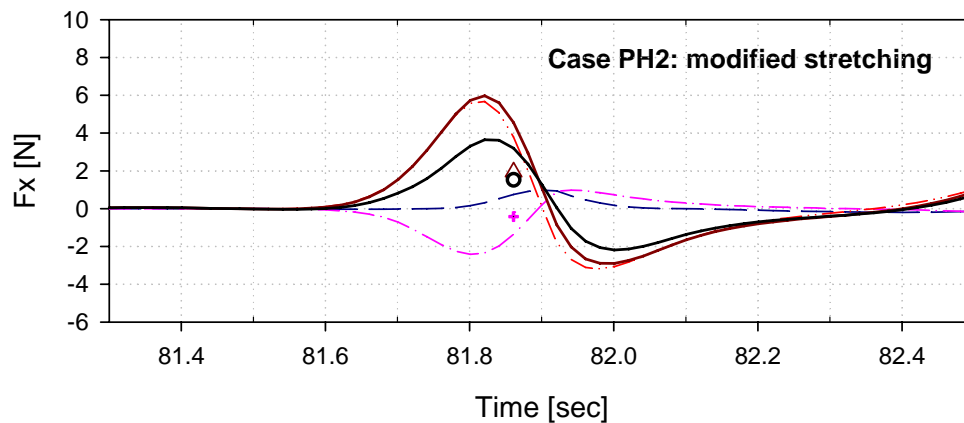
Fig. 6.21 Continued.

(f) Modified stretching method for Case PH2.

Fig. 6.21 Continued.

Fig. 6.22 (a), (b), (c), (d), (e) and (f) shows the time series of wave horizontal forces on a vertical truncated cylinder at the wave crest for Case PH3 and Case PH4. The region of computation for forces is from $z= -6$ cm to 3 cm. The Wheeler stretching underpredicts the wave forces for the both cases as shown in Fig. 6.22 (b) and (e). The results of the linear extrapolation overpredict the horizontal wave forces in the Case PH3 and Case PH4 as shown in Fig. 6.22 (a), and (d). In general, the modified stretching overpredicted the horizontal force generally in the both cases as shown in Fig. 6.22 (c) and (f). However, the discrepancies with computation based on measurements decreased noticeably. It is also obvious in the Fig. 6. 22 (c) and (f) that the magnitudes of convective terms of the modified stretching predict measurement based computations with different trend. The horizontal wave forces are not normalized in Fig. 6.22.
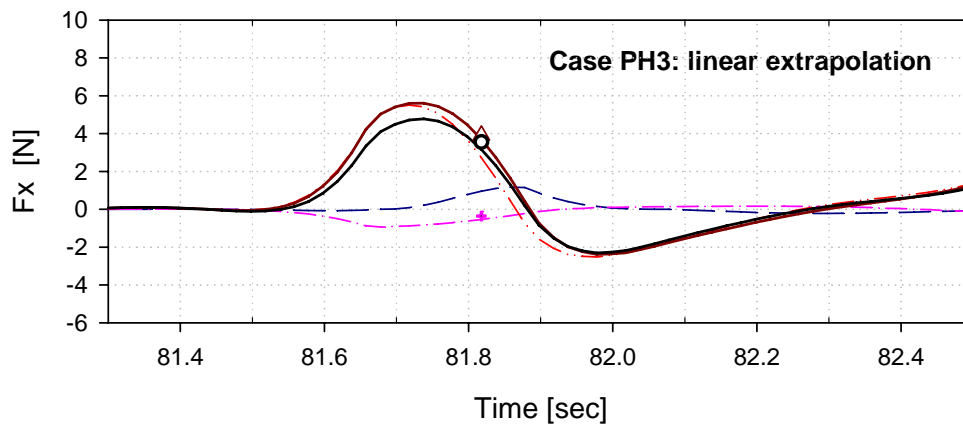
(a) Linear extrapolation method for Case PH3.
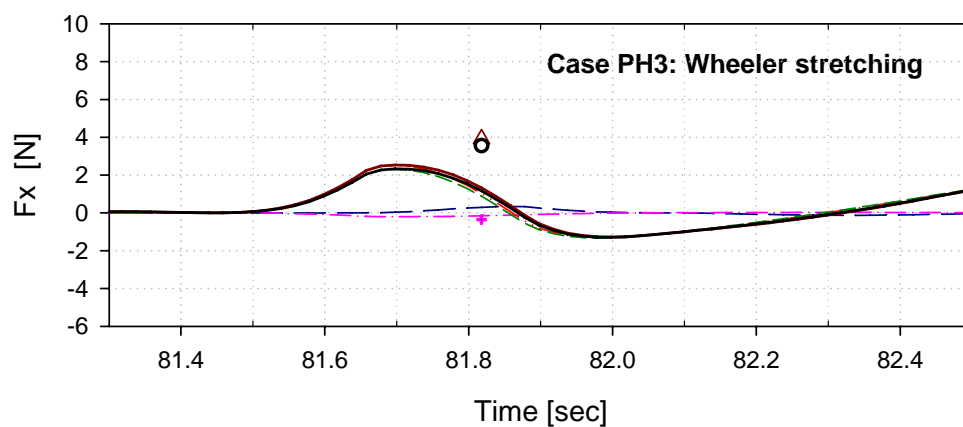
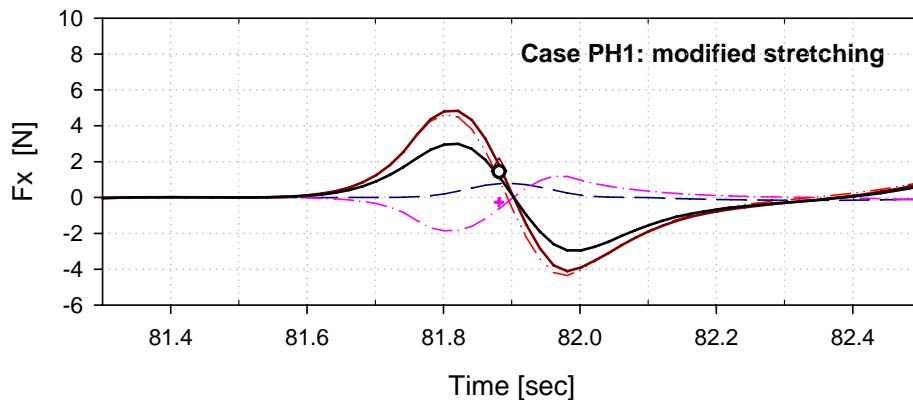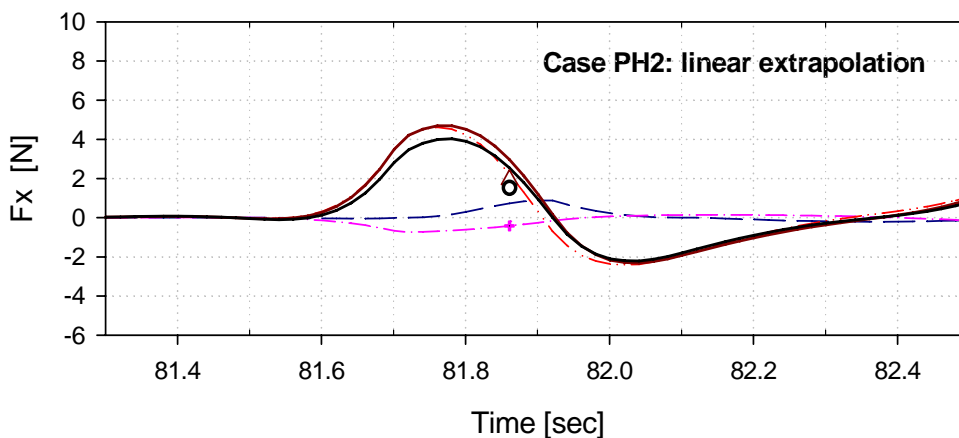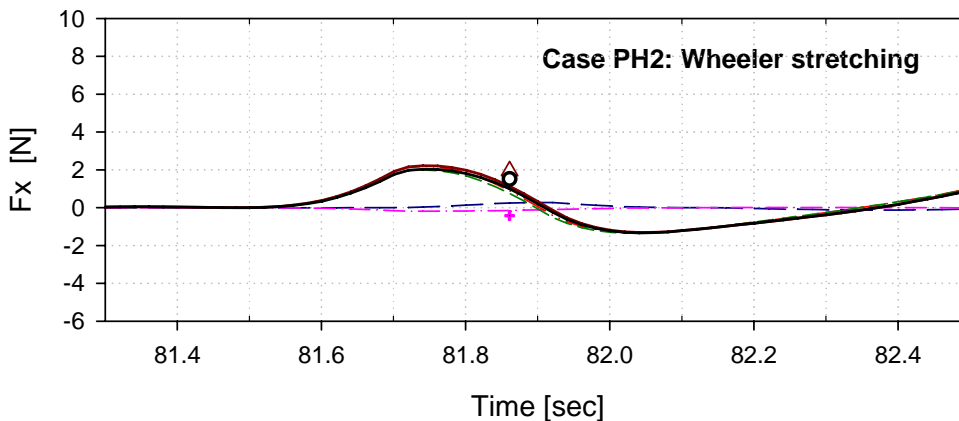(b) Wheeler stretching method for Case PH3.
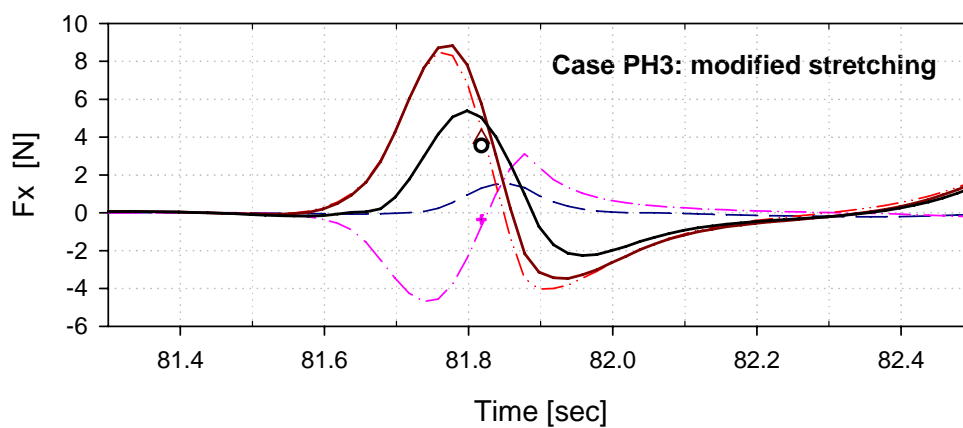
(c) Modified stretching method for Case PH3.

Fig. 6.22 Time series of the horizontal wave forces from z = -6cm to z= 3cm   according

to the prediction methods for the rogue waves in the irregular wave train.

(d) Linear extrapolation method for Case PH4.

(e) Wheeler stretching method for Case PH4.

(f) Modified stretching method for Case PH4.

Fig. 6.22 Continued.
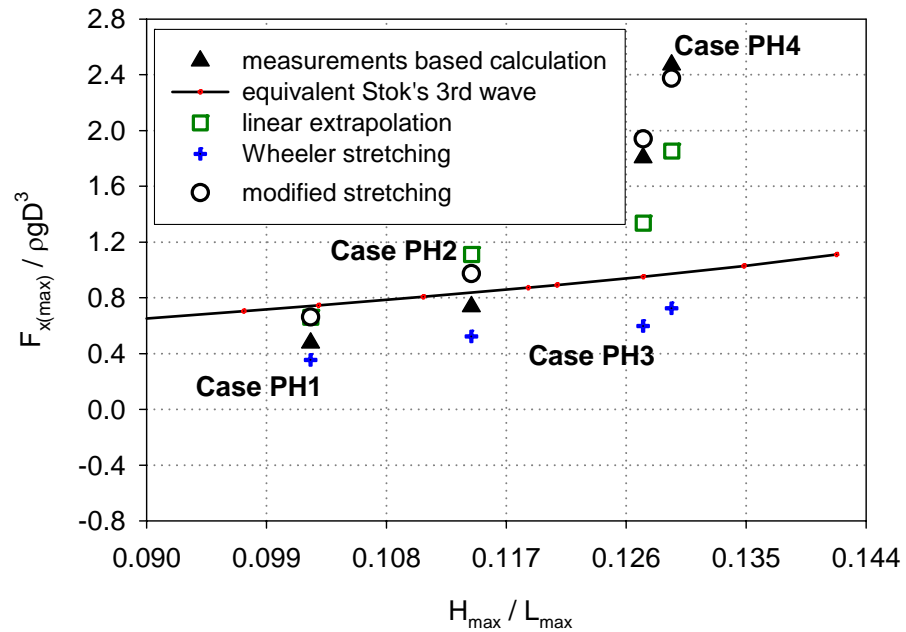
(a) Summation of Total inertia force and drag force.
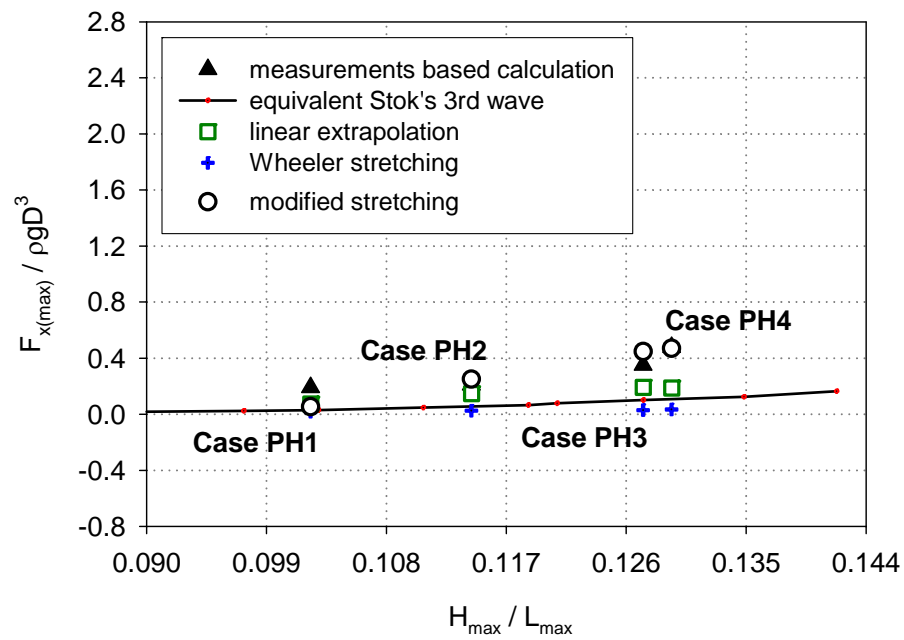
(b) Drag force.

Fig. 6.23 Maximum horizontal forces from z = -6cm to z= 3cm on a vertical truncated

cylinder in highest elevation waves or rogue waves in the irregular wave train.
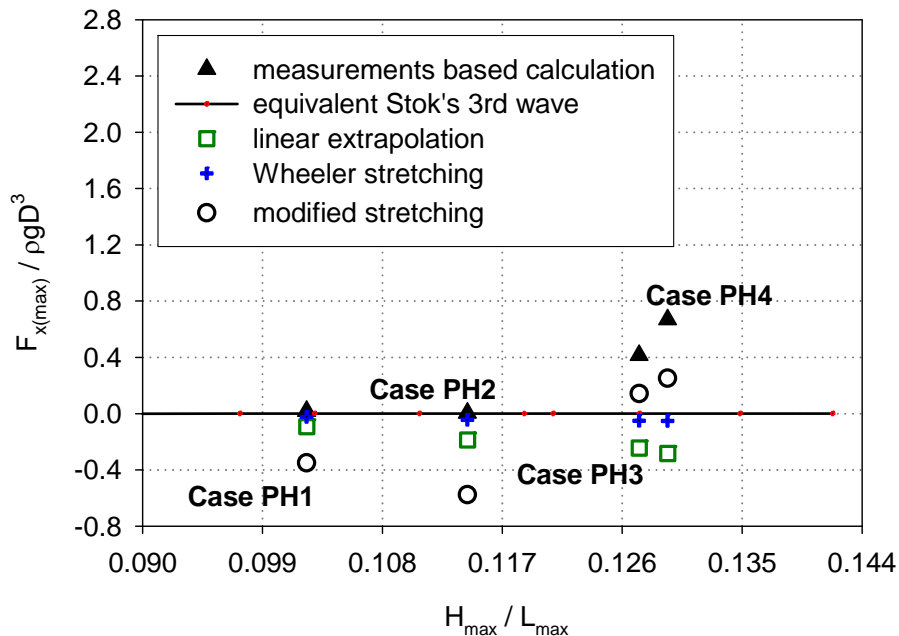
(c) Convective term of inertia force.
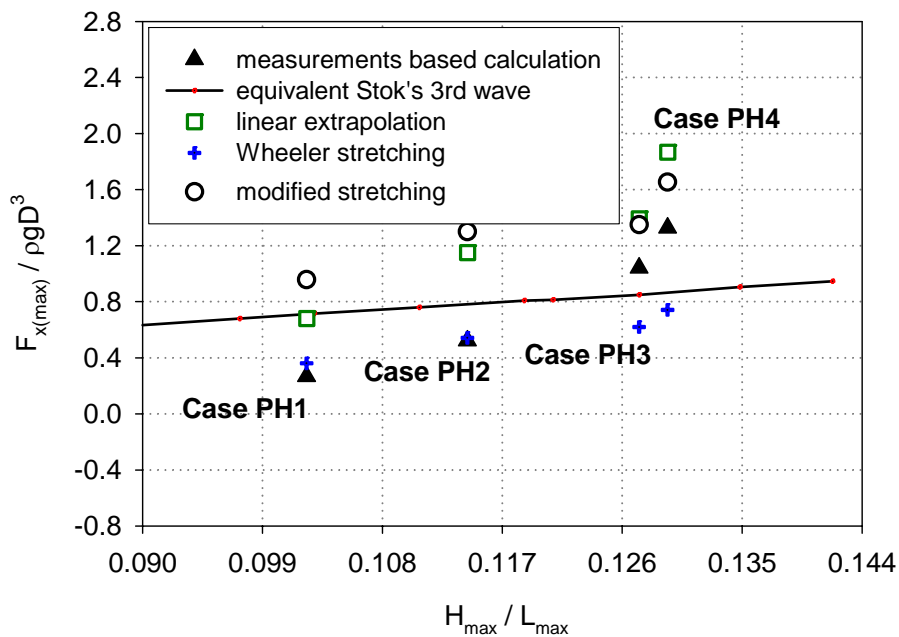
(d) Local term of inertia force.

Fig. 6.23 Continued.

Fig. 6.23 (a), (b), (c), and (d) shows the maximum horizontal wave force on a vertical truncated cylinder at vertical region from $z=$ -6 cm to $z=$ 3 cm. This vertical region is caused to the longitude length of FOV of PIV and missing data of local acceleration from measurement-based computation, therefore, the data from the PIV measurements only available in this vertical region. The total forces predicted by modified stretching are agreed well with computations based on measurements for Case PH3 and Case PH4. However, the magnitudes of convective terms and local terms show differences. The magnitude of drag force is much smaller than that of inertia forces for all cases. It is also observed in Fig. 6.23 (c) that the convective term of inertia for Case PH1 and Case PH2 is not dominant as like drag force. The magnitude of total forces for Case PH4 is more than twice as great as that of Case PH2.

Fig. 6.24 (a), (b), (c), (d), (e) and (f) shows the time series of wave horizontal forces on a vertical truncated cylinder at the wave crest for Case PH1 and Case PH2. Because there is no measured kinematics under $z=$ -6 cm, the kinematics was obtained by interpolating based on measurements. The results of the linear extrapolation and the modified stretching overpredict the horizontal wave forces in the Case PH1 and Case PH2 as shown in Fig. 6.24 (a), (c), (d), and (f). The convective terms of the modified stretching were not predicted well as shown in Fig. 6.24 (c) and Fig. 6.24 (f). The Wheeler stretching underpredicts the wave forces for the both cases as shown in Fig. 6.24 (b), and Fig. 6.24 (e). The horizontal wave forces are not normalized in Fig. 6.24.
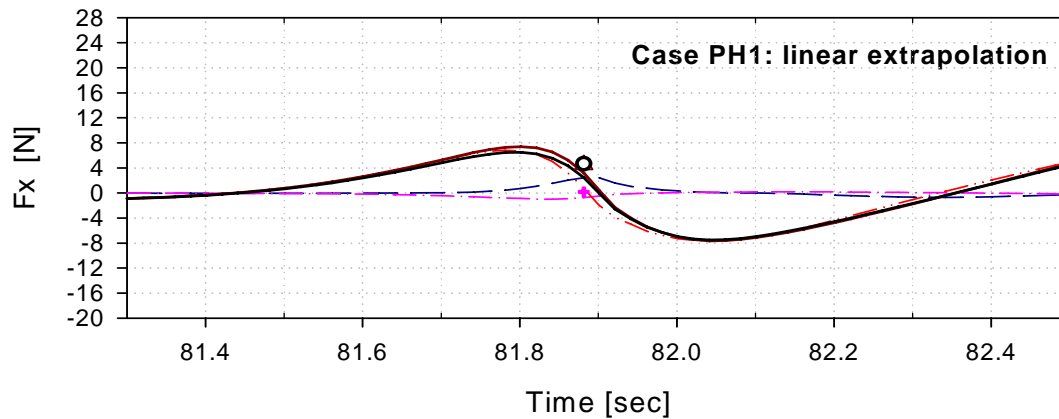
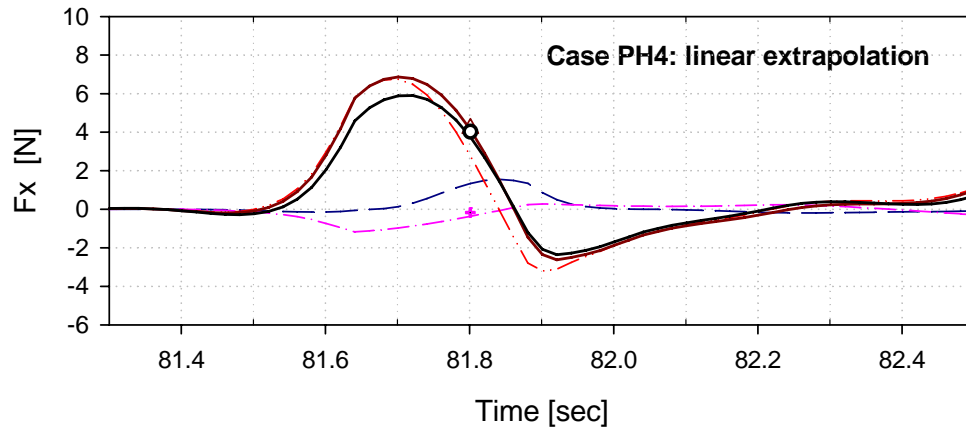(a) Linear extrapolation method for Case PH1.
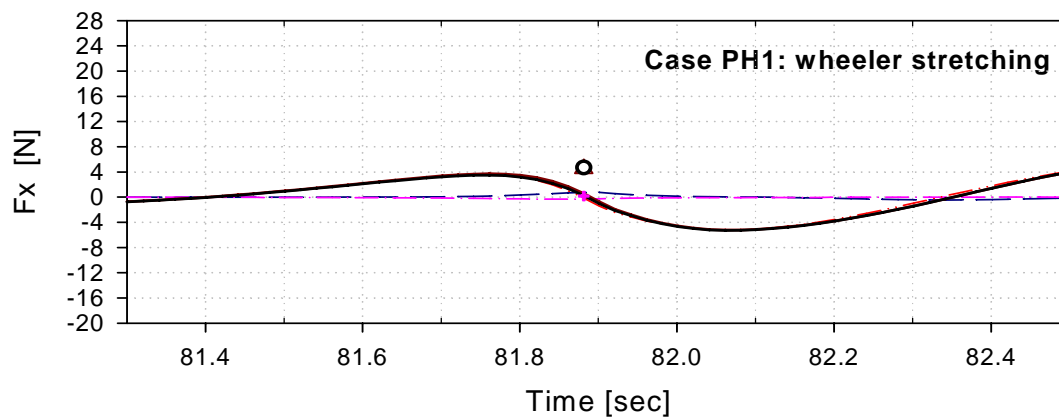
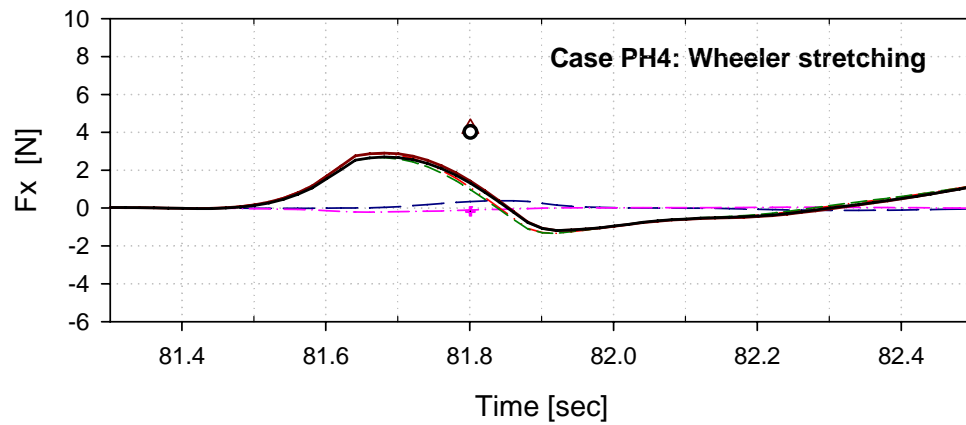
(b) Wheeler stretching method for Case PH1.
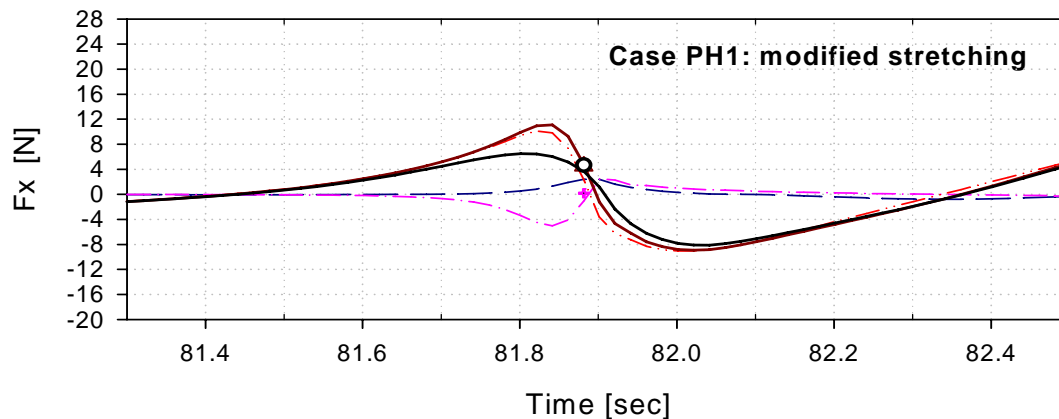
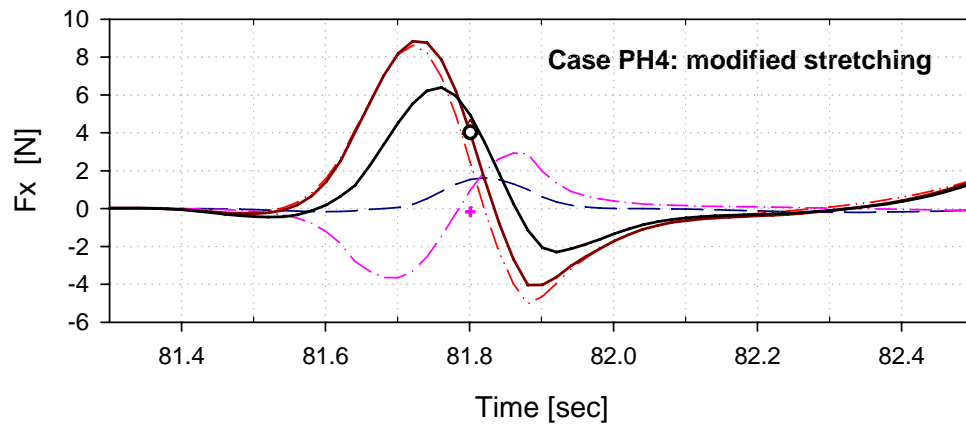(c) Modified stretching method for Case PH1.

Fig. 6.24 Time series of the horizontal wave forces from $z = -30$cm to $z=\eta$ according to the prediction methods for the highest elevation waves in the irregular wave train.
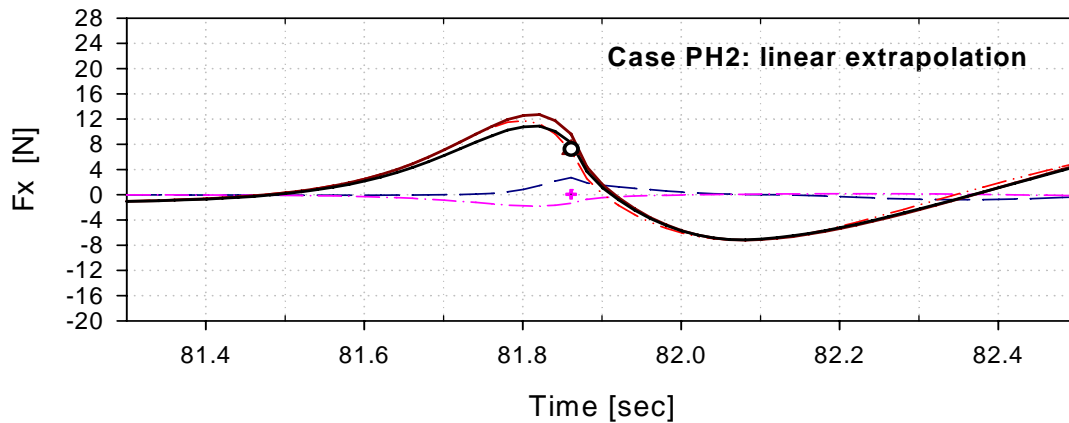
(d) Linear extrapolation method for Case PH2.
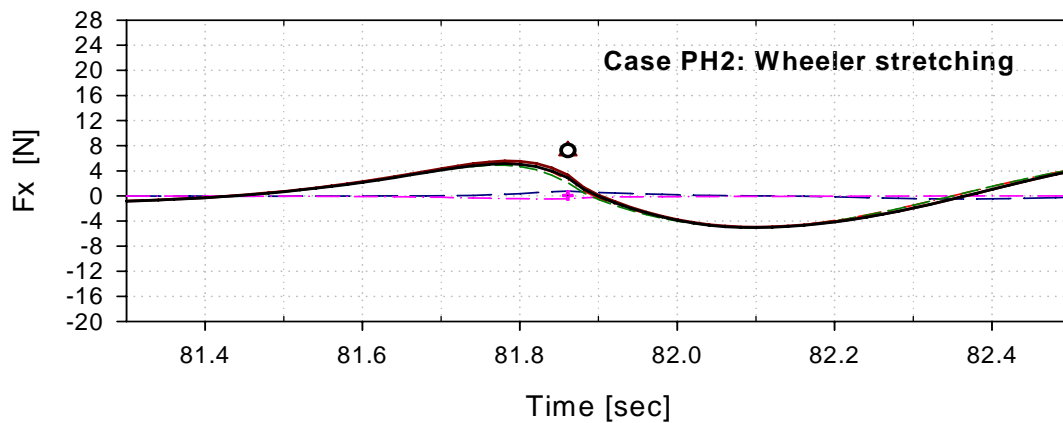

(e) Wheeler stretching method for Case PH2.
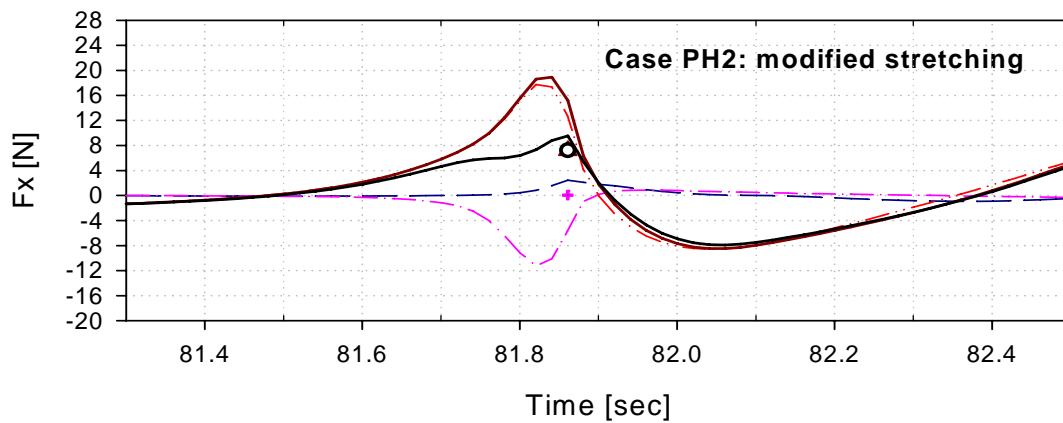
(f) Modified stretching method for Case PH2.

Fig. 6.24 Continued.

Fig. 6.25 (a), (b), (c), (d), (e) and (f) shows the time series of wave horizontal forces on a vertical truncated cylinder at the wave crest for Case PH3 and Case PH4. The region of computation for forces is from $z= -30$ cm to $z=\eta$. The Wheeler stretching and linear extrapolation underpredicts the wave forces for the both cases as shown in Fig. 6.25 (a), (b), (d) and (e). It is interesting that the results of linear extrapolation were underestimated in the rogue waves of Case PH3 and Case PH4 as shown in Fig. 6.25 (a) and (d). Prediction of the modified stretching shows good agreements with the horizontal forces of measurements based computations generally as shown in Fig. 6.25 (c) and (f). However, it is also obviously observed in the Fig. 6. 25 (c) and (f) that the trends of convective terms of the modified stretching are quite different with measurement based computations. The horizontal wave forces are not normalized in Fig. 6.25.
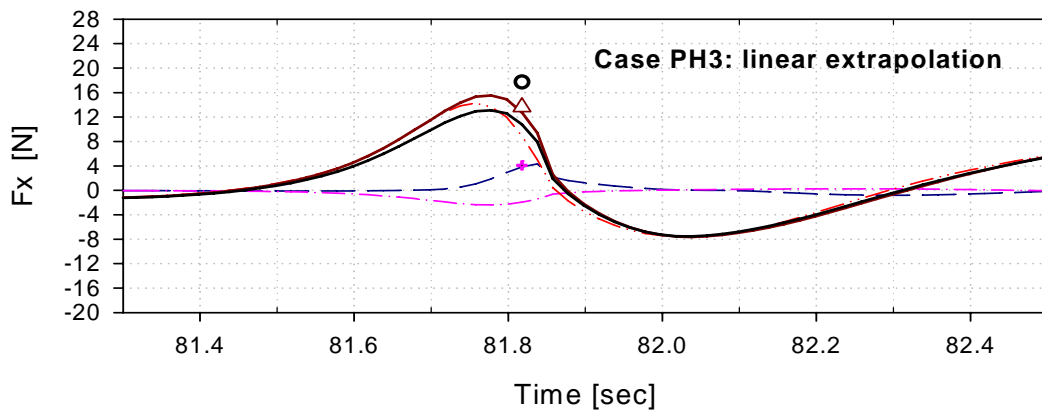
(a) Linear extrapolation method for Case PH3.

Fig. 6.25 Time series of the horizontal wave forces from $z = -30$cm to $z=\eta$ according to the prediction methods for the rogue waves in the irregular wave train.
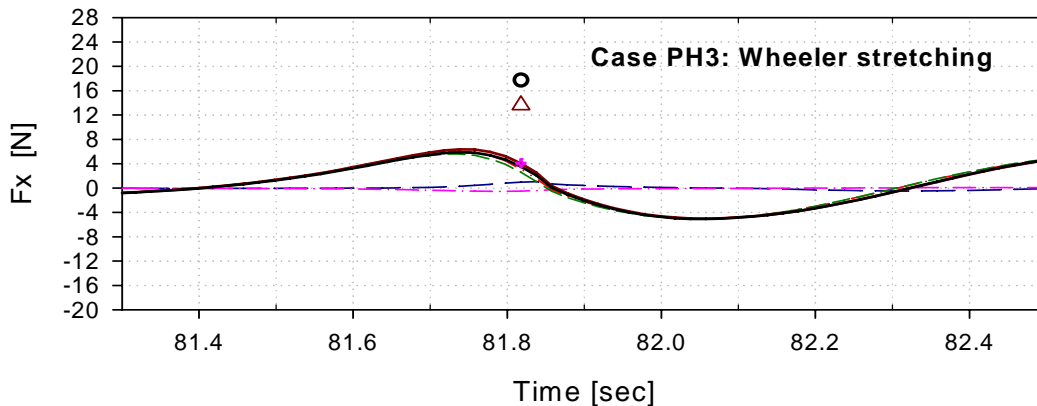
(b) Wheeler stretching method for Case PH3.
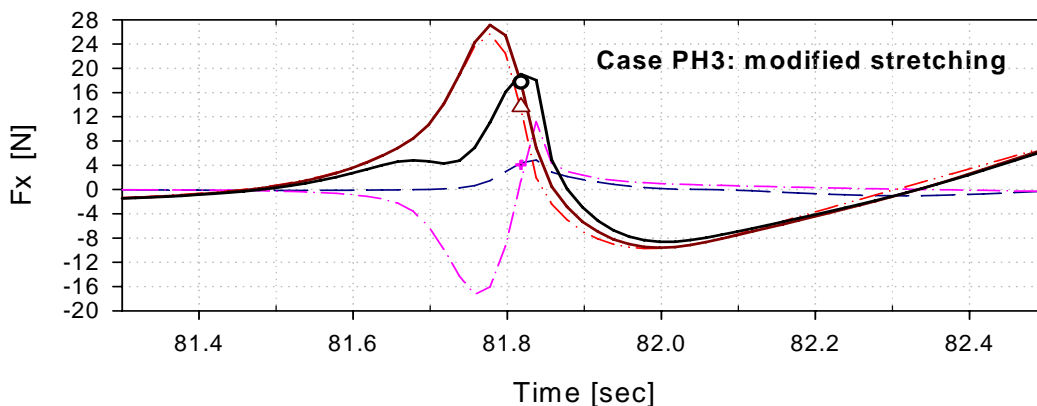
(c) Modified stretching method for Case PH3.
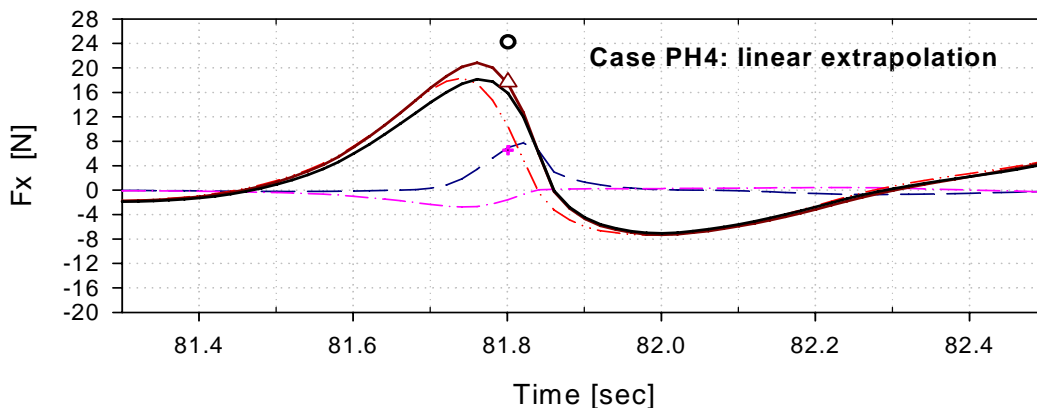
(d) Linear extrapolation method for Case PH4.

Fig. 6.25 Continued.
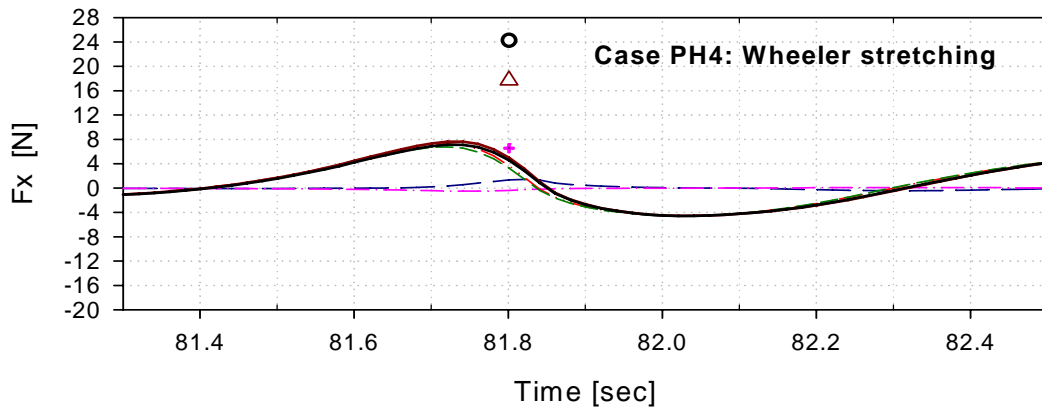
(e) Wheeler stretching method for Case PH4.
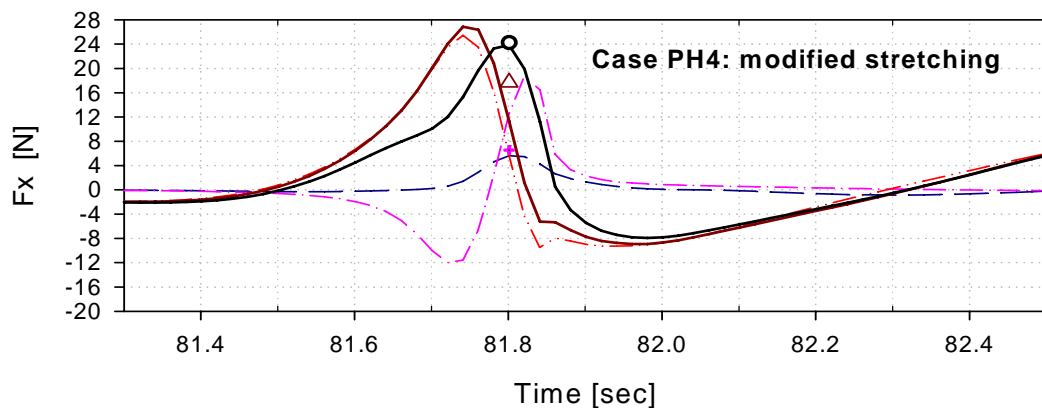
(f) Modified stretching method.

Fig. 6.25 Continued.

Fig. 6.26 (a), (b), (c), and (d) shows the maximum horizontal wave force on a vertical truncated cylinder at vertical region from $z=-30$ cm to $z=\eta$. The total forces predicted by modified stretching agreed well with values of measurement-based computation for Case PH3 and Case PH4. However, the magnitudes of convective terms and local terms show differences. The magnitude of drag forces is much smaller than that of inertia forces for all cases. It is also observed in Fig. 6.26 (c) that the convective terms of inertia for the Case PH1 and Case PH2 is not dominant as like drag force. The magnitude of total forces for Case PH4 is more than three times as great as that of Case PH2.
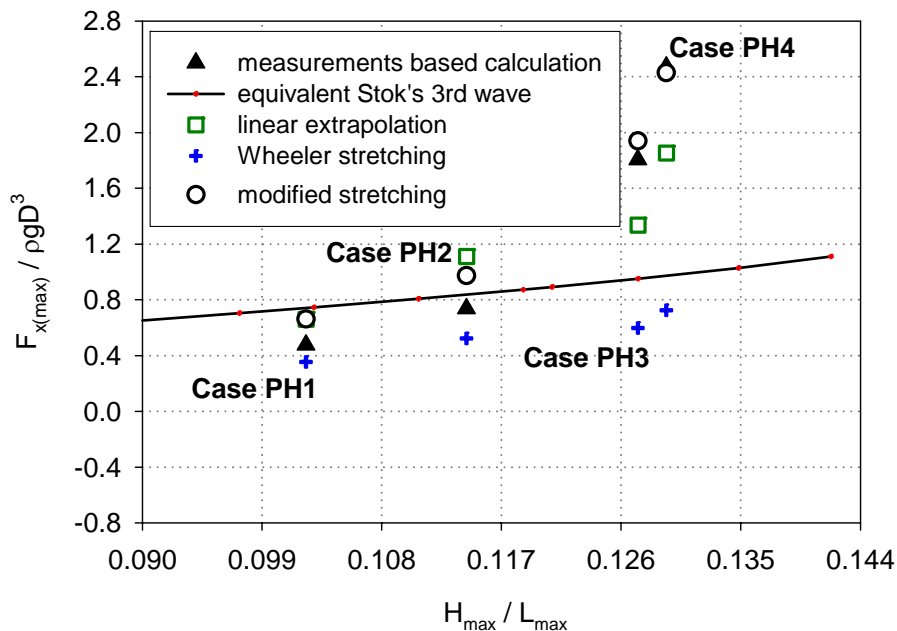
(a) Summation of total inertia force and drag force.
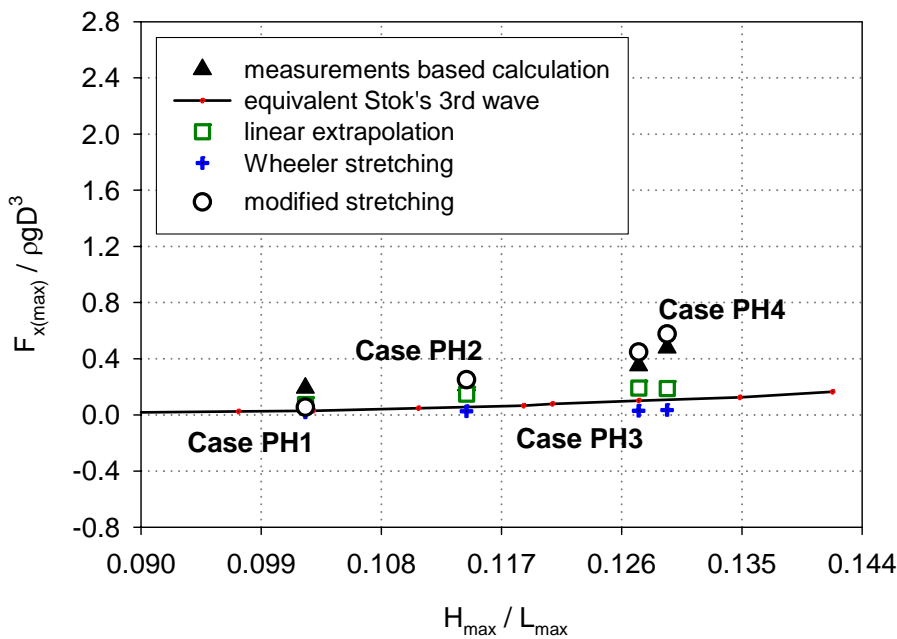
(b) Drag force.

Fig. 6.26 Maximum horizontal forces from $z = -30$cm to $z = \eta$ cm on a vertical truncated

cylinder in highest elevation waves or rogue waves in the irregular wave train.
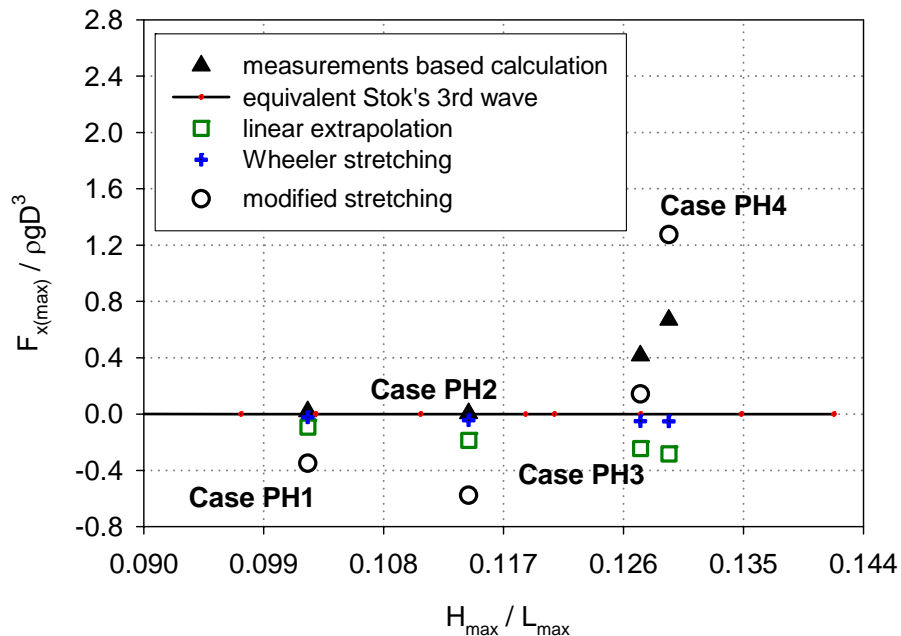
(c) Convective term of inertia force.
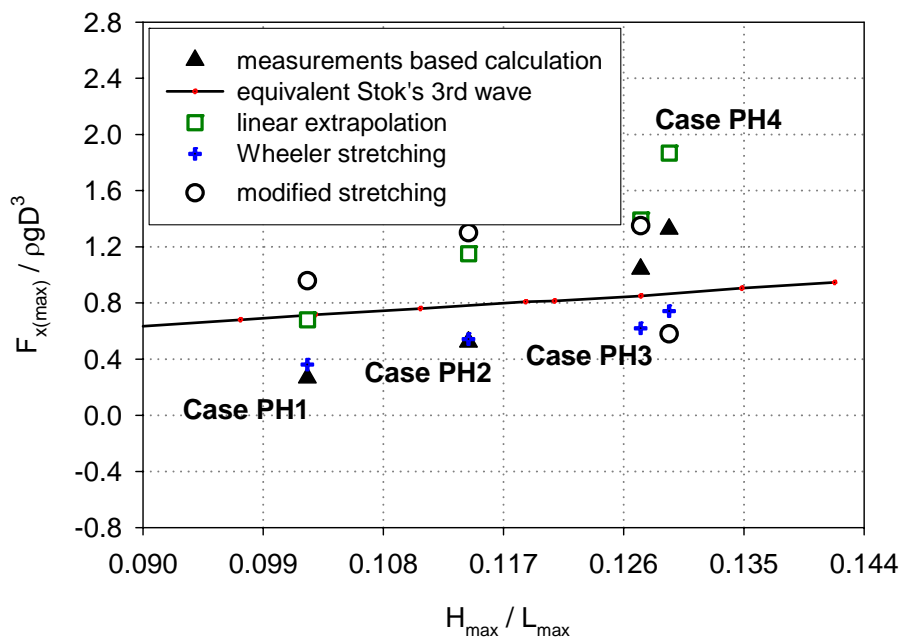
(d) Local term of inertia force.

Fig. 6.26 Continued.

6.6 Concluding remarks

Rogue wave kinematics and maximum wave kinematics in the irregular wave trains are investigated experimentally using the particle image velocimetry (PIV) system. The examined wave kinematics include elevation, velocity, local acceleration, convective acceleration and wave force. Four irregular wave trains with the four different significant wave heights H_S, the same peak wave period T, and the same JOSWAP spectrum are obtained in the 2-D wave tank. The kinematics for each case is compared with three prediction methods.

After investing experimental data of rogue wave kinematics, the rogue wave kinematics above the SWL show very highly nonlinear phenomena. The wave velocities and convective acceleration above the SWL under the wave crest increased abruptly with at the close free surface. The vertical components of kinematics under the wave crest have similar magnitude with the horizontal components, unlike in cases of regular waves.

The local accelerations under the crest of rogue waves in this study were obtained successfully except near the free surface. The convective accelerations of rogue waves were focused in this study. It is found in this study that the convective terms of total accelerations in the rogue waves contribute to total wave forces much more than those of regular waves. It could not predict well with present prediction methods for rogue waves. Compared with only the total forces of rogue waves, the total horizontal forces predicted by the modified stretching method agreed well with values of measurement-based computation.

CHAPTER VII

SUMMARY, CONCLUSIONS, AND FUTURE WORK

7.1 Summary

Some offshore structures inevitably meet extremely severe sea conditions. The extremely high wave is sometimes predictable but usually unpredictable. A precise understanding of extremely high wave kinematics is required to design offshore structures, and research is supposed to be conducted in extreme sea state conditions.

In order to understand rogue wave kinematics, a series of experiments was conducted in the 2-D wave tank. In the first step of this study, higher-order Stokes waves were generated in the 2-D wave tank, and regular wave velocities were measured using the LDV/PIV system. The measured velocities were used to compute the regular wave accelerations using the centered finite difference scheme. The local term and convective term of total acceleration were considered and computed from measurements. The regular wave loading forces were obtained by applying measured results to the Morison equation. The experimental results were compared with solutions of the third-order Stokes wave theory.

In the second step of this study, the methods for predicting irregular wave kinematics were reviewed. The higher-order Stokes wave theory is not valid to predict the maximum wave in the irregular wave train. The rogue wave is an extremely high elevation wave in the surrounding sea condition. The prediction method for rogue wave kinematics in the

irregular wave train is needed for a more precise prediction of wave kinematics.

In the third step, the laboratory rogue wave was generated in the 2-D wave tank and measured velocities near the free surface zone using PIV system. The measured velocities were used to compute the rogue wave accelerations using the centered finite difference scheme. The local acceleration and convective acceleration were studied and computed from experimental measurements. The regular wave loading forces were obtained by applying the results of direct measurement and measurement-based computation to the Morison equation. The experimental results were compared with predictions of linear extrapolation, Wheeler stretching method, and modified stretching method.

Following are the detailed conclusions drawn from each study case of the regular and rogue wave in Chapters V and VI. Finally, suggested future work is discussed at the end of this chapter.

7.2   Regular wave kinematics

The regular wave kinematics was investigated comprehensively by a series of experiments. The wave particle velocities were measured for whole wave length of five different wave slope regular waves. The solutions of the third-order Stokes wave theory were used for comparison of the measured results. From the evaluation of the experimental and analytical results for regular waves the following conclusions may be drawn:

- The higher-order Stokes wave could be generated in the 2-D wave tank.
- The magnitude of velocities under the wave crest may correlate with the wave elevation.

- As wave slope increases, the solutions of the third-order Stokes wave theory could not predict the experimental results exactly. This means that the relatively steep laboratory regular wave includes effects of uncertain nonlinearities.

- As the wave is steeper, the velocities under the wave crest are rapidly increased above the SWL but linearly increased below the SWL.

- If the regular wave has a large wave slope, the velocities under the trough wave are slightly larger than those under the wave crest.

- As the wave is steeper, the measured velocities under the zero-down crossing point are larger than that under the zero-up crossing point, but analytical solutions are always the same as each other.

- The PIV system can obtain the local acceleration, which is the time derivative of velocities. The local acceleration obtained by the PIV system was confirmed by comparing with the results of the LDV system.

- The magnitude of convective acceleration for regular waves is negligibly small comparing to that of local acceleration.

- As wave slope increases, the magnitude of convective acceleration under the wave crest is increased considerably near the crest water level.

- The wave loading forces on the slender truncated cylinder are computed and compared with solution of the third-order Stokes wave theory. This means that the measurement of wave velocities can extend to predict wave forces.

7.3   Rogue wave kinematics

The solution of the higher-order Stokes wave theory is not valid with the real sea wave. In order to predict rogue wave kinematics, the understanding of rogue wave kinematics is needed. The study of laboratory rogue waves has advantages in terms of cost, repeatability, accuracy of experiments. The rogue wave kinematics was investigated with a series of experiments. The rogue wave was obtained from a maximum wave in four different steepness irregular wave trains. The wave particle velocities were measured for whole rogue wave length. The velocities under the wave crest were the focus of this study. From the evaluation of the experimental and analytical results for rogue waves the following conclusions may be drawn:

- The rogue wave could be generated in the 2-D wave tank.

- The magnitude of velocities under the rogue wave crest is two times larger than that of the equivalent height of regular waves.

- The linear extrapolation predicts the rogue wave kinematics very sensitively due to the high cutoff frequency of wave spectra.

- In the prediction of linear extrapolation, the proper selection only of cutoff frequency can estimate the value of rogue wave kinematics accurately.

- The Wheeler stretching method always underestimated wave kinematics above the SWL in the irregular waves.

- The magnitude of convective acceleration under the rogue wave crest is very considerable.

- In the experimental results of rogue wave kinematics, the magnitude of convective acceleration under the wave crest is increased considerably near the crest water level.

- The magnitude of vertical convective acceleration under the rogue wave crest is similar to the horizontal convective acceleration.

- The modified stretching method could predict the maximum values of rogue wave kinematics well. However, it is not considered an exact component values of rogue wave kinematics. This means that the laboratory extreme rogue wave includes effects of unknown nonlinearities.

- The magnitude of convective acceleration for the rogue wave can be same as that of local acceleration.

- The horizontal wave forces on the slender vertical truncated cylinder are computed and compared with the prediction from linear extrapolation, Wheeler stretching and modified stretching. This means that the measurement of wave velocities can extend to predict wave forces.

- The maximum horizontal regular wave force is between the crest and zero-up crossing point, but the maxima horizontal rogue wave force is located very near the wave crest.

7.4   Future work

This study can be developed with the following topics. First, the effects of wave-wave interaction and multi-direction should be included in the modified stretching method to predict more precise rogue wave kinematics. Second, the wave forces of measurement base computation will be needed to verify through the measuring forces directly in the same experimental conditions. Third, the PIV system, such as the illumination source and using two high speed cameras, should be developed for the higher temporal resolution to reduce missing data of wave local accelerations near the free surface. If the PIV illumination source gives continuous exposure like the LDV system, the high temporal resolution could be obtained.

REFERENCES

Adrian,R. J., 1995. Limiting resolution of particle image velocimetry for turbulent flow. In: Proceedings of the 2nd Turbulence Research Association Conference-1. Pohang Institute of Technology, Pohang, Korea, pp. 1-19.

Airy, G. B., 1845. Tides and waves. Encyclopedia Metropolitana, London, 5, 241-396.

Alex, H., Kim, C. H., 2000. Laboratory Stokes 5th order waves on a vertical truncated cylinder. In: Proceedings of the 10th International Offshore and Polar Engineering Conference, Seattle, vol. 3, pp. 303-311.

Anastasiou, K., Tickel, R.G., Chaplin, J.R., 1982. Measurements of particle velocities in laboratory-scale random waves. Coastal Engineering, 6, 233-254.

Bea, R.G., Xu, T., Stear, J., Ramos, R., 1999. Wave forces on decks of offshore platform. Journal of Waterway, Port, Coastal, and Ocean Engineering 125 (3), 136-144.

Bonmarin, P., Kjeldsen, P., 2001. Some Geometric and kinematic properties of breaking waves. In: Olagnon, M., and Athanassoulis, G. (Eds.) Rogue Waves 2000. Ifremer, Brest, pp. 169-180.

Bosma, J., Vugts, J.H., 1981. Wave kinematics and fluid loading in irregular waves. In: Proceedings of International Symposium on Hydrodynamics in Ocean Engineering, Norwegian Hydrodynamics Laboratories, Trondheim, Norway, pp. 136-165.

Cenedese, A., Doglia, G., Romano, G. P., De Michele, G., Tanzini G., 1994. LDV and PIV velocity measurements in free jets. Experimental Thermal and Fluid Science, 5, 125-134.

Chang, K-A., Liu, PL-F., 1998. Velocity, acceleration and vorticity under breaking waves. Physics of Fluid, 10, 327-329.

Chapplear, J.E., 1961. Direct numerical calculation of nonlinear ocean waves. Journal of Geophysical Research, 66 (2), 501-508.

Choi, H., Cox, D.T., Kim, M.H., Ryu, S., 2001. Laboratory investigation of nonlinear irregular wave kinematics. In: Edge, B.L., Hemsley, J.M. (Eds.) Ocean Wave Measurement and Analysis: Proceedings of the Fourth International Symposium, Waves 2001, San Francisco, vol. 2, pp. 1685-1694.

Clamond, D., Grue, J., 2002. Interaction between envelop solitons as a model for freak wave formulations-part 1: Long time interaction. Comptes Rendus. Mecanique, 330, 575-580.

Clauss, G. F., 2002. Dramas of the sea: episodic waves and their impacts on offshore structures. Applied Ocean Research, 24, 147-161.

Cokelet, E.D., 1977. Steep gravity waves in water of arbitrary uniform depth. Philosophical Transactions of the Royal Society of London Series A-Mathematical Physical and Engineering Sciences, 286 (1335), 183-230.

De, S.C., 1955. Contributions to the theory of Stokes waves. Proceedings of Cambridge Philosophical Society, 51, 713-736.

Dean, R.G., 1965. Stream function representation of nonlinear ocean waves. Journal of Geophysical Research, 70 (18), 4561-4572.

Dean, R.G., 1970. Relative validities of water wave theories. Journal of Waterways Harbors and Coastal Engineering Division, ASCE, 96 (1), 105-119.

Dean, R.G., 1990. Freak wave: a possible explanation. In: Tørum, A., and Gudmestad, O.T. (Eds.) Water Wave Kinematics, NATO ASI Series, Kluwer, Dordrecht, The Netherlands, pp. 609-612.

Draper, D., 1965. Freak ocean waves. Marine Observer, 35, 193-195.

Dysthe, K.B., Trulsen, K., 1999. Note on breather type solutions of the NSL as a model for freak-waves. Physica Scripta, T82, 48-52.

Faulkner, D., 2001. Rogue waves − defining their characteristics for marine design. In: Olagnon, M., and Athanassoulis, G. (Eds.) Rogue Waves 2000. Ifremer, Brest, pp. 3-18.

Fenton, J.D., 1985. A fifth-order Stokes theory for steady waves. Journal of Waterway, Port, Coastal, and Ocean Engineering, ASCE, 111 (2), 216-234.

Forristall, G.Z., Ward, E.G., Borgman, L.E., Cardone, V.J., 1978. Storm wave kinematics. In: Proceedings of Offshore Technology Conference, Houston, No. 3227, pp. 1503-1514.

Funke, E.R., Mansard, E.P.D., 1982. The control of wave asymmetries in random waves. In: Proceedings of the 18th International Conference on Coastal Engineering, Cape Town, South Africa, pp.725-744.

Gorf, P., Barltrop, N., Okan, B., Hodgson, T., Rainey R., 2001. FPSP bow damage in steep waves. In: Olagnon, M., and Athanassoulis, G. (Eds.) Rogue Waves 2000. Ifremer, Brest, pp. 37-46.

Grue, J., 2002. On four highly nonlinear phenomena in wave theory and marine hydrodynamics. Applied Ocean Research, 24, 261-274.

Gudmestad, O.T., Connor, J.J., 1986. Engineering approximations to nonlinear deepwater waves. Applied Ocean Research, 8 (2), 76-88.

Gudmestad, O.T., 1990. A new approach for estimating irregular deep water kinematics. Applied Ocean Research 12 (1), 19-24.

Haver, S., 2001. Evidences of the existence of freak waves. In: Olagnon, M., and Athanassoulis, G. (Eds.) Rogue Waves 2000. Ifremer, Brest, pp. 129-140.

Haver, S., 2004. Freak waves: a suggested definition and possible consequences marine structures. In: Proceedings of Rogue Waves 2004 Conference, October 2004, Brest, France, Ifremer (In press).

Henderson, K.L., Peregrine, D.H., Dold, J.W., 1999. Unsteady water wave modulations: Fully nonlinear solutions and comparison with the nonlinear Schrödinger equation. Wave Motion, 29, 341-361.

Jakobsen, M.L., Dewhirst, T.P., Greated, C.A., 1997. Particle image velocimetry for predictions of acceleration fields and force within fluid flow. Measurement Science and Technology, 8, 1502-1516.

Jansen, P.A.E.M., 2003. Nonlinear four-wave interactions and freak waves. Journal of Physical Oceanography, 33, 863-884.

Jensen, A., Sveen, J.K., Grue, J., Richon, J.-B., Gray, C., 2001. Accelerations in water waves by extended particle imagine velocimetry. Experiments in Fluids, 30 (5), 500-510.

Kharif, C., Pelinovsky, E., Talipova, T., Slunyaev, A., 2001. Focusing of nonlinear wave groups in deep water. JETP Letters, 73 (4), 170-175.

Kim, C.H., Randall, R.E., Boo, S.Y., Krafft, M.J., 1992. Kinematics of 2-D transient water waves using laser Doppler anemometry. Journal of Waterway, Port, Coastal, and Ocean Engineering, 118 (2), 147-165.

Kim, C.H., Xu, Y., Zou, J., 1997. Impact and nonimpact on vertical truncated cylinder due to strong and weak asymmetric wave. International Journal of Offshore and Polar Engineering, 7 (3), 161-167.

Kim, N.S., Kim, C.H., 2003a. Investigation of a dynamic property of Draupner freak wave. International Journal of Offshore and Polar Engineering, 13 (1), 38-42.

Kim, N.S., Kim, C.H., 2003b. Simulation of Draupner freak wave impact force on a vertical truncated cylinder. International Journal of Offshore and Polar Engineering, 13 (4), 260-265.

Kjeldsen, P., 2001. A sudden disaster-in extreme waves. In: Olagnon, M., and Athanassoulis, G. (Eds.) Rogue Waves 2000. Ifremer, Brest, pp. 19-35.

Lavrenov, I.V., 1998. The wave energy concentration at the Agulhas current off South Africa. Journal of Natural Hazards, 17, 117-127.

Lemire, J., Freak wave rocks cruise. http://www.nydailynews.com/front/story/300826p-257523c.html, Accessed April, 2005.

Lo, J.M., Dean, R.G., 1986. Evaluation of a modified stretched linear wave theory. In: Proceedings of the 20th Coastal Engineering Conference, Taipei, Taiwan, ASCE, New York, November 1986, pp. 522-525.

Longridge, J.K., Randall, R.E., Zhang, J., 1996. Comparison of experimental irregular water wave elevation and kinematic data with new hybrid wave model predictions. Ocean Engineering, 23 (4), 277-307.

Longuet-Higgins, M.S., 1953. Mass transport in water waves, Journal of Philosophical Transactions of the Royal Society of London Series A-Mathematical Physical and Engineering Sciences, 245 (903), 535-581.

Mastroianni, M., Giant wave hits semester at sea ship. http://www.pittnews.com/vnews/display.v/ART/2005/01/28/41f9e1e0b91d4, Accessed March, 2005.

MaxWave, http://w3g.gkss.de/projects/maxwave, Accessed March, 2005.

Met Office, 1996. Hurricane 'Luis', the Queen Elizabeth 2, and a rogue wave. Marine Observer, 66 (333), 134-137.

Mofat, R. J., 1985. Using uncertainty analysis in the planning of an experiment. Journal of Fluid Engineering, 107, 173-178.

Mori, N., Yasuda, T., 2001. Effects of high-order nonlinear wave-wave interactions on gravity waves. In: Olagnon, M., and Athanassoulis, G. (Eds.) Rogue Waves 2000. Ifremer, Brest, pp. 229-244.

Myrhaug, D., Kjeldsen, S.P., 1986. Steepness and asymmetry of extreme waves and the highest waves in deep water. Ocean Engineering, 13 (6), 549-568.

Olagnon, M., van Iseghem, S., 2001. Some cases of observed rogue waves and an attempt to characterize their occurrence conditions. In: Olagnon, M., and Athanassoulis, G. (Eds.) Rogue Waves 2000. Ifremer, Brest, pp. 105-116.

Onorato, M., Osborne, A.R., Serio, M., 2002. Extreme wave events in directional, random oceanic sea state. Journal of Physics of Fluids, 14 (4), L25-L28.

Osborne, A.R., Onorato, M., Serio, M., 2000. The nonlinear dynamics of rogue waves and holes in deep-water gravity wave trains. Journal of Physics Letters A, 274, 386-393.

Peregrine, D.H., 1976. Interaction of water waves and currents. Advances in Applied Mechanics, 16, 9-117.

Raffel, M., Willert, C.E., Kompenhans, J., 1998. Particle Image Velocimetry, Springer-Verlag, Berlin.

Randall, R.E., Zhang, J., Longridge, J.K., 1993. Laser Doppler anemometer measurements of irregular water wave kinematics. Ocean Engineering, 20 (6), 541-554.

Rosenthal, W., Lehner, S., 2004. Results from the MAXWAVE project. In: Proceedings the 23th OMAE conference, Vancouver, Canada (In press).

Rodenbusch, G., Forristall, G.Z., 1986. An empirical model for random directional wave kinematics near the free surface. In: Proceedings the 18th Annual Offshore Technology Conference, Houston, pp. 137-146.

Schwartz, L.W., 1974. Computer extension and analytic continuation of Stokes' expansion for gravity waves. Journal of Fluid Mechanics, 62, 553-578.

Skjelbreia, L., Hendrickson, J.A., 1962. Fifth Order Gravity Wave Theory with Tables of Functions. National Engineering Science Company, Pasadena, California.

Skjelbreia, J., Berek, E., Bolen, Z., Gudmestad, O.T., Heideman, J., Ohmart, R.D., Spidsoe, N., Tørum, A., 1991. Wave kinematics in irregular waves. In: Proceedings the 10th OMAE conference, Stavanger, Norway, 1A, 223-228.

Smith, R., 1976. Giant waves. Journal of Fluid Mechanics, 77, 417-431.

Smith, S.F., and Swan, S., 2002. Extreme two-dimensional water waves: an assessment of potential design solutions. Ocean Engineering, 29 (4), 387-416.

Sobey, R.J., 1990. Wave theory predictions of crest kinematics. In: Tørum, A., and Gudmestad, O.T. (Eds.) Water Wave Kinematics, NATO ASI Series, Kluwer, Dordrecht, The Netherlands, pp. 215-231.

Stokes, G. G., 1847. On the theory of oscillatory waves. Trans. Cambridge Philosophical Society, 8, 441-455.

Swan, C., 1990. A viscous modification to the oscillatory motion beneath a series of progressive gravity waves. In: Tørum, A., and Gudmestad, O.T. (Eds.) Water Wave Kinematics, NATO ASI Series, Kluwer, Dordrecht, The Netherlands, pp. 313-329.

Swan, C., Bashir, T., Gudmestad, O.T., 2002. Nonlinear inertial loading. Part 1: Accelerations in steep 2-D water waves. Journal of Fluids and Structures, 16 (3), 391-416.

Thrasher, L.W., Aagaard, P.M., 1969. Measured wave force data on offshore platforms. In: Proceedings of Offshore Technology Conference, Houston, No. 1007, pp. 83-94.

Trulsen, K., Dysthe, K.B., 1997. Freak waves-A three dimensional wave simulation. In: Proceedings of the 21th Symposium on Naval Hydro-dynamics, The National Academy of Sciences, Washington, D.C., pp. 550-560.

Tulin, M.P., Waseda, T., 1999. Laboratory observations of wave group evolution, including breaking effects. Journal of Fluid Mechanics, 378, 197-232.

Wheeler, J.D., 1970. Method for calculating forces produced by irregular waves. Journal of Petroleum Technology, 249, 359-367.

Westerweel, J. 1993. Digital particle image velocimetry – Theory and application, Ph.D Dissertation, Delft University, The Netherlands.

Westhuis, J., van Groesen, E., Huijsmans, R., 2001. Experiments and numerics of bichromatic wave groups. Journal of Waterway, Port, Costal, and Ocean engineering, 127 (6), 334-342.

Willert, C.E., Gharib, M., 1991. Digital particle image velocimetry. Experiments in Fluids, 10(4), 181-193.

Wu, C.H. Nepf, H., 2002. Breaking criteria and energy losses for three-dimensional wave breaking. Geophysical Research, 107 (c10), (41)1-18.

Wu, C.H., Yao, A., 2004. Laboratory measurements of limiting freak waves on currents. Geophysical Research, 109(c12002), 1-18.

Zelt, J.A., Gudmestad, O.T., Skjelbreia, J.E., 1995. Fluid accelerations under irregular waves. Applied Ocean Research, 17, 43-54.

Zhang, J., Chen, L., Ye, M., Randall, R.E., 1996. Hybrid wave model for unidirectional irregular waves-part I. Theory and numerical scheme. Applied Ocean Research, 18, 77-92.

Zhang, J., Randall, R.E., Spell, C.A., 1992. Component wave interactions and irregular wave kinematics. Journal of Waterway, Port, Coastal, and Ocean Engineering, 118 (4), 401-416.

Zou, J., Kim, C.H., 2000. Generation of strongly asymmetric wave in random seaway. In: Proceedings of the 10th International Offshore and Polar Engineering Conference, Seattle, pp. 95-100.

VITA

Hae-jin Choi was born in Busan, Korea on September 8, 1965. He graduated from Pusan National University with a Bachelor of Science in naval architecture and ocean engineering in February, 1992. He entered the graduate school at Texas A&M University and received a Master of Science in ocean engineering in December, 1997. After graduation, he entered the graduate program at Texas A&M University in January, 1998 and received a Ph.D. in ocean engineering in December, 2005. He is married to Joo-Youn Lee and is a father of Ho-Jeong Choi, Chi-Won Choi and Sang-Won Choi.

His permanent address is:

Busan-si, Dongnae gu,

Onchoen2-dong, Lucky Apt 15-1405

Busan, Korea 607-062

e-mail address: moses@pnu.edu